Constraining the Diffuse Supernova Neutrino Background in Super-Kamiokande with Gadolinium and Precision Measurements of Photosensors for Hyper-Kamiokande

Soniya Samani
University College
University of Oxford

A thesis submitted for the degree of
Doctor of Philosophy

Hilary 2024

Abstract

The detection of neutrinos produced from core-collapse supernovae will provide invaluable insights into constraining cosmological models, explosion dynamics, star formation and neutrino properties. Given the low burst rate of Milky Way supernovae, there is strong interest in detecting the accumulated flux of neutrinos from more distant supernovae, known as the Diffuse Supernova Neutrino Background (DSNB). The gadolinium-loaded Super-Kamiokande (SK) experiment currently exhibits the best sensitivity for the discovery of the DSNB flux due to enhanced neutron tagging capability with 0.011% $Gd_2(SO_4)_3 \cdot 8H_2O$, as per this analysis. However, the low-energy signal is dominated by cosmic muon spallation and atmospheric neutrino backgrounds. This thesis presents a novel approach to atmospheric NCQE background reduction by leveraging the spatial and temporal features of events in SK with the discriminative power of Convolutional Neural Networks (CNNs). The techniques developed in this work were applied to a full DSNB search using 552.2 days of data from the SK-VI phase and demonstrated a 40 - 60% reduction in the expected NCQE background spectrum compared to the previous analysis. Since no significant excess of signal events was observed in the data, the observed and expected upper limits of the DSNB flux were determined to be 0.27 – 16.03 and 0.31– 49.53 $\mathrm{cm}^{-2}\mathrm{s}^{-1}\mathrm{MeV}^{-1}$, across the energy bins. The results highlight the potential that further developing Machine Learning techniques has to improve sensitivity to the DSNB flux.

The Hyper-Kamiokande experiment is a next-generation water Cherenkov detector that will be able to constrain neutrino oscillation parameters, measure supernova neutrinos, and measure CP violation in the lepton sector with unprecedented statistical precision. However, these analyses will rely on an effective outer detector (OD) to veto against cosmic muon backgrounds. In this thesis, the OD's photosensor arrangement has been optimised and the performance of wavelength-shifting (WLS) plates was evaluated in two unique setups. The optical measurements made in this work improved on existing absorbance results and demonstrated a previously unknown artefact of Mie Scattering present in all samples. In addition, a new water-based test facility, called BabyK, was constructed to determine the light collection efficiency of all samples in ultra-pure water. This work proposes instrumenting $\sim$7,200 photosensors and using either V.A. Kargin POPOP50-PPO3000 or Kuraray B2 WLS plates in the OD design.

Acknowledgements

I am truly fortunate to have had the guidance and support of my supervisor, colleagues, friends, and, above all, my family throughout this DPhil. Completing this thesis would not have been possible without each one of you.

Firstly, my deepest thanks to my supervisor, Dave Wark, for your mentorship over the past four years. I am grateful for your extensive expertise and input, which have shaped my progress and myself as a researcher. I will always treasure our discussions on neutrino physics and life, especially those with a guitar in hand.

To Jeff Lidgard, Rich Gardner, and Johnny Fill, thank you for helping me bring BabyK to life. Despite the equipment failures, rust, power cuts, and a global pandemic, you dedicated your spare time and energy to help with the design, construction and running of BabyK. For the analysis, I extend my most sincere appreciation to the HyperK OD group, especially to Federico Nova, Oleg Mineev, Roger Wendell, Francesca Di Lodovico, and Anna Holin, for your time and expertise during all of my HyperK projects.

Thank you to Robert Taylor for allowing me to use his incredibly sophisticated optical laser setup and for graciously teaching me about spectrophotometry. I would also like to thank George Burton for joining me in the lab and helping me with the endless measurements. You made the long days more enjoyable with conversations, laughter, and even some Elton John.

I extend my humble thanks to all the SuperK collaborators who I have worked with. I thoroughly enjoyed working with Sonia El Hedri, Ashida-san, and Alberto Giampaolo, and I appreciate their guidance and time in teaching me the ins and outs of the DSNB analysis. Also, I give my thanks to the SuperK lowE group leaders, convenors and to the WatChMaL group members for their expertise.

To members of the Oxford accelerator neutrino group, especially Giles Barr, Alfons Weber, Kirsty Duffy, Daniel Barrow, Laurence Cook, Clarence Wret, Phil Rodrigues, Patrick Green, and Babak Abi, thank you for your advice and input over the last few years. Thank you to all of my fellow students for making the office an enjoyable place to be, in particular to John Plows and Tom Holvey for their friendship. Also, I give my thanks to Daniela Bortoletto and Sue Geddes for welcoming me into Oxford.

I very much appreciate the love and support of all my friends, near and far, who kept me grounded and reminded me to have fun every once in a while. A special thank you to my partner for your support, kindness, and encouragement during the most challenging, yet happiest part of my DPhil.

Finally, and most importantly, to my dearest mother and sister, Charu and Preeya: you are two of the strongest, bravest, and most loving women I know. Preeya, I am deeply thankful for the physical, emotional, and financial assistance throughout these years, and for being a wonderful older sister to me. Mum, your strength, wisdom, and love inspire me every day. You have stood by my side through every hardship, challenge, failure, and success without faltering. This thesis is dedicated to you, Mum. I wouldn't be who I am today, nor would I have accomplished anything, without your love and support.

Statement of Originality

I confirm that the work presented in this thesis is entirely my own original work. Any research, figures, or results sourced externally have been appropriately acknowledged and referenced. This thesis has not been submitted for any other qualification. Below is a summary of each chapter:

- Chapter 2 outlines the theoretical groundwork done by other researchers.
- Chapter 3 discusses the Super-Kamiokande (SK) experiment, referencing published SK collaboration papers.
- Chapter 4 describes simulation and reconstruction tools used in the analysis, produced by the SK collaboration and referenced groups.
- Chapter 5 overviews the relevant signal and backgrounds, referencing work by other researchers.
- Chapter 6 provides a theoretical overview of Machine Learning. It details the development of the Gamma and Positron CNN model (GAPNet), adapted from ResNet18 and the WatChMaL framework. All of the work was then carried out by the author.
- Chapter 7 discusses reduction techniques developed by SK collaborators. The author optimised the third reduction cuts and developed the novel fifth reduction step using the GAPNet model.
- Chapter 8 uses techniques from other experiments and SK collaborators, with references. The author carried out the NCQE spectrum shape uncertainty for the SK-IV analysis and the final background spectra comparisons.
- Chapter 9 presents the author's DSNB analysis results of the SK-VI dataset.
- Chapter 10 introduces the Hyper-Kamiokande (HK) experiment, referencing technical notes. The author completed the photosensor configuration optimisation study using HK simulations and SK atmospheric data and reduction tools.
- Chapter 11 describes absorption and attenuation length measurements of wavelength-shifting (WLS) plates using a UV-VIS Spectrophotometry setup, provided by Prof. Robert Taylor. George Burton did four measurements; the author performed all other measurements and the full analysis.
- Chapter 12 details the design and construction of the BabyK water-based WLS test facility, carried out by the author and University of Oxford technicians. The author carried out all of the measurements, analysis, and the results.

Contents

Appendices

List of Figures

List of Tables

1

Introduction

The first and only direct observation of neutrinos from SN 1987A provided evidence of neutrino transport and an opportunity to further develop supernova models. Given the low statistics from this event and other theoretical uncertainties, there are still many unknowns and computational challenges related to neutrino-driven explosion mechanisms. A galactic core-collapse supernova (CCSN) would provide an abundance of supernova neutrinos, however, it is estimated that these occur at a rate of a 1.63 ± 0.46 per century within the Milky Way galaxy [1]. Therefore, there is strong motivation to extend the search window and measure the accumulated, steady source of neutrinos produced from supernovae farther away, referred to as the Diffuse Supernova Neutrino Background (DSNB). The detection of the DSNB flux would offer unique insights into the core-collapse mechanism, supernova neutrino emission, star formation, and the expansion of the universe. The DSNB analysis in the Super Kamiokande experiment forms one of the key topics covered in this thesis.

The Super-Kamiokande (SK) experiment has set the most stringent upper limits on the DSNB $\overline{\nu}_e$ flux above 13 MeV. In 2020, 13 tons of gadolinium sulfate octahydrate ($\mathrm{Gd_2(SO_4)_3 \cdot 8H_2O}$) were loaded into the detector to enhance neutron detection efficiency and increase sensitivity to the DSNB flux. Despite only having 20% of the dataset size, the first search conducted in the SK-Gd era produced results comparable to previous searches. However, the analysis remains challenging due to dominant backgrounds, such as the atmospheric NCQE background, even with the addition of gadolinium. This work presents the first implementation of a Machine Learning technique designed to target the atmospheric NCQE background in the SK DSNB analysis, which is described in the Chapters 2, 3, 4, 5, 6, 7, 8, and 9.

Hyper-Kamiokande (HK) is the next-generation water Cherenkov detector that will have enhanced sensitivity to neutrino oscillation parameters, the neutrino mass hierarchy as well as increased capability to detect neutrinos from supernovae. To achieve its physics goals, the detector will require an efficient outer detector (OD) for vetoing cosmic-ray muons and reducing low-energy backgrounds. This work focuses on optimising the HK-OD design and assessing the optical properties and performance of critical photosensor components in two custom-built setups, which is presented in Chapters 10, 11, and 12.

Part I

The Diffuse Supernova Neutrino Background Search at Super-Kamiokande with Gadolinium

2

Supernova Neutrinos

2.1 Neutrinos

The neutrino is an electrically neutral fundamental particle with a half-integer spin that is subject to the Pauli Exclusion Principle [2]. They exist in three flavour eigenstates corresponding to the charged leptons: electron (ν_e), muon (ν_μ) and tau (ν_τ). Neutrinos primarily interact through the weak nuclear force and experience gravitational effects due to their small, non-zero mass. These properties allow neutrinos to traverse immense distances across space almost unimpeded, carrying information from the universe's most extreme and distant environments. This section provides an overview of neutrino oscillations in a vacuum, an essential component in modelling the neutrino flux from supernovae.

2.1.1 Neutrino Oscillations

The neutrino weak eigenstates (ν_e, ν_μ, ν_τ), referring to the states involved in weak interactions, are not equivalent to the mass eigenstates (ν_1, ν_2, ν_3), which are the states with definite masses (m_1, m_2, m_3). In a vacuum, the mixing of flavour eigenstates $|\nu_\alpha\rangle(\alpha = e, \mu, \tau)$ and the mass eigenstates $|\nu_i\rangle(i = 1, 2, 3)$

are related by:

$$|\nu_\alpha\rangle = \sum_{i=1}^{3} \mathbf{U}_{\alpha i} |\nu_i\rangle, \tag{2.1}$$

where **U** is the Pontecorvo-Maki-Nakagawa-Sakata (PMNS) mixing matrix:

$$\mathbf{U} = \begin{pmatrix} 1 & 0 & 0 \\ 0 & \cos(\theta_{23}) & \sin(\theta_{23}) \\ 0 & -\sin(\theta_{23}) & \cos(\theta_{23}) \end{pmatrix} \begin{pmatrix} \cos(\theta_{13}) & 0 & \sin(\theta_{13})e^{-i\delta_{CP}} \\ 0 & 1 & 0 \\ -\sin(\theta_{13})e^{i\delta_{CP}} & 0 & \cos(\theta_{13}) \end{pmatrix} \begin{pmatrix} \cos(\theta_{12}) & \sin(\theta_{12}) & 0 \\ -\sin(\theta_{12}) & \cos(\theta_{12}) & 0 \\ 0 & 0 & 1 \end{pmatrix}$$

The matrix is unitary and can be expressed by three rotation submatrices with mixing angles θ_{ij} and a complex phase δ_{CP}, which represents the charge-parity (CP) violating phase for the lepton sector [3, 4]. The full form of **U** contains an additional matrix with Majorana phases, which is not included here as it does not impact the oscillation calculation.

The time (t) evolution of the flavour eigenstate is

$$|\nu_\alpha(t)\rangle = \sum_i \mathbf{U}_{\alpha i} e^{-iE_i t} |\nu_i(t)\rangle, \tag{2.2}$$

where E_i is the energy eigenvalue of the ν_i mass state. The probability for a neutrino oscillating from flavour state ν_α to ν_β is calculated as

$$\begin{aligned} P\left(\nu_\alpha \to \nu_\beta\right) &= \left|\left\langle \nu_\beta \mid \nu_\alpha(t)\right\rangle\right|^2 \\ &= \left|\left(\sum_j \mathbf{U}^*_{\beta j} e^{iE_j t} \left\langle \nu_j\right|\right)\left(\sum_i \mathbf{U}_{\alpha i} e^{-iE_i t} \left|\nu_i(t)\right\rangle\right)\right|^2 \\ &= \left|\sum_j \sum_i \mathbf{U}^*_{\beta j} \mathbf{U}_{\alpha i} e^{i(E_j - E_i)t} \left\langle \nu_j | \nu_i(t)\right\rangle\right|^2 \\ &= \left|\sum_i \mathbf{U}^*_{\beta i} \mathbf{U}_{\alpha i}\right|^2 + \sum_{i \neq j} \left|\mathbf{U}^*_{\beta j} \mathbf{U}_{\alpha i}\right|^2 e^{-i(E_i - E_j)t}. \end{aligned} \tag{2.3}$$

In Equation 2.3, the time-dependent component becomes zero when the neutrinos are considered massless as $E_i - E_j \propto m_i^2 - m_j^2 = 0$, resulting in no oscillation. Therefore, neutrino oscillations can only occur for non-degenerate mass states ($m_i \neq m_j$) with non-zero mixing ($\mathbf{U} \neq I$), where I is the identity matrix.

For a neutrino with non-zero mass propagating in a vacuum, the neutrino energy E_i can be expressed as

$$E_i = \sqrt{p_i^2 + m_i^2} \simeq p_i + \frac{m_i^2}{2p_i} \simeq E + \frac{m_i^2}{2E}, \tag{2.4}$$

where the neutrino momentum is approximated as $p_i \approx E$ due to the relativistic nature of neutrinos. In the case of two-flavour neutrino oscillations, the weak and mass eigenstates are related by a 2×2 unitary mixing matrix with an angle θ, written as

$$\begin{pmatrix} \nu_\alpha \\ \nu_\beta \end{pmatrix} = \begin{pmatrix} \cos\theta & \sin\theta \\ -\sin\theta & \cos\theta \end{pmatrix} \begin{pmatrix} \nu_1 \\ \nu_2 \end{pmatrix}. \tag{2.5}$$

Using this equation and the energy relation from Equation 2.4, the oscillation probability from Equation 2.3 becomes

$$P(\nu_\alpha \to \nu_\beta) = \sin^2(2\theta)\sin^2\left(\frac{\Delta m^2 t}{4E}\right), \tag{2.6}$$

where $\Delta m^2 = m_1^2 - m_2^2$ represents the mass-squared difference of the ν_1 and ν_2 mass eigenstates. In an experiment, neutrinos are observed over a distance $L = ct$ from a production site to a detector. By expressing the distance L in terms of km, the energy in GeV, and the mass-squared difference in eV^2, the following conversion can be applied

$$\frac{\Delta m^2 t}{4E} \approx \frac{\frac{\Delta m^2}{c^4} L \cdot c^4}{4E \cdot \hbar c} \approx 1.27 \frac{\Delta m^2 \left[\mathrm{eV}^2\right] L[\,\mathrm{km}]}{E[\mathrm{GeV}]},$$

which gives the two-neutrino oscillation probability (*appearance* mode) in the form

$$P\left(\nu_\alpha \to \nu_\beta\right) = \sin^2(2\theta) \cdot \sin^2\left(1.27\frac{\Delta m^2 L}{E}\right). \tag{2.7}$$

The *survival* probability for the original neutrino to propagate without oscillating into another flavour state is given by $P\left(\nu_\alpha \to \nu_\alpha\right) = 1 - P\left(\nu_\alpha \to \nu_\beta\right)$. In this approximation, θ determines the amplitude of the oscillation and Δm^2 influences the frequency of the oscillation between different neutrino flavours. Note that in the three-flavour case, $\Delta m^2 = m_i^2 - m_j^2$. Finally, the ratio of L/E is a crucial parameter determined by the experimental conditions.

Seven neutrino oscillation parameters have been precisely measured using data from solar, atmospheric, reactor, and beam neutrino sources. The mixing angle θ_{12} and mass-squared difference Δm^2_{21} were determined through combined observations from solar and reactor neutrino experiments, including contributions from Super-Kamiokande [5], Sudbury Neutrino Observatory (SNO) [6], and KamLAND [7]. Atmospheric and long-baseline neutrino experiments have measured the θ_{23} and Δm^2_{23} parameters via the ν_μ disappearance mode. The θ_{13} is measured by several reactor neutrino experiments [7, 8]. However, the ordering of the mass-squared eigenstates, which is either $\Delta m^2_{23} > 0$, referred to as normal hierarchy (NH) or $\Delta m^2_{23} < 0$, defined as inverted hierarchy (IH) is yet to be determined, along with the δ_{CP} phase. However, NH is moderately favoured by recent experiments and the latest results from the Tokai to Kamioka (T2K) experiment have excluded $\sin(\delta_{CP}) = 0$ at the 3σ level [9].

2.2 Supernovae

The term *supernova* was first introduced by Baade and Zwicky to describe the powerful explosion and transformation of an *"ordinary star into a neutron star"* [10, 11]. They proposed that supernovae release a substantial amount of gravitational energy, comparable to the rest mass of the progenitor star, to form a compact neutron star with high density. This concept forms the basis of our current understanding of the supernova mechanism and the birth of neutron stars.

Supernova explosions that undergo *core-collapse* typically occur for stars more massive than eight solar masses ($M_\odot$), and the process radiates $\mathcal{O}(10^{53}\,\mathrm{erg})$ of energy [12]. It was first accepted that thermonuclear burning of material surrounding the core liberated enough energy to drive the explosion [13, 14]. However, it was later demonstrated in numerical simulations that neutrino interactions play a vital role in the dynamics of the explosion [15]. Further theoretical advancements in the field led to the understanding that the shock expansion after the initial phase is reignited by a delayed neutrino-driven mechanism [16].

This section outlines the process of the core-collapse explosion mechanism, with emphasis on neutrino dynamics.

2.2.1 Supernova Classification

Supernovae are classified according to their observed spectral features and time evolution of their emission [11, 17]. Figure 2.1 shows the primary types of supernovae, classified as types Ia, Ib, Ic, IIP (Plateau), and IIL (Linear). Type I supernovae are characterised by the lack of hydrogen lines (Balmer series), whereas those showing this feature are classified as Type II. Type I events are further subdivided into supernovae that contain silicon lines (Type Ia), helium lines (Type Ib), or neither (Type Ic). Type II supernovae are separated into Type IIP, which exhibit a period of constant luminosity in their light curve, and Type IIL, characterised by a linear decline in brightness over time.

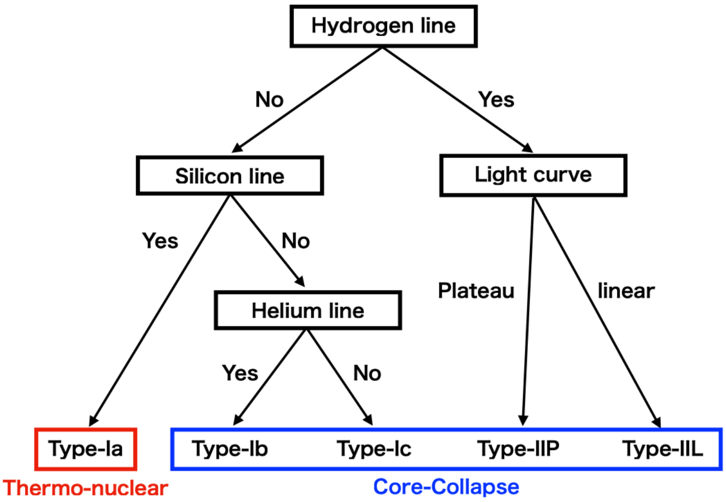

Figure 2.1: Schematic diagram of the supernova classification system. This diagram is taken from Ref. [18].

Type Ia supernovae occur in binary star systems, resulting from the thermonuclear explosion of white dwarfs accreting mass from the accompanying star. The kinetic energy released by these supernova explosions amounts to approximately $\sim 10^{51}$ erg. Neutrinos do not significantly impact this explosion mechanism and are mostly created through electron capture processes,

$$e^- + (A, Z) \rightarrow (A, Z-1) + \nu_e \tag{2.8}$$

$$e^- + p \rightarrow n + \nu_e. \tag{2.9}$$

The Ib, Ic, IIP, and IIL types of supernovae occur due to the gravitational collapse of their cores, which is facilitated by a neutrino-driven explosion mechanism. These events are collectively known as core-collapse supernovae (CCSN). The process releases a significant amount of gravitational energy (E_g) according to the formula

$$E_{\mathrm{g}} \approx 3.6 \times 10^{53} \left(\frac{M_{\mathrm{ns}}}{1.5 M_{\odot}}\right)^2 \left(\frac{R_{\mathrm{ns}}}{10\ \mathrm{km}}\right)^{-1} \mathrm{erg}, \tag{2.10}$$

where M_{ns} represents the mass of the neutron star and R_{ns} denotes its radius [12]. Approximately 99% of the total explosion energy is emitted in the form of neutrinos. Therefore, measuring the neutrino flux produced from CCSN provides insights into the internal mechanisms and explosion dynamics of these types of supernovae.

2.2.2 Core-Collapse Supernova Explosions

This section describes the neutrino-driven explosion mechanism of a CCSN. Figure 2.2 shows a schematic diagram of the full process, where the numbering of each subfigure corresponds to the steps in the below headings.

Stellar Nucleosynthesis: Steps 1 - 3

Stars originate from the gravitational collapse of interstellar matter, which forms a small dense core. During the main sequence phase, the star maintains hydrostatic equilibrium as the nuclear fusion of hydrogen into helium generates enough pressure to counteract gravitational forces (1). Once hydrogen burning ends, the core contracts, which leads to the thermal expansion of the outer layers containing residual hydrogen. At this point, the internal temperature becomes sufficient to ignite helium fusion within the core, resulting in the formation of a layered structure (2). In massive stars (8 $M_{\odot}$ < M < 10 $M_{\odot}$), this process of self-regulating

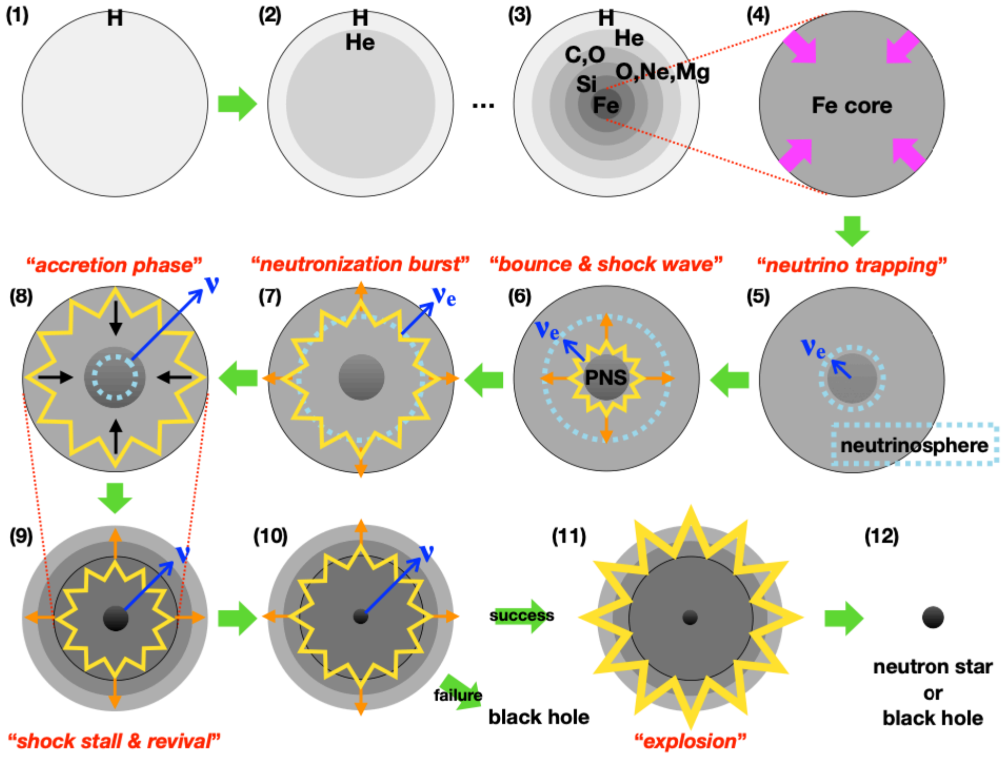

Figure 2.2: Schematic diagram of the core-collapse supernova explosion mechanism. This figure is taken from Ref. [18].

nuclear burning continues until a degenerate oxygen-neon-magnesium (O-Ne-Mg) core is produced. For $M \geq 10\,M_\odot$, oxygen burning produces silicon, which rapidly undergoes fusion leading to the formation of an inert iron core (^{56}Fe) (3).

Gravitational Instability and Core-Collapse: Steps 4 - 5

The gravitational instability of the degenerate stellar core triggers the core-collapse mechanism. In O-Ne-Mg cores with a central density of approximately 10^9 g cm^{-3}, electron capture processes on ^{24}Mg and ^{20}Ne (see Equation. 2.8) reduce the electron degeneracy pressure. As a result, this initiates gravitational contraction and eventually leads to core-collapse. This type of CCSN is sometimes referred to as an *electron capture supernova* and is typically observed for Type II supernovae [19].

Stars with an inert iron core are primarily supported by electron degeneracy pressure. The iron core continues to accumulate mass until it reaches the

Chandrasekhar mass limit, defined as

$$M_{\mathrm{ch}} \approx 1.4\,\mathrm{M}_{\odot} \times \left(\frac{Y_{\mathrm{e}}}{0.5\,\mathrm{M}_{\odot}}\right)^{2}, \tag{2.11}$$

where Y_{e} represents the electron fraction [20]. As the stellar mass approaches this critical threshold, electron capture processes and partial photodissociation of iron nuclei lead to the gradual loss of electron degeneracy pressure. The typical reaction for photodissociation is defined as

$$\gamma +^{56}\mathrm{Fe} \rightarrow 13\alpha + 4n - 124.4\,\mathrm{MeV}. \tag{2.12}$$

These processes, combined with increasing temperature and density, triggers a core-collapse. The inner part of the core collapses with a velocity proportional to the radius, whereas the outer core collapses at about half the free-fall velocity (4). During this phase, neutrinos generated by electron capture processes within the core are initially free-streaming as their mean free path ($\sim 10^{9}$ cm) exceeds the size of the core. As the core density approaches approximately 10^{12} g cm^{-3}, the mean free path for coherent scattering off heavy nuclei decreases such that the neutrinos begin to diffuse. *Neutrino trapping* sets in when the timescale of outward neutrino diffusion becomes comparable to that of the gravitational collapse of the core [21]. This creates a boundary called the *neutrinosphere*, beyond which the neutrinos can freely escape (5). The size of the neutrinosphere depends on the neutrino flavour, production site within the core and its initial energy.

Core Bounce and Shock Formation: Step 6

The core-collapse and infall of surrounding matter continues until the inner core reaches a density of $\sim 10^{14}$ g cm^{-3} and the radius reduces to 50 km. In addition, the Y_{e} in the core falls to ≤ 0.3 as the rate of electron capture increases [12]. At this point, the inner core is highly incompressible due to the repulsive component of the strong force and the core-collapse halts. The infalling material undergoes a rebound effect, referred to as a *core bounce*, which initiates an outward shockwave from the inner core. As this shockwave propagates, the inner core transitions into a compact neutron-rich object called a *proto-neutron star* (PNS) (6).

Shockwave Propagation and Neutronisation Burst: Step 7

As the newly formed shockwave propagates through the outer core, the temperature increases due to the dissipation of kinetic energy in the surrounding matter. This creates high-energy photons that increase the rate of photodissociation of iron nuclei (see Equation. 2.12). The process requires approximately 1.5×10^{51} erg per $0.1\mathrm{M}_{\odot}$, which subsequently drains the shockwave of energy [22].

At the same time, the rate of electron capture processes accelerates given the abundance of free nucleons. This results in the *neutronisation* of the inner core and electron neutrinos produced in the post-shockwave medium escape. The flash of neutrinos generated, called the *neutronisation burst*, lasts for 1 ms and produces $\sim 10^{51}$ erg (7) [23].

Shockwave Stall and Neutrino Heating: Steps 8 - 9

Following the propagation of the shockwave, surrounding matter accretes onto the PNS (8). In this *accretion phase*, thermal neutrinos are produced from electron and positron capture processes, as well as by pair production:

$$e^- + e^+ \rightarrow \nu_{e,\mu,\tau} + \overline{\nu}_{e,\mu,\tau}. \tag{2.13}$$

This, coupled with the photodissociation of iron nuclei and neutrino emission, stalls the expansion of the shockwave and converts it into an accretion shockwave with a radius of $\sim$150 km (9). At this point, the thermal energy contained within the PNS is roughly 10^{53} erg.

The shockwave can be revived by a *neutrino heating* mechanism that involves two predominant processes (9). In this regime, the interior PNS cools diffusively by neutrinos, which are absorbed by the matter liberated by photodissociation formed behind the stalled shockwave. The heating and cooling is mediated by the following interactions:

$$\nu_e + n \underset{\text{cooling}}{\overset{\text{heating}}{\rightleftharpoons}} p + e^- \tag{2.14}$$

$$\overline{\nu}_e + p \underset{\text{cooling}}{\overset{\text{heating}}{\rightleftharpoons}} n + e^+ \tag{2.15}$$

Shockwave Revival and Explosion: Steps 10 - 12

The shockwave can relaunch if the heating region, referred to as the *gain region*, can capture approximately 10% of the neutrinos diffusely streaming through. Further studies have demonstrated that several other critical components including convection processes, rotational magnetic fields and nonradial fluid instabilities can accelerate the neutrino heating mechanism (10) [24–26]. Failure to revive the shockwave results in the total collapse of the core into a black hole. In the event of shockwave revival, the runaway expansion of the shockwave triggers explosive nucleosynthesis as it propagates through the outer layers (11). The PNS continues to cool by emitting neutrinos and transitions into a neutron star or a black hole, depending on the mass and the metallicity of the progenitor star (12) [24–26].

Figure 2.3 shows the predicted time evolution of the neutrino luminosity and the average energy for a numerical simulation. The prominent peak at 1 ms corresponds to the neutronisation burst and the following distribution is generated by the PNS cooling phase.

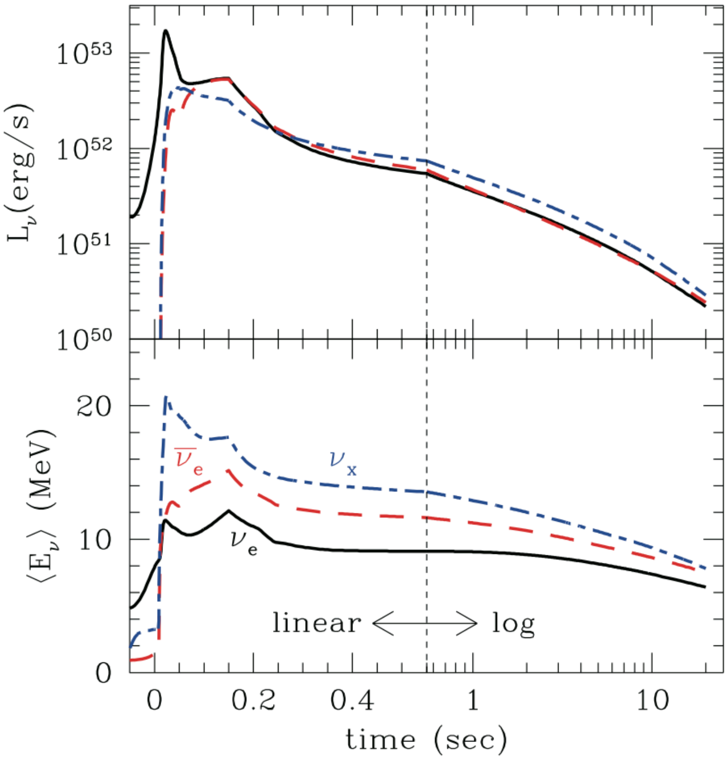

Figure 2.3: Time evolution of the neutrino luminosity L_ν (top) and the average energy $\langle E_\nu \rangle$ (bottom) for ν_e, $\overline{\nu}_e$ and $\nu_x = \frac{1}{4}(\nu_\mu + \overline{\nu}_\mu + \nu_\tau + \overline{\nu}_\tau)$. This figure is taken from Ref. [27].

2.3 Diffuse Supernova Neutrino Background

Measuring the neutrino flux produced by a galactic CCSN will provide valuable insight into the supernovae mechanism and star formation. Given that the CCSN burst rate is estimated to be 1.63 ± 0.46 per century, efforts also focus on measuring the integrated flux from more distant SN in the observable universe [1]. This is referred to as the Diffuse Supernova Neutrino Background (DSNB). The isotropic and time-independent signal of the DSNB flux consists of neutrinos and antineutrinos of all flavours with expected energies up to 40 MeV [28].

The general formalism of the DSNB flux (Φ_{DSNB}) is expressed as the convolution of three key components:

$$\Phi_{\text{DSNB}} \propto \frac{dN_\nu}{dE_\nu} \circledast R_{\text{CCSN}}(z) \circledast P_{\text{osc}}, \tag{2.16}$$

where $\frac{dN_\nu}{dE_\nu}$ represents the average CCSN neutrino energy spectrum, $R_{\text{CCSN}}(z)$ is the CCSN rate per comoving volume at redshift z, and P_{osc} encompasses effects from neutrino oscillations in matter. The neutrino flux spectrum also considers the failed supernova rate. This section provides an overview of the key components of the theoretical formalism, based on Refs.[29, 30]. The flux predictions are made for the $\overline{\nu}_e$ spectrum as this type has the highest interaction cross section in current neutrino experiments (see Section 4.4).

DSNB Flux Model

The current number density of DSNB neutrinos emitted with energies $E_\nu \sim E_\nu + dE_\nu$ and in the redshift interval $z \sim z + dz$ is given by

$$dn_\nu(E_\nu) = R_{\text{CCSN}}(z)\frac{\mathrm{d}t}{\mathrm{d}z}\,\mathrm{d}z\frac{\mathrm{d}N_\nu\,(E'_\nu)}{\mathrm{d}E'_\nu}(1+z)\mathrm{d}E_\nu, \tag{2.17}$$

where $E'_\nu = (1+z)E_\nu$ is the redshifted energy and t is time. The relation between z and t is determined by the Friedmann equation, which is given by

$$\frac{dt}{dz} = \frac{1}{H_0(1+z)\sqrt{\Omega_m(1+z)^3 + \Omega_\Lambda}}, \tag{2.18}$$

where H_0 is the Hubble constant, and Ω_m and Ω_Λ represent the matter density and cosmological constant (dark energy density), respectively [31]. These constants are approximated as ($\Omega_m = 0.3, \Omega_\Lambda = 0.7$, and $H_0 = 70\, h_{70}\, \mathrm{km\ s^{-1}\ Mpc^{-1}}$) and are used to describe the expansion of the universe. The differential flux of the DSNB ($d\Phi_{\mathrm{DSNB}}(E_\nu)/dE_\nu$) is then calculated as

$$\begin{aligned} \frac{d\Phi_{\mathrm{DSNB}}(E_\nu)}{dE_\nu} &= c \cdot \frac{dn_\nu(E_\nu)}{dE_\nu} \\ &= \frac{c}{H_0} \int_0^\infty R_{\mathrm{CCSN}}(z) \frac{\mathrm{d}N_\nu\left(E'_\nu\right)}{\mathrm{d}E'_\nu} \frac{\mathrm{d}z}{\sqrt{\Omega_{\mathrm{m}}(1+z)^3 + \Omega_\Lambda}}. \end{aligned} \tag{2.19}$$

Cosmic Supernova Rate

The CCSN rate $R_{\mathrm{CCSN}}(z)$ is determined by the cosmic star formation rate density (CSFRD) $\dot{\rho}_*(z)$, representing the star formation rate per unit time and comoving volume, and the initial mass function (IMF) $\psi_{\mathrm{IMF}}(M)$, which characterises the distribution of stellar masses at birth. It is defined as

$$R_{\mathrm{CCSN}}(z) = \dot{\rho}_*(z) \times \frac{\int_{M_{\min}}^{M_{\max}} \psi_{\mathrm{IMF}}(M) dM}{\int_{0.1M_\odot}^{100M_\odot} M\psi_{\mathrm{IMF}}(M) dM}, \tag{2.20}$$

where $M_{\min}$ and $M_{\max}$ are the masses of the progenitor stars that generate the DSNB flux and $\psi(M) \propto M^{-\eta}$ where η is a constant dependent on the specific model selected. For CCSN, this is expected to be in the range $8M_\odot < M < 70M_\odot$, although the actual upper limit is currently unknown. In this approximation, $R_{\mathrm{CCSN}}(z)$ is obtained by essentially rescaling the $\dot{\rho}_*(z)$ by the probability of undergoing gravitational collapse. Model predictions of the CSFRD from several studies demonstrated that the spectrum generally increases between 0 < z < 1, but different models tend to deviate at higher redshift [29]. Since larger redshifts refer to galaxies further away this impacts the overall normalisation of the DSNB flux predictions at lower energies. This effect is evident in the flux predictions described in Section 2.3.1.

Supernova Neutrino Emission

The energy spectrum is estimated using a *pinched* Fermi-Dirac distribution:

$$f(E) = \frac{(1+\alpha)^{1+\alpha}}{\Gamma(1+\alpha)} \frac{E_\nu^{\mathrm{tot}} E^\alpha}{\epsilon_\nu} \exp\left[-(1+\alpha)\frac{E}{\epsilon_\nu}\right], \tag{2.21}$$

where $E_\nu^{\rm tot}$ is the total liberated energy by the neutrino, ϵ_ν is the mean energy, and α represents a pinching parameter [30]. In this formula, a value of $\alpha = 0$ corresponds to a standard Fermi-Dirac distribution, where the spectrum smoothly decreases with increasing energy. However, when $\alpha \neq 0$ it introduces a pinching effect, causing the spectrum to become narrower around the peak energy. Therefore, the pinching parameter encompasses physical processes occurring in the supernovae that can impact the neutrino emission spectrum. The mean neutrino emission is based on rescaling $f(E)$ with a weighted IMF function:

$$\frac{dN}{dE} = \sum_i \frac{\int_{\Delta M_i} \psi(M)dM}{\int_{M_{\rm min}}^{M_{\rm max}} \psi(M)dM} f_i(E), \tag{2.22}$$

where ΔM_i is the mass range for the progenitor i and $\psi(M)$ is the IMF. *Failed* supernovae that result in the formation of a black hole produce more energetic neutrinos in the final stages of the core-collapse. Therefore, the overall rate of progenitor stars that transition into black holes impacts the end-point of the observed DSNB spectrum.

Neutrino Oscillation Effects

The propagation of neutrinos in matter is influenced by the forward scattering of neutrinos with electrons. Therefore, the formulation of neutrino oscillations needs to be modified to incorporate these matter effects. This adjustment is described by the MSW effect, named after Mikheyev, Smirnov, and Wolfenstein, which describes how neutrinos encounter an effective potential in matter [32]. This potential depends on various factors, including the neutrino energy, electron density, and weak mixing angles.

In high-density environments, such as in the core of a supernova, the MSW effect can lead to a resonant enhancement or suppression of the flavour composition of the DSNB flux observed on Earth. Therefore, the expression for the differential neutrino yield, $\mathrm{d}N_\nu\left(E_\nu'\right)/\mathrm{d}E_\nu'$, is modified in DSNB flux predictions to account for this. The modification alters the prediction for NH and IH scenarios differently [29].

2.3.1 DSNB Flux Predictions

This subsection provides a summary of the different DSNB $\overline{\nu}_e$ flux predictions, which are presented in Figure 2.4.

The *Galais+10* [33] model incorporates effects from the shockwave revival time, which results in lowering the DSNB flux prediction. The *Tabrizi+20* [34] model includes effects from neutrino decay. The *Kresse+20* [35] model considers the contribution from helium stars and black hole formation and the highest prediction is shown. The *Nakazato+15* [29] model includes cosmic metallicity evolution, and black hole formation, and investigates two variations of the CSFRD and shock revival time for the NH and IH. The *Kaplinghat+00* [36] model investigates supernova rate using observations of the universal metal enrichment history. The *Totani+96* [23] model considers the delayed explosion mechanism in the time evolution of the $\overline{\nu}_e$ luminosity and spectrum. The *Horiuchi+18* [30] model adjusts the *critical compactness* parameter, which determines whether a star undergoes a successful explosion. The ***Horiuchi+09*** [37] model investigates CCSN neutrino emission parameters related to cosmic star formation. The effective neutrino temperature is set to 6 MeV. This model is used as the DSNB flux prediction for this analysis. The *Ando+03* [38] model considers various neutrino oscillation models and was updated at the NNN2005 conference. The *Lunardini+09* [39] model incorporates effects from failed and successful supernovae separately. The *Malaney+97* [40] model includes effects from the redshift evolution of interstellar matter. The *Hartmann+97* [41] model considers the chemical evolution of the universe.

2.4 Current Status of DSNB Searches

The detection of the DSNB flux will provide constraints on the theoretical models and their associated uncertainties. Despite several experimental efforts, the DSNB flux has not yet been observed. Most experimental searches are based on detecting the positron signal produced from the inverse beta decay (IBD)

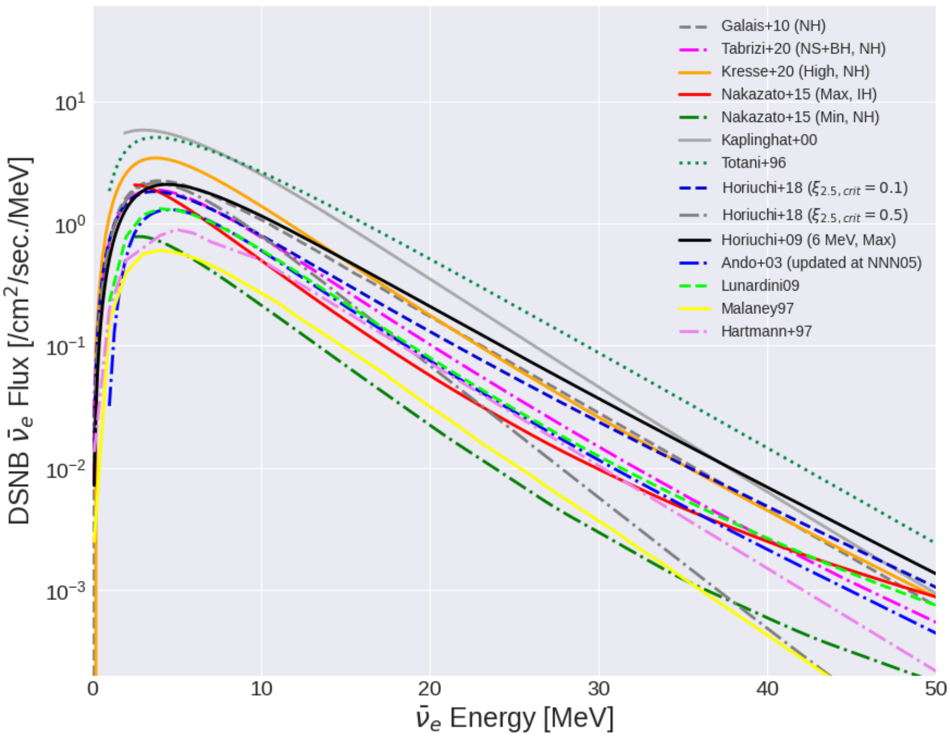

Figure 2.4: DSNB $\overline{\nu}_e$ flux predictions from several theoretical models [23, 29, 30, 33–36, 38–41]. The Horiuchi+09 model [37] is used for this analysis.

interaction of electron antineutrinos as it has the largest cross section of all the possible interaction channels (see Section 4.4).

The Super-Kamiokande (SK) detector and the KamLAND liquid scintillation detector have placed the most stringent upper limits on the DSNB flux. In SK, the first analysis performed spectrum fitting with various backgrounds using 1496 live days and placed an upper limit on the DSNB flux for $\overline{\nu}_e$ energies $E_{\overline{\nu}_e} > 19.3$ MeV [43]. The search was updated using improved analysis techniques and a statistically more significant 2853 live day dataset [44]. In 2008, an electronics upgrade facilitated longer trigger periods, allowing for the detection of delayed neutron captures on hydrogen, which produces a 2.2 MeV γ-ray. The detection of this coincidence signature reduced low-energy muon spallation backgrounds prominent below 17.3 MeV. The first energy binned analysis used a lower energy threshold $E_{\overline{\nu}_e} > 13.3$ MeV with neutron tagging over 960 days livetime [45]. Given that the neutron tagging efficiency on hydrogen is $\sim$20%, this analysis suffered from low statistics. The KamLAND experiment sets more competitive upper

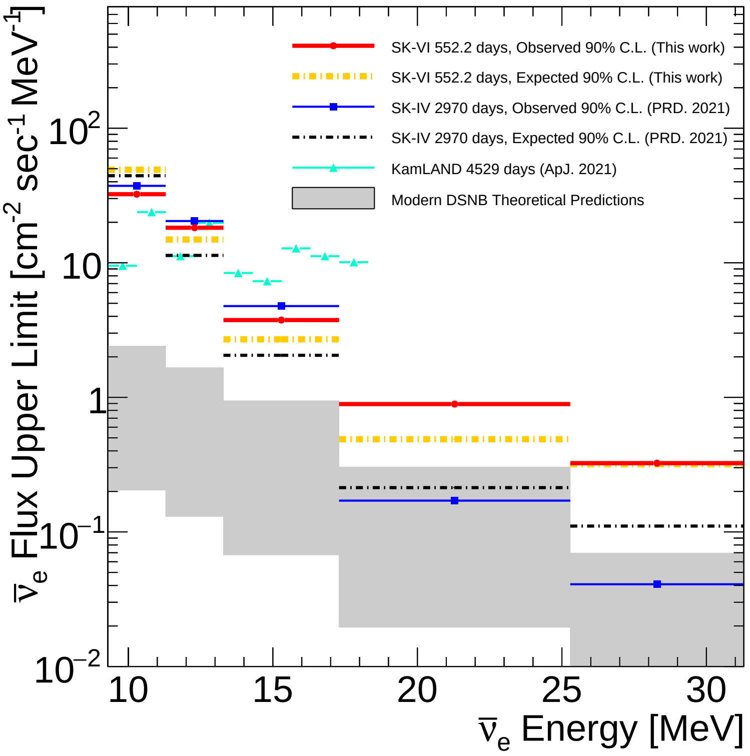

Figure 2.5: DSNB $\overline{\nu}_e$ flux upper limits from the most recent SK and KamLAND searches. This figure is taken from Ref. [42].

limits in the lower energy region due to its ~100% neutron tagging efficiency on hydrogen [46].

The DSNB search during the pure-water phase of the SK detector was completed in 2021 using 2970 days of livetime and neutron tagging on hydrogen. The result was comparable with that from KamLAND below 17.3 MeV, and similar to the SK spectral analysis results above 17.3 MeV [47]. In 2020, the detector enabled enhanced neutron tagging on gadolinium by adding 0.011% of $Gd_2(SO_4)_3 \cdot 8H_2O$ into the water. In the SK-Gd era, the first energy binned analysis was performed using 552.2 days of livetime with approximately 50% neutron tagging efficiency on gadolinium and enhanced neutron identification techniques [42]. The analysis achieved stringent upper limits comparable to the results obtained in the 2970 days pure-water phase, shown in Figure 2.5. This thesis aims to further constrain the upper limits achieved in the first SK-Gd analysis by reducing dominant low-energy atmospheric backgrounds using Machine Learning (ML) techniques.

3

The Super-Kamiokande Experiment

The Super-Kamiokande (SK) detector is a cylindrical stainless-steel tank, 39.3 m in diameter and 41.4 m in height, filled with 50 ktons of ultra-pure water [48]. The detector is situated in the Kamioka mine in Japan with a 1000 m rock overburden. This provides effective shielding from the cosmic ray muon flux, which is 2 Hz at a depth of 2700 m-water-equivalent (m.w.e.). The tank is optically separated into regions containing the inner detector (ID) and the outer detector (OD), which have a total water mass of 32.5 ktons and 17.5 ktons, respectively. The ID is 33.8 m in diameter and 36.2 m in height, instrumented with 11,129 20-inch photomultiplier tubes (PMTs) to provide a 40% photocathode coverage. An outward-facing array of 1,885 8-inch PMTs operates as the OD, serving as an active veto against backgrounds. The OD region is 2 m thick between the PMT support structure and the tank. Figure 3.1 shows schematic diagrams of the detector setup. The detector hosts various physics analyses including proton decay, atmospheric neutrino and beam neutrino oscillation measurements, reactor, dark matter, and neutrinos from galactic and extragalactic sources.

The SK experiment started collecting data on the 1st of April 1996 and has continued to operate through seven-run periods since then (SK-I to SK-VII), summarised in Table 3.1. SK-I operated for five years until July 2001 and some dead PMTs were replaced following a shutdown period. On the 12th of November

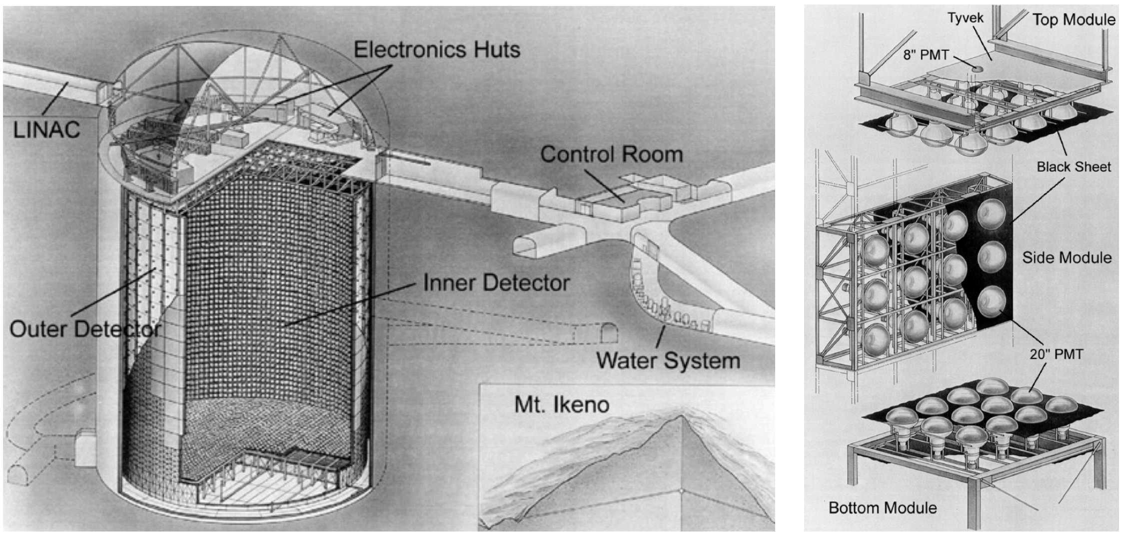

(a) (b)

Figure 3.1: Schematic diagram of the Super-Kamiokande detector (left) and of the PMT wall (right). These figures are taken from Ref. [48].

2001, a PMT imploded, which triggered a chain reaction that destroyed ∼7900 PMTs. The following run period (SK-II) started in October 2002 with 5182 PMTs, each encased in a new protective acrylic covering. SK-III began operation in July 2006, after new ID PMTs were installed to restore the photocoverage to its original 40%. In SK-IV, new electronics, called QBEE boards were implemented in 2008 to guarantee the stable operation of the front-end electronics and an improved water temperature control system was introduced. In May 2018, the detector underwent tank refurbishment in preparation for gadolinium loading. The SK-V period began with preparations for the upcoming SK-Gd experiment, including adjustments to water flow, repairs for water leakage, and replacements of PMTs. From July 2020 to May 2022, the first operational phase of the SK-Gd era began with the loading of 13 tons of $Gd_2(SO_4)_3 \cdot 8H_2O$ into the experiment (0.011 ppm of Gd) for enhanced neutron identification. In June 2022, the SK-VII phase introduced three times more Gd (0.03 ppm of Gd) into the detector to increase the neutron capture efficiency by 50% compared to SK-VI.

Phase	Dates	Livetime (Days)	Photo coverage	Electronics	Target
SK I	1996-2001	1489.2	40%	ATM	H_2O
SK II	2002-2005	798.6	19%	ATM	H_2O
SK III	2006-2008	518.1	40%	ATM	H_2O
SK IV	2008-2018	3244.4	40%	QBEE	H_2O
SK V	2019-2020	461.0	40%	QBEE	H_2O
SK VI	2020-2022	552.2	40%	QBEE	H_2O + Gd
SK VII	July 2022-	ongoing	40%	QBEE	H_2O + Gd

Table 3.1: The operating conditions for each of the seven completed and ongoing SK run periods.

3.1 Detection Principle

In SK, charged particles propagating through the detector volume at speeds exceeding that of light in water emit Cherenkov radiation, which is detected by the PMT array. The light is produced as a cone with an opening angle θ_C, which follows the relation:

$$\cos(\theta_C) = \frac{1}{\beta n}, \quad \beta = \frac{v}{c}, \tag{3.1}$$

where v and c are the velocities of the charged particle and light in a vacuum, respectively. In water, the Cherenkov angle for particles propagating with $\beta \approx 1$ is 42°. The Cherenkov photon emission spectrum per unit length is given by the Frank-Tamm formula [49],

$$\frac{d^2N}{dxd\lambda} = \frac{2\pi\alpha Z^2}{\lambda^2}\left(1 - \frac{1}{n^2\beta^2}\right) \tag{3.2}$$

where n is the refractive index of the medium (n $\approx$ 1.33 in water), λ is the wavelength, Z is the charge, and α represents the fine structure constant. The minimum energy of the charged particle, referred to as the Cherenkov threshold, is 0.57 MeV/c for electrons and 118 MeV/c for muons. Particle identification and vertex reconstruction rely on the timing, charge and topological information from the hit PMTs. Figure 3.2 shows a typical event display image with a characteristic Cherenkov ring pattern.

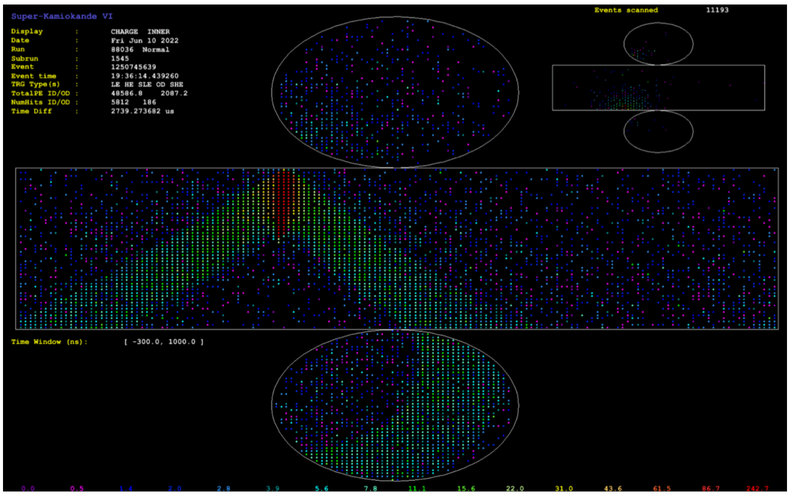

```
Super-Kamiokande VI
Display       :    CHARGE  INNER
Date          :    Fri Jun 10 2022
Run           :    88036  Normal
Subrun        :    1545
Event         :    1250745639
Event time    :    19:36:14.439260
TRG Type(s)   :    LE HE SLE OD SHE
TotalPE ID/OD :    48586.8    2087.2
NumHits ID/OD :    5812   186
Time Diff     :    2739.273682 us
```

```
Events scanned    11193
```

```
Time Window (ns):      [ -300.0, 1000.0 ]
```

Figure 3.2: Event display image of a cosmic muon event. Each pixel corresponds to an ID PMT and the colour scale represents the total charge deposition. The OD is shown in the upper right corner. This figure is taken from Ref. [50].

3.2 Detector Systems

This sections provides a summary of the key detector systems used in SK.

3.2.1 Photomultiplier Tubes

The ID is instrumented with 11,129 R3600 20-inch hemispherical PMTs manufactured by Hamamatsu Photonics K.K., shown in Figure 3.3a [48, 51]. The photocathode is made from bialkali material (Sb-K-Cs), which provides 21% peak quantum efficiency (QE) at ∼360 nm, as depicted in Figure 3.3b. The PMT operates at a gain of 10^7 and a transit-time spread of 2.2 ns for an input high-voltage (HV) of ∼2000 V. Since SK-II, each PMT is encased in a fibre-reinforced plastic (FRP) cover to reduce the impact of PMT implosion.

The OD contains R1408 8-inch PMTs repurposed from the IMB experiment [52] and R5912 8-inch PMTs installed after the PMT implosion accident. Each PMT is optically coupled to a 60 × 60 cm wavelength-shifting (WLS) plate made from acrylic doped with 50 mg/L of bis-MSB ($C_{24}H_{22}$). At present, 1,275 OD photosensors are instrumented in the barrel region, 302 in the top endcap, and 308 in the bottom endcap of the detector. Further information on the role of

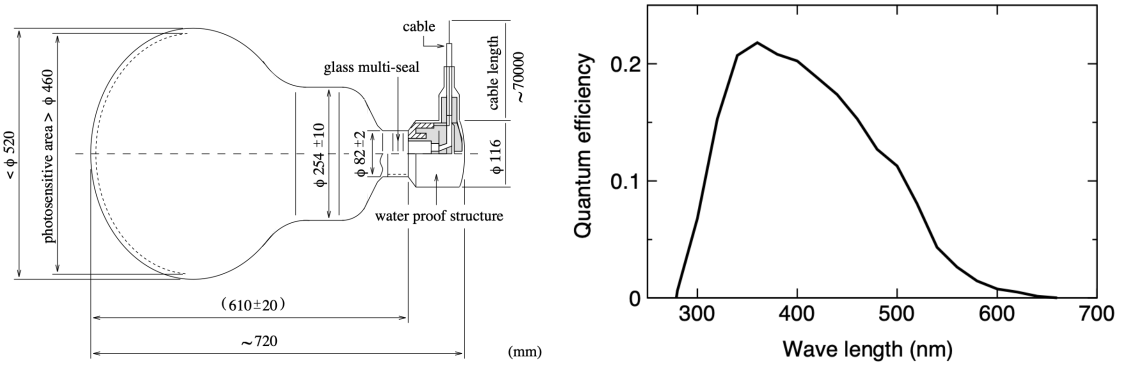

(a) **(b)**

Figure 3.3: Schematic diagram of the R3600 20-inch PMT manufactured by Hamamatsu (left) and the quantum efficiency of the PMT as a function of wavelength (right). These figures are taken from Ref. [48].

an OD similar to the SK-OD and its photosensor components is provided in full detail in Chapter 10.

3.2.2 Compensation Coils

The geomagnetic field is 450 mG, which impacts the photoelectron trajectories and timing in the PMTs. This significantly reduces the overall collection efficiency of each PMT. To mitigate this effect, the inner surfaces of the tank are surrounded by 26 sets of Helmholtz coils that lower the average field in the detector to $\sim$50 mG [48].

3.2.3 Water and Air Purification System

The SK-I to SK-IV phase of the experiment relied on an ultra-pure water system to purify water from the Kamioka mine [53]. Since SK-V, the SK-Gd water system was integrated into the experiment to dissolve Gd, purify, and circulate water to produce 50 kton of Gd-loaded water in preparation for the forthcoming Gd-loaded phase [54]. The system is essential for filtering out impurities, bacteria and radioactive contaminants that induce low-energy backgrounds and degrade the water transparency. Figure 3.4 shows a schematic diagram of the full setup. The Gd-dissolving system transports and dissolves Gd into buffer tanks containing SK water, resulting in a Gd solution with the desired concentration. This solution

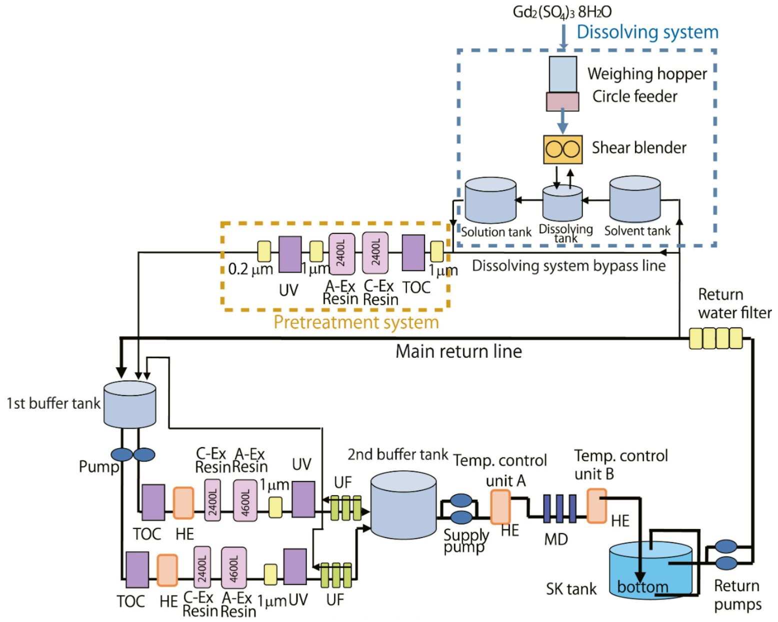

Figure 3.4: Schematic diagram of the SK-Gd Gd-loading and water purification system. This figure is taken from Ref. [54].

is processed through a pretreatment system to remove impurities while retaining Gd and sulfate ions in the water. In the first stage, the solution is irradiated with a UV total organic carbon reduction light (TOC) to oxidise carbon and other residual compounds. Charged impurities and radioactive contaminants such as radium and uranium are subsequently removed by ion-exchange resins (A-ex and C-ex Resins) and a UV steriliser is applied to kill bacteria. The main system continuously recirculates and purifies Gd-loaded water through two lines that operate at a flow rate of 120 m^3/h and 60 m^3/h when both are activated. Heat-exchange (HE) units are used to maintain a stable water temperature of 13°C with a precision of 0.01°C. The system also incorporates a membrane degasifier (MD) to remove radon dissolved in the solution and ultrafiltration (UF) modules for the reduction of minuscule impurities. In addition, an air purification system is used to reduce the radon concentration in the mine air to < 3 mBq/m^3.

3.3 Electronics and Data Acquisition

From SK-IV, the front-end electronics were upgraded from the Analog Timing Module (ATM) system to the Charge-to-Time (QTC) Based Electronics with

Ethernet (QBEE) system (see Figure 3.5). Each QBEE board holds eight 3-channel QTCs that process data from 24 PMTs and generate square pulses proportional to the integrated charge. The QTC has small, medium and large gain ranges with gain ratios of 1/49, 1/7 and 1, respectively, covering a dynamic range of 0.2 - 2500 pC. Following this, the pulses are digitised by a Time-to-Digital Converter (TDC), which calculates the charge and timing information by Field-Programmable Gate Arrays (FPGAs). The signals are then fed to front-end PCs connected to subsequent merger PCs, which handle the event-building process and implement software triggers. These triggered events are finally sent to an organiser PC before being sorted onto disk. Figure 3.5 shows a schematic diagram of the full data acquisition (DAQ) system.

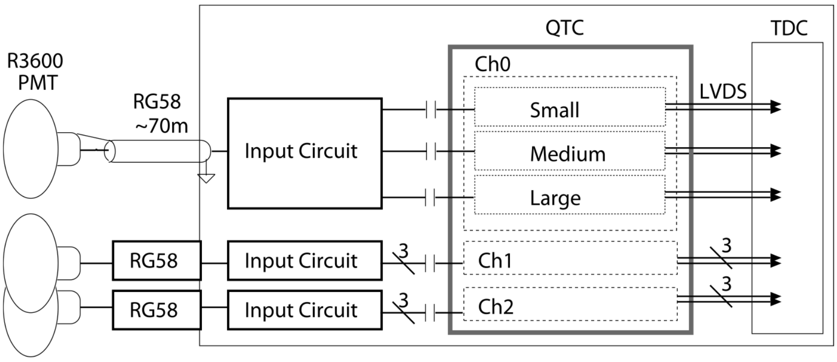

Figure 3.5: Schematic diagram of the QBEE system created for SK-IV onwards. This figure is taken from Ref. [55].

3.3.1 Software Triggers

In the merger PCs, software triggers are applied to the processed pulses when the number of PMT hits in a 200 ns time window (N_{200}) exceeds pre-defined thresholds. There are five types of triggers: Super-Low Energy (SLE), Low-Energy (LE), High-Energy (HE), Super High-Energy (SHE) and an Outer Detector (OD) trigger. An additional After (AFT) trigger was introduced from SK-IV onwards to record the delayed neutron capture signals. The trigger conditions are summarised in Table 3.2. This thesis uses data acquired from the SHE+AFT triggers, which is described in further detail in Section 7.1.

Trigger type	N_{200} Threshold $[/\mu\ \mathrm{sec}\ ]$	Event window $[\mu\ \mathrm{sec}\ ]$	Trigger rate [Hz]
SLE	34	$[-0.5, +1.0]$	$3.0 - 4.0$
LE	49	$[-5, +35]$	80
HE	52	$[-5, +35]$	30
SHE	60	$[-5, +35]$	3
OD	22 (in OD)	$[-5, +35]$	2

Table 3.2: Summary of the software triggers for the SK-VI operational period.

3.4 Detector Calibration

Routine calibration measurements are carried out to assess the PMT response, water quality, and detector stability. These results are crucial for fine-tuning detector simulation and reconstruction methods to ensure accurate physics analyses (see Chapter 4). This section provides an overview of the main calibration procedures.

3.4.1 PMT Calibration

The following subsections describe the input HV tuning procedure, gain, quantum efficiency, and timing measurements for the calibration of ID PMTs.

High-Voltage Tuning

The charge response for a dedicated set of 420 reference pre-calibrated ID PMTs is evaluated to perform input HV tuning. These PMTs are arranged in four vertical strip patterns along the barrel region and as a cross along the endcaps. Light from a xenon lamp is injected into a scintillator diffuser ball via an optical fibre to provide an isotropic light source from the centre of the tank that uniformly illuminates all PMTs. The input HV of all non-reference ID PMTs is adjusted to match the charge response of the reference PMTs at an equivalent distance from the light source.

Gain and QE Measurements

The relative gain differences across the PMTs are evaluated using a variable-intensity light source. During high-intensity flashes, the charge response (Q)

of each PMT (i) is calculated as

$$Q_i \propto I_{\text{High}} \times a_i \times QE_i \times G_i, \tag{3.3}$$

where a represents the geometric acceptance factor, QE is the quantum efficiency and G is the gain. Following this, a low-intensity measurement is made such that all registered hits (N) correspond to single photoelectrons, which is given by

$$N_i \propto I_{\text{Low}} \times a_i \times QE_i. \tag{3.4}$$

The relative gain for each PMT is determined on the basis that G_i is proportional to Q_i/N_i. The absolute PMT gain is evaluated by analysing the charge distribution generated using a nickel-californium (Ni-Cf) source. Since the source emits 9 MeV photons essentially all PMT hits correspond to a single photoelectron. The charge distribution is corrected according to each PMT's relative gain and then the 1 p.e peak is fit to establish a charge-to-gain conversion factor. The variation of the QE is evaluated by performing data-MC comparisons of the average PMT hit count generated due to the Ni-Cf source.

Timing Response

The PMT timing response is calibrated to account for variations in the transit time, cable lengths, readout electronics, and pulse amplitude. The latter is referred to as the *time walk* effect, whereby larger pulses tend to arrive earlier compared to smaller pulses. The measurement utilises fast-pulsing light emitted by nitrogen lasers, which is directed into a diffuser ball positioned at the centre of the tank, as shown in Figure 3.6a. The recorded hit times are time-of-flight subtracted according to the PMT's relative distance to the calibration source. For each PMT, the timing offset is calculated as a function of charge to generate a *TQ map*, as shown in Figure 3.6b. These distributions are fit to determine a correction function that is then applied to all raw hits in data and incorporated into the simulation of the detector response.

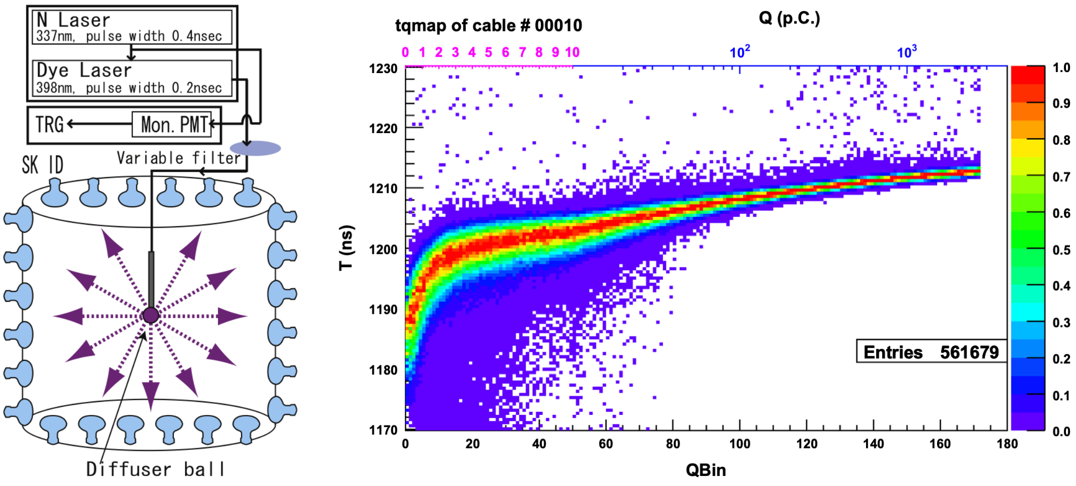

(a) (b)

Figure 3.6: Left: Schematic diagram of the timing calibration. Right: The TQ map for an ID PMT, which is the time-of-flight subtracted hits as a function of integrated charge. Larger values of T correspond to earlier hits and vice versa, to demonstrate the *time walk* effect. These figures are taken from Ref. [56].

3.4.2 Water Transparency Measurement

Measuring the absorption and scattering properties of water is crucial for accurately modelling photon tracking in detector simulations. In SK, photon propagation in water is modelled using the photon track length and the attenuation length $L(\lambda)$, which is given by

$$L(\lambda) = \frac{1}{\alpha_{\text{abs}}(\lambda) + \alpha_{\text{sym}}(\lambda) + \alpha_{\text{asym}}(\lambda)}, \tag{3.5}$$

where α_{abs} represents the absorption coefficient, α_{sym} is the symmetric term that incorporates both Rayleigh and Mie scattering, and α_{asym} contains the asymmetric component of Mie scattering. The scattering and absorption of light in the water are measured using a monochromatic laser with five discrete wavelengths between 337 - 473 nm. The laser beam is orientated to transmit light from the top of the tank downwards via an optical fibre, as shown in Figure 3.7a. The parameters of $L(\lambda)$ are determined by comparing the data and MC PMT time-of-flight subtracted hits of the target PMTs at the bottom of the tank. The drop in intensity of the target PMTs establishes the α_{abs}, whereas measurements of scattered light from surrounding PMTs determine the α_{sym} and

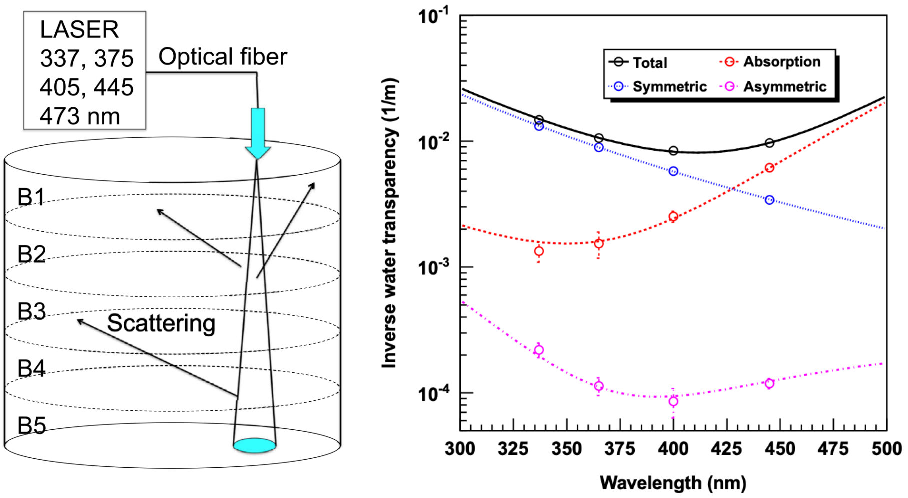

(a) (b)

Figure 3.7: Left: Schematic diagram of the laser calibration setup, with B1 to B5 indicating the barrel regions used for the measurements. Right: Distribution of water transparency measurement coefficients, showing data points (dots) and model predictions tuned from MC simulations (solid lines). The figures are adapted from Ref. [56].

α_{asym}. These results are presented in Figure 3.7b. During normal run periods, the water transparency measurement can be continuously monitored using the cosmic muon sample as they deposit energy uniformly along their track length. This track length is reconstructed using ID PMTs and the expected number of hits on each PMT is calculated in MC. The scattering and absorption parameters are determined by comparing the expected charge and the measured charge on each PMT.

3.4.3 Energy Calibration

The electron linear accelerator (LINAC) is used to determine the energy scaling factor applied to low-energy simulations. The LINAC injects downward-going monoenergetic electrons into the detector volume with target energies between 6 - 15 MeV and beam positions in the z-direction of -12 m, 0 m, and 12 m. The N_{eff} is calculated for LINAC data and MC at each beam position and for each energy (refer to Section 4.6.3 for the description of N_{eff}). The energy scale parameter is then determined by comparing the data and MC N_{eff} distributions. For SK-VI, this is found to be $\sim$0.88 and is used to scale the QE of ID PMTs in the simulations.

4
Event Simulation and Reconstruction

The Monte Carlo (MC) event simulation is crucial for determining the reduction criteria, signal efficiency and accurately estimating the expected background spectrum. This chapter describes the principles of MC production including flux predictions, interaction models and the detector response. Event reconstruction is performed using specialised algorithms to compute the vertex, direction and energy of electrons, muons, and other hadronic particles. An overview of these tools for low-energy events is detailed in the second half of this chapter.

4.1 Atmospheric Neutrinos

Atmospheric neutrinos are produced in hadronic cascades initiated by cosmic-ray interactions in the Earth's atmosphere, as shown in Figure 4.1. At high energies $\mathcal{O}(\text{GeV})$, inelastic hadronic interactions involving primary cosmic-ray protons result in the production of unstable pions (π) and kaons (K). The decay of charged pions generates a flux of muons and muon neutrinos with a branching ratio of 99.98% [57]. The full decay chain, including secondary processes from muon decay, is as follows

$$\begin{array}{ll} \pi^- \to \mu^- + \overline{\nu}_\mu & \qquad \pi^+ \to \mu^+ + \nu_\mu \\ \qquad\;\; \downarrow & \qquad\qquad\;\; \downarrow \\ \qquad\;\; e^- + \overline{\nu}_e + \nu_\mu & \qquad\qquad\;\; e^+ + \nu_e + \overline{\nu}_\mu . \end{array} \tag{4.1}$$

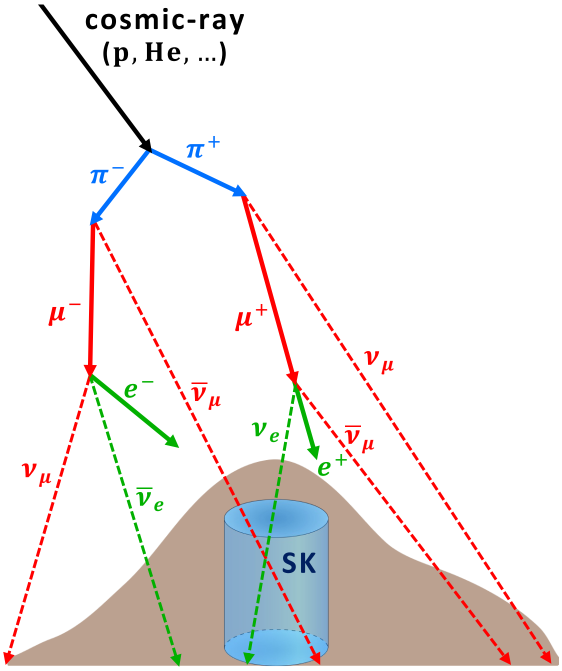

Figure 4.1: Schematic diagram of atmospheric neutrino production from a cosmic-ray interaction above the SK detector.

Given that π^+ and π^- are created in approximately equal proportions, the flux ratio for $(\nu_\mu + \overline{\nu}_\mu)/(\nu_e + \overline{\nu}_e)$ is two. Atmospheric neutrino production is predominantly driven by pion decay up to a *critical energy* of ~115 GeV [58]. Beyond this threshold, the likelihood of pion interactions decreases and the dominant contribution to the neutrino flux shifts towards the decay of kaons until ~850 GeV [58]. The resulting spectrum from these decay modes is commonly referred to as the *conventional* atmospheric neutrino flux.

4.2 Neutrino Flux Prediction

The atmospheric neutrino flux calculations in SK are performed using the Honda-Kajita-Kasahara-Midorikawa (HKKM) 2011 model [59]. The model incorporates factors such as the primary cosmic-ray flux and cross sections, hadronic interactions within the atmosphere, and the propagation of particles in a three-dimensional space.

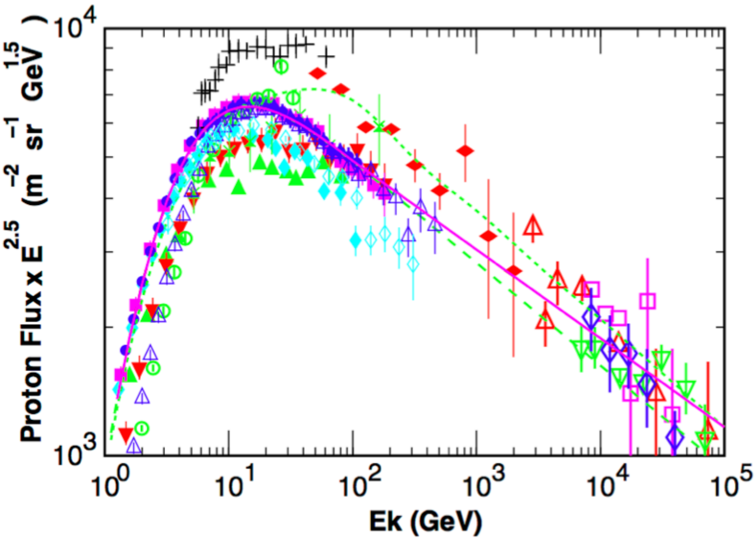

Figure 4.2: Primary cosmic-ray proton flux at the solar minimum from various experiments, including AMS (closed horizontal diamonds) and BESS (closed circles). See Ref. [63] for the full list of experiments. The magenta line shows the spectrum used in the HKKM 2011 model. The figure is taken from Ref. [63].

4.2.1 Primary Cosmic-Ray Flux Model

The primary cosmic-ray flux below 100 GeV is derived from experimental data provided by the space-based AMS [60] and balloon-borne BESS [61] magnetic spectrometers. Above 100 GeV, the spectrum is modified using emulsion chamber data [58, 62] as the energy determination is less precise with spectrometers. Figure 4.2 shows experimental data and the primary cosmic-ray flux prediction used in the HKKM 2011 model. The model incorporates adjustments for both solar modulation and the geomagnetic field, which influence the cosmic-ray spectrum. During heightened solar activity, the solar wind scatters low-energy cosmic rays, resulting in a suppression of the flux. This varies throughout the eleven-year solar cycle, with a potential reduction of up to a factor of two for cosmic rays, below 1 GeV [64]. Additionally, the geomagnetic field induces an East-West asymmetry by deflecting cosmic rays in an anisotropic manner, leading to a subsequent low-energy cutoff in the cosmic-ray spectrum. To account for these effects, the flux is reweighted according to the solar activity and the geomagnetic field is accurately described using the IGRF2005 model

[65] [66]. The structure of the atmosphere is modelled with the US standard atmospheric model [67].

4.2.2 Hadronic Interactions

The primary cosmic-ray flux is convolved with hadronic interaction models to produce secondary particles (π, K, μ). High energy hadronic collisions, above 32 GeV, are calculated using the DPMJET-III MC event generator [68], which is based on the Dual Parton Model (DPM) [69]. The PHOJET event generator is embedded into the framework to simulate hadronic interactions involving photons. In the HKKM 2011 model, DPMJET-III is refined using cosmic muon flux data to better reproduce the observed flux at high energies [59]. However, this modification results in poor agreement between calculations and data at lower energies. Therefore, the JAM hadronic cascade model, used in the Particle and Heavy-Ion Transport code System (PHITS) [70], is adopted for calculations below 32 GeV. Figure 4.3 shows a comparison between the performance of the JAM and DPMJET-III models against data from the Hadron Production (HARP) experiment.

4.2.3 Neutrino Flux Spectrum

The atmospheric neutrino flux at Kamioka, as calculated by the HKKM 2011 model, is presented in Figure 4.4a. The energy spectrum is suppressed below $\sim$1 GeV, which is attributed to the cutoff effect on primary cosmic rays by the geomagnetic field. In Figure 4.4b, the flux ratio for $(\nu_\mu + \overline{\nu}_\mu)/(\nu_e + \overline{\nu}_e)$ is approximately two at $\sim$1 GeV due to the decay of secondary muons. Higher energy muons have an increased decay length, which allows for more muons to reach the Earth's surface before decaying. This shifts the main source of electron neutrinos to kaon decay, resulting in a deficit in the electron neutrino contribution and a pronounced rise in the flavour ratio.

In Figure 4.5, the zenith angle dependence of the atmospheric neutrino flux at Kamioka is shown for three distinct energy bins. The distributions are

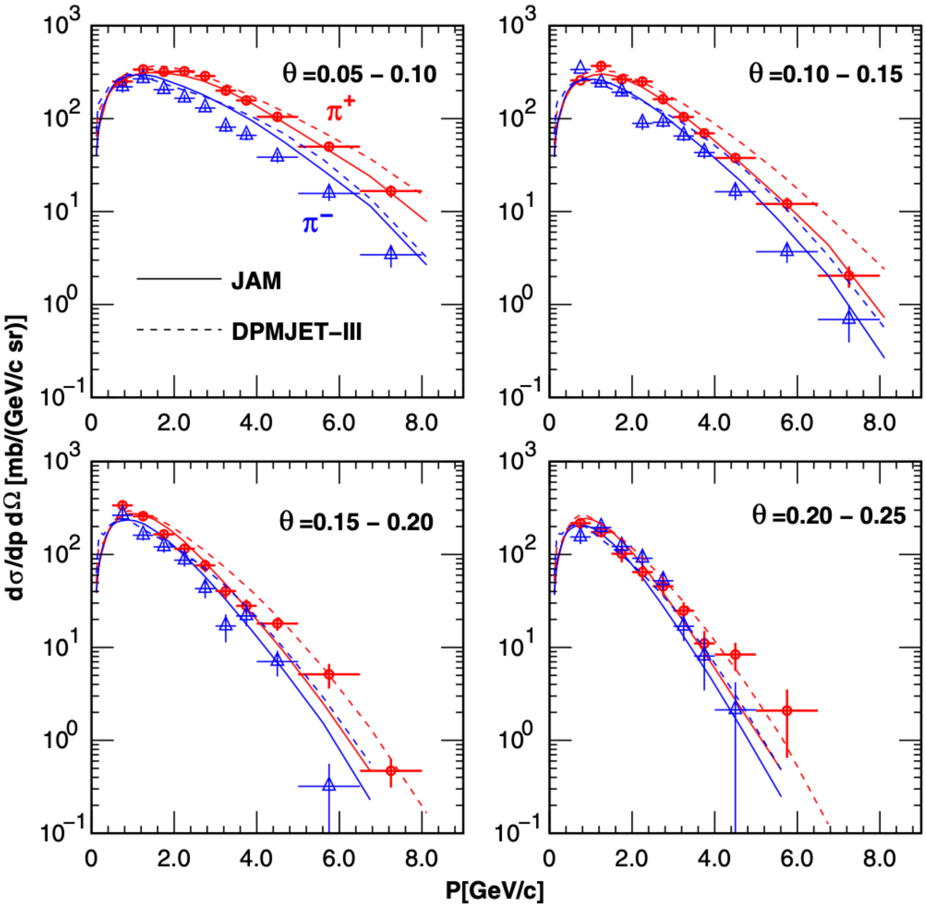

Figure 4.3: The differential cross section of charged pion production from proton interactions on thin N_2 and O_2 targets. Comparisons between experimental data from HARP (triangles and circles) and model predictions from JAM (solid line) and DPMJET-III (dashed line). The figure is taken from Ref. [59].

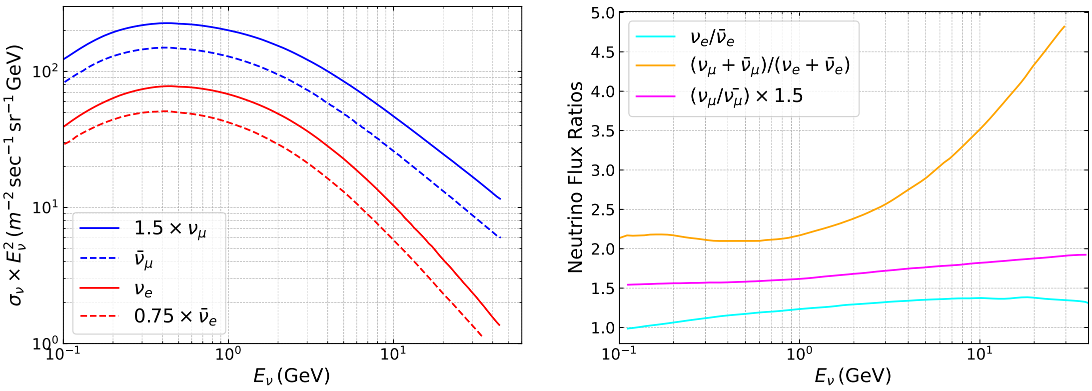

(a) **(b)**

Figure 4.4: Atmospheric neutrino fluxes calculated from the HKKM11 for the Kamioka site averaged over all directions (left) and the flux ratios (right) for different neutrino flavours. The figures are adapted from Ref. [59].

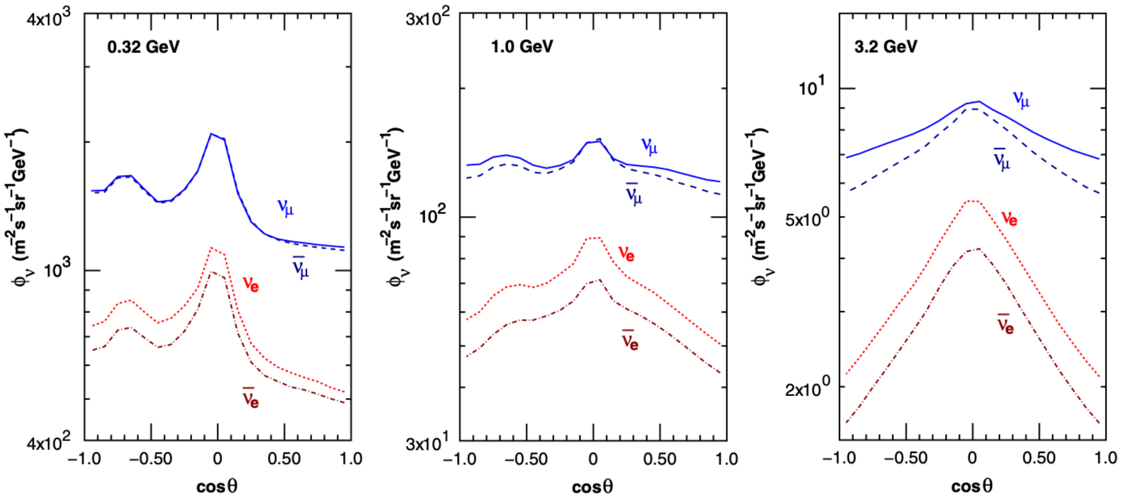

Figure 4.5: Zenith angle (θ) distribution of the atmospheric neutrino flux at Kamioka, averaged over the azimuth angles at 0.32 GeV (left), 1.0 GeV (middle) and 3.2 GeV (right), calculated by the HKKM 2011 model. The figure is taken from Ref. [59].

Parameter	Value
Δm^2_{21}	$7.53 \times 10^{-5}\,\text{eV}^2$
Δm^2_{32}	$2.50 \times 10^{-3}\,\text{eV}^2$
$\sin^2\theta_{12}$	0.304
$\sin^2\theta_{13}$	0.0219
$\sin^2\theta_{23}$	0.588
δ_{CP}	4.18

Table 4.1: Neutrino oscillation parameters used to reweight atmospheric neutrino MC events simulated with the HKKM 2011 model. The values are taken from the latest neutrino oscillation analysis results found in Ref. [71].

peaked along the horizontal as pions and muons follow longer paths in this direction, resulting in an increased likelihood of decay. The up-down asymmetry observed in the lowest energy bin is attributed to the local geomagnetic field. Neutrino oscillation effects are applied to the simulated atmospheric neutrino flux spectrum by reweighting each event based on its oscillation probability, as determined by the most recent analysis results [71]. The oscillation parameters are shown in Table 4.1.

4.3 Neutrino Interaction Model

An accurate simulation of neutrino interactions, combined with the flux prediction, is essential as neutrinos are observed solely through the detection of their interaction products. The NEUT interaction event generator (version 5.4.0.1) is used to simulate neutrino-nucleon and subsequent final-state interactions in the SK detector [72]. NEUT incorporates several theoretical interaction models to simulate interactions with nuclei in both water and rock over a broad range of energy scales $E_\nu \in (100\,\mathrm{MeV}, \sim 1\,\mathrm{TeV})$. Nuclear effects are included in the cross section and kinematics of final-state particles. In the atmospheric neutrino simulation, interactions with electrons are excluded as the cross section is 10^3 times smaller compared to bound nucleon states [73]. Therefore, the simulation considers only the following charged-current (CC) and neutral-current (NC) neutrino-nucleon interactions:

- CC quasi-elastic scattering: $\nu + N \rightarrow l + N'$
- NC (quasi)-elastic scattering: $\nu + N \rightarrow \nu + N'$
- CC meson exchange current: $\nu + NN^* \rightarrow l + N'N'^*$
- CC (NC) single meson production: $\nu + N \rightarrow l(\nu) + N' + \text{meson}$
- CC (NC) coherent pion production: $\nu + N \rightarrow l(\nu) + N' + \pi$
- CC (NC) deep inelastic scattering: $\nu + N \rightarrow l(\nu) + N' + \text{hadrons}$

where ν is a neutrino or antineutrino, N/N^* and N'/N'^* represent the incoming and outgoing nucleons and l is the lepton flavour (e, μ). CC interactions involve the exchange of a $\mathrm{W}^\pm$ boson, which produces a charged lepton with the same flavour as the neutrino. In NC interactions, the incident neutrino scatters from a Z^0 boson without generating a charged lepton required for flavour identification. An overview of the physics models used for calculating these CC and NC interactions in NEUT is described in the following sections.

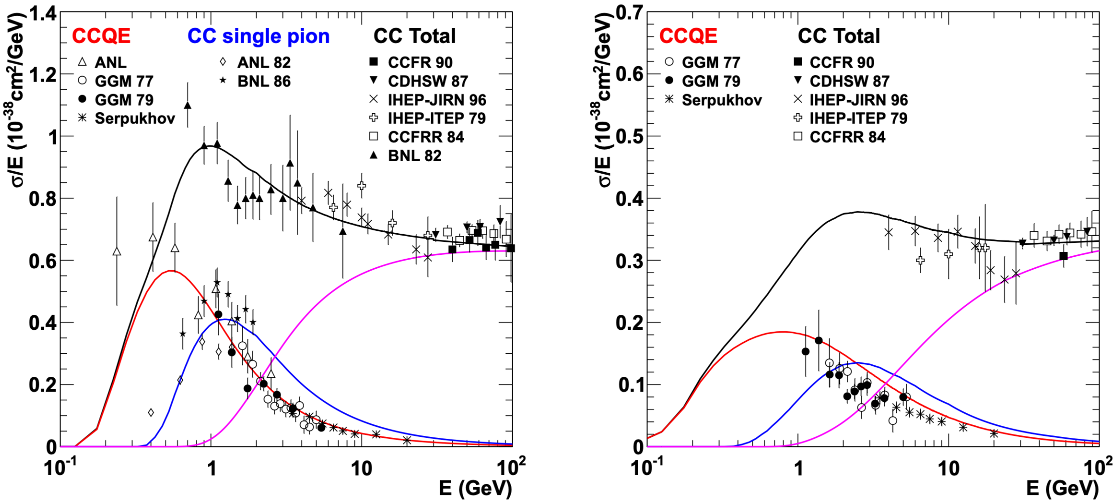

Figure 4.6: Cross sections of CC interactions of muon neutrinos (left) and muon antineutrinos (right). The NEUT calculation of CCQE scattering, CC single pion production, and CC deep inelastic scattering are shown by the red, blue and black lines, respectively. The data points represent measurements from several experiments. The figure is taken from Ref. [76].

4.3.1 Elastic and Quasi-Elastic Scattering

NC elastic scattering occurs when an incident neutrino interacts with a target nucleon, resulting in a momentum transfer without generating new particles. In CC quasi-elastic scattering (CCQE) processes, a charged lepton is produced, and the target nucleon undergoes a charge-conserving transformation. The interaction processes are explicitly defined as,

$$\text{NC elastic scattering} : \nu_l(\overline{\nu}_l) + N \rightarrow \nu_l(\overline{\nu}_l) + N',$$

$$\text{CCQE} : \nu_l(\overline{\nu}_l) + N \rightarrow l(\bar{l}) + N'.$$

In NEUT, the CCQE interaction is simulated using the Llewellyn-Smith model [74] for free protons and the relativistic Fermi gas model for bound nucleons [75]. The comparison of calculated cross sections against various experimental results is shown in Figure 4.6.

The neutrino-oxygen NCQE interaction is a crucial process for the research conducted in this thesis. The nucleon-knockout processes are expressed as:

$$\nu(\bar{\nu}) + ^{16}O \rightarrow \nu(\bar{\nu}) + ^{15}O + \gamma + n,$$

$$\nu(\bar{\nu}) + ^{16}O \rightarrow \nu(\bar{\nu}) + ^{15}N + \gamma + p,$$

where the residual nucleus emits one or more de-excitation γ-rays. This process becomes dominant over the NC elastic process for neutrino energies greater than 200 MeV [77]. The NCQE cross section is modelled in NEUT using the oxygen spectral function from Ankowski and Benhar et al. [77, 78] with the BBBA05 vector and dipole axial form factors [79]. Figure 4.7 shows the NCQE cross section per nucleon for neutrino and antineutrino interaction modes.

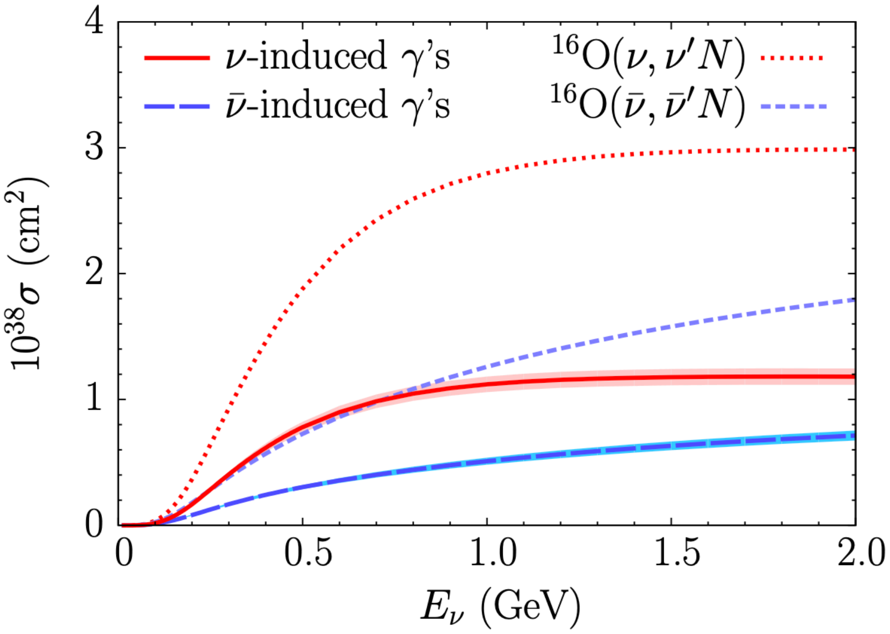

Figure 4.7: The NCQE interaction cross section for γ-ray production for neutrino (red solid line) and antineutrino (blue long-dashed line) modes compared to the NCQE cross section for ^{16}O in neutrino (red dashed line) and antineutrino modes (blue short-dashed line). The figure is taken from Ref. [77].

The residual nucleus occupies one of four states, $(p_{1/2})^{-1}$, $(p_{3/2})^{-1}$, $(s_{1/2})^{-1}$, and *others* in the simple shell model, with spectroscopic factors of 0.1580, 0.3515, 0.1055, and 0.3850, respectively [80]. No γ-ray emission occurs from the $(p_{1/2})^{-1}$ ground state, whereas the energy emitted from the $(p_{3/2})^{-1}$ is 6.32 MeV or 9.93 MeV for proton knock-out and 6.18 MeV for neutron knock-out [81]. The de-excitation channels for the $(s_{1/2})^{-1}$ state, which releases both nucleons and γ-rays, is selected according to results from the RCNP-E148 experiment [82]. The *others* state covers all channels not included in the above three states. Since no data or model predictions exist for γ-ray emission from this state, it is absorbed into the $(s_{1/2})^{-1}$.

4.3.2 Meson Exchange Current

The calculation for CCQE interactions, as outlined in Section 4.3.1, assumes no intra-nuclear correlations in the target nucleus, effectively modelling it as a single nucleon. However, incorporating such effects is crucial, given that neutrinos can interact with multiple nucleons in a meson exchange current (MEC) process. In particular, an important channel for this analysis is the two-particle-two-hole (2p2h) interaction, which results in the ejection of two nucleons from the nucleus and the creation of a corresponding pair of holes in the nuclear structure.

The MEC was regarded as the primary cause of the tension observed between the MiniBooNE results and existing models [83]. This result has since prompted numerous theoretical studies dedicated to enhancing the description of scattering from a bound multi-nucleon state beyond the relativistic Fermi gas model [83]. Hence, NEUT includes the MEC process for CCQE interactions by integrating the model proposed by Nieves et al. [84] into the framework.

4.3.3 Single Meson Production

The primary mechanism for hadron production in the region where the hadronic invariant mass (W) is below 2.0 GeV/c^2 is single meson production via resonances. The process occurs in two steps:

$$\text{Resonance production} : \nu + N \to l(\nu) + N^*,$$

$$\text{Resonance decay} : N^* \to N' + \text{meson}.$$

Here, N and N′ are initial and final state nucleons, respectively, and N^* denotes the baryonic resonance responsible for generating a single meson. NEUT simulates both the cross section for producing a baryon resonance, accounting for interference effects between various possible resonance states, and the subsequent decay into single mesons. For resonant pion production, NEUT considers 18 processes, with the most substantial contribution coming from $\Delta(1232)$, the lowest-mass resonance above the pion production threshold. These processes, including the final kinematics of the hadronic system, are calculated using the Rein-Sehgal model [85].

4.3.4 Coherent Pion Production

Coherent pion production involves the emission of a pion through the coherent scattering of a neutrino with an entire nucleus, without inducing fragmentation. The neutrino-oxygen interaction is expressed as,

$$\nu +^{16} O \rightarrow l +^{16} O + \pi$$

where the outgoing lepton and pion experience forward scattering due to the small four-momentum transfer to the nucleus. In SK, this process is indistinguishable from resonant pion production and the cross section is expected to be lower than the Rein-Seghal model prediction $\sim$1 GeV [85]. In NEUT version 5.4.0.1, the interaction model was updated to the Berger-Sehgal model [86], which uses pion-carbon scattering data and considers lepton-mass corrections.

4.3.5 Deep Inelastic Scattering

At high energies, neutrinos undergo CC deep inelastic scattering (DIS), probing the internal nucleon structure by scattering off individual quark constituents. The target nucleon breaks apart due to the significant momentum transfer, resulting in the production of multiple hadrons in the final state. In NEUT, this interaction is simulated when $W > 1.3$ GeV/c^2, using the PYTHIA/JETSET programs [87]. To prevent potential double counting due to an overlap in the invariant mass ranges defined for single pion production ($W \leq 2\,\mathrm{GeV/c^2}$) and DIS processes ($W > 1.3\,\mathrm{GeV/c^2}$), NEUT only considers multiple pion production below $2\,\mathrm{GeV/c^2}$. The nucleon structure is modelled with parton distribution functions from GRV98 [88], incorporating corrections from the Bodek and Yang model [89].

4.4 Inverse Beta Decay Simulation

The DSNB flux is uniformly distributed across all neutrino flavours and is detectable through several interaction channels. Figure 4.8 shows the effective cross section for each process in a water Cherenkov detector. Below ∼30 MeV, the primary detection channel is via the IBD of electron antineutrinos,

$$\overline{\nu}_e + p \rightarrow e^+ + n,$$

where an electron antineutrino interacts with a proton, resulting in the production of a positron and a neutron. Since the cross sections of subleading channels are several orders of magnitude lower than the IBD interaction, these contributions are excluded from the search. This work utilises the well-established IBD cross section (σ_{IBD}) calculation by Strumia and Vissani, which has an uncertainty of a fraction of a percent [90].

The SKSNSIM event generator is used to create the IBD simulation [92]. Events are generated uniformly in positron energy between 1 - 90 MeV, isotropically across the entire ID volume and at a rate of one per minute over the SK-VI livetime. To obtain the DSNB signal, the positron energy is renormalised by the flux prediction from each DSNB model convolved with the σ_{IBD}. This process enables each DSNB spectrum, shown in Figure 2.4, to be modelled from a generalised IBD simulation. Since some crucial backgrounds undergo IBD interactions with a shared final state ($e^+ + n$) and analogous kinematics, the IBD simulation is repurposed and normalised according to their specific flux predictions (see Chapter 5).

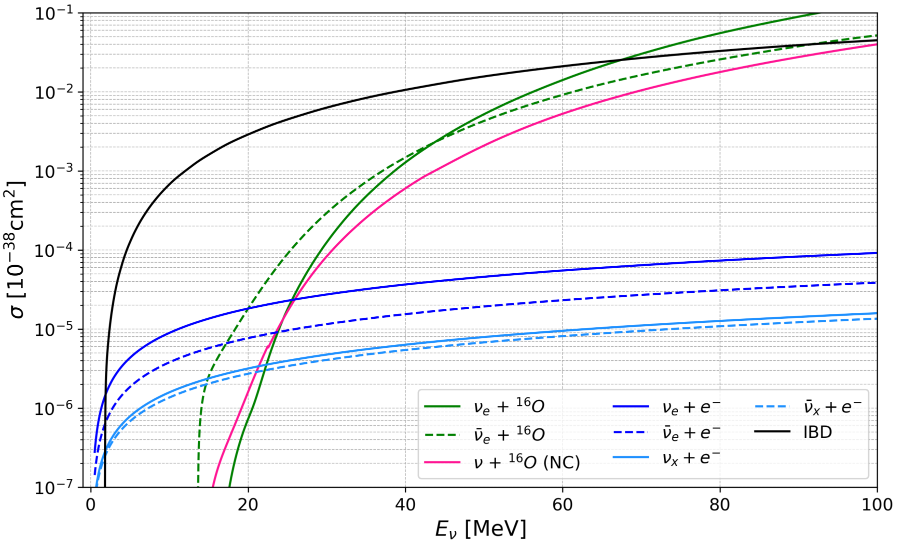

Figure 4.8: Cross sections (σ) of the main interaction channels for SN neutrinos in water Cherenkov detectors. The main interaction channel in SK is the IBD of electron antineutrinos (black). Further contributions from neutrino CC interactions with ^{16}O (green lines), with electrons in ^{1}H (blue lines) and neutrino NC interactions with ^{16}O (pink line) are shown. The σ_{NC} is for any ν or $\overline{\nu}$ flavour and ν_x refers to either ν_μ or ν_τ. The data in this plot is obtained from Ref. [91].

4.5 Detector Simulation

The SKG4 simulation package, based on GEANT4 [93], is used to model interactions and propagation of final state particles, Cherenkov and scintillation light emission, PMT and electronics response in the SK detector volume. The framework provides more accurate neutron interaction models, compared to the standard SK DETector SIMulation (SKDETSIM) GEANT3-based MC toolkit. Therefore, SKG4 is now the preferred choice for neutron tagging-based analyses in SK-Gd.

In GEANT4, electromagnetic and hadronic interactions are modelled with the FTFP_BERT_HP physics list [93]. The relevant processes for neutron capture on ^{155}Gd and ^{157}Gd isotopes and its subsequent interactions are simulated as

$$n +^{155}\text{Gd} \rightarrow^{156}\text{Gd}^* \rightarrow^{156}\text{Gd} + \gamma - \text{rays (8.536 MeV total)}$$
$$n +^{157}\text{Gd} \rightarrow^{158}\text{Gd}^* \rightarrow^{158}\text{Gd} + \gamma - \text{rays (7.937 MeV total)},$$

with the ANNRI-Gd γ-ray emission model. This selection is based on the strong agreement, within 17%, between the model predictions and data obtained from the ANNRI experiment [94]. To simulate pion interactions below 500 MeV/c^2, a custom model [95] is implemented using data from $\pi - p$ and $\pi -^{16} O$ scattering experiments [96, 97]. Optical photons produced by Cherenkov emission are generated with wavelengths ranging from 300 - 700 nm to align with the spectral sensitivity of the PMT. Detector effects, such as water transparency, Rayleigh and Mie scattering, absorption, PMT gain stability and dark noise, are tuned through calibration procedures (see Section 3.4). Similarly, the PMT response, signal integration and digitisation of charge and timing are also simulated based on photosensor calibration measurements. In SKG4, random noise simulation is not applied to the entire MC event. Instead, data from the T2K dummy-trigger and the SK-wide random trigger are superimposed onto all MC events after a delay of 2.7 μs.

4.6 Event Reconstruction

The event vertex, direction, and energy reconstruction are performed via dedicated software tools designed for SK analyses. The Branch Optimisation Navigating Successive Annealing Iterations (BONSAI) algorithm uses the PMT hit information from the SKG4 output to reconstruct low-energy electron-like events [98]. Separate algorithms, designed for high-energy events with more hits and multiple Cherenkov rings, are applied for atmospheric neutrino reconstruction (APFIT) [99] and muon identification (MuBoy) [100, 101]. This section provides an overview of the low-energy reconstruction methods relevant to this analysis.

4.6.1 Vertex Reconstruction

The vertex reconstruction relies on the timing information obtained from hit PMTs. Low-energy electron-like events are treated as point-like sources, as their short track lengths $\sim$10 cm are well within the $\sim$50 cm vertex resolution of the SK detector. BONSAI performs a maximum likelihood fit to the timing residual

($t_{res,i}$) of each hit PMT, defined as

$$\mathcal{L}(\mathbf{x}, t_0) \equiv \sum_{i=1}^{N_{\text{hit}}} \log P(t_{\text{res},i}), \tag{4.2}$$

$$t_{\text{res},i} = t_i - t_{\text{TOF},i} - t_0.$$

where $\mathbf{x}$ is the reconstructed test vertex, N_{hit} is the number of hit PMTs, t_i is the PMT hit timing, $t_{\text{TOF},i}$ is the time-of-flight (TOF) from the vertex to the hit PMT, and t_0 is the time of the interaction. The probability density function (PDF) of the timing residuals, $P(t_{\text{res},i})$, is obtained from LINAC calibration data, shown in Figure 4.9.

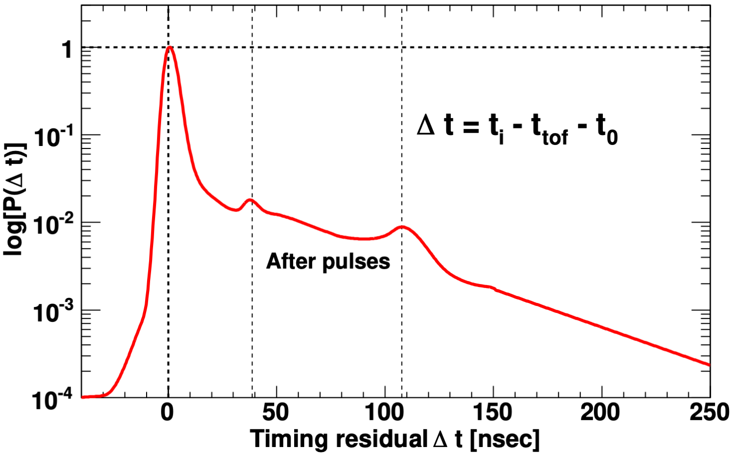

Figure 4.9: The BONSAI likelihood function for the timing residuals produced with LINAC calibration data. After pulses at ∼40 ns and ∼110 ns are labelled accordingly. The figure is taken from Ref. [102].

Computing the likelihood for each potential test vertex in a global search is computationally intensive and susceptible to misreconstruction in a large-scale detector. Accidental coincidences of dark noise hits, following TOF subtraction, may generate localised maxima far from the true vertex. Hence, BONSAI simplifies this process by selecting combinations of four PMT hits, generating test vertices for each combination, and then determining the maximum likelihood from this list of vertex candidates.

The goodness of the fit (g_{vtx}) to the reconstructed vertex is evaluated as the weighted average of a Gaussian function of the TOF-subtracted time of each PMT hit:

$$g_{\mathrm{vtx}} = \frac{\sum_{i=1}^{N_{\mathrm{hits}}} w_i \mathrm{e}^{-\frac{1}{2}\left(\frac{t_{\mathrm{res},i}-t_0}{\sigma}\right)^2}}{\sum_{i=1}^{N_{\mathrm{hits}}} w_i} \quad \text{where} \quad w_i = -\frac{1}{2}\left(\frac{t_{\mathrm{res},i}-t_0}{\omega}\right)^2. \tag{4.3}$$

The parameter w_i is the weight for the i-th PMT hit to account for dark noise, ω is the PMT time resolution, and σ is the effective time resolution for Cherenkov events. The values of ω and σ are 60 ns and 5 ns, respectively. The g_{vtx} is used as part of the event selection for the analysis, detailed in Chapter 7.

4.6.2 Direction Reconstruction

Direction reconstruction is based on the ring-like angular distribution of the PMT hits. A scan across all possible event directions is performed and the reconstructed direction is selected by maximising the following likelihood function

$$\mathcal{L}(\boldsymbol{d}) \equiv \sum_{i=1}^{N_{20}} \log\left\{f\left(\cos\theta_i, E\right)\right\} \times \frac{\cos\theta_i}{a\left(\theta_i\right)}, \tag{4.4}$$

where $\boldsymbol{d}$ is the reconstructed event direction, N_{20} is the largest number of PMT hits within a 20 ns window after TOF subtraction, independent of the BONSAI t_0[1], θ_i is the opening angle of the reconstructed event direction, $f\left(\cos\theta_i, E\right)$ is the expected distribution of the θ_i between the true and the observed event direction for an event with energy E and $a\left(\theta_i\right)$ is a parameter to correct for the acceptance of the PMT geometry. In SK, the angular resolution is found to be 25° for an event with 10 MeV, based on LINAC calibration data of downward-going electrons [103].

4.6.3 Energy Reconstruction

The energy of an event is roughly proportional to the number of true photoelectrons detected by the hit PMTs, with each hit generally corresponding to the detection of a single photon. To correct for detector effects and remove accidental hits caused by the PMT's dark rate, the energy reconstruction is based

---

[1] This window is determined on an event-by-event basis but most likely lies in an interval of [-7, 13] ns.

on calculating the effective number of hits N_{eff} in a 50 ns TOF-subtracted time window. This is defined as

$$N_{\mathrm{eff}} = \sum_{i}^{N_{50}} \left[(X_i + \epsilon_{\mathrm{tail}} - \epsilon_{\mathrm{dark}}) \times \frac{N_{\mathrm{all}}}{N_{\mathrm{normal}}} \times \frac{1}{S(\theta_i, \phi_i)} \times e^{\frac{r_i}{L_{\mathrm{att}}}} \times \frac{1}{QE_i} \right], \tag{4.5}$$

where each PMT hit i of the N_{50} total hits in the time interval is assigned a weight based on the following parameters:

- **Hit occupancy $\mathbf{X_i}$**: The assumption of proportionality between the number of hit PMTs and event energy breaks down for higher energy events. In such cases, a single hit-PMT is capable of detecting multiple photons, along with its neighbouring PMTs. Therefore, the occupancy parameter X_i is introduced, defined as

  $$X_i = \begin{cases} \frac{\log \frac{1}{1-x_i}}{x_i} & x_i < 1 \\ 3 & x_i = 1 \end{cases}, \tag{4.6}$$

  where x_i is the ratio of the number of PMT hits to the total number of PMTs in a 3×3 grid around the i-th PMT hit. This correction accounts for the multiple photoelectron effect in the i-th PMT, based on the hit distribution in neighbouring PMTs and the total number of PMT hits in the event.

- **Late hits $\epsilon_{\mathbf{tail}}$**: The i-th PMT may detect photons that undergo delays resulting from a combination of scattering in the water and reflection from detector components. These delayed hits might fall outside the 50 ns TOF-subtracted window. Therefore, a correction term for the late hits is used to integrate delayed hits into the N_{eff} calculation.

- **Dark hits $\epsilon_{\mathbf{dark}}$**: This parameter corrects for the expected contribution of dark noise hits within the signal window, based on the dark rate for the i-th PMT.

- **Non-operational PMTs $\frac{\mathbf{N_{all}}}{\mathbf{N_{normal}}}$**: The ratio of the number of total ID PMTs (N_{all}) to the number of normally operating PMTs (N_{normal}) is applied to correct for the detection inefficiency due to non-operational PMTs in the current data run.

- **Effective photocoverage $S(\theta_i, \phi_i)$**: The detection inefficiency due to the geometrical acceptance of the PMT, represented in the function $S(\theta_i, \phi_i)$, is corrected for considering the incident angle of the photon (θ_i) and the azimuth angle of the PMT (ϕ_i).
- **Water transparency $e^{r_i/L_{\text{att}}}$**: This correction accounts for light attenuation L_{att} in the water for the i-th PMT at distance r_i from the event vertex.
- **Quantum efficiency 1/QE**: This correction is applied to include the effects of the variation in the QE across each PMT.

The N_{eff} of an event is converted into energy using a polynomial function derived from electron MC simulations, with coefficients tuned by calibration data. Further details of the energy reconstruction process can be found in Ref. [104].

4.6.4 Cherenkov Angle Reconstruction

The Cherenkov opening angle (θ_C) is determined based on the distributions of PMT hits in the event with timing residuals within 15 ns of the reconstructed vertex. For each event, a scan is performed with a 0.9° window, across a distribution of opening angles (θ) generated for all possible three-hit combinations. The reconstructed θ_C is selected as the central value within the window that maximises the number of hits. Figure 4.10 displays the θ distribution for various event types, which shows its discriminating power for particle identification.

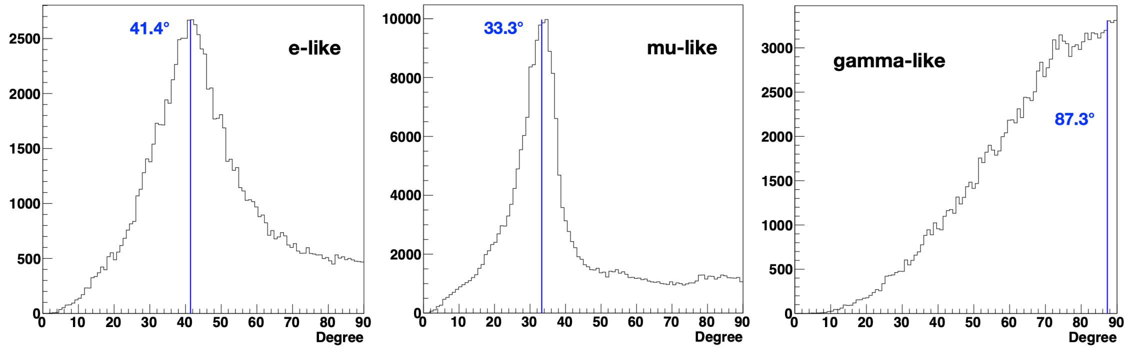

Figure 4.10: The opening angle θ distributions for low-energy events: e-like (left), μ-like (middle) and multiple γ-ray emission (right). The reconstructed Cherenkov angle θ_C for each distribution is shown by the blue line. The figure is taken from Ref. [18].

5

Signal and Backgrounds

This chapter describes the DSNB signal, the main background sources, and the corresponding models used in the analysis.

5.1 The DSNB Signal

The dominant channel for DSNB detection in SK is the IBD interaction of electron antineutrinos ($\overline{\nu}_e + p \rightarrow e^+ + n$), as described in Section 4.4. This interaction produces a coincidence signature characterised by the *prompt* positron and *delayed* neutron capture events. A schematic diagram of the IBD event signature is shown in Figure 5.1.

The prompt signal is directly detected through the emission of Cherenkov radiation. Most of the antineutrino energy ($E_{\overline{\nu}}$) is transferred to the positron (E_e) by $E_e = E_{\overline{\nu}} - \Delta_{n,p}$, where $\Delta_{n,p} = 1.293$ MeV represents the nucleon mass difference. The neutron thermalises and is captured by ^{155}Gd and ^{157}Gd isotopes, which feature neutron capture cross sections of 60,900 barns and 254,000 barns, respectively [105]. In SK-VI, the $\mathrm{Gd_2(SO_4)_3 \cdot 8H_2O}$ mass concentration in the tank is 0.011%, corresponding to ~50% neutron capture efficiency on Gd isotopes, with a time constant of ~115 μs [54]. Following this process, de-excitation γ-rays are emitted with a total energy of ~8 MeV, and detected via Compton scattering

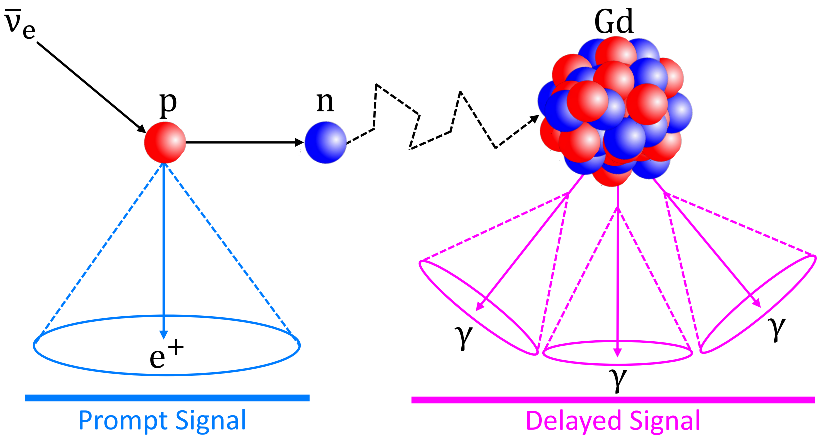

Figure 5.1: Schematic diagram of the IBD interaction between an electron antineutrino and a proton producing a *prompt* positron and a *delayed* neutron capture signal on Gd.

on electrons [106]. For cascades containing several γ-rays, if the energy of one or more recoil electrons falls below the Cherenkov threshold ($E_e > 0.8$ MeV), the resulting visible energy will be less than the total emitted energy.

5.2 Background Sources

The delayed-coincidence signal from IBD interactions, combined with neutron tagging on Gd, effectively reduces single-event backgrounds without neutron emission. These backgrounds include solar neutrinos, most decay isotopes from muon spallation, and radioactivity from the surrounding rock. However, correlated background events that mimic both the prompt and delayed signal still dominate the signal region. This section provides an overview of these backgrounds and the various techniques used to model them.

5.2.1 Atmospheric Neutrinos

Atmospheric neutrinos significantly contribute to the background of the DSNB search. In SK, oxygen nuclei and free protons are primary targets for CC and NC neutrino interactions. The resulting secondary particles often reconstruct with energy levels falling within the signal region and can be accompanied by neutrons. The following section covers the main background processes relevant to this analysis.

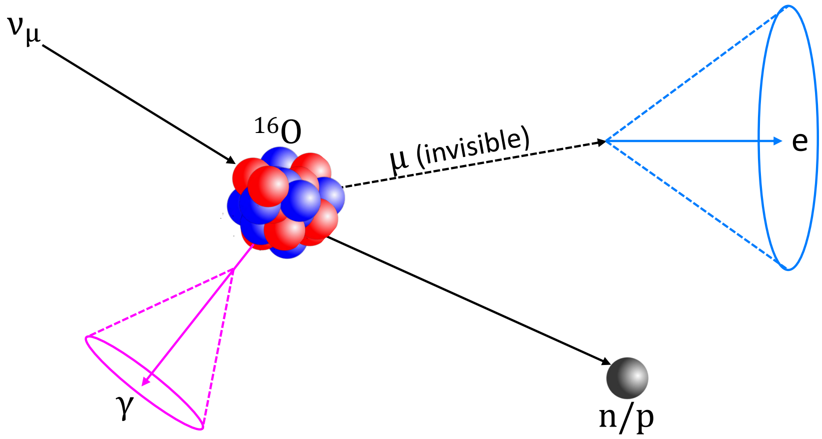

Figure 5.2: Schematic diagram of a CC ν_μ interaction with an oxygen nucleus producing a nucleon, invisible muon and subsequent decay electron in the final state.

Charged Current ν_μ Interactions

CC ν_μ interactions can generate *invisible* muons, below the Cherenkov threshold, that decay into visible electrons, as shown in Figure 5.2. The resulting decay electron is characterised by the well-known Michel electron spectrum, which covers an energy range between 16 - 90 MeV. The event signature closely resembles an IBD prompt signal and contributes as an irreducible background when detected in coincidence with a final-state neutron. Similarly, observable decay electrons can be produced by the decay of pions into muons, where both parent particles are invisible. In SK, the Michel electron spectrum, measured precisely with the stopped muon sample, is used to estimate the expected number of invisible muons and pions in data sidebands (see Section 8.2) [107].

Charged Current ν_e Interactions

Electrons (positrons) produced from CC $\nu_e(\overline{\nu}_e)$ interactions are almost indistinguishable from DSNB signals when accompanied by a neutron. The only distinction is that the CC ν_e interaction cross section scales linearly with incident neutrino energy. Similarly, sideband data is used to estimate the expected contribution to the overall background. Figure 5.3 shows the schematic diagram for this interaction.

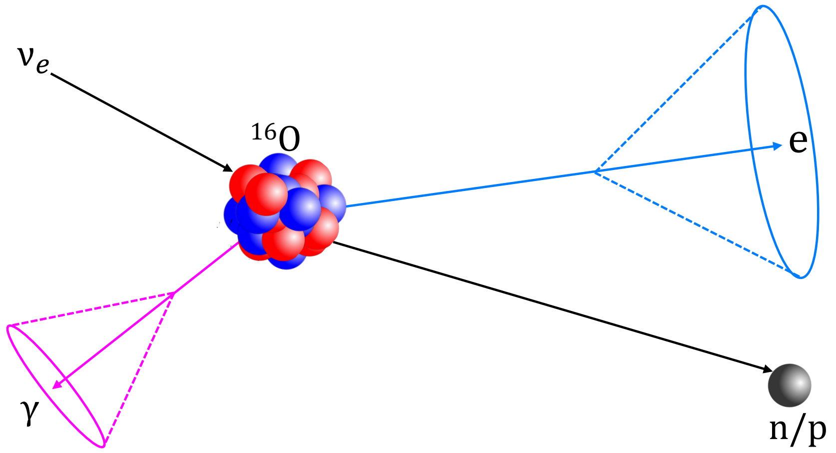

Figure 5.3: Schematic diagram of a CC ν_e interaction with an oxygen nucleus producing a nucleon and an electron in the final state.

Visible Muons and Pions

CC and NC interactions induced by atmospheric neutrinos can produce observable pions and muons in the final state. These backgrounds are generally unproblematic, as their higher mass and momentum lead to event topologies that can be easily separated from the prompt signal.

Neutral Current Quasi-Elastic Interactions

NCQE interactions of atmospheric neutrinos with oxygen nuclei is a dominant background below 20 MeV, where the predicted DSNB flux is high [108]. For neutrino energies $E_\nu \geq 200$ MeV, the nucleon knock-out process produces primary γ-rays from the de-excitation of residual nuclei, with energies between 6 - 8 MeV [108]. Final-state protons often fall below the Cherenkov threshold, whereas outgoing neutrons undergo hadronic interactions with other nuclei in the detector, prompting the production of secondary γ-rays and additional neutrons. After thermal propagation, these neutrons can be captured by Gd isotopes and emit 8 MeV γ-rays, as shown in Figure 5.4. The detection of the primary γ-ray coupled with a delayed-coincidence signal mimics the IBD event signature, which limits the DSNB search sensitivity. In this thesis, a novel ML-based reduction technique has been developed to mitigate the impact of the NCQE background, which is described in Chapter 6.

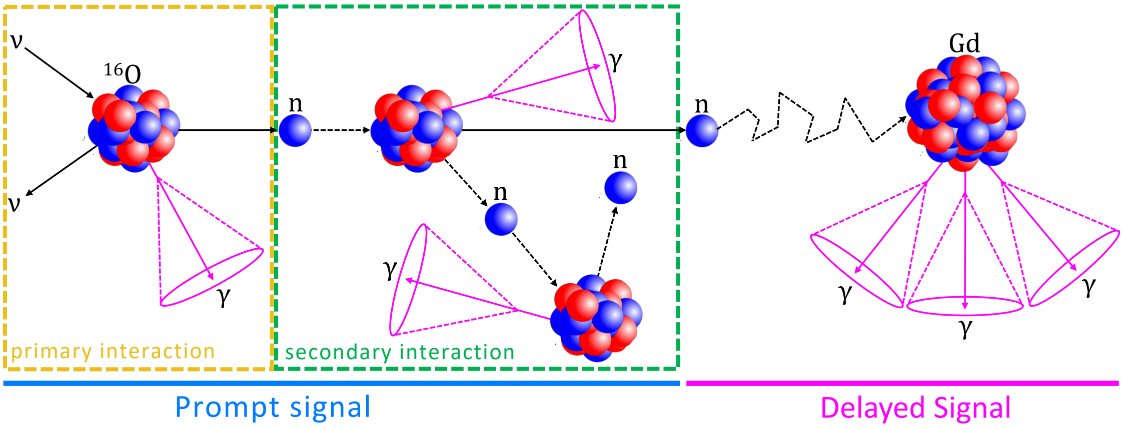

Figure 5.4: Schematic diagram of an NCQE interaction of atmospheric neutrinos with oxygen nuclei. The prompt signal consists of γ-rays produced by neutrino-oxygen (primary) and neutron-nucleus (secondary) interactions.

5.2.2 Muon Spallation Products

The cosmic ray muon flux at SK, measured as $9.6\,\mathrm{m}^{-2}\,\mathrm{hr}^{-1}$, corresponds to a muon rate of $\sim$2 Hz through the detector [109, 110]. While muons are easily identified, their highly energetic interactions with oxygen nuclei in the water, referred to as *spallation*, and energy-loss processes generate hadrons and unstable radioactive isotopes. The subsequent beta decay (β) of these isotopes significantly contributes to the background spectrum below 20 MeV. Since the spallation rate is $O(10^6)$ greater than the predicted DSNB flux, detailed simulations and effective spallation reduction techniques are required for the analysis.

Table 5.1 provides a summary of the FLUKA simulation results described in Refs. [111–113], which investigated the half-lives, decay modes, yields, and primary processes of isotopes in water. The isotopes form three decay classes: neutrons, β-decay isotopes with and without accompanying hadrons and γ-rays, and more stable long-lived isotopes that do not exhibit a visible signature in SK. The end-point energy with respect to the half-life of spallation isotopes is shown in Figure 5.5.

Most isotopes generating $\beta + n$ pairs, such as ^{8}He, ^{11}Li, and ^{16}C, are considered subdominant processes due to their low branching ratios and yields. Since ^{11}Li is short-lived, it can be easily correlated with the incident muon and

Isotope	**Half-life** [s]	**Decay mode**	**Yield** $[\times 10^{-7} \mu^{-1}\ \mathrm{g}^{-1}\ \mathrm{cm}^2]$	**Primary process**
n			2030	
$^{18}\mathrm{N}$	0.624	β^-	0.02	$^{18}\mathrm{O}(n,p)$
$^{17}\mathrm{N}$	4.173	$\beta^- + n$	0.59	$^{18}\mathrm{O}(n,n+p)$
$^{16}\mathrm{N}$	7.13	$\beta^- + \gamma(66\%)$ $\beta^-(28\%)$	18	(n,p)
$^{16}\mathrm{C}$	0.747	$\beta^- + n$	0.02	$(\pi^-,n+p)$
$^{15}\mathrm{C}$	2.449	$\beta^- + \gamma(63\%)$ $\beta^-(37\%)$	0.82	$(n,2p)$
$^{14}\mathrm{B}$	0.0138	$\beta^- + \gamma$	0.02	$(n,3p)$
$^{13}\mathrm{O}$	0.0086	β^+	0.26	$(\mu^-,p+2n+\mu^-+\pi^-)$
$^{13}\mathrm{B}$	0.0174	β^-	1.9	$(\pi^-,2p+n)$
$^{12}\mathrm{N}$	0.0110	β^-	1.3	$(\pi^+,2p+2n)$
$^{12}\mathrm{B}$	0.0202	β^+	0.02	$(n,\alpha+p)$
$^{12}\mathrm{Be}$	0.0236	β^-	12	$(n,\alpha+p+n)$
$^{11}\mathrm{Be}$	13.8	$\beta^-(55\%)$ $\beta^-(31\%)$	0.10	$(n,\alpha+2p)$
$^{11}\mathrm{Li}$	0.0085	$\beta^- + n$	0.01	$(\pi^+,5p+\pi^++\pi^0)$
$^{9}\mathrm{C}$	0.127	β^+	0.89	$(n,\alpha+4n)$
$^{9}\mathrm{Li}$	0.178	$\beta^- + n(51\%)$ $\beta^-(49\%)$	1.9	$(\pi^-,\alpha+2p+n)$
$^{8}\mathrm{B}$	0.77	β^+	5.8	$(\pi^-,\alpha+2p+2n)$
$^{8}\mathrm{Li}$	0.838	β^-	13	$(\pi^-,\alpha+{}^{2}\mathrm{H}+p+n)$
$^{8}\mathrm{He}$	0.119	$\beta^- + n(16\%)$ $\beta^- + n(16\%)$	0.23	$(\pi^-,{}^{3}\mathrm{H}+4p+n)$
$^{15}\mathrm{O}$			351	$(\gamma+n)$
$^{15}\mathrm{N}$			773	$(\gamma+p)$
$^{14}\mathrm{O}$			13	$(n,3n)$
$^{14}\mathrm{N}$			295	$(\gamma,n+p)$
$^{14}\mathrm{C}$			64	$(n,n+2p)$
$^{13}\mathrm{N}$			19	$(\gamma,{}^{3}\mathrm{H})$
$^{13}\mathrm{C}$			225	$(n,{}^{2}\mathrm{H}+p+n)$
$^{12}\mathrm{C}$			792	(γ,α)
$^{11}\mathrm{C}$			105	$(n,\alpha+2n)$
$^{11}\mathrm{B}$			174	$(n,\alpha+p+n)$
$^{10}\mathrm{C}$			7.6	$(n,\alpha+3n)$
$^{10}\mathrm{B}$			77	$(n,\alpha+p+2n)$
$^{9}\mathrm{Be}$			24	$(n,\alpha+2p+n)$
$^{9}\mathrm{Be}$			38	$(n,2\alpha)$
Sum			3015	

Table 5.1: List of radioactive isotopes produced in the muon spallation processes at SK calculated by FLUKA. ^{9}Li decay has been highlighted as it forms the largest spallation background in the DSNB analysis. This table has been taken from Ref. [114].

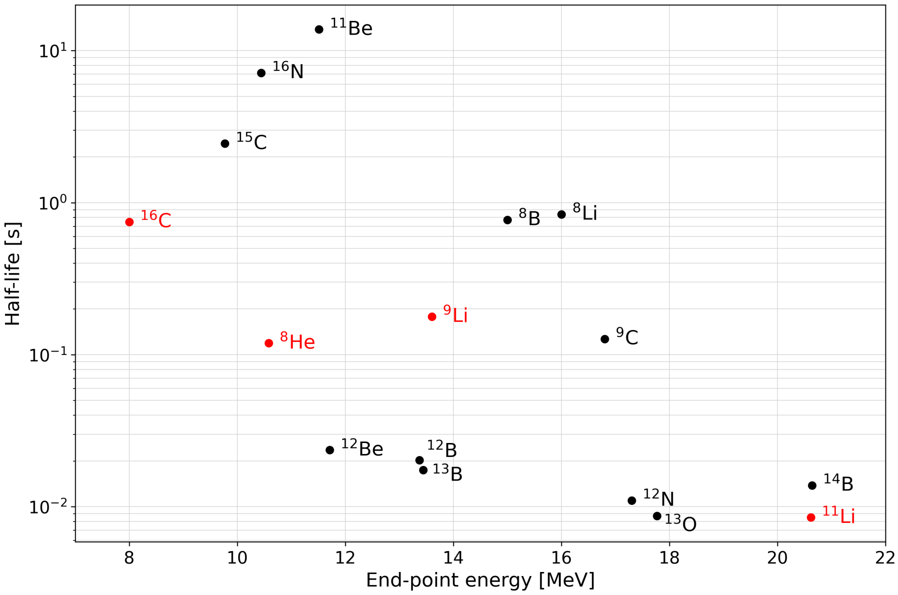

Figure 5.5: Scatter plot of the end-point energy with respect to the half-life of radioactive isotopes produced by muon spallation processes. Isotopes that produce a neutron in the final state are highlighted in red.

rejected using simple cuts. However, ^{9}Li presents a significant challenge due to its high yield, longer half-life of ∼0.178 s, and decay into a $\beta + n$ pair with a branching ratio of ∼51%. This decay closely mimics the IBD interaction and cannot be reduced with neutron tagging alone. Since SK lacks sensitivity to subtle differences between e^-/e^+ production and neutron energy levels, ^{9}Li decay with neutron emission is an irreducible background to the analysis.

The BESTIOLE code is used to simulate the β energy spectrum of ^{9}Li decays [115]. This model accounts for resolution effects and extends up to approximately 14 MeV in reconstructed energy. The flux weights of the model are applied to the IBD prompt signal MC to produce the spectrum shown in Figure 5.6. To estimate the decay rate in the signal energy window, the ^{9}Li production rate measurement of $0.86 \pm 0.12(\text{stat.}) \pm 0.15(\text{syst.})\ \text{kton}^{-1}\text{day}^{-1}$ is used [45].

5.2.3 Reactor Neutrinos

Electron antineutrinos produced from the beta decay of fission fragments in nuclear reactors form an irreducible background. The $\overline{\nu}_e$ flux primarily originates from the decay-chains of neutron-rich ^{235}U and ^{239}Pu isotopes, contributing to

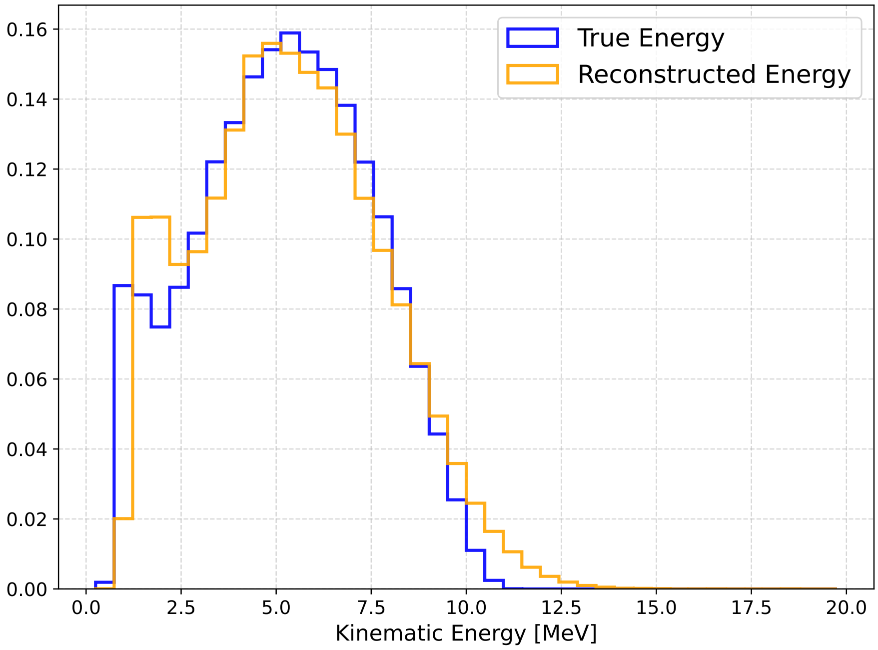

Figure 5.6: True (blue) and reconstructed (orange) β kinetic energy for ^{9}Li decay with neutron emission.

about 90% of the total neutrino production [116]. Each fission event releases ~200 MeV of energy, with an expected emission of 6×10^{20} $\overline{\nu}_e$ per second for a 3 GW thermal reactor power [117]. While most of the energy generated remains confined within the reactor as heat, approximately 5% is carried away by the antineutrinos. The energy spectrum of the $\overline{\nu}_e$ flux depends on the fractional contribution of each fissile isotope in the reactor and the detector's proximity to it. The activity of several reactors near the SK site is presented in Figure 5.7.

To simulate the reactor neutrino background, the IBD simulation (see Section 4.4) is reweighted according to the expected flux calculated by SKReact [119]. The event production and oscillation probabilities are modelled based on the Power Reactor Information System (PRIS) database from IAEA [120]. The resulting flux at the SK site per year for the SK-VI period is shown in Figure 5.8. While the spectrum exhibits a pronounced peak at low energies, its distribution extends up to 8 MeV within the DSNB search window. Since the reactor neutrino rate surpasses the predicted DSNB flux by about two orders of magnitude above 6 MeV, this limits the lower energy threshold for the DSNB analysis.

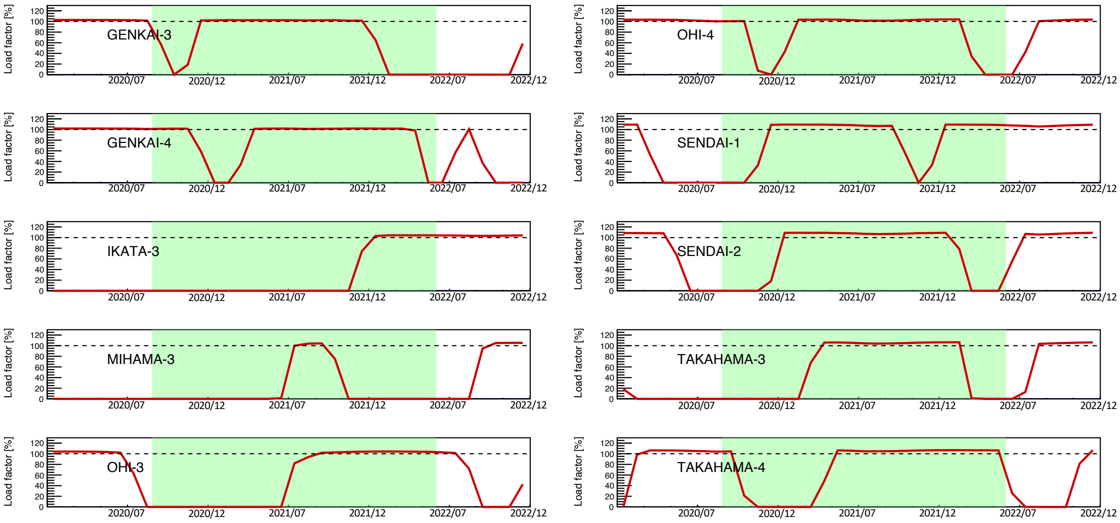

Figure 5.7: Activity trend from Japanese nuclear reactors located near to the SK site from July 2020 to July 2022. The green-shaded region refers to the data-taking period of the SK-VI run. The figure is taken from Ref. [118].

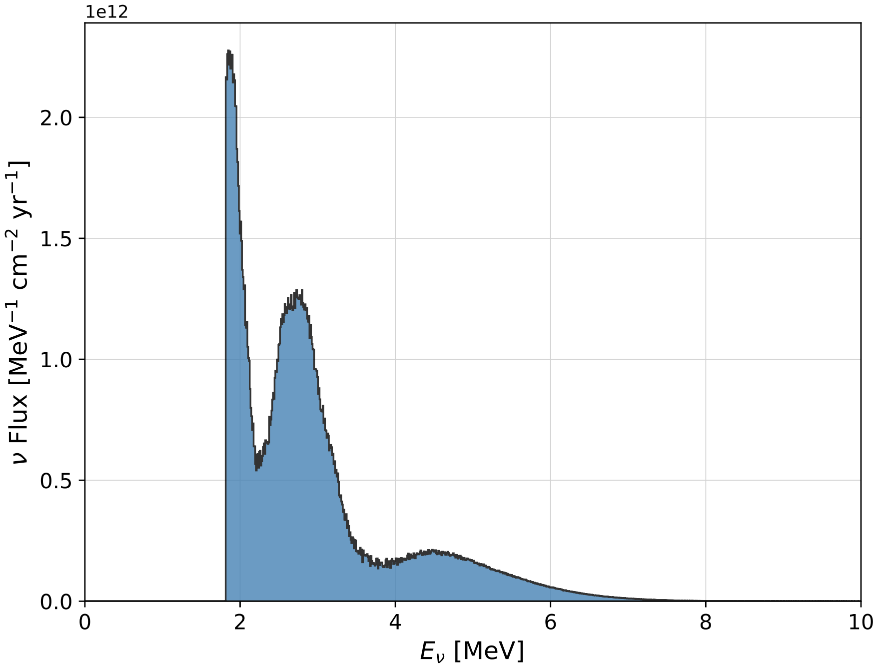

Figure 5.8: Expected reactor $\overline{\nu}_e$ flux at the SK site, including neutrino oscillation effects, for the SK-VI run period.

5.2.4 Accidental Coincidences

An electron-like signal, combined with an uncorrelated true neutron from muon spallation or noise hits, can mimic an IBD event. These backgrounds are categorised as true and false accidental coincidences, respectively. Removing events with true neutron signals is challenging and requires strict spallation cuts. On the other hand, false neutrons, originating from PMT dark noise and low-energy radioactive backgrounds, can be eliminated with neutron tagging. Since SKG4 lacks an accurate simulation of random noise produced by radioactive decay, accidental coincidences are modelled using real data. A 532 μs data sample from the T2K dummy-trigger and the SK-wide random trigger is superimposed onto each MC event in the neutron search window. These events are triggered during T2K beam inactivity and periodically throughout normal SK runs. This step reduces neutron misidentification in the neutron tagging algorithm (see Section 7.5) and facilitates estimating the accidental coincidence background spectrum.

6

Convolutional Neural Networks for Event Classification

This chapter presents the first implementation of a Convolutional Neural Network (CNN) model for image-based classification in the DSNB analysis in SK. The first section introduces a theoretical background to neural networks, supervised learning, and CNNs. The Gamma And Positron CNN model (GAPNet), developed by the author using the Water Cherenkov Machine Learning (WatChMaL) framework, is then described in detail including model training, performance, and systematic uncertainties.

6.1 Motivation

Low-energy neutrino physics analyses usually implement cut-based background rejection techniques to improve the signal-to-background ratio. In the DSNB analysis, a series of boolean cuts are applied to variables obtained from likelihood-based reconstruction algorithms to target atmospheric neutrino and spallation backgrounds (see Chapter 7). For example, the Cherenkov angle (θ_C) cut is optimised to reduce the NCQE background. Despite its general effectiveness, the discriminating power of the cut diminishes in the lowest energy region, where the expected signal is highest. This highlights a limitation of traditional methods in distinguishing subtle feature differences between positrons and γ-rays in sparse low-energy datasets. Therefore, these techniques alone are insufficient for achieving the required background reduction to observe the DSNB signal.

Improving traditional reconstruction is challenging due to the need for more intricate algorithms with extended computational time. Therefore, ML techniques are increasingly being used for various particle physics applications. In neutrino physics, the SNO experiment first explored using neural networks for event classification based on hit patterns [121]. More recently, deep learning networks have proven effective in electron neutrino appearance searches within the NOνA experiment [122] and in neutrino identification using the Faster R-CNN algorithm in MicroBooNE [123].

The WatChMaL organisation was formed to develop deep learning classification and reconstruction models for analyses in SK and HK [124]. The group has achieved promising results for ML-based neutron captures [125] and particle identification (PID) studies [126]. A recent study, conducted by a group external to SK, has proposed using ML techniques to enhance NCQE background rejection [127]. This result has provided a strong incentive to explore similar methods in the DSNB analysis at SK.

6.2 Neural Networks

Neural networks are powerful nonlinear models effective in various applications, including pattern recognition, classification, regression, and reinforcement learning [128]. The basic computational unit in a feed-forward neural network is the artificial neuron, illustrated in Figure 6.1. The input layer takes in a vector of D input features $\mathbf{x} = [x_1, x_2, ..., x_D]$, each associated with a set of weights $\mathbf{w} = [w_1, w_2, ..., w_D]$ and a bias term w_0. The weights represent the strength of the connections between the input features and the neuron, and the bias term defines the minimum activation threshold of the neuron. In *forward propagation*, the

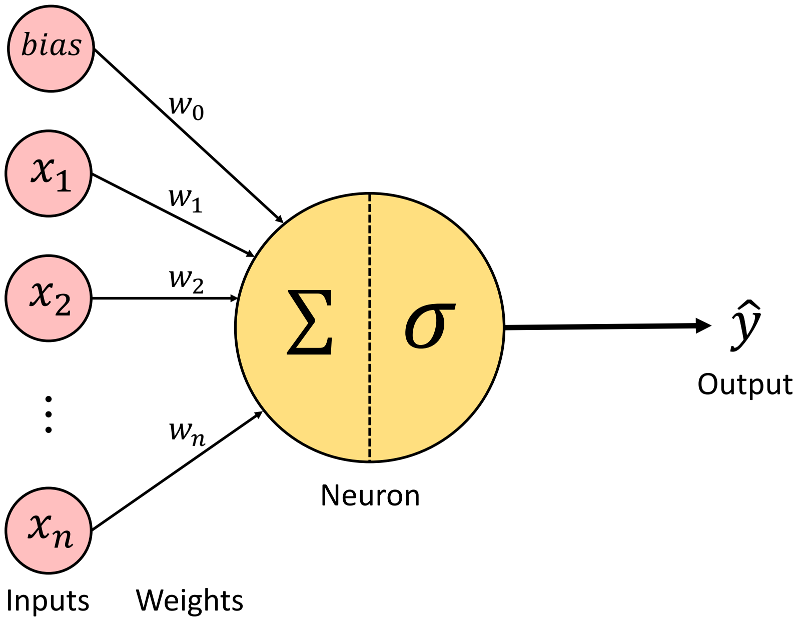

Figure 6.1: Schematic diagram of an artificial neuron. The weights w_n from an input vector x_n with a bias term w_0 are summed via element-wise multiplication, and processed through a non-linear activation function σ to output a scalar quantity $\hat{y}$.

neuron processes these inputs through a series of linear combinations, followed by a nonlinear activation function σ, to generate a scalar output $\hat{y}$,

$$\hat{y} = \sigma(a), \tag{6.1}$$

$$a = w_0 + \sum_{i=1}^{D} w_i \cdot x_i,$$

where a represents the activation of the neuron.

Multiple layers of artificial neurons can be stacked to construct more complex fully connected neural networks, commonly known as *multilayer perceptrons* (MLPs) (see Figure 6.2) [129]. The intermediate *hidden* layers play a crucial role in extracting and learning more robust and invariant features from the input data. The output function for a network with M neurons in the hidden layer takes the form,

$$\hat{y}_k = \sigma_{\text{out}} \left(w_{k,0}^{(2)} + \sum_{j=1}^{M} w_{k,j}^{(2)} \cdot \sigma(a_j) \right), \tag{6.2}$$

$$a_j = w_{j,0}^{(1)} + \sum_{i=1}^{D} w_{j,i}^{(1)} \cdot x_i,$$

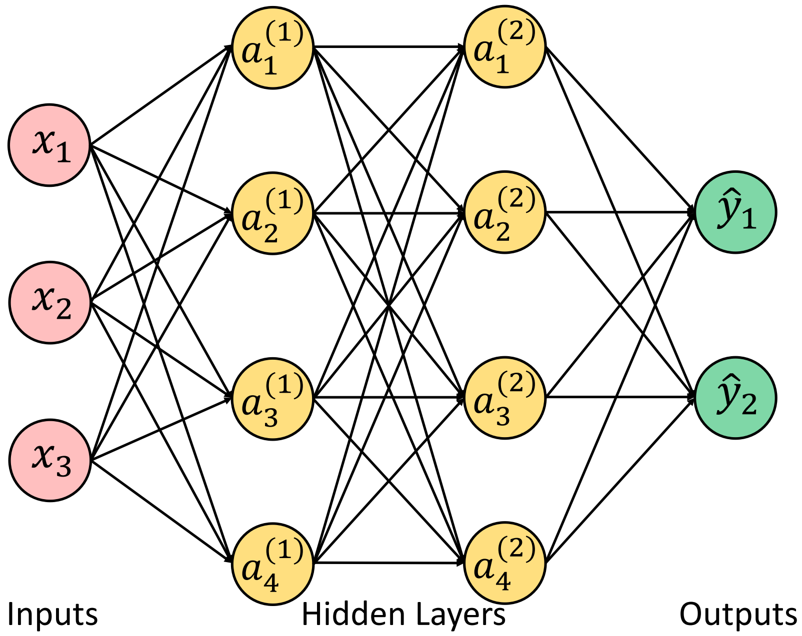

Figure 6.2: Schematic diagram of a multilayer perceptron (MLP) containing an input vector x_n with three elements, two hidden layers with neurons $a_i^{(j)}$, and two outputs $\hat{y}_k$. The connections represent the weights and biases for each layer.

where σ_{out} represents the nonlinear activation function for the output layer and the superscripts (1) and (2) denote the network parameters of the first and second layers, respectively.

The choice of the nonlinear activation function determines the neural network's ability to learn complex patterns in the data and make accurate predictions. The *perceptron*, an early model introduced by Frank Rosenblatt, is a specific example of an artificial neuron that used a unit-step activation function for binary classification [130]. However, the step function produces zero derivatives (*vanishing gradients*) everywhere except for an input of zero during gradient-based training processes (see Section 6.2.1) [131]. Therefore, modern deep neural networks opt for non-saturating activation functions such as variants of the Rectified Linear Unit (ReLU) function [132, 133]. These piecewise linear functions return the input for positive values and zero (or close to) for negatives, making it highly efficient for training computations. Figure 6.3 shows the common activation functions used for training artificial and deep learning neural networks.

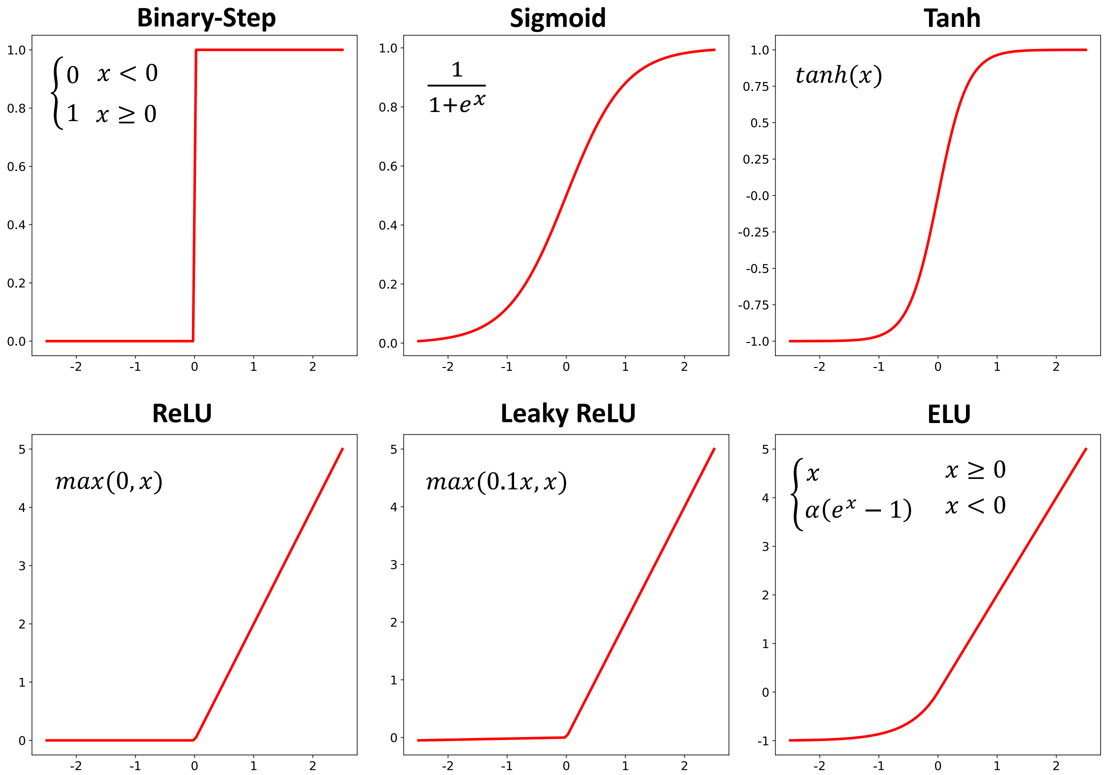

Figure 6.3: Standard non-linear activation functions used for neural networks and deep learning models.

6.2.1 Supervised Learning

In *supervised learning*, the neural network is trained on a labelled dataset containing a set of N pairs $\{\mathbf{x}_n, y_n\}_{n=1,\ldots,N}$, where $\mathbf{x}_n$ represents input feature vectors and y_n is the target outputs [128]. The dataset is split into three subsets for training, validation, and testing. The network parameters ($\mathbf{w}$ and w_0) are initially assigned random values before training. The training process iteratively adjusts these parameters using a gradient-based optimisation algorithm to maximise model performance.

The *cross-entropy* loss function $\mathcal{L}(\hat{y}^{(i)}, y^{(i)})$, also known as the logarithmic loss, is typically used to estimate the differences between model predictions and target outputs in the training dataset [128]. It is expressed by the negative log-likelihood formula,

$$\mathcal{L}(\hat{y}^{(i)}, y^{(i)}) = -(y^{(i)} \log(\hat{y}^{(i)}) + (1 - y^{(i)})) \log(1 - \hat{y}^{(i)})), \tag{6.3}$$

where a lower loss indicates better agreement between the model's predictions and target outputs. This function is well suited for binary classification tasks where the objective is to categorise input data into two classes (0 or 1). In addition, it excels in gradient-based optimisation when model outputs are represented as probabilities, resulting in faster training compared to alternatives such as the Mean Squared Error [134].

The *cost* function $E(\boldsymbol{\theta})$ used to train the neural network is the average of the loss function over the entire training dataset, written as

$$E(\boldsymbol{\theta}) = -\frac{1}{N}\sum_{i=1}^{N} \mathcal{L}(\hat{y}^{(i)}, y^{(i)}), \tag{6.4}$$

where $\boldsymbol{\theta}$ represents the network parameters $\mathbf{w}$ and w_0. During training, the primary objective is to determine optimal values for the weights and biases that converge the cost function towards the global minimum. This process, known as *gradient-descent* [135], involves computing the partial derivatives of $E(\boldsymbol{\theta})$ and updating the network parameters over t iterations via

$$\boldsymbol{\theta}_{t+1} = \boldsymbol{\theta}_t - \eta_t \nabla_{\boldsymbol{\theta}} E(\boldsymbol{\theta}). \tag{6.5}$$

The parameter $\eta_t > 0$ is the *learning rate*, which defines the size of the step taken in the direction of the gradient at each iteration. The performance of the gradient-descent optimisation algorithm is highly sensitive to the value of η_t. A higher learning rate can lead to a faster convergence but may overshoot the best solution and cause training instabilities. On the other hand, a lower learning rate mitigates training fluctuations but can result in the cost function converging to suboptimal local minima. Figure 6.4 shows an illustration of the gradient descent procedure.

Backpropagation is used to calculate the gradients $\nabla_{\boldsymbol{\theta}} E(\boldsymbol{\theta})$ at each step [136]. The full derivation of the method is described in Ref. [128]. To summarise the key points, a forward pass is first performed to process the input data through the randomly initialised network, and the outputs are determined using the procedure detailed in Section 6.2. Following this, the errors of the output layer

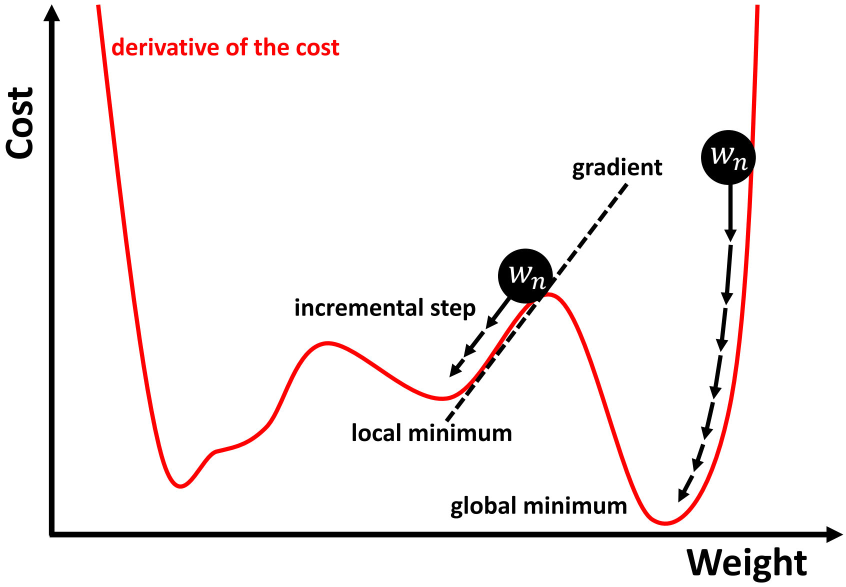

Figure 6.4: Schematic diagram of the gradient descent method. The same weight w_n is shown to reach a global and local minimum of the cost function.

are computed, which correspond to the partial derivatives of the cost function, neuron activations, and model predictions. The subsequent step involves propagating this error backwards through the network by recursively applying the chain rule. The final gradients are then evaluated to provide the relative adjustments to the weights and biases required to minimise the cost function.

The gradient-descent algorithm becomes computationally expensive for large datasets as it requires calculating gradients over the entire training sample. Therefore, modern deep learning models use more efficient variants such as Stochastic Gradient Descent (SGD) or Adaptive Moment Estimation (Adam), where a single sample or a random subset (*mini-batch*)[1] of the training dataset is processed per iteration [137]. This approach enables faster *parallelised* training since the gradients can be computed simultaneously for separate mini-batches using higher-level resources such as graphical processing unit (GPU) devices. In addition, processing mini-batches helps prevent *overfitting* to noise in the training dataset, which enhances the model's generalisation to unseen test data [138].

---

[1] The SGD method with a mini-batch size greater than one is also referred to as Mini-Batch Gradient Descent in the literature.

The complete training process involves several passes through the entire training dataset, referred to as *epochs*. The validation dataset is applied after each epoch to iteratively evaluate the performance throughout training. Monitoring the validation loss trend is crucial for fine-tuning *hyperparameters*, which are specific training-related and model architecture parameters. Regularisation techniques, such as *early-stopping*, can be triggered if the validation loss exceeds a predefined threshold or shows no improvement after a specified number of epochs [128]. At this point, the training is stopped and the model from the epoch with the best validation accuracy is retained. This technique improves training efficiency and mitigates overfitting. Finally, the trained model undergoes evaluation using an unseen testing sample to qualify its overall performance.

6.3 Convolutional Neural Networks

Artificial neural networks excel in basic pattern recognition and classification tasks, such as identifying handwritten digits with the MNIST database [139]. However, these models struggle to handle the computational complexity required for advanced image processing. In a neural network, high-dimensional image data is flattened into a one-dimensional input vector, resulting in the loss of all localised and hierarchical features. In addition, training becomes inefficient and prone to overfitting as the number of network parameters significantly increases in a fully connected system. For example, a network processing a 100×100 black and white image will have a minimum of $10,000^2$ parameters in the first layer alone. Therefore, specialised model architectures, such as Convolutional Neural Networks (CNNs), are necessary for more complex classification challenges [140]. The following sections outline the basic structure of a CNN, including a conceptual overview of the relevant operations.

6.3.1 Convolutional Layer

In computer vision tasks, images are represented by three-dimensional grid-like structures, where each point corresponds to a *pixel* encoded with red, green, and

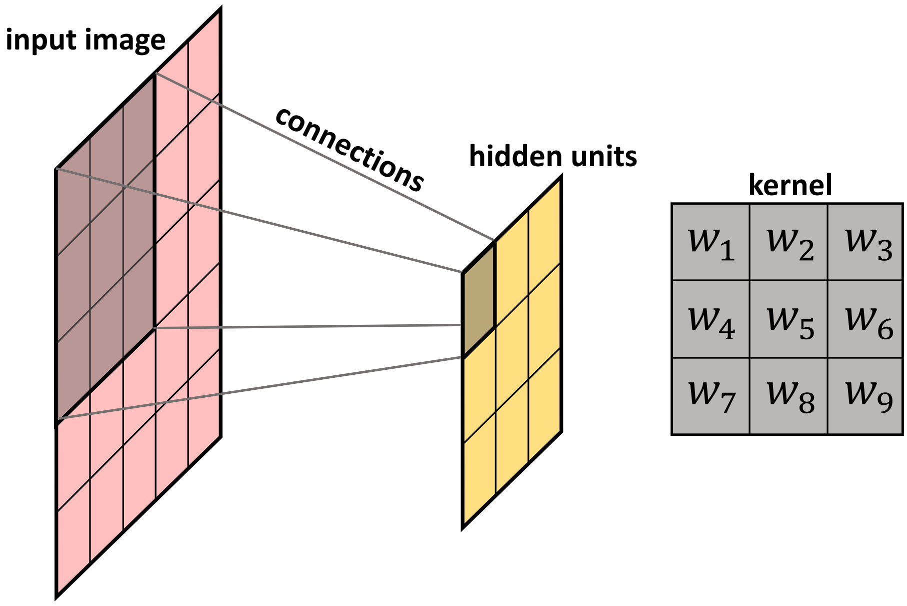

Figure 6.5: Schematic diagram of a 3 × 3 kernel applied to an input image, which forms the receptive field for a single unit in the hidden layer. The number of weights n associated with the kernel are depicted as a 3 × 3 matrix with values w_n.

blue (RGB) values. CNNs utilise *convolutional* layers to extract features from image data in a way that preserves and fully exploits the spatial correlations between the pixels [141]. This involves connecting small patches of the input image to individual units in the hidden layer, as illustrated in Figure 6.5. This constrains the *receptive field* of each unit to the size of the viewed patch. Every connection is associated with a weight, which forms a two-dimensional pixel map, or *kernel*. These connections are established over the entire input by sliding the kernel across the image grid in both dimensions. At each position, element-wise multiplication and addition are performed between the kernel and viewed image patch to generate a *feature map* in the hidden layer. This process is a mathematical operation known as *convolution*[2] in ML literature [139].

For a two-dimensional input image with pixel values $I(i,j)$ and a kernel with weights $W(m,n)$, the output feature map $F(i,j)$ is given by

$$F(i,j) = (K * I)(i,j) = \sum_m \sum_n I(i+m, j+n)\, W(m,n). \tag{6.6}$$

---

[2] The definition of this operation is formally referred to as *cross-correlation* using pure mathematics terminology [141].

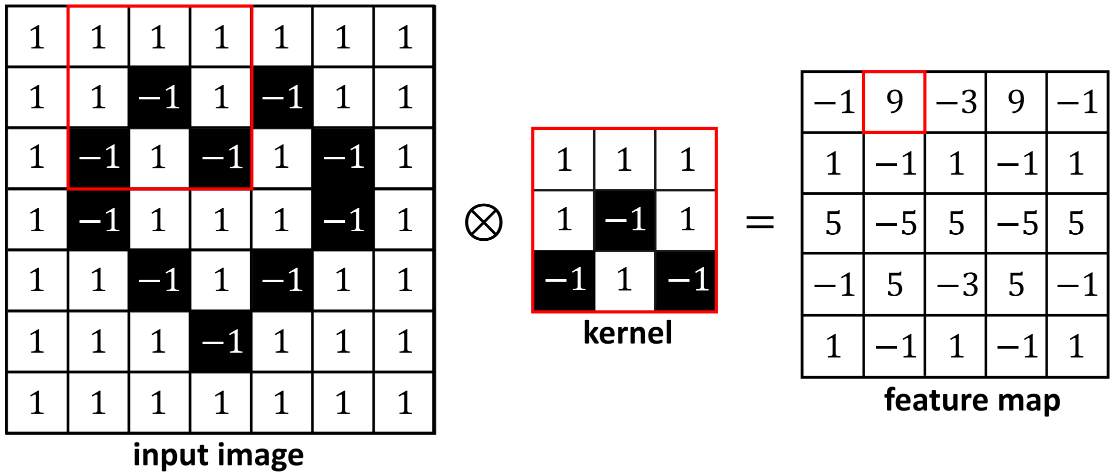

1	1	1	1	1	1	1
1	1	−1	1	−1	1	1
1	−1	1	−1	1	−1	1
1	−1	1	1	1	−1	1
1	1	−1	1	−1	1	1
1	1	1	−1	1	1	1
1	1	1	1	1	1	1

input image

$\otimes$

1	1	1
1	−1	1
−1	1	−1

kernel

$=$

−1	9	−3	9	−1
1	−1	1	−1	1
5	−5	5	−5	5
−1	5	−3	5	−1
1	−1	1	−1	1

feature map

Figure 6.6: Illustration of the convolution operation between a 7 × 7 input black and white image with 3 × 3 edge-detection kernel. The output feature map produced from the operation is shown on the right. The placement of the kernel on the image, depicted by a red square, corresponds to the value outlined in the output feature map.

Figure 6.6 illustrates the convolution operation applied to a 7 × 7 input image using a single 3 × 3 kernel. In this example, the input black and white image is represented by a heart, and the kernel is designed to detect a curved edge. This edge is characterised by significant differences in the local intensity of the pixels. The kernel slides across the image pixel-by-pixel with the convolution operation applied to detect the presence of this specific feature. The resulting 5 × 5 feature map exhibits heightened pixel intensity in regions where the feature is present.

The convolution operation in the above example reduces the size of the output feature map relative to the input image. In general, for an input $A \times B$ convolved with a $M \times M$ square kernel the resulting feature map will have the dimensions $(A - M + 1) \times (B - M + 1)$. This type of reduction is not desirable for preserving crucial features along the borders of the input. This is resolved by *padding* (P) the original image with additional pixels, generally zeros, around the outside edges.

The *stride* (S) is another crucial hyperparameter that determines the step size the kernel takes when sliding across an input. Adjusting the stride influences how the network learns spatial features and controls the number of output features (N_{out}) via the relation

$$N_{\text{out}} = \frac{N_{\text{in}} - K + 2P}{S} + 1. \tag{6.7}$$

Here, N_{in} is the number of input features and K is the kernel size. Increasing the stride is useful for reducing the spatial dimensions of the output feature map as well as the computational load. On the other hand, a smaller stride allows the network to detect more fine-grained localised features in the input data. In Figure 6.6, the input image is padded with ones and the stride of the kernel is one.

A single convolutional layer can detect multiple features by applying multiple kernels to the input, which generates a volume of feature maps. In each layer, the height (H) and width (W) represent the spatial dimensions of the kernel, while the depth (D) corresponds to the number of kernels applied to the input. Analogous to the artificial neural network, the output feature maps are processed through a nonlinear activation function, typically the ReLU function (see Section 6.2). This step injects non-linearity into the network, which allows it to learn complex features within the data.

6.3.2 Pooling

Pooling is a down-sampling operation, applied after convolutional layers to progressively reduce the dimensionality of feature maps [142]. It involves sliding a window over the input, according to a specific stride, and computing either the maximum (*max pooling*) or the average (*average pooling*) at each position, as demonstrated in Figure 6.7. This process aggregates local features into a more compact representation, which improves computational efficiency by decreasing the number of layers required to process the input data. Max pooling emphasises the most prominent features within the window, whereas average pooling provides a smoother representation of the features. Furthermore, pooling operations are advantageous for improving *translational invariance* in CNNs. This allows the network to learn and recognise features irrespective of their precise position and orientation within the image. Typically, max pooling operations are applied in between hidden layers of a CNN, whereas average pooling is used before the final output layers.

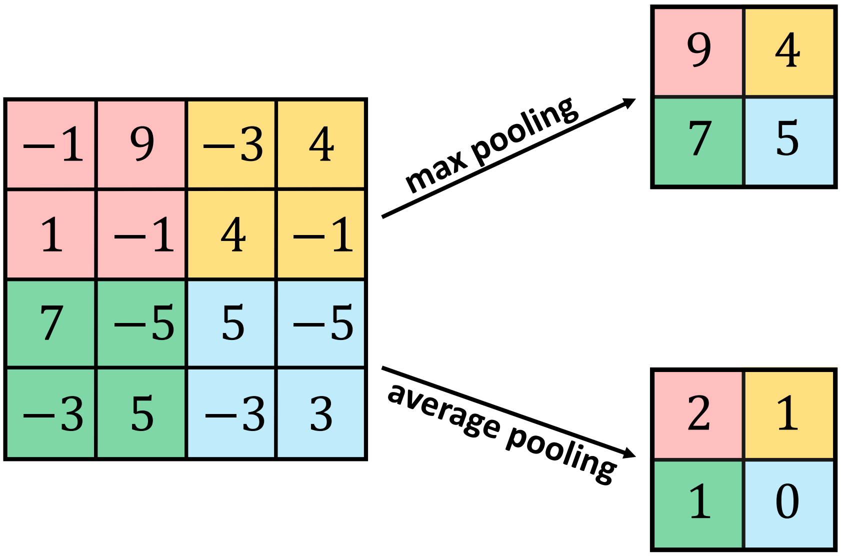

Figure 6.7: Max pooling and average pooling 2 × 2 operations applied to an input with a stride of two.

6.3.3 Network Architecture

Figure 6.8 shows the architecture of a CNN, which consists of a series of *convolutional* layers with non-linearities applied, interleaved with *pooling* layers, to extract high-level features from input image data. The height, width, and depth of the kernels change depending on the size of the stride applied to these operations. The number of layers of the network depends on the classification task and performance requirements of the model. The resulting output feature map is flattened into a one-dimensional vector and processed by one or more fully-connected layers for image classification. The softmax function is applied to convert the final output into a categorical probability distribution, defined as

$$\sigma_{\text{softmax}}(y_i) = \frac{e^{y_i}}{\sum_{j=1}^{N} e^{y_j}}, \tag{6.8}$$

where y_i is the output value for the class i and the summation is over all the output values for N possible classes.

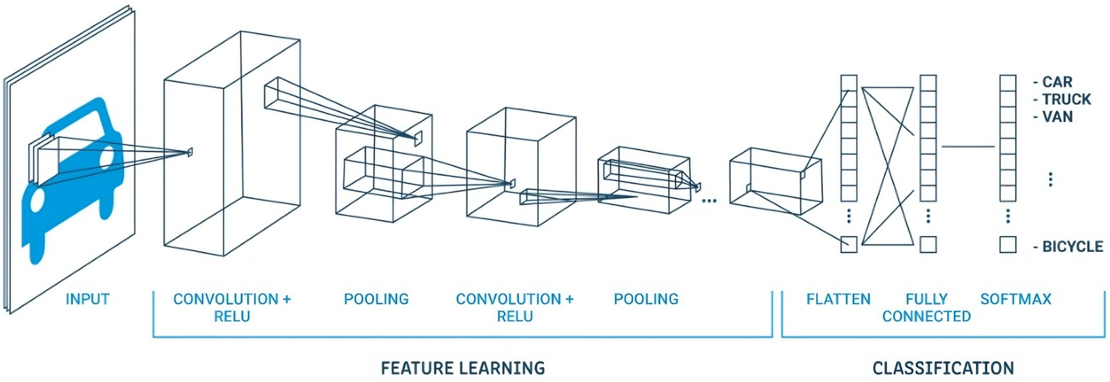

Figure 6.8: Schematic diagram of a standard CNN architecture containing convolutional, pooling, and fully-connected layers. The final output layer shows the softmax function typically used for image-based classification tasks. The figure is taken from Ref. [143].

6.4 The GAPNet Model

The Gamma And Positron (GAPNet) model for e^+/γ classification has been developed to enhance NCQE background rejection in the DSNB analysis. This CNN is trained on a labelled dataset of simulated IBD and NCQE prompt events, which are transformed into two-dimensional event display images. The model makes predictions on the event type, based on the spatial distribution of PMT hits, without relying on reconstructed variables. The output is a classification score (softmax), representing the "IBD-likeness" of an event. In this analysis, the softmax score is implemented as an additional positron selection variable, with new cuts optimised to eliminate residual NCQE background events (see Chapter 7). This section outlines the processes involved in generating the training dataset, formatting images, network architecture, and training the GAPNet model.

6.4.1 Event Selection

The training dataset contains IBD signal and NCQE background events, simulated with a livetime equivalent to 552.2 days and 5000 years, respectively. Both MC samples are generated using the simulation and low-energy reconstruction processes outlined in Chapter 4. The delayed-event reconstruction variables are obtained by processing the output through the neutron tagging algorithm, discussed in Chapter 7. The output ROOT MC files are converted into training files using a dedicated software framework developed for this work.

The Super-K Python Library for Analysis Software Hub (SPLASH)[3] has been extended to integrate a new ML-based data preparation and cut optimisation pipeline into the DSNB analysis. The framework leverages the uproot and pandas libraries to extract and organise event information from IBD and NCQE simulations into two-dimensional dataframes [144, 145]. In this format, analysis cuts can be applied to the entire dataset using vectorised operations rather than through event-by-event iterations. This approach enables efficient and rapid pre-processing of large datasets for training the CNN. The final samples are labelled and combined into HDF5 training files for input into the WatChMaL Python-based CNN architecture.

SPLASH is used to apply a set of low-level cuts to the signal and background training samples. The cuts select events with a prompt energy between 8 - 100 MeV, a reconstructed interaction vertex within the fiducial volume, and one detected neutron in the final state (see Sections 7.2 and 7.5). The neutron criterion ensures that the CNN is trained to effectively differentiate NCQE background events that most closely resemble IBD candidates. These cuts form part of the first and fourth reduction criteria, detailed in Chapter 7.

The prompt event information is extracted from each event by selecting PMT hit charges and times contained within a 300 ns time window around the trigger time. This interval is chosen to capture the full e^+/γ hit distribution without feeding the network with unnecessary noise hits. Since both IBD and NCQE interactions produce an identical neutron capture signal in the final state, the delayed event is not used for training. Figure 6.9 shows the energy distribution of the DSNB signal and NCQE background events with the training preselection cuts applied. Given the significant background event rate, the GAPNet model will need to perform well in the lowest energy region, where traditional cut-based techniques are less effective.

---

[3] SPLASH was first created for the reactor neutrino analysis [119].

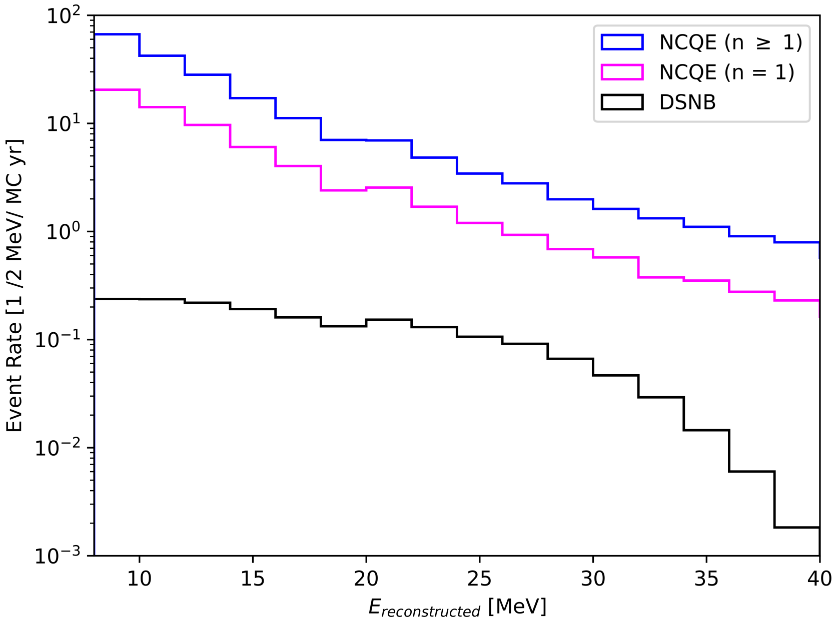

Figure 6.9: Event rates for the simulated DSNB signal (black) and atmospheric NCQE background as a function of reconstructed energy. NCQE events with a single neutron (magenta) and multiple neutrons (blue) in the final state are shown. Note that no positron selection cuts are applied to these distributions.

6.4.2 Data Preparation

The model is trained using event-display images of simulated IBD and NCQE prompt events in the SK detector. These images are created by unfolding the cylindrical geometry of the inner detector into a two-dimensional event display., which provides a visual representation of the detector's response to neutrino interactions. This process generates a 147 × 150 image map containing the barrel, with 7650 PMTs, and two circular endcaps placed above and below, each with ∼1740 PMTs. Each pixel represents a single PMT with a two-channel input for the hit charges and the hit times. The hit times are offset relative to the reconstructed vertex time to ensure that the first photon arrival time is centred around 0 ns and the hit charges are normalised for each PMT hit-map.

In Figure 6.10, hit-time maps are presented for two IBD and NCQE events, with reconstructed energies of $E \approx 14$ MeV and $E \approx 20$ MeV. The CNN will learn to identify key topological features in the spatial arrangement of PMT hits to perform event classification. The IBD and NCQE events (see Figures 6.10a and

6.10b) can both contain a Cherenkov ring produced by an e^+ and a γ-ray, respectively. These event types are difficult to discriminate as they are reconstructed with a Cherenkov angle that falls into the signal window. In the majority of cases, NCQE events exhibit a dispersed distribution of PMT hits from secondary γ-rays, which form no distinct ring-like features (see Figure 6.10d). CNNs and traditional reconstruction methods can easily discriminate this event signature from an IBD candidate due to their distinct hit patterns. However, detecting the Cherenkov ring in IBD events at very low energies can be challenging due to the scarcity of PMT hits, as illustrated in Figure 6.10c. Therefore, the CNN must be robust to subtle feature differences between clear rings and sparse hits to achieve high classification accuracy.

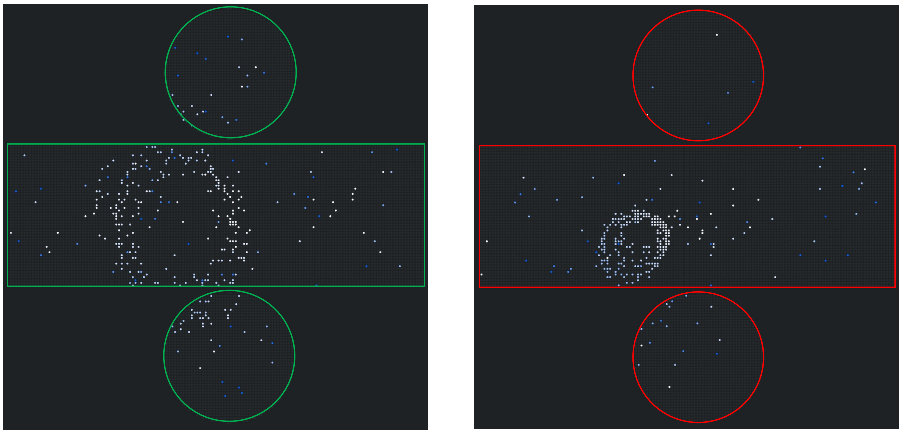

(a) **(b)**

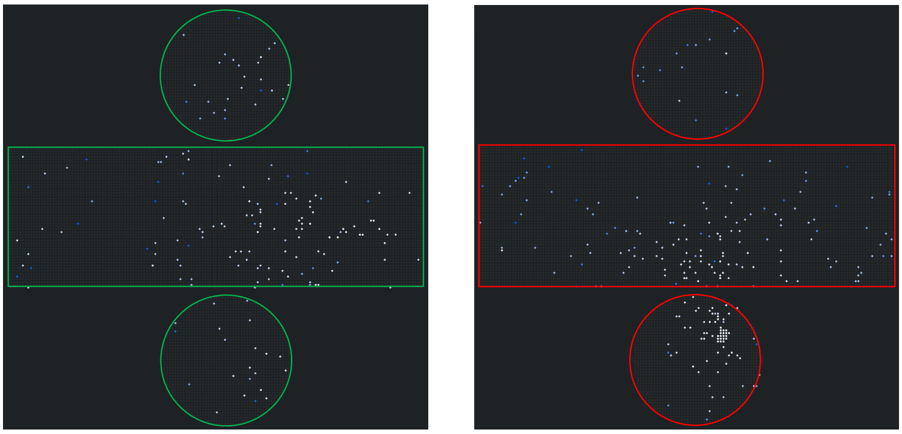

(c) **(d)**

Figure 6.10: PMT hit-time image maps for IBD (green) and NCQE (red) events with energies E ≈ 20 MeV (upper) and E ≈ 14 MeV (lower). The colour scale represents the early-to-late hits in ns.

6.4.3 Residual Networks

The model architecture is based on a modified version of the deep residual neural network (ResNet) from the WatChMaL framework [124]. ResNet is a specific type of CNN designed to facilitate the training of deeper networks [146]. This network has been proven to achieve high accuracy for several image recognition and classification tasks, including applications within neutrino physics [147].

The basic structure consists of several *residual blocks* with *skip connections* that bypass one or more layers [148]. Figure 6.11a shows a simplified representation of the residual block, which consists of three stacked convolutional and activation layers. The input denoted as x, flows directly through the layers and simultaneously through a skip connection around the block. The computations within the residual block and the input x are combined via element-wise addition to produce a final output $H(x)$. In this case, the network layers are no longer responsible for producing the desired output, as in standard deep learning models. Instead, they learn the difference or the *residual* mapping $F(x)$ between the input and corresponding output, given as

$$F(x) = H(x) - x. \tag{6.9}$$

This approach allows for information to pass more smoothly through the network and accelerates the training process. The skip connections provide shorter paths for the gradients to travel during backpropagation, which leads to faster convergence. Furthermore, the residual block can learn an *identity mapping*, such that the output produced is identical to the input ($H(x) = x$). In this instance, the block has learned that no modification to the input is necessary ($F(x) = 0$). This allows the network to bypass the block entirely and reduces the likelihood of producing *vanishing gradients* (see Section 6.2). Therefore, it is relatively easy to stack several residual blocks to build a deeper, more powerful network.

The selected architecture for this work is ResNet18, featuring eighteen layers, as illustrated in Figure 6.12. The input layer takes in the 147×150 image maps detailed in Section 6.4.2. This is processed through the initial 1×1 convolutional

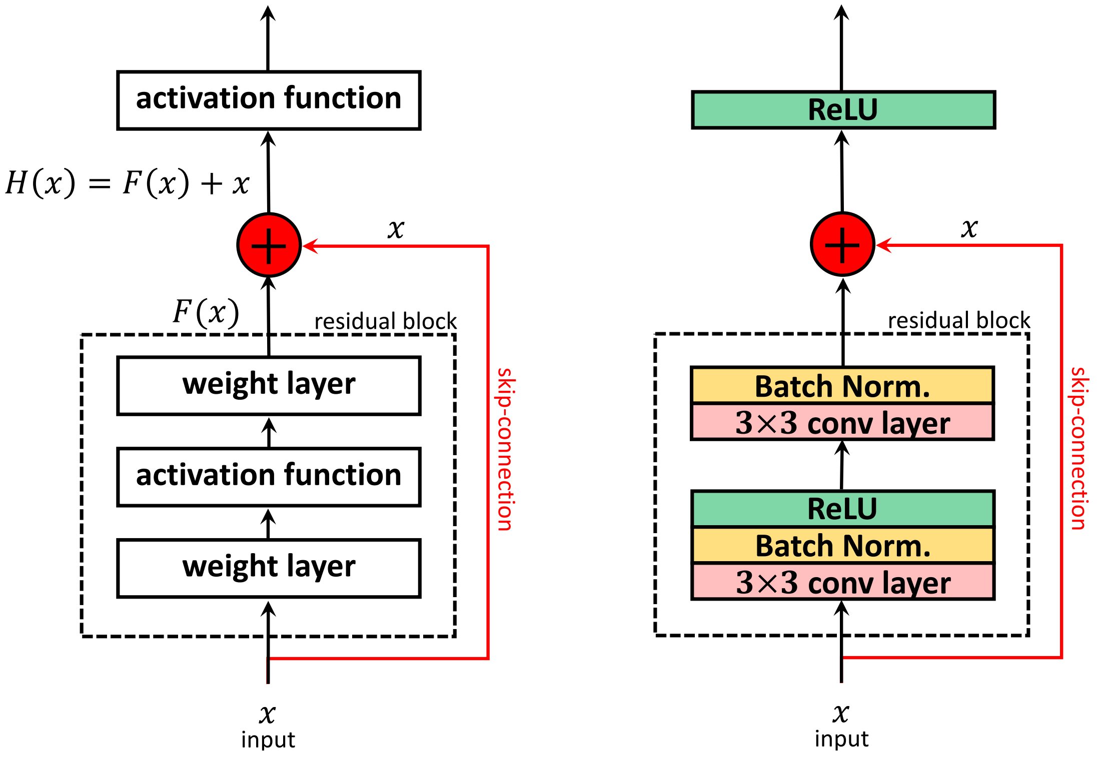

(a) **(b)**

Figure 6.11: Schematic diagrams of the structure and element-wise operations of the generic residual block (left) and the specific residual block used in the ResNet18 CNN architecture (right).

layer, followed by max pooling with a stride of two. The core structure consists of four sets, each containing two stacked residual blocks. Within each block, there are two 3×3 convolutional layers accompanied by *batch normalisation* and ReLU activation functions [141]. Batch normalisation is a regularisation technique used to normalise the inputs of each layer to facilitate faster training. The number of kernels for each set doubles as a stride of two is applied. Additionally, a skip connection is incorporated at the output of the second convolutional layer, as depicted in Figure 6.11b.

Following the last residual block, global average pooling generates a 1×1 feature map for each channel. Subsequently, a fully-connected layer with two output neurons is employed, followed by the softmax function to determine the class probabilities.

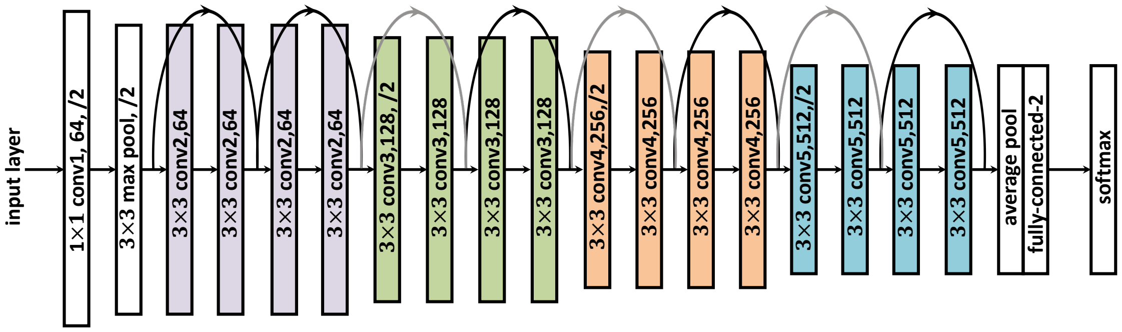

Figure 6.12: The ResNet18 architecture used in this work. The skip connections represent an identity mapping (black lines) and a 1×1 convolution with a stride of two (grey lines).

6.4.4 Training Procedure

The GAPNet model was trained within the WatChMaL framework using Python 3.9.12 and the PyTorch 1.11.0 library on two NVIDIA TITAN RTX GPUs [149]. The PyTorch DataLoader class is implemented in the framework to provide an efficient input data pipeline during training. The model is trained on a dedicated dataset with event selection cuts applied, containing 400,000 images for training (90%), and 20,000 images each for validation (5%) and testing (5%). Each subset has an equal number of IBD and NCQE events to prevent biases towards any particular class during training.

The training procedure follows supervised learning via mini-batch gradient descent. The cost function selected for training was the binary cross-entropy loss, which was implemented using PyTorch's built-in functions. Model parameters were optimised using the Adam optimisation algorithm with an initial learning rate of 0.001 [150]. The Adam optimiser iteratively updates the weights and biases to minimise the cost function, whilst dynamically adjusting the learning rate for each parameter. The level of the adjustment is controlled by the *weight decay*, which was set to 1×10^4.

Figure 6.13 shows the accuracy and loss curves for the training process, where the accuracy represents the fraction of correctly classified events. Throughout the training, the validation loss and accuracy were monitored every 100 iterations using a mini-batch size of 256 events. These hyperparameters were

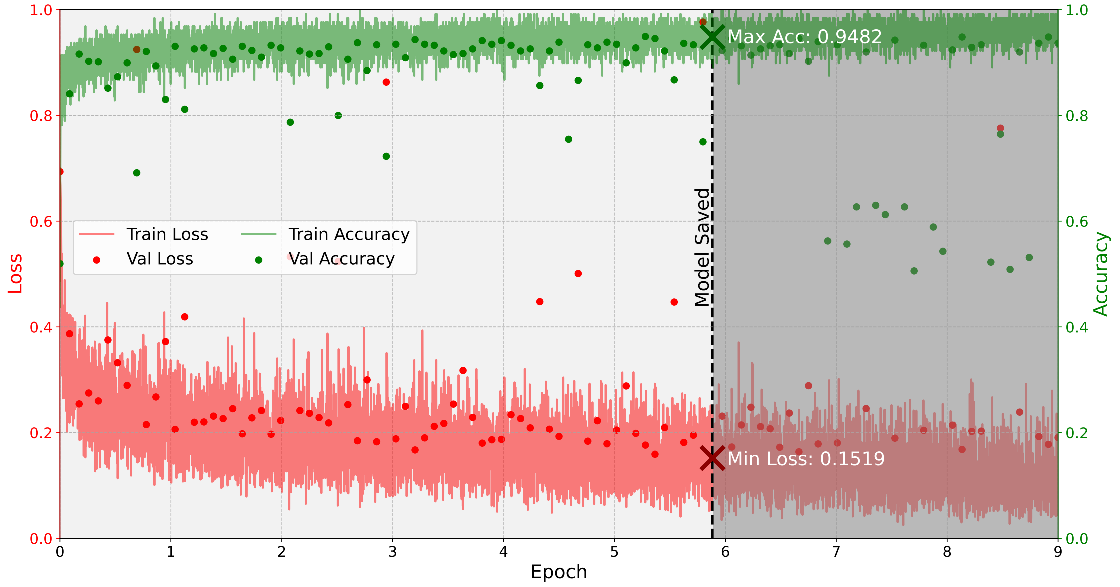

Figure 6.13: Training and validation loss (red) and accuracy (green) for the training progress of the GAPNet model over ten epochs. Early-stopping retains the model at the best validation performance at epoch six.

optimised through manual adjustment and retraining of the model. Both the loss and accuracy curves exhibit consistent behaviour in the initial epochs, which indicates stable learning and adaptation to the data. The training process is performed over ten epochs, with the early-stopping technique implemented at epoch six to retain the model with the optimised performance. Beyond this point, overfitting becomes apparent as the validation accuracy fluctuates, while the training accuracy continues on an upward trend.

6.5 Performance Metrics

The GAPNet model's performance is evaluated on an independent dataset of simulated IBD and NCQE events, used in the final analysis (see Chapter 7). These samples are produced following the same event generation, detector simulation, and selection criteria as the training dataset, outlined in Section 6.4.2. The events are weighted to match the expected DSNB and NCQE spectra observed at SK.

This section provides a comprehensive evaluation of the ML-specific performance metrics, including the distribution of classification scores and the confusion matrix. The overall performance is evaluated using the Receiver Operating Characteristic (ROC) curve on the test dataset. The objective is to determine the effectiveness of an ML-based reduction step, considering its potential as a complementary technique for NCQE background removal.

6.5.1 Classification Scores

The model's performance is determined by the classification scores computed by the softmax function in the output layer. These scores represent the model's predictions for categorising each input into either the DSNB (P_{DSNB}) or NCQE (P_{NCQE}) class. This forms a two-dimensional vector of normalised scores, where

$$P_{\mathrm{DSNB}} = 1 - P_{\mathrm{NCQE}} \quad \text{and} \quad P \in [0, 1].$$

In binary classification tasks, the softmax output provides an estimate of the probability that an event belongs to a specific class. For example, when P_{DSNB} is closer to one, the model confidently predicts the event as a DSNB event, while values closer to zero have a higher likelihood of being NCQE type. For optimal performance, the model should achieve a clear separation between the classification scores of the events.

Figure 6.14 shows the probability distribution functions of the P_{DSNB} classification scores. The GAPNet model exhibits considerable discriminatory power as the signal and background distributions are predominantly peaked around one and zero, respectively. However, the model misclassifies a moderate proportion of DSNB events with lower scores, while maintaining accurate classification for NCQE events. This suggests that potential biases related to specific physical quantities and event features have impacted the model's ability to perform well on a particular subset of DSNB events. This effect is investigated in the systematics evaluation in Section 6.6.

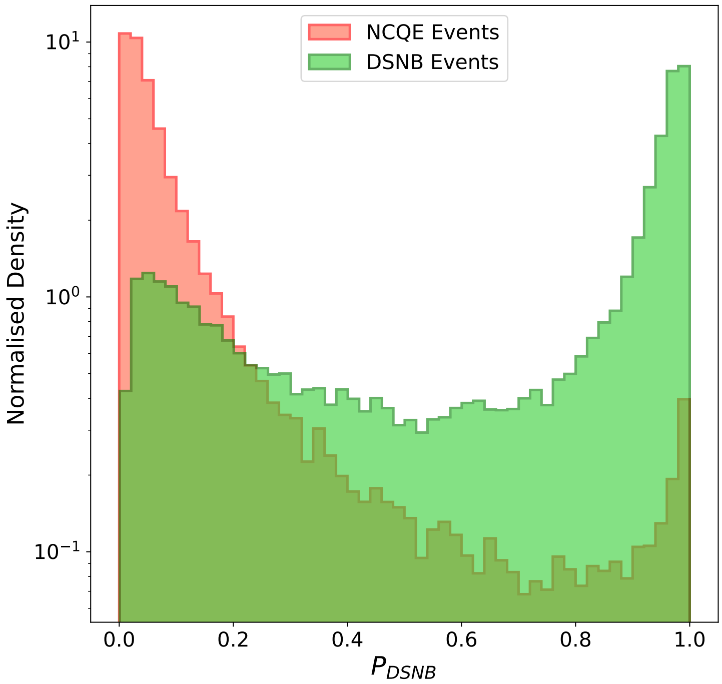

Figure 6.14: Distributions of the softmax signal classification scores (P_{DSNB}) for DSNB (green) and NCQE (red) weighted events.

6.5.2 Confusion Matrix

The *confusion matrix*, is a crucial metric for visualising and assessing the performance of the GAPNet model [128]. In this binary classification task, the matrix is divided into four quadrants, where the rows and columns correspond to the actual and predicted classes, respectively. The matrix is calculated using a chosen softmax output value P_{DSNB}, which represents the selection criterion or threshold utilised by the model to classify events as either DSNB or NCQE. Each cell in the matrix is occupied with the following metrics:

- **True Positive (TP)**: Number of events correctly identified as DSNB events.
- **True Negative (TN)**: Number of events correctly identified as NCQE events.
- **False Positive (FP)**: Number of NCQE events misclassified as DSNB.
- **False Negative (FN)**: Number of DSNB events misclassified as NCQE.

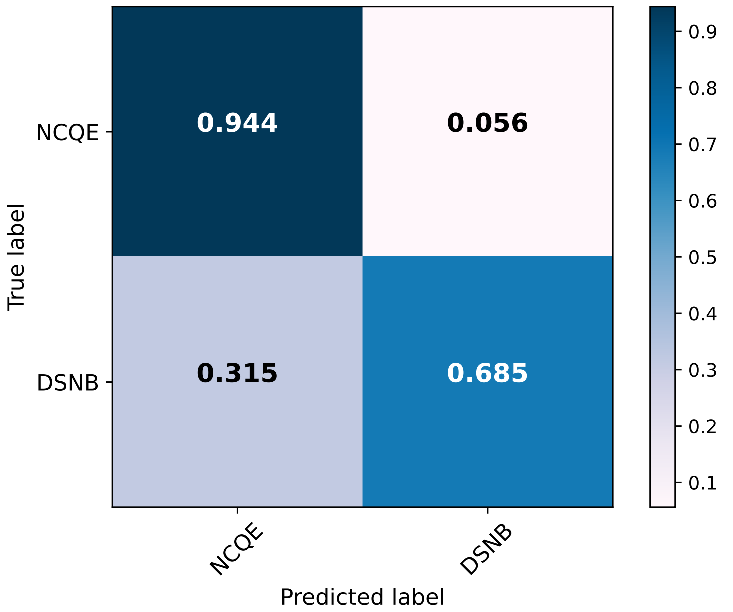

Figure 6.15: The confusion matrix for the GAPNet model normalised on the ground truth. The rows represent true class labels and the columns represent model predictions.

Figure 6.15 illustrates the normalised confusion matrix. The elements in the main diagonal (left to right) represent instances that are correctly classified, while off-diagonal elements show the proportion of misclassified events. The model demonstrates a satisfactory ability to correctly classify 68% of DSNB events and excels in classifying 94% of NCQE events. This discrepancy is attributed to the fact that a subset of DSNB events exhibit spatial features that are more representative of the NCQE class (see Section 6.6).

6.5.3 Receiver Operating Characteristic Curve

The ROC curve evaluates the model's overall performance at varying signal thresholds [151]. The curve depicts the True Positive Rate (TPR), representing the fraction of correctly classified positive events, as a function of the False Positive Rate (FPR), defined as the fraction of negative events incorrectly classified. The Area Under the Curve (AUC) metric summarises the model's classification accuracy across all possible thresholds.

Figure 6.16 shows the ROC curve for the GAPNet model in terms of the DSNB signal efficiency with respect to the NCQE background efficiency at each

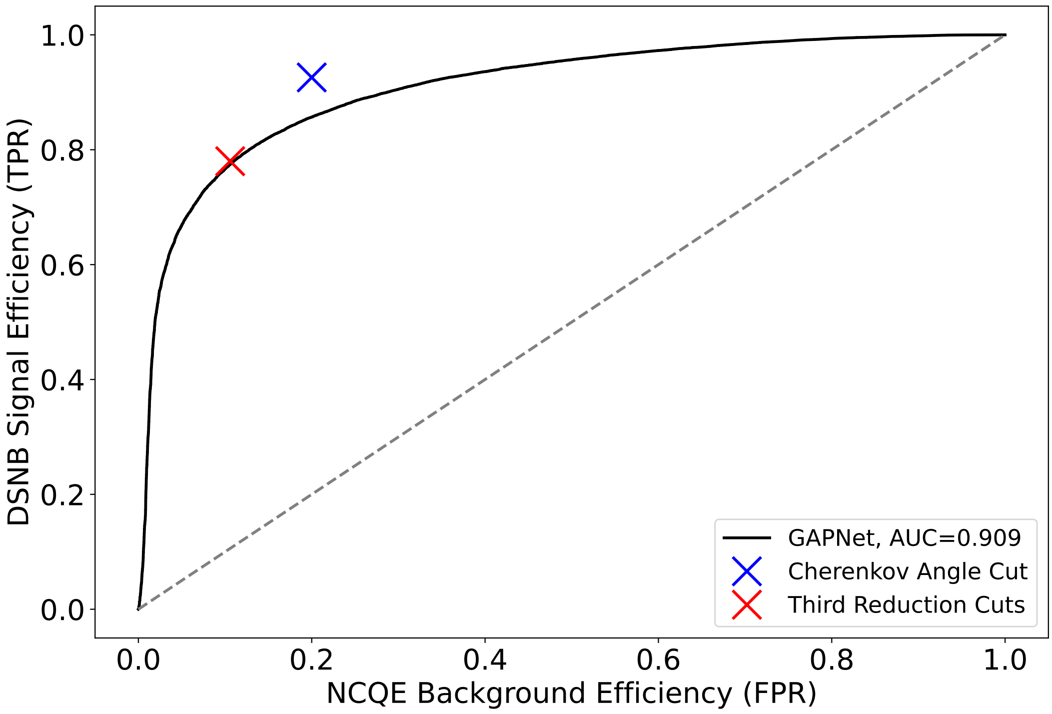

Figure 6.16: The Receiver Operating Characteristic (ROC) curve for the GAPNet model (black) in terms of DSNB signal and NCQE background efficiencies. The Cherenkov angle (blue cross) and Third Reduction (red cross) cut efficiencies are shown. The grey dashed line represents a model with no classification capability.

classification threshold (P_{DSNB}). To compare the model's performance against traditional methods, the selection efficiencies for the Cherenkov angle and Third Reduction cuts[4] are superimposed.

The GAPNet model slightly underperforms in comparison to the Cherenkov angle cut, due to its inherent energy-dependence bias and misclassification rate for DSNB events between 8 - 12 MeV, as explained in Section 6.6. However, since GAPNet and the Cherenkov angle cut target the NCQE background rejection differently, the classification cut can be advantageous as a complementary reduction technique to the analysis. Overall, the model rejects 83% of the NCQE background at 78% signal acceptance, which aligns with the performance of the Third Reduction. This result is interesting and highlights that a CNN model trained on low-level features can achieve comparable background rejection without relying on several complex reconstruction methods and cuts.

---

[4] Based on the cut criteria optimised for the SK-VI DSNB analysis conducted in 2023 [152].

6.6 Systematic Uncertainties

Evaluating the systematic uncertainties is crucial for assessing the robustness of the ML technique against variations, such as model dependence in the training dataset and its influence on detector responses. These factors offer insights into potential improvements for future iterations of the GAPNet model and whether more sophisticated training techniques, such as data augmentation and other regularisation methods, need to be introduced.

This section summarises the potential biases in the classification performance of the GAPNet model. The model output has been analysed with respect to reconstructed energy and validated against LINAC calibration data. Finally, a conceptual overview of further systematics studies is presented.

6.6.1 Energy Dependence

The classification performance of the GAPNet model relative to the reconstructed positron energy is depicted in Figure 6.17. These distributions show that the classification output P_{DSNB} is strongly correlated to the energy for both event classes. Below 12 MeV, DSNB events are predominantly misclassified as NCQE events due to the absence of distinctive features, such as a clear Cherenkov ring. The model learns to characterise this event signature as background since NCQE interactions emit γ-rays isotropically that undergo Compton scattering, which produces a sparse spatial distribution of PMT hits. Above 12 MeV, the model demonstrates robustness in classifying DSNB events, as these events exhibit more discernible features compared to NCQE backgrounds. In particular, NCQE interactions at higher energies lead to fast neutron-nucleon interactions that emit multiple secondary γ-rays in the prompt window, which are more easily separated from positron-induced Cherenkov rings. As a result, the threshold for the softmax score is optimised for each energy bin in the final event selection process.

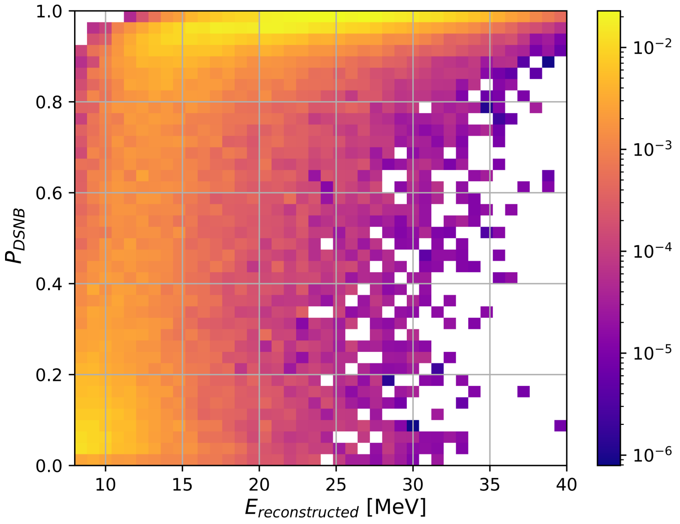

(a) DSNB MC

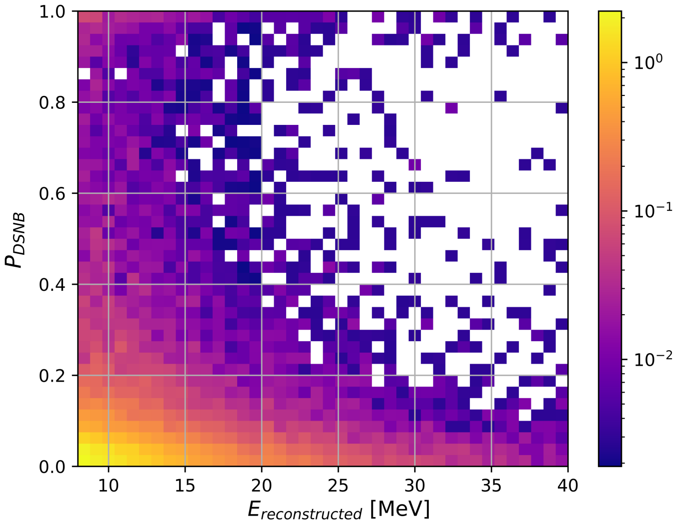

(b) NCQE MC

Figure 6.17: Distributions of the reconstructed energy as a function of softmax score for DSNB MC events (left) and NCQE MC events (right). The colour scale is represented for both histograms.

6.6.2 Validation on LINAC Calibration Data

The GAPNet model's ability to generalise to unseen data is validated using LINAC MC and data. Since the LINAC generates monoenergetic electrons that mimic positron signatures produced in IBD interactions, all events should receive high signal classification scores. However, localised features present in the training dataset, such as simulated noise patterns, may bias the model's performance.

To assess the extent of this systematic, the GAPNet model is tested on three

SK-VI LINAC MC and data runs, featuring target energies of 8 MeV, 12 MeV, and 15 MeV, as depicted in Figure 6.18. The energy-dependence effect is evident, with the model's classification capability being poorer at lower energies and improving steadily as energy increases. The model tends to perform slightly better on MC compared to data, particularly in the high softmax region. This may indicate a potential effect of overtraining, as the model more confidently predicts the classification for MC events compared to data. Since the overall discrepancy is $\sim$10% across the entire distribution, this study tentatively validates the model's capability to generalise to SK-VI data. Further investigations are required to fully assess the performance of the model.

6.6.3 Further Studies

In this work, an additional cut using the softmax score is integrated into the full analysis without a quantitative treatment of the GAPNet model-specific systematics. Since further studies are ongoing to estimate the specific systematic uncertainties, this subsection provides a conceptual overview of some of the sources of potential bias.

DSNB Models

To evaluate the sensitivity of the GAPNet model to the selection of the DSNB model, the ROC curve has been reweighted based on the Horiuchi+09, Nakazato+15, and Ando+03 models, as illustrated in Figure 6.19. Minimal discrepancies are evident in the ROC curves, indicating that the choice of the DSNB model has negligible impact on the overall performance.

NCQE Cross Section

Various systematic uncertainties are associated with the atmospheric neutrino NCQE background spectrum, related to the models implemented within NEUT. In this analysis, the NCQE cross section uncertainty is set at 44%, derived from the scaling factor of the T2K measurement (see Chapter 8). The GAPNet model can

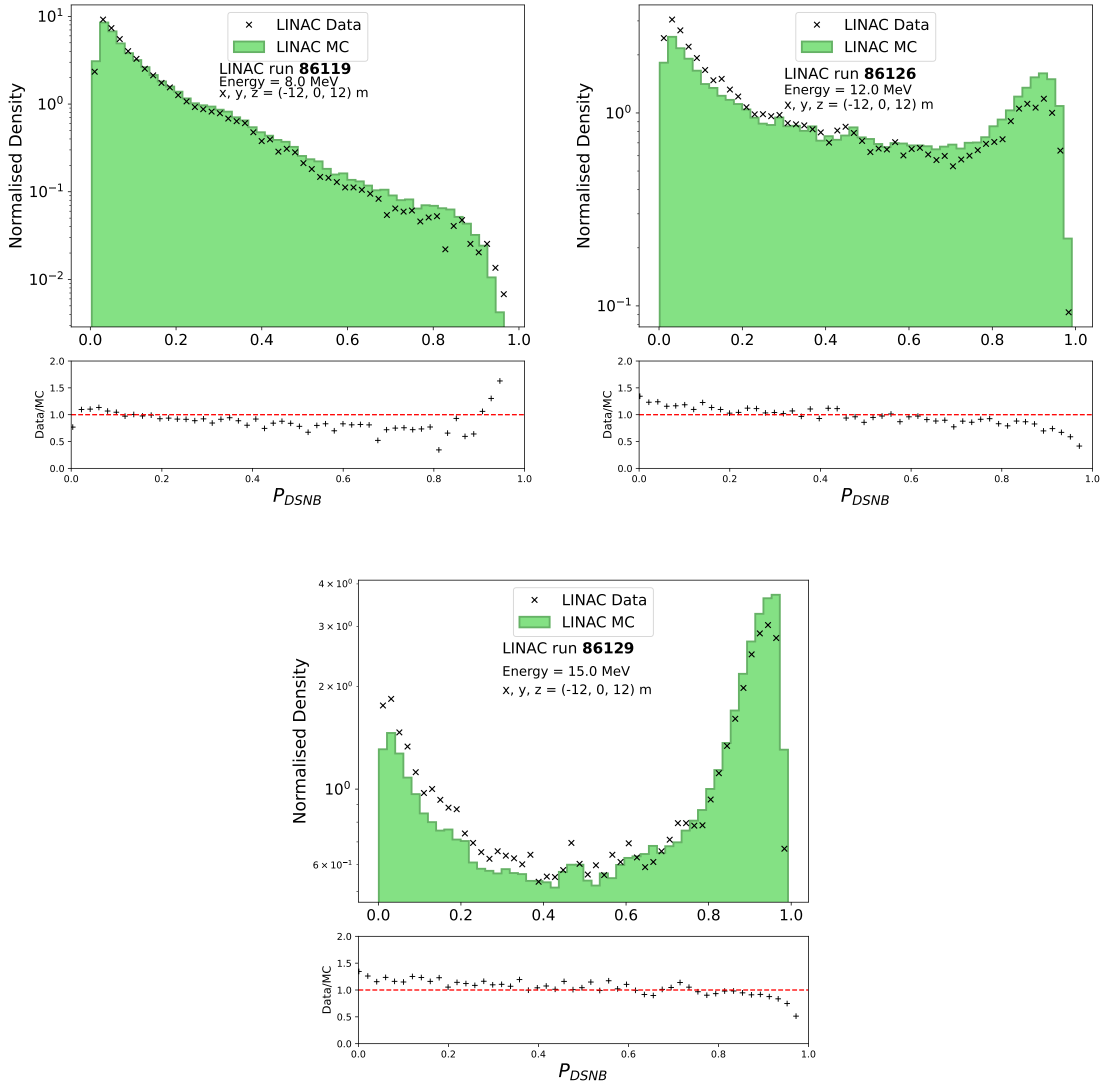

Figure 6.18: Distributions of softmax signal classification scores P_{DSNB} for LINAC data (black) and MC (green). The LINAC energy for each plot is 8 MeV (upper left), 12 MeV (upper right), and 15 MeV (centre) and the position is (-12, 0, 12) m.

be tested on several NCQE MC test sets, reweighted according to each available cross section model in NEUT. The relative differences observed in the ROC curves would be quantified as the systematic uncertainty.

NCQE Spectroscopic Factors

There are uncertainties associated to the γ production model used in NEUT for NCQE interactions. When the nucleus de-excites it can eject a different number

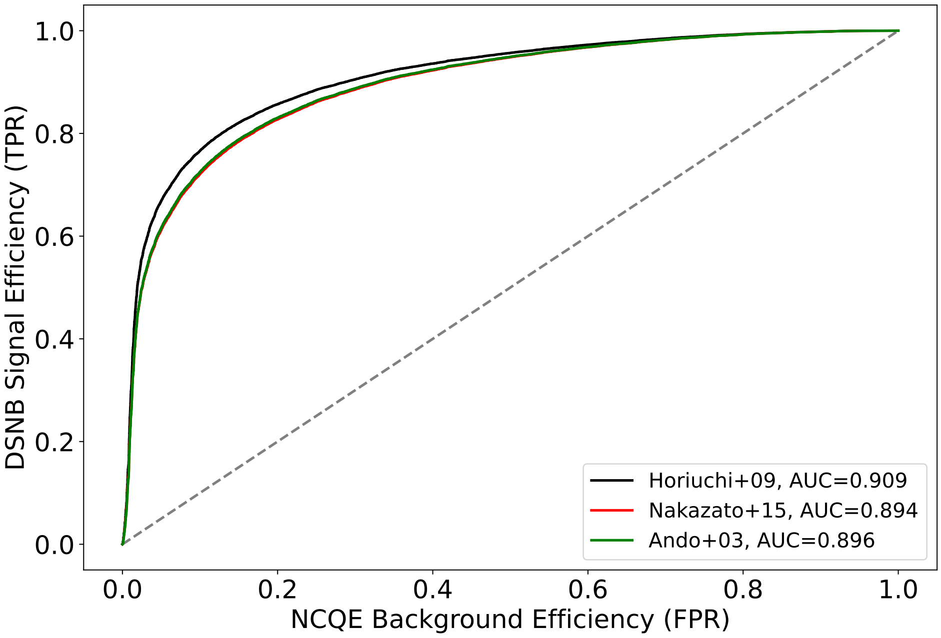

Figure 6.19: The Receiver Operating Characteristic (ROC) curve for the GAPNet model weighted with Horiuchi+09 (black), Nakazato+15 (red), and Ando+03 (green) DSNB flux models.

of γ-rays and nucleons depending on the interaction state it occupies. This has a direct impact on the spatial distribution of PMT hits for NCQE events and thus, the input PMT hit-map images that the model learns from. The model can be tested on NCQE MC test sets generated with different spectroscopic factors to quantify the systematic uncertainty related to this effect.

NCQE De-excitation Models

The secondary-interaction model in SKG4 is based on the Bertini Cascade model (BERT). However, studies have shown that the Binary Cascade (BIC) model and the Liège intranuclear cascade (INCL++) model provide a better fit to T2K data [80]. The model's performance can be evaluated with NCQE test sets generated with different nuclear de-excitation models to parameterise this systematic uncertainty.

7

Event Selection

This chapter describes the event selection applied to the SK-VI dataset to target the removal of dominant backgrounds. The selection involves five stages:

- **First Reduction**: Eliminates nonphysical and background noise events.
- **Second Reduction**: A data-driven approach is implemented to remove energetic muons and subsequent spallation isotopes that dominate the signal region.
- **Third Reduction**: Following the spallation cuts, significant backgrounds from atmospheric neutrino interactions and low-energy radioactive decays remain. To select the IBD positron candidates, a series of cuts are applied based on reconstructed positron observables to target these backgrounds. In this work, new energy-dependent cuts are optimised using the SPLASH framework to improve background reduction.
- **Fourth Reduction**: This step uses a dedicated neutron tagging algorithm to select IBD events with a single delayed neutron capture signal on Gd.
- **Fifth Reduction**: This is a new reduction step developed by the author, designed to enhance atmospheric neutrino NCQE background rejection based on the output of the GAPNet CNN model (see Chapter 6).

7.1 Data Sample

This analysis uses data acquired with the SHE+AFT combined trigger during the SK-VI period. This period begins 43 days after the Gd-loading phase to ensure that stable detector and trigger conditions are maintained throughout normal physics runs. The operational livetime is 552.2 days, accounting for dead time, calibration runs, and the removal of poor-quality data.

The SHE event trigger captures signals within a [-5, 35] µs window around the main activity peak. The threshold of this trigger establishes the lower limit of the analysis energy window, set at 7.49 - 29.49 MeV in this study. The upper limit is determined by the expected background contribution and the predicted DSNB search sensitivity at higher energies. An AFT trigger is issued immediately after the SHE event to record neutron signals within a 500 μs window. From the middle of SK-V onwards, the AFT trigger is activated following every OD trigger to facilitate the detection of secondary neutrons produced by cosmic muons. The AFT trigger rate was increased from one to three events in a 21 ms timeframe to account for the increased load on the DAQ. A summary of the trigger conditions and livetime for the full SK-VI period is provided in Table 7.1.

SHE triggers can occur without a subsequent AFT trigger due to variations in the AFT trigger rate. For each 2 MeV energy bin, the AFT trigger efficiency

Start date	End date	Livetime [days]	SHE threshold [hits]	AFT rate [/21 ms]
Jul. 14, 2020*	Aug. 26, 2020	43	–	–
Aug. 26, 2020	Aug. 26, 2021	365.6	60	1
Aug. 26, 2021	Sep. 12, 2021	10.97	52	1
Sep. 12, 2021	Mar. 3, 2022	157.49	60	1
Mar. 3, 2022	Jun. 1, 2022	78.15	60	3

Table 7.1: The SHE+AFT trigger conditions and operational livetime during the full SK-VI period. * refers to data taken during the Gd-loading phase, which is not used in this analysis.

ϵ_{AFT} is defined as

$$\epsilon_{\text{AFT}} = \frac{N_{\text{AFT}}}{N_{\text{SHE}}},$$

where N_{AFT} is the number of AFT-triggered events and N_{SHE} is the number of SHE-triggered events. The ϵ_{AFT} is included in the normalisation of MC events. Table 7.2 shows the values of ϵ_{AFT} used for this analysis.

Energy bin [MeV]	**AFT-trigger efficiency [%]**
8–10	85.3
10–12	80.4
12–14	74.3
14–16	70.0
16–18	67.9
18–20	63.4
20–22	89.7
22–24	90.0
24–26	90.0
26–28	100.0
28–30	90.5
>30	93.7

Table 7.2: The AFT-trigger efficiencies for each 2 MeV energy bin.

7.2 First Reduction

This section describes the first set of cuts applied to eliminate non-physics events, cosmic muons and decay electrons, and poorly reconstructed events. The cuts are designed to target obvious backgrounds in data so they have minimal impact on the signal MC efficiencies.

7.2.1 Non-physics Event Cut

The analysis only uses data from normal physics runs, excluding calibration runs, test runs, and periodic triggered events. The normal runs selected must last for more than five minutes, without any hardware faults occurring during the runtime. In the event of HV failure, the run must start at least fifteen minutes after the HV system has recovered. Within each run, pedestal events, incomplete events, and badly processed events are removed. Any event associated with an OD trigger is discarded as these are often induced by cosmic muons. In addition, the events triggered by the T2K beam trigger, which is issued every 2.48 s during beam time operations, are excluded.

Additionally, to exclude events caused by PMT dark noise, which typically generate fewer hits and lower charge compared to real signals, the following criterion is applied

$$\frac{N(Q < 0.5\,\text{p.e.})}{N_{\text{all}}} < 0.55,$$

where $N(Q < 0.5\,\text{p.e.})$ is the number of PMT hits with charge deposition less than 0.5 photoelectron (p.e.), and N_{all} represents the total number of hits.

7.2.2 Cosmic Muon Event Cut

The cosmic muon rate in the SK detector is $\sim$2 Hz. These muons typically produce easily identifiable signals in the OD and can generate decay electron events with a lifetime of 2.2 μs. In some instances, the decay electron generates hits in the ID volume without triggering the OD and thus reconstructs as a separate event. Therefore, any events within 50 μs following the detection of a muon are excluded from the final sample as a precautionary measure. This cut also eliminates short-lived isotopes produced from muon spallation.

7.2.3 Fiducial Volume Cut

Low-energy radioactive backgrounds produced near detector walls are eliminated by applying the fiducial volume (FV) cut, which removes events reconstructed within 2 m from the ID walls.

7.2.4 Fit-quality Cut

The BONSAI reconstructed goodness-of-fit parameter (g_{vtx}) defines the fit-quality of the event (see Section 4.6.1). Figure 7.1 shows the reconstructed kinetic energy (E_{rec}) as a function of g_{vtx} for the data and signal MC. The cut $g_{\text{vtx}} > 0.5$ is applied

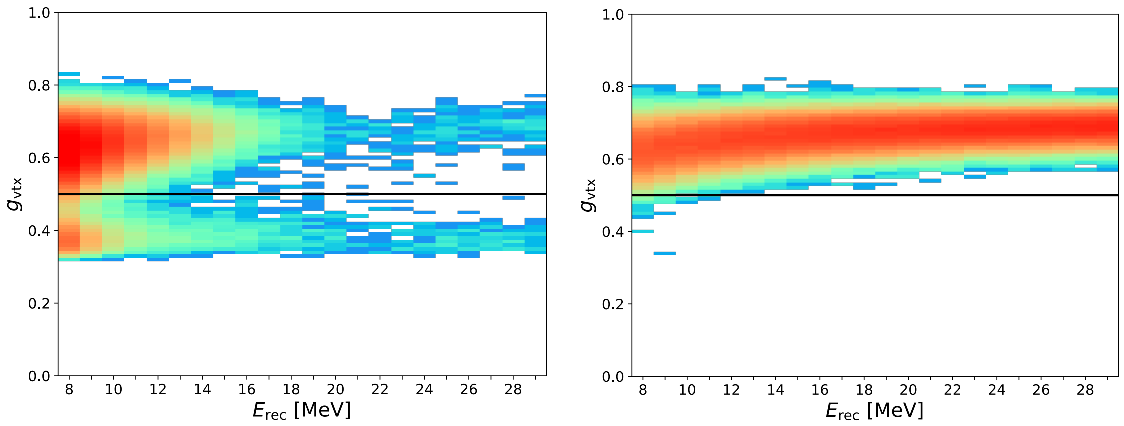

(a) Data. **(b)** IBD MC.

Figure 7.1: Distributions of the goodness-of-fit (g_{vtx}) as a function of reconstructed energy (E_{rec}) for the data (left) and signal MC (right). The black line represents the g_{vtx} cut.

after the non-physics event and FV cuts to remove poorly reconstructed events, typically from muon spallation and residual radioactive backgrounds. This selection criterion maintains a signal efficiency of >99% above 8 MeV.

7.3 Second Reduction

The dominant physics background in the signal region comes from the beta decay of cosmic muon spallation products. While FLUKA-based spallation simulations are currently under development to directly model these backgrounds [153], they have not yet been integrated into the full analysis pipeline. Therefore, this analysis adopts a data-driven approach to target spallation backgrounds. The cuts are designed to eliminate DSNB candidate events (SHE events) correlated with preceding muons, based on the expected behaviour of the spallation backgrounds. Since muon spallation events dominate the spectrum by $\mathcal{O}(10^6)$ in the search window, highly effective spallation cuts are required to provide a robust constraint on the DSNB flux. The second reduction is dedicated to tuning below 24 MeV as the highest endpoint energies from ^{14}B and ^{11}Li are 20.6 MeV (see Section 5.2.2).

This section summarises the second reduction techniques applied to SK-VI data, which were developed independently of this thesis's work [18, 42, 152].

7.3.1 Muon Selection

The spallation reduction strategy involves examining correlations between SHE events and nearby muons. Events occurring within a ±60 s window of a SHE event that meets the first reduction criteria are selected for further analysis. This extended search window is chosen to cover radioactive decays of abundant and long-lived spallation isotopes such as ^{11}Be and ^{16}N (refer to Table 5.1). Subsequently, the HE and OD software triggers are applied over this search window to identify candidate muons, resulting in approximately 240 muons for each SHE event. These muons are divided into *pre* and *post*-samples. The pre-sample consists of muons within the time interval [-60, 0] s relative to the SHE event, while muons within [0, +60] s are assigned to the post-sample, as illustrated in Figure 7.2. This separation distinguishes correlated preceding muons that may induce a SHE event consistent with spallation (pre-sample) from muons entirely uncorrelated with the SHE event (post-sample). For each muon and SHE event pair, the relative time difference and the muon properties are reconstructed using the flagship muon fitter.

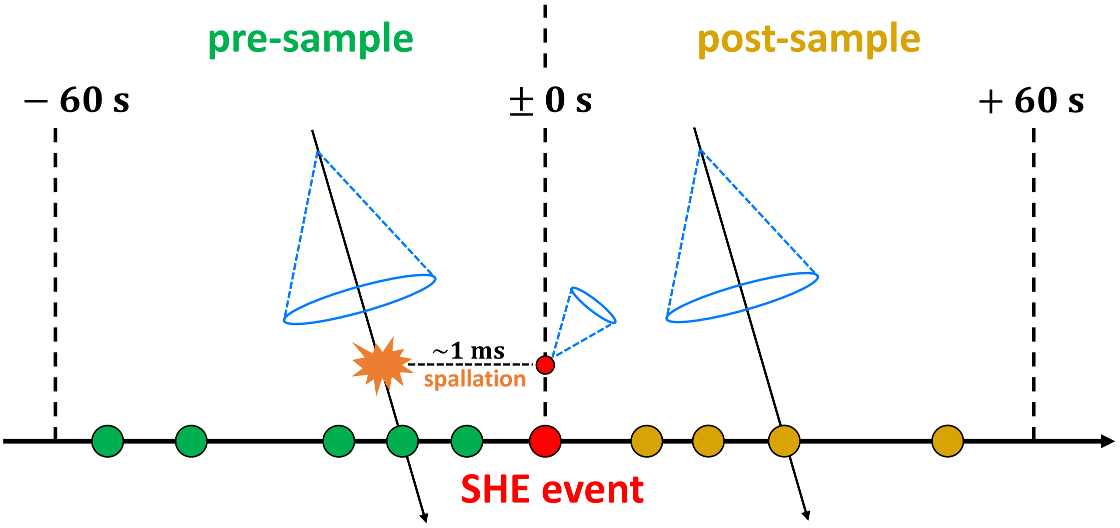

Figure 7.2: Schematic diagram of the pre- and post-samples defined around a SHE event.

7.3.2 Muon Fitter

High-energy cosmic muons are characterised by their track-like trajectories and tend to deposit more charge per PMT in the detector volume compared to prompt events. In SK, dedicated muon reconstruction algorithms have been developed to identify muon interactions and reconstruct their direction, tracks, and energy deposition (dE/dx) along the track length. This work utilises the output of the general-purpose muon fitter, called Muboy [100, 101], which classifies muons based on their topological features into the following event types:

- **Single through-going**: Single muons passing through the detector with well-defined entry and exit points that contribute significantly to the spallation background spectrum (∼83%).
- **Stopping**: Single muons that stop within the detector volume, identified by the lack of an exit point (∼5%). These muons produce decay electrons that can be characterised by the Michel electron spectrum.
- **Multiple-track**: Split into two sub-categories: muons with either exactly one reconstructed track (∼2%) or multiple reconstructed tracks (∼5%).
- **Corner-clippers**: Through-going muons with short track lengths (< 7m) near the corners of the ID, which have minimal contribution to muon spallation (∼4%).
- **Misfit**: Muons failing to meet classification criteria defined for the other categories (<1%).

Figure 7.3 illustrates the distribution of the muon event classes as a function of the reconstructed goodness-of-fit parameter for the SK-VI dataset. These muon categories and reconstructed parameters are essential components of the spallation cuts.

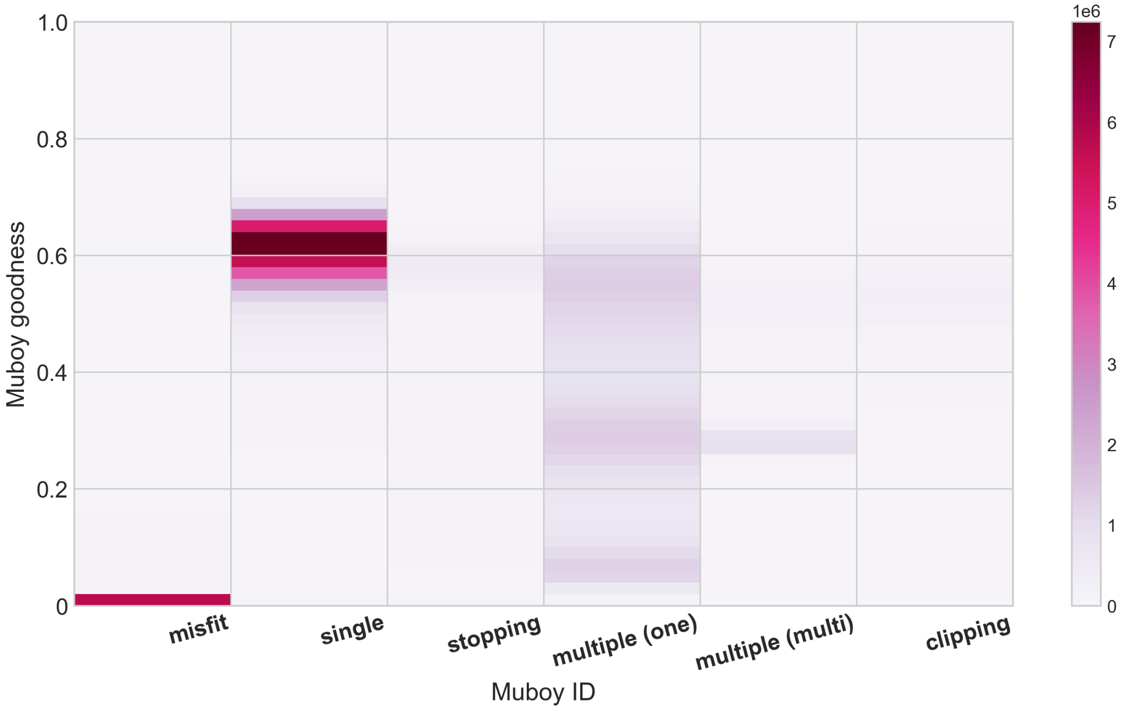

Figure 7.3: Muon event classes as a function of Muboy reconstructed goodness-of-fit for the SK-VI dataset.

7.3.3 Preselection Cuts

There are three preselection cuts applied to remove spallation backgrounds from high-energy muons, defined as follows:

1-ms Cut

Muon spallation events that generate high-energy cascades can induce subsequent hadronic interactions. Secondary particles produced from these processes can activate SHE triggers and mimic IBD events if paired with a delayed neutron capture signal. Therefore, all SHE events within 1 ms of a preceding muon are excluded from the final sample. Given the 2 Hz muon event rate in SK, this cut has minimal impact on the signal efficiency (1 ms/0.5 s = 0.2%).

Multiple Spallation Cut

High-energy muons can induce multiple spallation events from a single interaction. Therefore, SHE events within ± 60 s and 4 m of subsequent low-energy events below 25 MeV are removed. This cut has a signal efficiency of 98%.

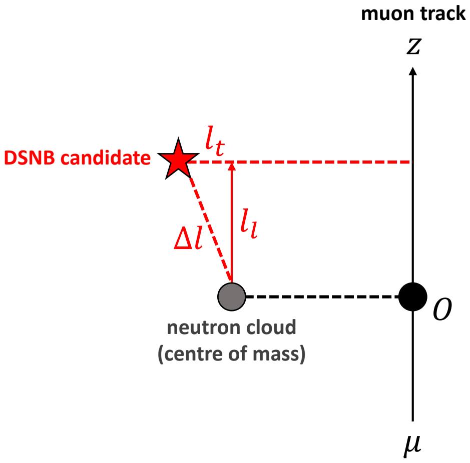

Figure 7.4: Schematic diagram of the new coordinate system for the neutron cloud cut.

Neutron Cloud Cut

SHE events associated with multiple clusters of secondary neutrons produced from muon spallation, referred to as *neutron clouds*, are removed from the analysis. These neutrons undergo capture on Gd isotopes within a timescale of $\mathcal{O}(100\ \mu s)$. The selection criteria, based on the methods established in the cosmogenic neutron yield analysis [154], are as follows:

- Events triggered with at least 25 hits in a 200 ns time window ($N_{200} \geq 25$).
- The event timing within [35, 535] μs from the parent muon.
- The goodness-of-fit criteria: $g_{vtx} > 0.4$ and $g_{dir} < 0.4$.
- The distance from the parent muon is within 5 m.

Spallation events with neutron clouds are more common in the pre-sample and closely correlated in time to the SHE event. In the SK-VI analysis, a new coordinate system $(\Delta_x, \Delta_y, \Delta_z)$ has been created to enhance the reduction of muon spallation events with neutron clouds. The vertex difference is calculated as $\Delta_l = \Delta_x^2 + \Delta_y^2 + \Delta_z^2$ and the time difference between the muon and SHE event is defined as Δ_T (see Figure 7.4). Table 7.3 displays the new cut criteria, tuned according to the number of neutrons following a parent muon N_{ncloud}. The neutron cloud cut reduces about 68% of the spallation events whilst retaining a $\sim$98% signal efficiency.

N_{ncloud}	**Time [s]**	**Spatial [cm]**
2+	$\Delta T < 0.1$	$\Delta l < 1200$
2+	$\Delta T < 1$	$\Delta l < 800$
2	$\Delta T < 30$	$\left(\Delta_x^2 + \Delta_y^2\right) / 200^2 + \Delta_z^2/400^2 > 1.2$
3	$\Delta T < 60$	$\left(\Delta_x^2 + \Delta_y^2\right) / \left(6 \times 10^4\right) + \Delta_z^2/500^2 > 1.2$
4, 5	$\Delta T < 60$	$\left(\Delta_x^2 + \Delta_y^2\right) / \left(1.2 \times 10^5\right) + \Delta_z^2/550^2 > 1.2$
$6-9$	$\Delta T < 60$	$\left(\Delta_x^2 + \Delta_y^2\right) / \left(2 \times 10^5\right) + \Delta_z^2/650^2 > 1.2$
10+	$\Delta T < 60$	$\left(\Delta_x^2 + \Delta_y^2\right) / 500^2 + \Delta_z^2/700^2 > 1.2$

Table 7.3: The neutron cloud cut criteria. The (+) in the N_{ncloud} column denotes equal to or more than the defined value. This table is taken from Ref. [152].

7.3.4 Spallation Observables

The preselection cuts remove ∼70% of the muon spallation events. Following these cuts, a statistical analysis based on computing the log-likelihood of spallation observables is performed to further eliminate spallation backgrounds. The key variables calculated for the pre- and post-samples are defined as follows:

- dt: Time difference between the muon and the SHE event. This corresponds to the half-life of the produced radioactive isotope for spallation events.
- ℓ_t: Transverse distance from the muon track to the SHE event (see Figure 7.5). Typically, this does not exceed a few metres for well-defined through-going muons paired with their spallation decay products.
- ℓ_l: Longitudinal distance between the SHE event vertex projected onto the muon track and the position where the energy deposition (dE/dx) is maximal (see Figure 7.5). The dE/dx peak is calculated by aggregating the hit PMT information into a single spatial point on the muon track, using the method outlined in Ref. [44]. The ℓ_l should not extend beyond a few metres, provided the spallation peak position is accurately reconstructed.
- Q_μ: Total charge deposited by the muons in the ID, where higher values are expected for spallation-induced particle showers.

- Q_{res}: Residual charge deposited by the muon relative to the value expected from a minimum ionising particle (MIP), given as

$$Q_{\mathrm{res}} = Q_{\mu} - Q_{\mathrm{MIP}} \times L, \tag{7.1}$$

  where Q_{MIP} represents the number of photoelectrons per centimetre expected from the MIP and L is the muon track length. In this context, Q_{MIP} is calculated separately for each run as it depends on several detector properties that vary with time. For multiple-track events, L corresponds to the length of the first track. While this observable is not directly associated with the SHE event, it provides insight into the likelihood of a particular muon triggering a shower.

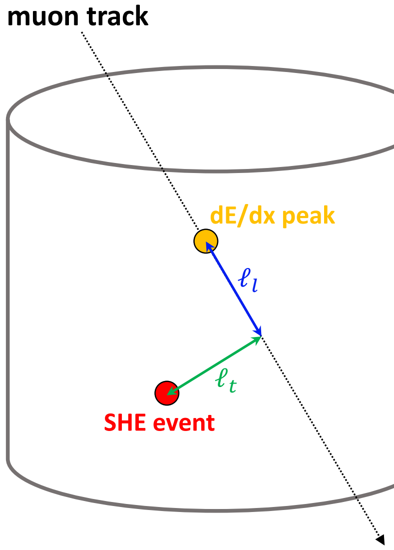

Figure 7.5: Schematic diagram of spallation likelihood variables.

7.3.5 Spallation Likelihood Cut

Two PDFs are constructed to define the log-likelihood ratios for each muon type across all spallation observables ($i = dt$, ℓ_t, ℓ_l, Q_μ, Q_{res}). The spallation PDF ($\mathrm{PDF}^i_{\mathrm{spall}}$) is obtained by subtracting the post-sample distributions from the relative pre-sample distributions after area normalisation. The random PDF ($\mathrm{PDF}^i_{\mathrm{random}}$) is the area-normalised post-sample distribution. The PDFs for ℓ_l,

Q_{μ}, and Q_{res} are tuned in three bins to account for correlations between these particular observables. These bins are defined as dt (0 – 0.05 s, 0.05 – 0.5 s, 0.5 – 60 s) and ℓ_t (0 – 300 cm, 300 - 1,000 cm, 1,000 – 5,000 cm). A Kernel Density Estimation (KDE) method is applied to the PDFs to smoothen out statistical variations. Figure 7.6 shows the PDFs of the spallation observables for the single through-going muon. The spallation component is evident because all distributions show an excess of events compared to the random sample. The ratios of the PDFs are combined to produce the spallation likelihood $\mathcal{L}_{\text{spall}}$,

$$\mathcal{L}_{\text{spall}} = \log \prod_i \left(\frac{\text{PDF}^i_{\text{spall}}(x)}{\text{PDF}^i_{\text{random}}(x)} \right). \tag{7.2}$$

The $\mathcal{L}_{\text{spall}}$ ratios are binned according to the reconstructed energy of the DSNB candidate. The cut criteria are determined separately for each bin as the spallation event rate is highly correlated with energy. Since single through-going and multiple-track muons are the primary sources of the spallation background, cut conditions with fine-grained dt and ℓ_t bins are implemented in this analysis. For misfit muons, only the dt variable is used to calculate $\mathcal{L}_{\text{spall}}$ as other spallation observables produce unreliable results. To provide an example of these distributions, Figure 7.7 depicts the likelihood distributions for different muon types in the 8 - 10 MeV bin.

7.3.6 Box Cut

Above 16 MeV, spallation backgrounds are primarily dominated by short-lived radioactive isotopes such as ^{14}B, ^{12}N, and ^{11}Li (see Table 5.1). These backgrounds are reduced by implementing a series of straightforward box cuts on the dt and ℓ_t spallation observables for each muon class. In particular, these cuts effectively eliminate higher energy spallation events by leveraging the correlation between the half-lives of the spallation isotopes and the event's energy (see Table 7.4).

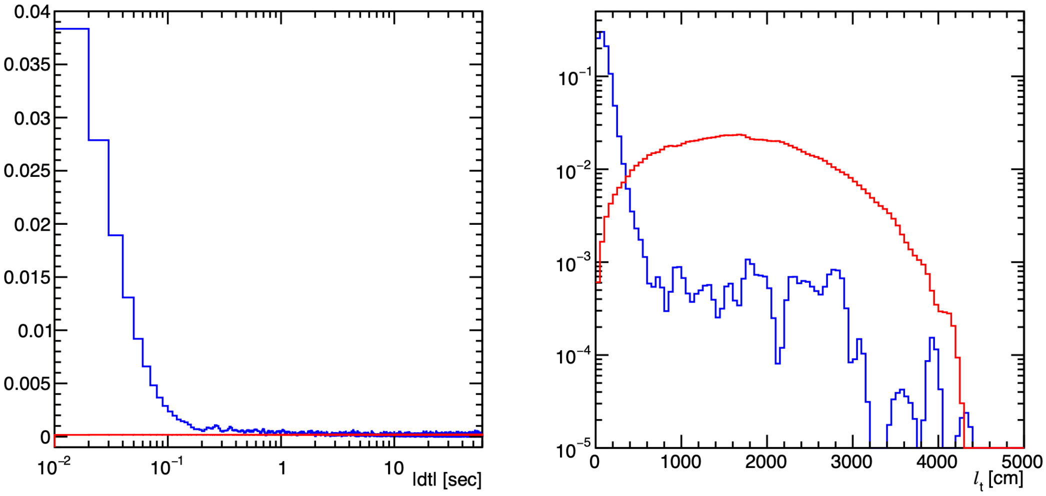

(a) dt **(b)** ℓ_t

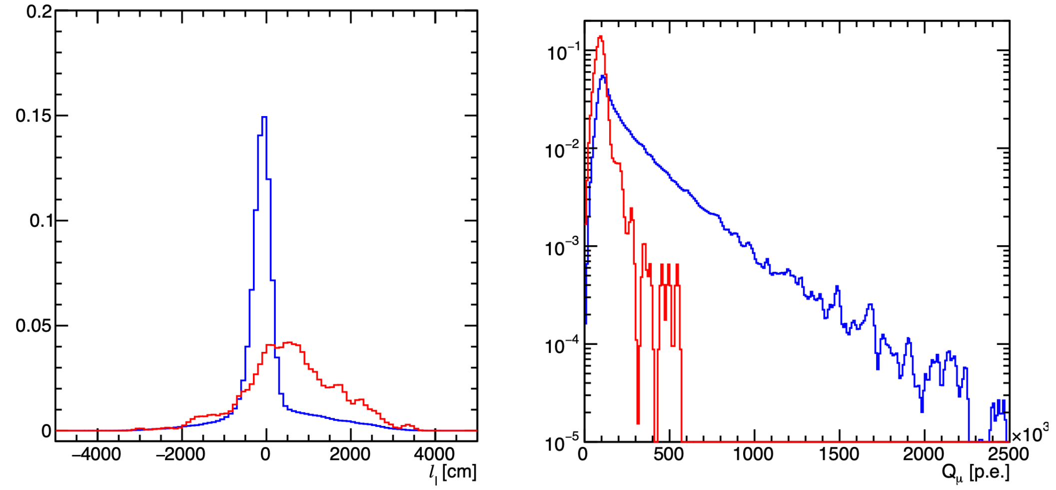

(c) ℓ_l **(d)** Q_μ

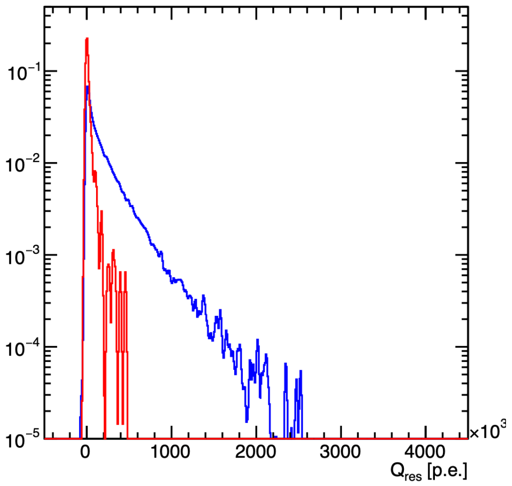

(e) Q_{res}

Figure 7.6: Spallation (blue) and random (red) PDFs of the spallation observables for single through-going muons with dt [0 , 0.05] s and ℓ_t [0 , 300] cm. This figure is taken from Ref. [152].

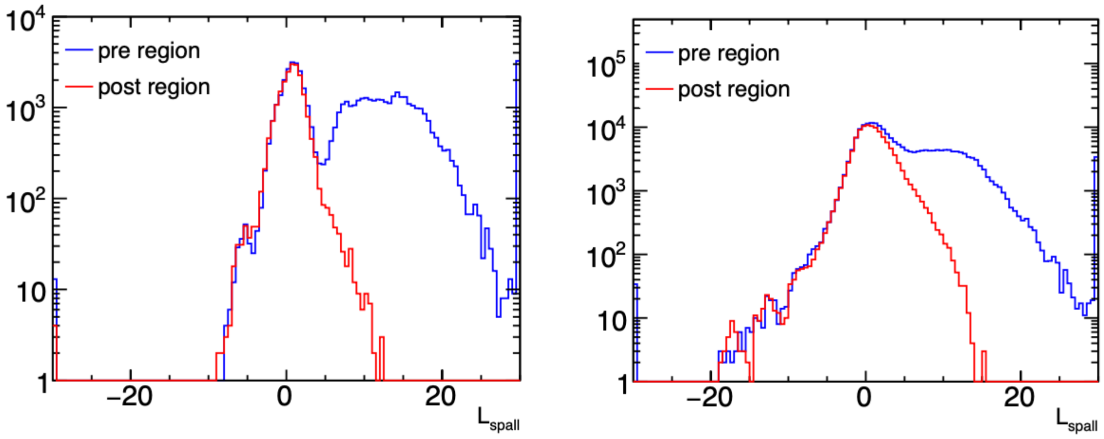

(a) single muon, $dt = 0 - 0.05$ s.

(b) single muon, $\ell_t = 0 - 200$ cm.

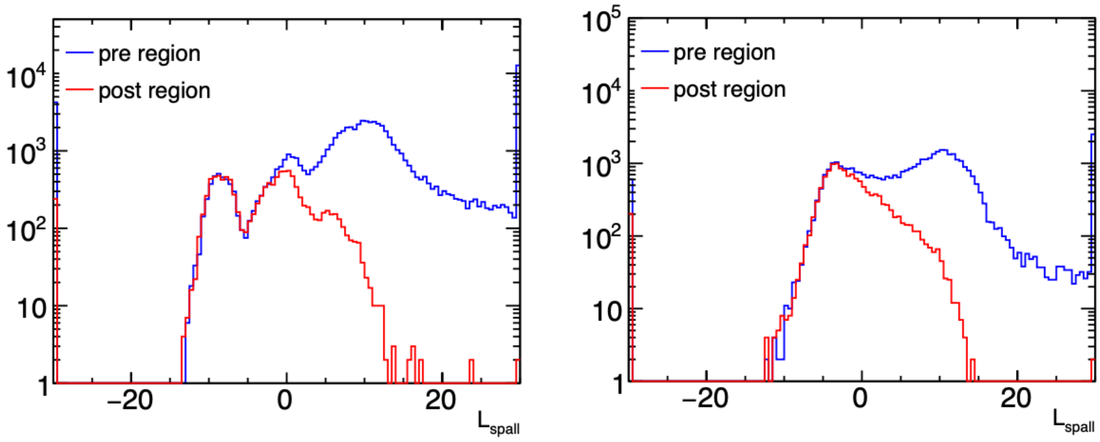

(c) multiple-track muon, $dt = 0 - 0.05$ s.

(d) multiple-track muon, $\ell_t = 0 - 200$ cm.

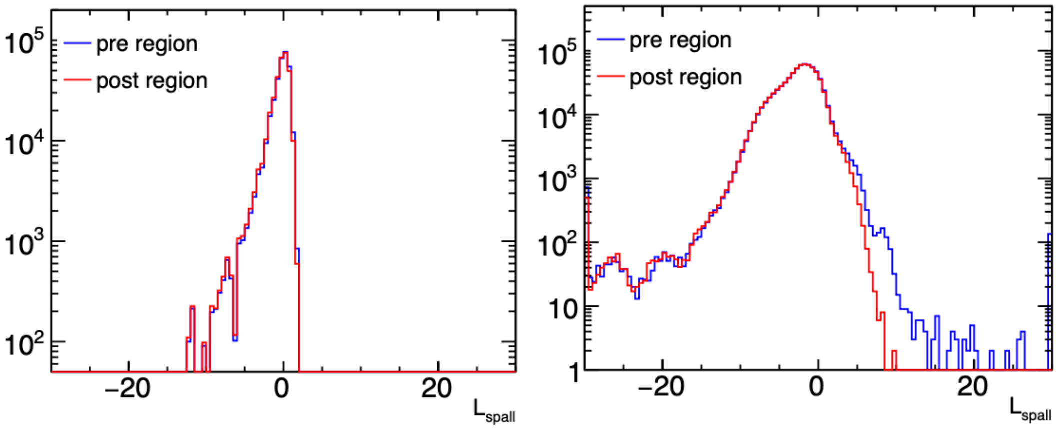

(e) misfit muon.

(f) stopping muon.

Figure 7.7: Spallation likelihood distrubtions ($\mathcal{L}_{\text{spall}}$) for the 8 - 10 MeV bin. The pre-region refers to the pre-sample (blue) and the post-region refers to the post-sample (red). This figure is taken from Ref. [152].

Energy region	Muon type	Cut criteria
$E < 24\text{MeV}$	-	$dt < 0.1$ s and $\ell_t < 400$ cm
$16 < E < 20\text{MeV}$	misfit	$dt < 1.5$ s
$16 < E < 18\text{MeV}$	single	$g_\mu < 0.4$ and $dt < 7$ s and $\ell_t < 150$ cm
$16 < E < 18\text{MeV}$	stopping	$g_\mu < 0.3$ and $dt < 6$ s
$16 < E < 20\text{MeV}$	stopping	$dt < 0.05$ s
$16 < E < 20\text{MeV}$	multiple	$dt < 0.1$ s and $\ell_t < 400$ cm

Table 7.4: Spallation box cut criteria for each reconstructed energy bin. This table is taken from Ref. [152].

7.3.7 Efficiency Calculations

In this section, the cut efficiencies after all preselection and spallation cuts are estimated for the remaining "signal" events in the dataset (including contributions from DSNB, solar, reactor, and atmospheric neutrino interactions) and the spallation backgrounds. The four types of efficiencies evaluated are the random event (ϵ_{random}), solar event (ϵ_{solar}), spallation event (ϵ_{spall}), and ^{9}Li event (ϵ_{li9}).

Random Event Efficiency

The signal efficiency after the preselection cuts is ~98%, as described in Section 7.3.3. The random event efficiencies ϵ_{random}, which are equivalent to the signal efficiencies, are estimated for the spallation likelihood and box cuts. This is represented by

$$\epsilon_{\text{random}} = \frac{N_{\text{post, after}}}{N_{\text{before}}}, \tag{7.3}$$

where N_{before} and $N_{\text{post, after}}$ are the number of SHE events before and after implementing the spallation cuts, respectively. Both variables are determined after the preselection cuts are applied.

Solar Neutrino Event Efficiency

The solar sample is used to validate the random event efficiency as these events are independent of the post-sample and thus should not correlate to any muon-induced spallation events. The angular correlation between the solar neutrino event direction and the sun's direction (θ_{sun}) is illustrated in Figure 7.8. Solar events align with the sun's direction ($\cos(\theta_{\text{sun}})\ \sim 1$) and non-solar events are uniformly distributed across the entire spectrum. The number of SHE-triggered solar events (N_{sol}) is estimated as

$$N_{\text{sol}} = N_{\cos\theta_{\text{sun}}>0.5} - N_{\cos\theta_{\text{sun}}<-0.5}, \tag{7.4}$$

where $N_{\cos\theta_{\text{sun}}>0.5}$ represents the number of SHE events in the sun's direction and $N_{\cos\theta_{\text{sun}}<-0.5}$ is the number of events in the opposite direction. The spallation cut efficiency for the solar neutrino event (ϵ_{solar}) is calculated as

$$\epsilon_{\text{solar}} = \frac{N_{\text{sol, pre, after}}}{N_{\text{sol, before}}}, \tag{7.5}$$

where $N_{\text{sol, before}}$ and $N_{\text{sol, pre, after}}$ are the number of SHE-triggered solar events in the pre-sample before and after the spallation cuts are applied, respectively. The ϵ_{solar} and ϵ_{random} were found to be linearly correlated, which implies that the ϵ_{random} can be used to estimate the signal efficiency in this analysis [152].

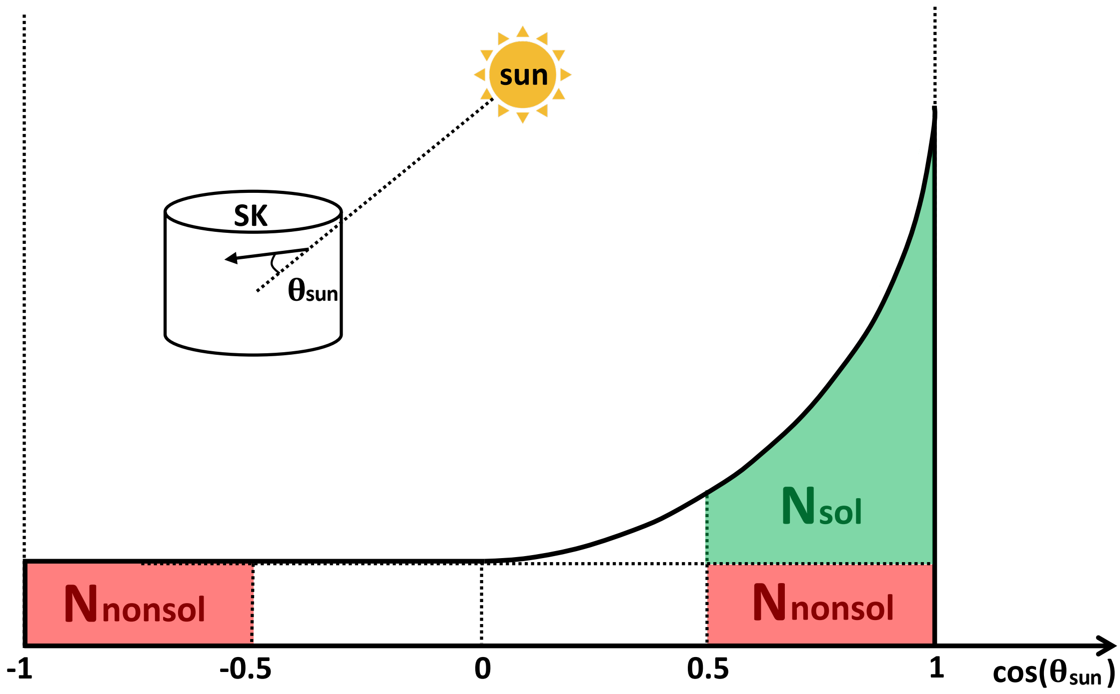

Figure 7.8: Schematic diagram of the θ_{sun} and $\cos(\theta_{\text{sun}})$ solar variables. A solar neutrino is shown to propagate through the SK detector with a reconstructed angular direction of θ_{sun} relative to the sun's direction. The red-shaded area refers to the non-solar events (N_{nonsol}) and the green-shaded area refers to solar events (N_{sol}).

Spallation Event Efficiency

The performance of the spallation cut is determined based on evaluating the spallation remaining event rate (ϵ_{spall}). Since the spectrum below 16 MeV is dominated by spallation and solar neutrino events at this stage in the reduction, the ϵ_{spall} is estimated using the region $\cos\theta_{\text{sun}} < 0$,

$$\varepsilon_{\text{spall}} = \frac{N_{\cos\theta_{\text{sun}}<0,\,\text{pre, after}} - N_{\text{atm, after}}}{N_{\cos\theta_{\text{sun}}<0,\,\text{before}} - N_{\text{atm, before}}}. \tag{7.6}$$

The $N_{\cos\theta_{\text{sun}}<0,\,\text{before}}$ and $N_{\cos\theta_{\text{sun}}<0,\,\text{pre, after}}$ parameters denote the number of non-solar events before and after the spallation cuts in the pre-sample, respectively. Above 14 MeV, the subleading background in the $\cos\theta_{\text{sun}} < 0$ region is atmospheric neutrinos. Therefore, the atmospheric neutrino contributions before ($N_{\text{atm, before}}$) and after ($N_{\text{atm, after}}$) the cuts are subtracted. The parameter $N_{\text{atm, before}}$ is determined from the atmospheric MC sample and $N_{\text{atm, after}}$ is calculated as $N_{\text{atm, before}} \times \epsilon_{\text{random}}$.

Lithium-9 Event Efficiency

The event efficiency for ^{9}Li decay is evaluated as a separate quantity since it is a prominent background even after all spallation cuts are applied. The calculation involves evaluating the survival probabilities for the pre- and post-samples, given a certain SHE event (see Figure 7.2). The muons are categorised into three classes: a muon that produces the target SHE event (ϵ_a), muons that create other SHE events (ϵ_b), and non-spallation-inducing muons uncorrelated to any SHE events (ϵ_c). For the target spallation SHE event, the pre-sample contains muon events from all classes whereas the post-sample contains those from only the latter two classes. The survival probabilities after applying all the spallation cuts for ϵ_{pre} and ϵ_{post} is

$$\epsilon_{\text{pre}} = \epsilon_a \times \epsilon_b \times \epsilon_c$$

$$\epsilon_{\text{post}} = \epsilon_b \times \epsilon_c.$$

Since ϵ_a, ϵ_b and, ϵ_c are independent of eachother, ϵ_a can be calculated as $\epsilon_a = \epsilon_{\text{pre}}/\epsilon_{\text{post}}$. The ^{9}Li event efficiency (ϵ_{li9}) is calculated in the same way, taking into account the ^{9}Li properties,

$$\epsilon_{\text{li9}} = \epsilon_{a,\text{ li9}} \times \epsilon_{\text{random}} \times \epsilon_{\text{multi+ncloud}}$$
$$\epsilon_{\text{multi+ncloud}} = \frac{\epsilon_{\text{spall}}}{\epsilon_{\text{1-ms+likelihood+box}}}.$$

The $\epsilon_{a,\text{ li9}}$ represents the survival probability for the spallation-causing muon (same as ϵ_a), $\epsilon_{\text{multi+ncloud}}$ denotes the efficiency after applying the multiple spallation and neutron cloud cuts, and $\epsilon_{\text{1-ms+likelihood+box}}$ is the efficiency after the 1-ms, likelihood, and box cuts. In this analysis, it is assumed that ^{9}Li events should have similar spallation observables compared to other isotopes, except for the dt variable [1]. Therefore, the $\epsilon_{a,\text{ li9}}$ is estimated by varying the dt according to the ^{9}Li half-life ($\tau = 0.178$s) in the calculations of the ^{9}Li likelihoods.

Final Efficiencies

The spallation cut criteria are optimised following the procedures outlined in Ref. [152]. This includes using ROC curves to evaluate the reduction performance and compare the relevant efficiencies. The final efficiencies calculated from this process for each energy bin are summarised in Table 7.5. The ϵ_{li9} is not evaluated above 16 MeV due to the end-point energy of ^{9}Li (see Table 5.1).

Energy [MeV]	ϵ_{random}	ϵ_{spall}	ϵ_{li9}
$8 < E < 10$	51.8%	5.1%	3.4%
$10 < E < 12$	78.2%	6.8%	5.0%
$12 < E < 14$	86.0%	6.8%	5.9%
$14 < E < 16$	93.1%	5.3%	5.5%
$16 < E < 18$	73.4%	0.01%	-
$18 < E < 20$	81.8%	< 0.001%	-
$20 < E < 24$	81.8%	< 0.001%	-

Table 7.5: Summary of the spallation cut efficiencies for each energy bin. This table is taken from Ref. [152].

---

[1] Further MC studies are investigating whether the ℓ_t parameter changes according to the isotope type.

7.4 Third Reduction

The third reduction targets the removal of atmospheric neutrino and residual radioactive decay backgrounds, which dominate the signal region after the spallation cuts. In particular, low-energy atmospheric neutrino interactions with protons and oxygen nuclei produce electron-like event signatures that mimic the prompt positron from the IBD signal. Additionally, visible pions, muons, and γ-rays generated from higher-energy interactions further contribute to the background spectrum. Therefore, a set of cuts based on characteristic variables is implemented to distinguish and eliminate these backgrounds from the final sample. The procedure for optimising energy-dependent cuts, developed by the author for this work, is outlined in Appendix A.1.

7.4.1 Cherenkov Angle

The opening angle of the Cherenkov light cone (θ_C) emitted by the prompt event is a crucial parameter for discriminating atmospheric backgrounds. Highly relativistic electrons and positrons are reconstructed with $\theta_C \sim 42^\circ$ in the SK detector. In contrast, heavier particles like pions and muons tend to be produced close to their Cherenkov threshold, resulting in smaller angles. Furthermore, events with multiple γ-ray emissions often misreconstruct with larger angles since individual γ-rays cannot be resolved separately, as illustrated in Figure 7.9.

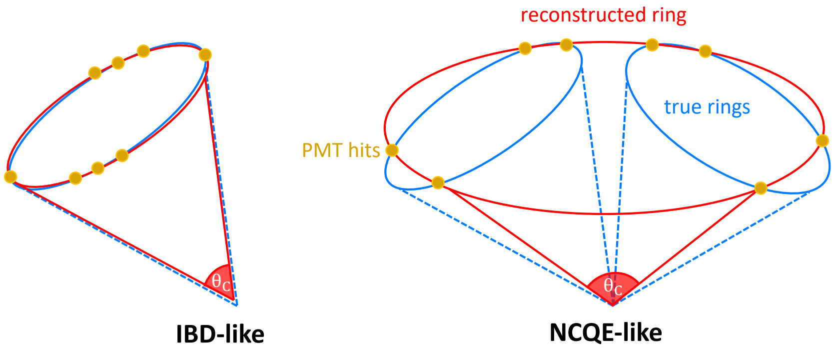

Figure 7.9: Schematic diagram of the Cherenkov angle (θ_C) reconstruction for IBD-like and NCQE-like prompt events.

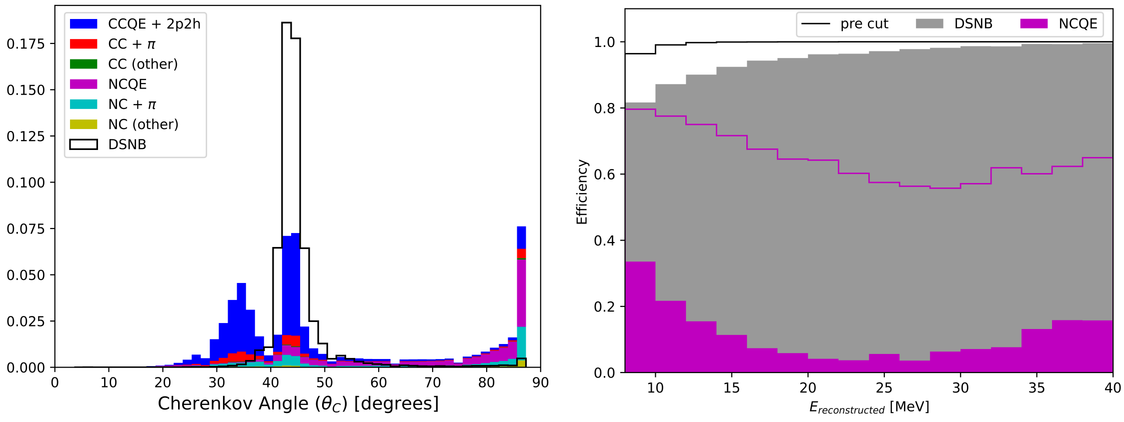

(a) **(b)**

Figure 7.10: Left: The Cherenkov angle (θ_C) distribution of the simulated atmospheric neutrino backgrounds separated by interaction type (colours) and the DSNB signal MC assuming the Horiuchi+09 flux model (black) [37]. Right: The DSNB (grey, black) and NCQE (magenta) efficiencies before (solid line) and after (filled histogram) the Cherenkov angle cut.

Figure 7.10a displays the Cherenkov angle distributions for both the DSNB signal and atmospheric neutrino backgrounds after the first reduction. The NCQE events predominantly exhibit larger angles, peaking near 90° due to multiple γ-ray emissions. On the other hand, low-energy muons, and pions produced from CC interactions reconstruct at angles below 40°.

This analysis introduces the first implementation of an energy-dependent Cherenkov angle cut optimised using the SPLASH framework. These cuts target low and high-angle components by selecting separate θ_C regions for each 2 MeV energy bin, listed in Table 7.6. Despite effectively reducing the majority of backgrounds, this method still retains over 30% of NCQE background events in the low-energy region, as illustrated in Figure 7.10b. Therefore, a new set of ML-based cuts are implemented in this analysis (see Section 7.6).

7.4.2 Charge Over Number of Hits

High-momentum muons deposit more charge per PMT than $\mathcal{O}(10\text{ MeV})$ electrons and positrons. This is primarily because low-energy electron-like events tend to scatter, leading to a lower charge deposition per PMT. The ratio of the charge to the number of hits in a 50 ns time-of-flight subtracted window around the main

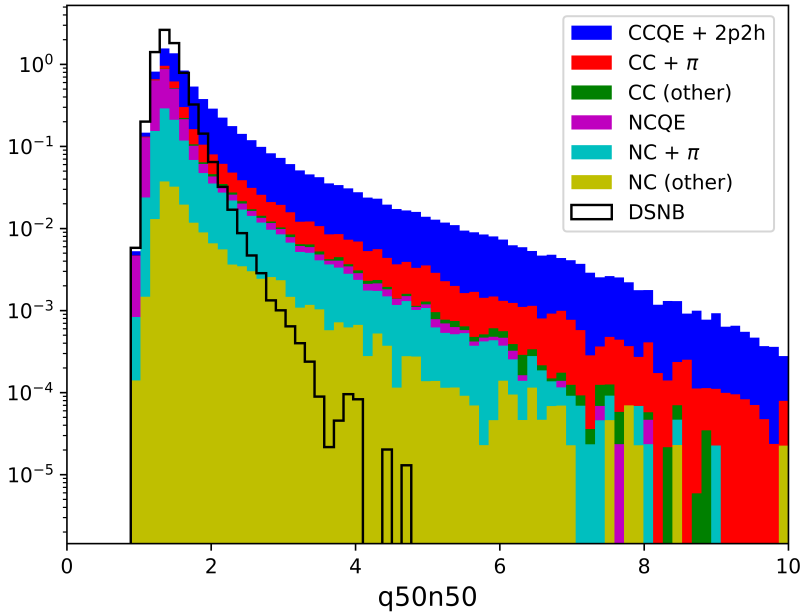

Figure 7.11: The *q50n50* distributions of the simulated atmospheric neutrino backgrounds separated by interaction type (colours) and the DSNB MC assuming the Horiuchi+09 flux model (black) [37].

activity peak (*q50n50*) is calculated to quantify this characteristic. Figure 7.11 shows the *q50n50* distribution for the DSNB and atmospheric MC after the first reduction is applied. Signal events typically produce around one photoelectron per PMT, while the distribution for higher-energy background events extends to larger values. In this analysis, energy-dependent cuts are optimised in the SPLASH framework, with the cut values provided in Table 7.6.

Energy bin [MeV]	**Cherenkov angle (θ_C) cut**	**Charge/Hit (*q50n50*) cut**
8 - 10	$[31°, 53°]$	2.81
10 - 12	$[35°, 54°]$	2.19
12 - 14	$[37°, 53°]$	2.21
14 - 16	$[36°, 53°]$	2.03
16 - 18	$[36°, 52°]$	1.98
18 - 20	$[37°, 52°]$	1.90
20 - 22	$[37°, 52°]$	2.08
22 - 24	$[38°, 53°]$	1.89
24 - 26	$[38°, 52°]$	1.81
26 - 28	$[38°, 52°]$	1.80
28 - 30	$[38°, 52°]$	1.83
30>	$[38°, 53°]$	2.00

Table 7.6: Summary of the energy-dependent cut values for the θ_C and *q50n50* cuts.

7.4.3 Pion Likeness

Electron-like events often undergo multiple scattering, resulting in dispersed hit patterns, while high-energy pions typically generate clear and well-defined Cherenkov rings. The pion-likeness parameter R_π is employed to distinguish pion and electron-like events based on the clarity of their Cherenkov rings. This is determined by calculating the opening angles (θ_0) for all possible three PMT-hit combinations within a 15 ns time-of-flight subtracted window centred around the main activity peak. The number of triplets (N_{triplets}) is then compared in two different angular intervals around θ_0 to give

$$R_\pi = \frac{N_{\text{triplets}}(\theta_0 \pm 3^\circ)}{N_{\text{triplets}}(\theta_0 \pm 10^\circ)} \tag{7.7}$$

Figure 7.12 presents the R_π distribution for the DSNB and atmospheric MC following the first reduction. Higher values of R_π often correspond to events producing pions. Therefore, a threshold of $R_\pi < 0.36$ was chosen for this analysis.

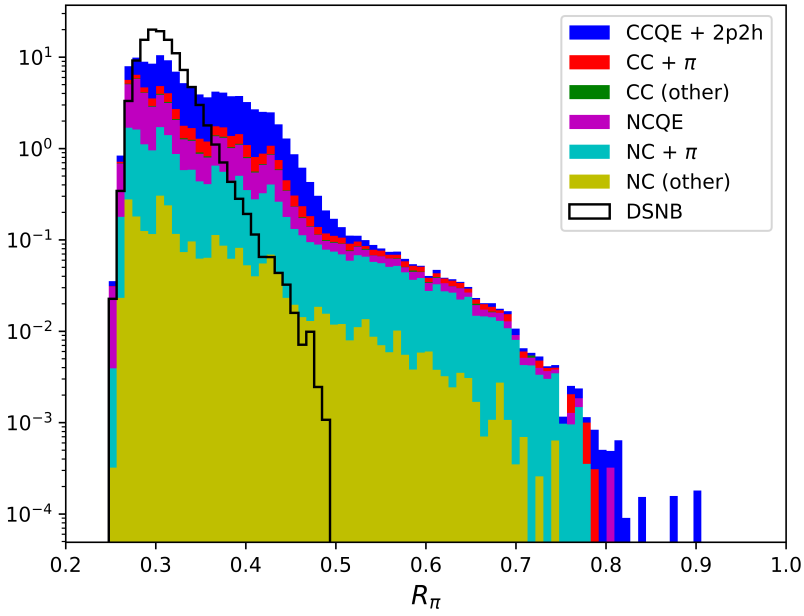

Figure 7.12: The pion-likeness (R_π) distributions of the simulated atmospheric neutrino backgrounds separated by interaction type (colours) and the DSNB MC assuming the Horiuchi+09 flux model (black) [37].

7.4.4 Pre- and Post-Activity

Atmospheric neutrino interactions may generate visible muons and pions, which subsequently decay into electrons. This can result in an event signature with two distinct activity peaks within the same trigger window. In such cases, abnormal activity may occur before (pre-activity) or after (post-activity) the trigger time, depending on which event exhibits the highest charge deposition.

To identify pre-activity, PMT hit-clusters are examined within a 15 ns time-of-flight subtracted window from the beginning of the trigger window until at least 12 ns before the main peak. Figure 7.13a shows the maximum number of hits calculated within this time window, denoted as $N_{\text{pre}}^{\text{max}}$. Given that IBD events are associated with fewer pre-activity hits a threshold of $N_{\text{pre}}^{\text{max}} < 12$ is chosen for this analysis. Post-activity is detected using an algorithm developed for other SK and T2K analyses, which computes the number of decay electrons ($N_{\text{decay-e}}$) from muon and pion events after the main peak time [155]. Figure 7.13b displays the $N_{\text{decay-e}}$ distributions for DSNB and atmospheric MC after the first reduction cuts. Since almost no decay electron-like events are observed for DSNB events, only events with $N_{\text{decay-e}} < 1$ are selected.

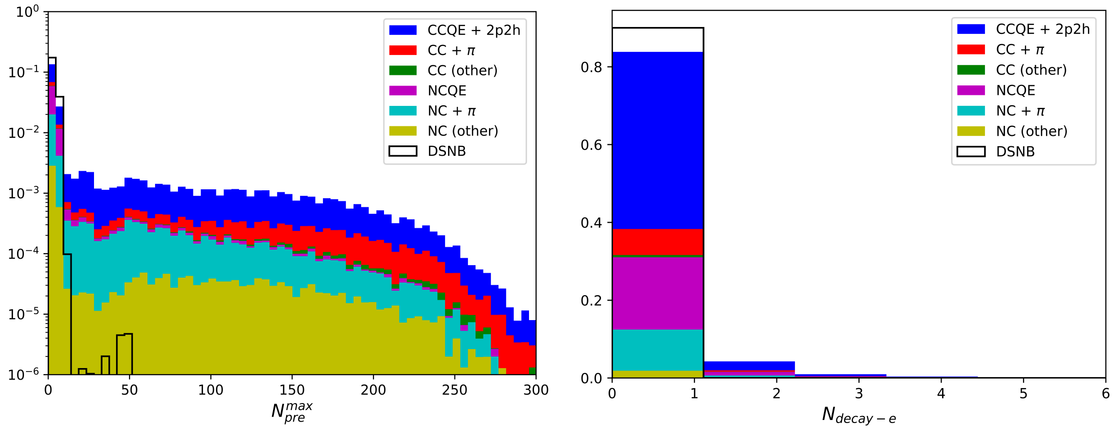

(a) **(b)**

Figure 7.13: Left: The $N_{\text{pre}}^{\text{max}}$ distribution of the simulated atmospheric neutrino backgrounds separated by interaction type (colours) and the DSNB MC assuming the Horiuchi+09 flux model (black) [37]. Right: The $N_{\text{decay-e}}$ distributions of the same.

7.4.5 Effective Wall Distance

Residual radioactive decay and muon spallation events occurring in the surrounding rock can occasionally be reconstructed within the FV. Instead of directly constraining the FV, the effective distance (d_{eff}) cut is implemented to eliminate such events while maximising the effective volume. The parameter is calculated as the distance from the event vertex to the nearest ID wall along the reconstructed track direction, as depicted in Figure 7.14. Since accurate simulations for modelling radioactive backgrounds are not available, the expected background distribution and cut thresholds are inferred from comparisons between data and DSNB MC.

Figure 7.15 shows the d_{eff} distributions for data and DSNB MC after the first reduction is applied. For direct comparison, the distributions are normalised to have the same area above 10 m, where the contribution from radioactive decay is expected to be negligible. The data shows a clear excess in background events at lower d_{eff} values, which becomes more significant at lower energies (see Appendix A.2). Therefore, an energy-dependent d_{eff} cut is applied, defined as

$$d_{\text{eff}} > \max\left\{300, 500 - \frac{E_{\text{rec}} - 16\ \text{MeV}}{1\ \text{MeV}} \times 50\right\}\ \text{cm} \tag{7.8}$$

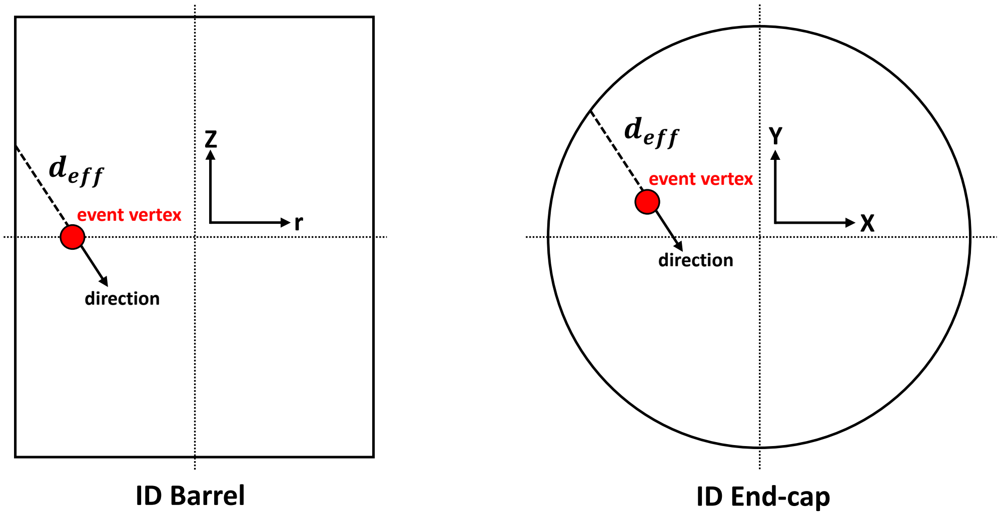

Figure 7.14: Schematic diagram of the d_{eff} parameter.

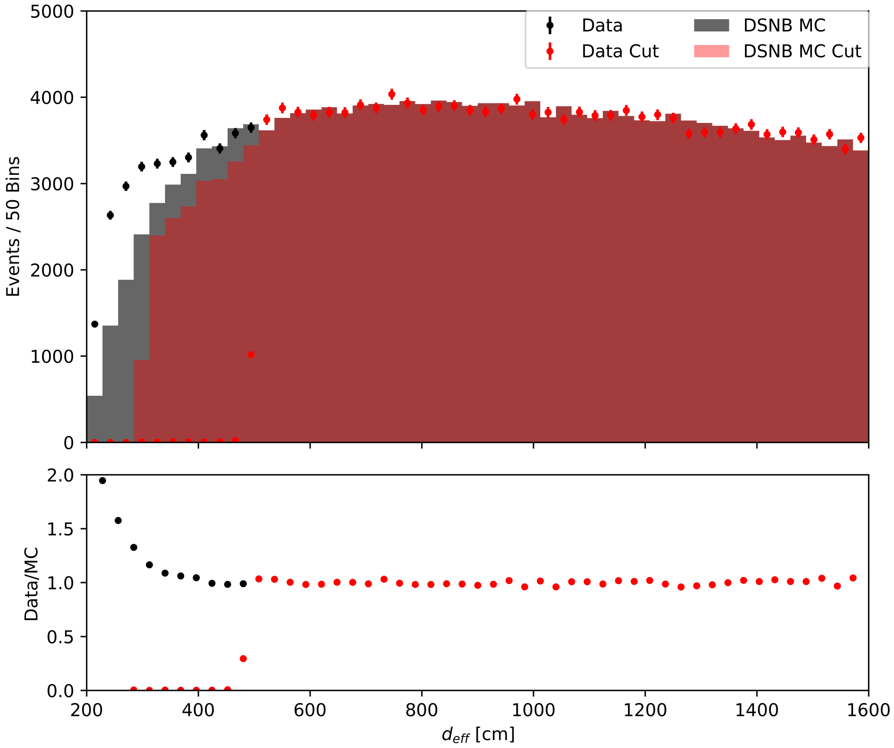

Figure 7.15: The d_{eff} distribution for data (points) and DSNB MC (histogram), with the Horiuchi+09 DSNB model [37], before (black, grey) and after (red) the cut is applied. The data/MC ratio is shown in the lower panel.

7.4.6 Systematic Uncertainties on the Cut Efficiencies

The systematic uncertainties on the third reduction cut efficiencies come from the detector model and simulated Cherenkov light pattern in the IBD MC. These uncertainties can be estimated using data and MC samples obtained from the SK-VI LINAC calibration. Both data and MC samples are processed through the low-energy reconstruction pipeline to generate the positron selection observables. Events that reconstruct more than 2 m away from the LINAC endcap are removed from the data to mitigate artificial discrepancies between the datasets. The distributions are compared for all runs and the uncertainty is evaluated as the largest difference between the measured (data) and predicted (MC) efficiencies. This process is carried out for the θ_C, $q50n50$, and R_π observables. Systematic uncertainties for the d_{eff} parameter are estimated using the method implemented in the solar analysis [104].

Cherenkov Angle Cut

Figure 7.16 shows the Cherenkov angle distribution for one of the LINAC data and MC runs with the cut $\theta_C \in [31^\circ, 53^\circ]$ applied as an example. Although there is a slight excess in data observed for higher angles, this has a negligible impact on the efficiencies as it is contained within the selected region. The comparison of the cut efficiencies is carried out for all energy-dependent θ_C cut values listed in Table 7.6. The largest discrepancy was found to be 1.1% for energies above 12 MeV, which is assigned as a systematic error. Further distributions are shown in Appendix A.3.

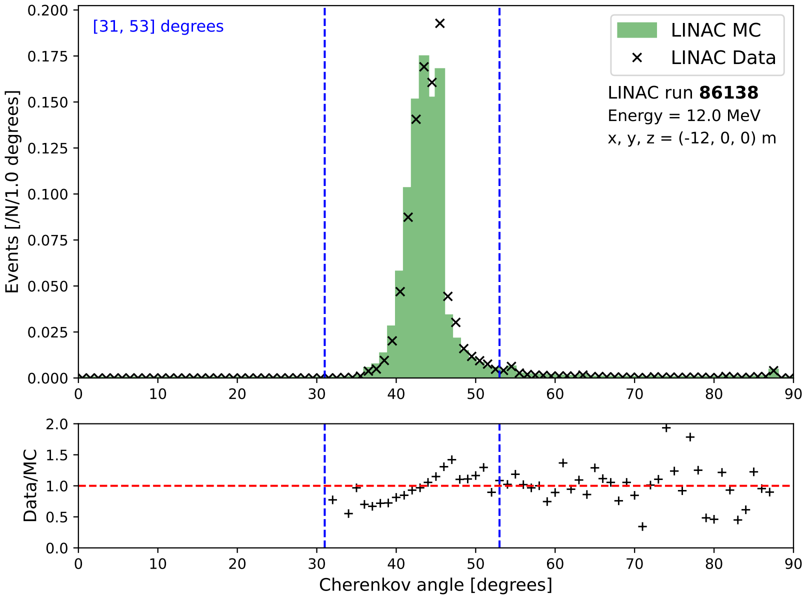

Figure 7.16: Distribution of the Cherenkov angle θ_C in the LINAC MC (green) and data (black points) calibration samples for run 86138 with E = 12 MeV. The cut window $\theta_C \in [31^\circ, 53^\circ]$ is displayed as two vertical blue lines. The data/MC ratio is shown below.

Charge Over Number of Hits Cut

Figure 7.17 displays the *q50n50* distribution in LINAC data and MC, with the cut criterion *q50n50* < 2.03 applied. This cut is selected to assess the systematic uncertainty as it covers the entire *q50n50* spectrum, however, the process was repeated for all the cut values listed in Table 7.6. The two distributions exhibit very little difference, leading to a systematic uncertainty evaluation of 0.5% for the cuts. Additional distributions can be found in Appendix A.3.

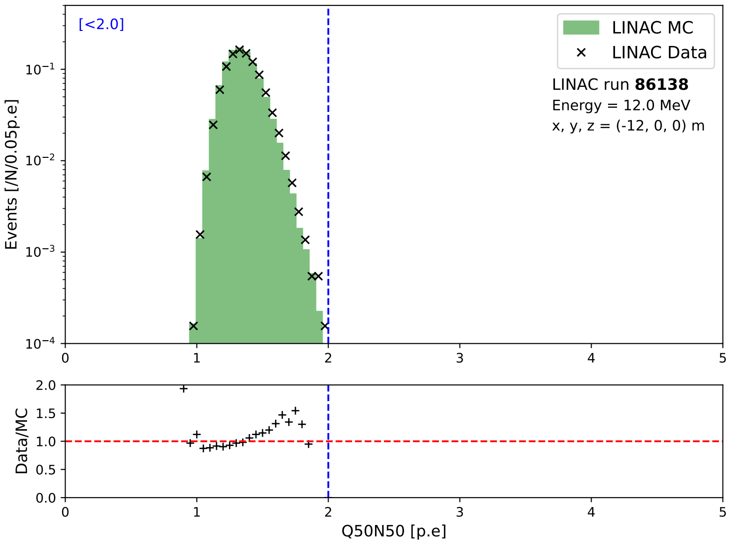

Figure 7.17: Distribution of *q50n50* in LINAC MC (green) and data (black points) calibration samples with E = 12 MeV. The vertical blue line represents the cut. The data/MC ratio is shown in the panel below.

Pion Likeness

Figure 7.18 shows the R_π distribution for LINAC data and MC with the $R_\pi < 0.36$ cut applied. A slight discrepancy is observed at the distribution's tail end, but its impact on the cut efficiencies is minimal. The systematic uncertainty is 1.1% for the R_π cut, derived from the data-MC comparison (see Appendix A.3).

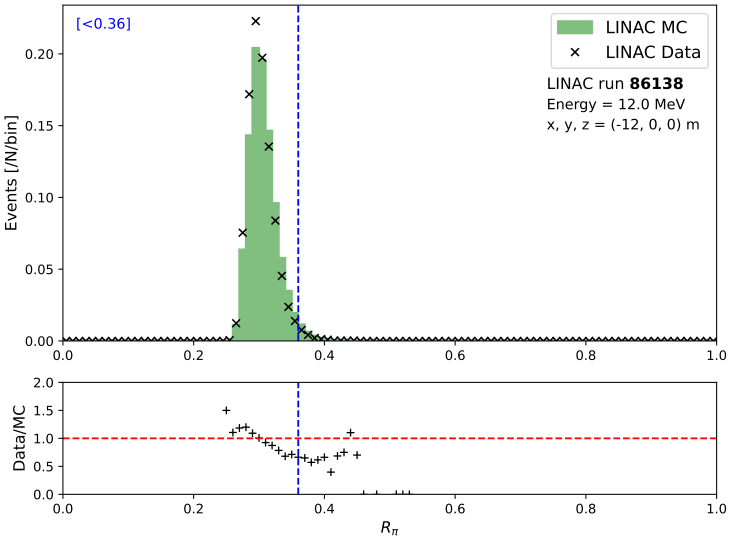

Figure 7.18: Distribution of the R_π in the LINAC MC (green) and data (black points) calibration samples for run 86138 with E = 12 MeV. The cut $R_\pi < 0.36$ is displayed as a vertical blue line. The data/MC ratio is shown in the below panel.

7.4.7 Reduction Efficiencies

The signal efficiencies with the associated systematic uncertainties for the positron selection cuts are summarised in Table 7.7. The cut with the largest difference between the data and MC efficiencies is taken as the systematic uncertainty for the energy-dependent cuts. The total systematic uncertainty on the third reduction is estimated to be 1.6% by summing all uncertainties in quadrature.

Positron Observable	**Cut Criteria**	**Efficiency $\pm$ (sys. unc.)**
Cherenkov angle (θ_C)	see Table 7.6	93.11 $\pm$ (1.1)%
Charge/Hit (*q50n50*)	see Table 7.6	97.93 $\pm$ (0.5)%
Pion Likeness (R_π)	$R_\pi < 0.36$	97.04 $\pm$ (1.1)%
Pre-Activity ($N_{\text{pre}}^{\text{max}}$)	$N_{\text{pre}}^{\text{max}} < 12$	99.98 $\pm$ (<0.1)%
Post-Activity ($N_{\text{decay-e}}$)	$N_{\text{decay-e}} < 1$	98.05 $\pm$ (<0.1)%
Effective Wall Distance (d_{eff})	see Equation7.8	94.49 $\pm$ (<0.1)%

Table 7.7: Summary of the third reduction signal efficiencies and systematic uncertainties.

7.5 Fourth Reduction

The fourth reduction step involves identifying delayed neutron capture signals using a dedicated neutron tagging algorithm. IBD interactions are characterised by the production of a single neutron, which can be captured by Gd isotopes to produce an 8 MeV γ-ray cascade (see Section 5.1). Therefore, this analysis selects SHE events associated with a single tagged neutron. This cut effectively filters out background events originating from muon spallation and solar neutrinos lacking neutron signals, as well as atmospheric neutrinos emitting multiple neutrons.

In this section, a brief overview of the neutron tagging algorithm and the relevant efficiencies for the analysis are provided. The cut criteria, neutron tagging efficiency, and misidentification rate are estimated using neutron MC simulations performed in SKG4. Calibrations with an americium-241/beryllium-9 (Am/Be) neutron source are performed to evaluate the algorithm's performance on SK-VI data. Further details of these studies can be found in [42, 152].

7.5.1 Neutron Candidate Preselection

In this analysis, the SHE+AFT combined trigger is employed to detect prompt positrons followed by delayed neutron capture events within a 535 μs window, detailed in Section 7.1. Neutron signals within the time interval of [4, 535] μs after the prompt event are examined to cover the full timescale of the event. This search window is dominated by PMT dark noise hits and residual low-energy radioactive decay events. To reduce the noise contribution, the initial step involves applying a preselection cut based on the maximum hits within a 200 ns window (N_{200}), as depicted in Figure 7.19. Events with $N_{200} \geq 25$ hits are selected as candidate neutron signals for further analysis. This cut criterion demonstrates a high efficiency exceeding 99%.

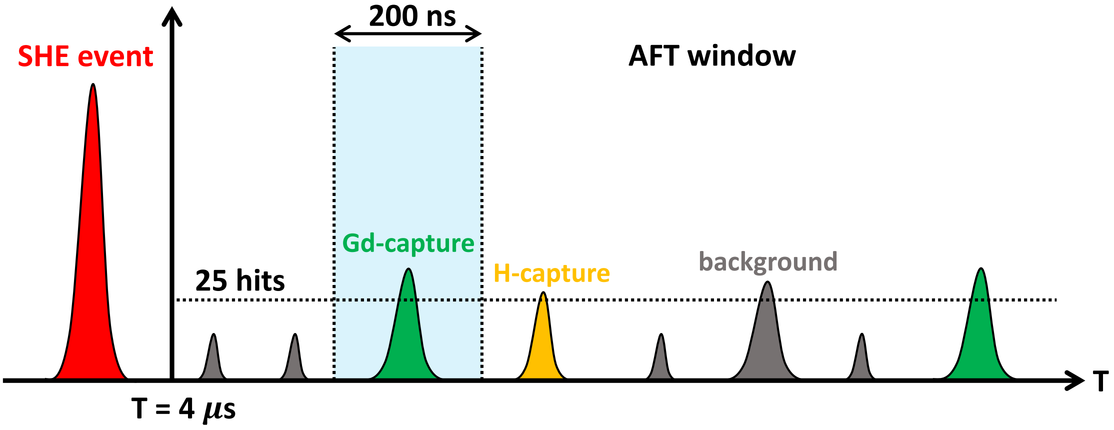

Figure 7.19: Schematic diagram of the neutron preselection over the SHE+AFT combined trigger window. The dashed line and shaded region refer to the N_{200} cut criterion, which slides over the full AFT window. All of the events above the threshold are neutron candidates.

7.5.2 Neutron Identification

The neutron capture signal on Gd emits multiple γ-rays, which can be effectively reconstructed using the standard BONSAI low-energy reconstruction algorithm. Following the preselection, basic cuts are applied to candidate neutrons to eliminate misreconstructed and low-energy background events near the detector walls. This includes the FV cut from the first reduction (see Section 7.2.3) and the goodness-of-fit criteria $g_{\text{vtx}} < 0.4$ and $g_{\text{dir}} > 0.4$ used in the neutron-cloud cut (see Section 7.3.3).

The remaining selection criteria focus on the reconstructed vertex and energy of the delayed event. In IBD interactions, the neutron capture vertex typically lies within a few tens of centimetres from the positron event vertex. Therefore, the reconstructed distance between prompt and delayed events (d_{prompt}) provides an effective technique for discrimination against time-correlated β + n spallation backgrounds. In this analysis, the cut is defined as $d_{\text{prompt}} < 300$ cm. In addition, a cut is applied to the reconstructed energy to minimise the impact of low-energy accidental coincidence backgrounds from PMT dark noise hits. Since the total reconstructed kinetic energy (E_{rec}) of the γ-ray cascade from neutron capture on Gd is between 4 - 5 MeV, as determined from Am/Be neutron source calibration studies, this analysis employs a $E_{\text{rec}} > 3.5$ MeV cut [156].

7.5.3 Neutron Tagging Efficiency

Table 7.8 shows the neutron selection criteria and the corresponding cut efficiencies, evaluated using neutron MC samples. These cuts resulted in a Gd-capture efficiency of 73.2% ± 0.2% and reduced the background rate to 10^{-5} on the MC sample [42]. The total neutron tagging efficiency is evaluated as 35.6% ± 2.5% obtained from measurements of the Am/Be source [42].

Cut Criteria	**Gd-capture Efficiency**	**Background Efficiency**
$4 < t < 535$ μs, and $N_{200} \geq 25$	95.0 %	100 %
$d_{\text{wall}} > 200$ cm	88.8 %	47.0 %
$g_{\text{vtx}} > 0.4$	85.4 %	11.6 %
$g_{\text{dir}} < 0.4$	84.6 %	10.3 %
$d_{\text{prompt}} < 300$ cm	81.9 %	0.06 %
$E_{\text{rec}} > 3.5$	73.2 %	0.002 %

Table 7.8: Summary of the neutron cut criteria and reduction efficiencies. This table is adapted from Ref. [152].

7.5.4 Misidentification Rate

The neutron tagging algorithm is essential for reducing the accidental coincidence background events from muon spallation. The performance relies on achieving a low misidentification rate (ϵ_{mis}) for neutron selection. To evaluate this, the algorithm was applied to SK-VI random trigger datasets, and ϵ_{mis} was determined to be $(2.8 \pm 0.1) \times 10^{-4}$ per event [42]. This confirms the algorithm's capability to effectively remove the majority of accidental coincidence events.

7.5.5 Neutron Multiplicity Cut

Figure 7.20 shows the neutron multiplicity distributions for the DSNB and atmospheric MC after the first and third reductions are applied. The spallation cut is omitted here as it has minimal impact on eliminating atmospheric backgrounds. The signal events produce either zero or one tagged neutron, whereas atmospheric NC interactions can produce multiple tagged neutrons. In this analysis, a single tagged neutron is required in the final state to reduce the atmospheric backgrounds.

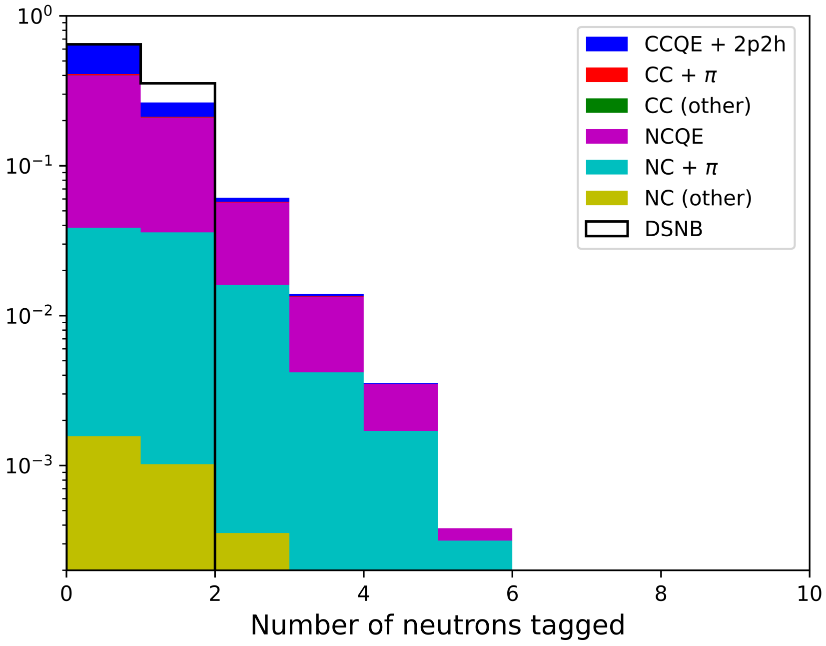

Figure 7.20: The neutron multiplicity distribution of the simulated atmospheric neutrino backgrounds separated by interaction type (colours) and the DSNB MC assuming the Horiuchi+09 flux model (black) [37]. The first and third reduction cuts are applied.

7.6 Fifth Reduction

The final reduction step uses a novel ML-based technique, developed by the author, to enhance NCQE background rejection after neutron tagging is applied. The output of the Gamma And Positron CNN (GAPNet) model for image-based e^+/γ classification is integrated as an additional positron observable in the analysis (see Chapter 6). This new parameter, referred to as the *softmax* classification score, represents the probability of a given event being a DSNB candidate.

As demonstrated previously, the model's ability to distinguish between DSNB and NCQE events is comparable to that of the third reduction when a single classification threshold is applied to the softmax parameter (see Section 6.5.3). This effect is attributed to an inherent energy dependence observed within the model. Therefore, the softmax cut is refined by optimising a set of energy-dependent cuts in combination with the Cherenkov angle cut criteria. This section details the cut optimisation process and performance of the new softmax cut criteria.

7.6.1 Softmax Cut Optimisation

The softmax cut optimisation is carried out on a dedicated test set containing DSNB and NCQE MC events, used for the GAPNet model performance evaluation in Section 6.5. Both datasets are processed through the BONSAI low-energy reconstruction algorithm and the GAPNet model to generate positron observables. The first reduction and neutron tagging cut criteria are applied to retain well-defined events with a single tagged neutron.

Figures 7.21 and 7.22 show the softmax scores for DSNB and NCQE events, respectively, as a function of the reconstructed Cherenkov angle per energy bin. Interestingly, the model's classification performance is not fully correlated with the Cherenkov angle cut as most NCQE events with $\theta_C \sim 42^\circ$ are correctly assigned lower softmax scores. This result indicates the model aggregates features across the entire PMT hit distribution differently compared to the reconstructed Cherenkov angle to infer the event class. Therefore, the softmax cuts are optimised within each angle bin as a complementary reduction step alongside the angle cut to leverage the information provided by both observables.

Below 12 MeV, the model shows minimal discriminatory power, likely due to sparse or indistinguishable spatial features between the Cherenkov light distributions of the events. However, at higher energies, the performance improves significantly, with clear separation in softmax scores between DSNB and NCQE events. This suggests that the model learns to not only discriminate events based on the spatial distribution of hits but also indirectly implements an energy-dependent cut. Therefore, the softmax cuts are chosen to be less restrictive at lower energies and gradually become more stringent with increasing energy to maximise signal efficiency.

The cut optimisation procedure carried out for each energy and angle bin is carried out in the SPLASH framework. The final cuts are presented in Table 7.9. The softmax reduction efficiency is investigated by comparing LINAC data and MC distributions, shown in Section 6.6. The maximum discrepancy in the cut efficiencies is determined to be 10 %. Further details on the systematics evaluation and related studies are provided in Chapter 6.

Energy bin [MeV]	**Cherenkov angle (θ_C) cut**	**Softmax cut**
8 - 10	$[31°, 53°]$	0.08
10 - 12	$[35°, 54°]$	0.14
12 - 14	$[37°, 53°]$	0.23
14 - 16	$[36°, 53°]$	0.27
16 - 18	$[36°, 52°]$	0.32
18 - 20	$[37°, 52°]$	0.39
20 - 22	$[37°, 52°]$	0.55
22 - 24	$[38°, 53°]$	0.68
24 - 26	$[38°, 52°]$	0.89
26 - 28	$[38°, 52°]$	0.90
28 - 30	$[38°, 52°]$	0.90
30>	$[38°, 53°]$	0.90

Table 7.9: Summary of the energy-dependent cut values for the θ_C and the softmax cuts.

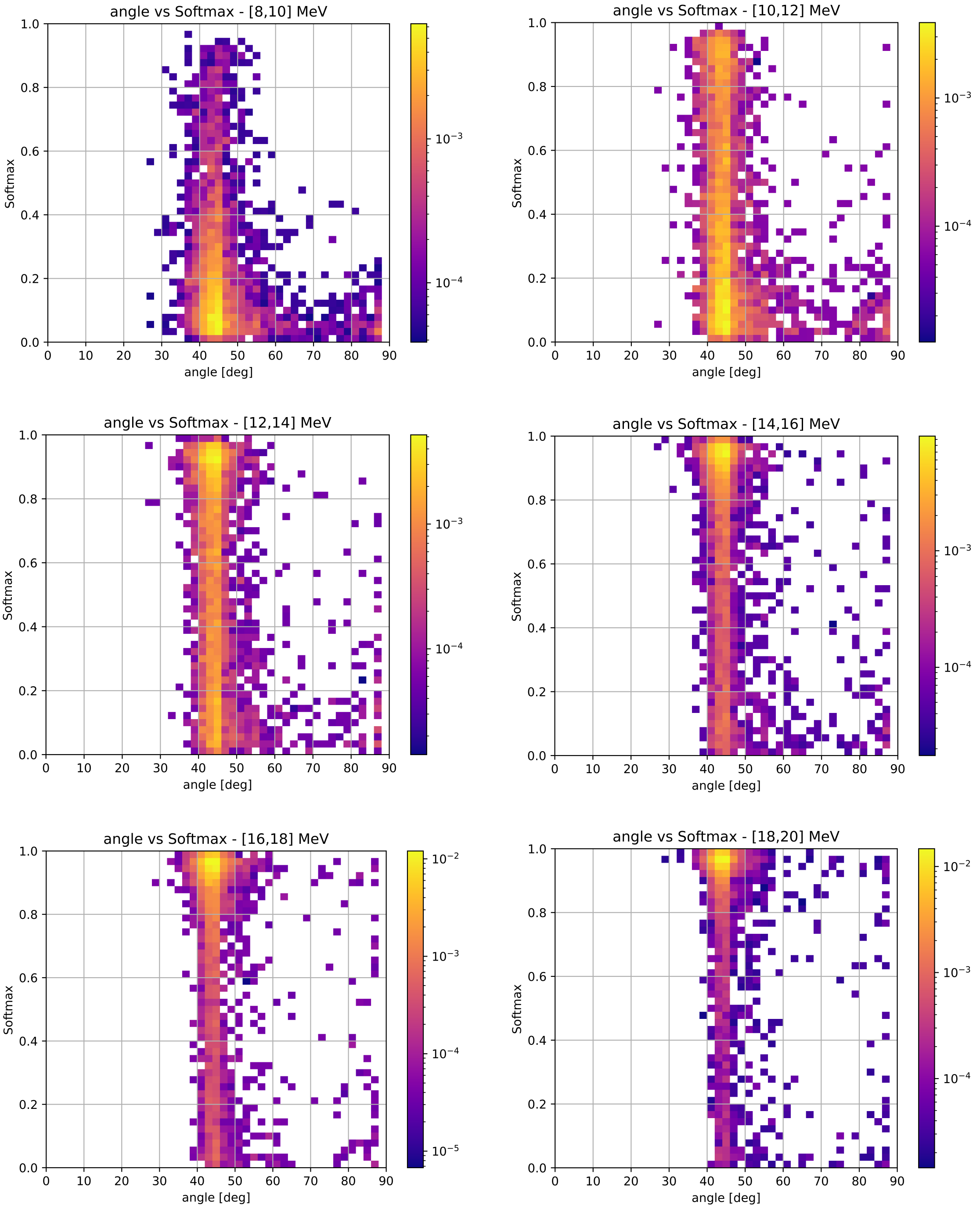

Figure 7.21: The distributions of the softmax classification score as a function of the reconstructed Cherenkov angle for the DSNB MC per 2 MeV energy bin.

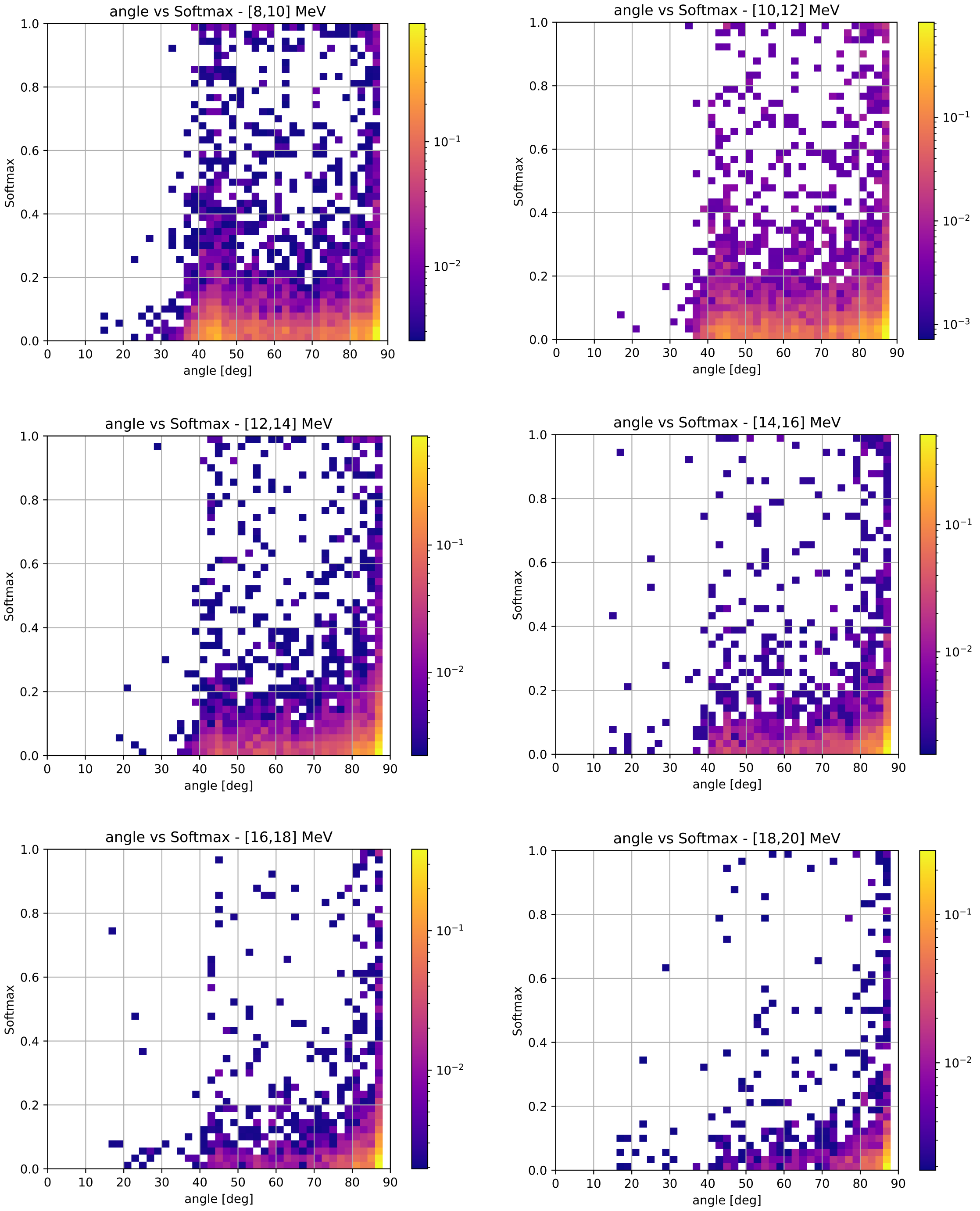
angle vs Softmax - [8,10] MeV

angle vs Softmax - [10,12] MeV

angle vs Softmax - [12,14] MeV

angle vs Softmax - [14,16] MeV

angle vs Softmax - [16,18] MeV

angle vs Softmax - [18,20] MeV

Figure 7.22: The distributions of the softmax classification score as a function of the reconstructed Cherenkov angle for the NCQE MC per 2 MeV energy bin.

7.6.2 Softmax Distribution

Figure 7.23 shows the softmax distributions for the DSNB and atmospheric MC after the first, third, and neutron tagging reduction steps are applied. The signal events are peaked towards higher softmax scores compared to NCQE events, which demonstrates the moderate classification capability of the GAPNet model. Although the classifier is not trained on NC-π events, the softmax cuts may demonstrate some effectiveness in reducing the background contribution from these events.

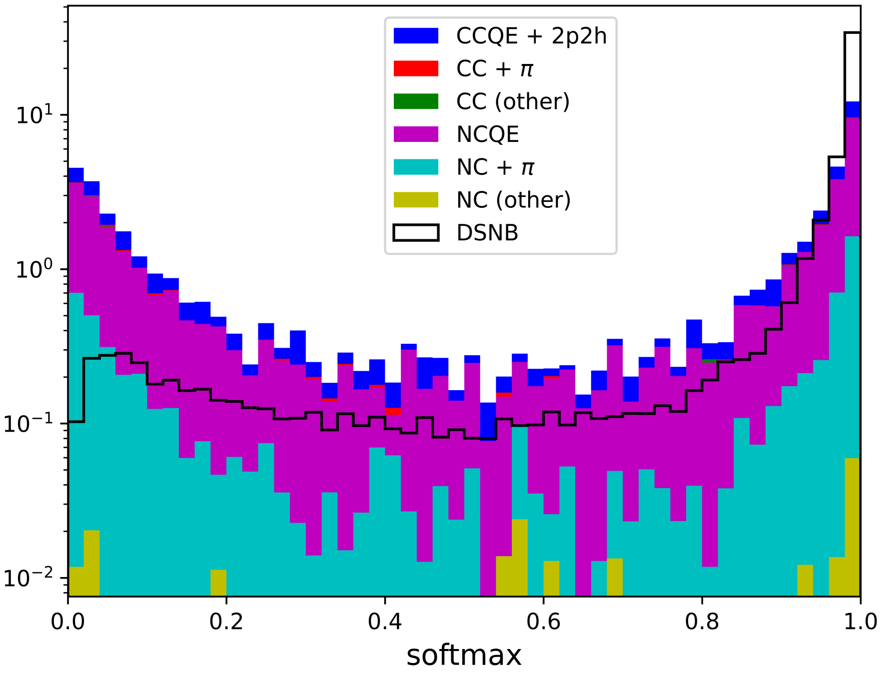

Figure 7.23: The softmax distribution of the simulated atmospheric neutrino backgrounds separated by interaction type (colours) and the DSNB MC assuming the Horiuchi+09 flux model (black) [37]. The first, third, and neutron tagging reduction cuts are applied.

7.7 Final Efficiencies

This section presents the NCQE background efficiencies after all atmospheric background reduction cuts and the final signal efficiencies following all five reduction stages.

7.7.1 NCQE Background Efficiency

Figure 7.24 shows the NCQE background efficiencies per 2 MeV energy bin after applying the first, third, neutron tagging, and softmax reduction cuts. The cut efficiencies are computed for events remaining after the first reduction.

The Cherenkov angle cut demonstrates robust performance by eliminating the bulk of events associated with multiple γ-ray emissions. Following this, the neutron tagging cut further reduces events with neutron multiplicities greater than one. These cuts are effective at higher energies where NCQE interactions generate multiple secondary γ-ray emissions in the prompt window via intermediate neutron-nucleon interactions. The newly integrated fifth reduction step targets challenging NCQE events that share similar topological features with IBD positrons. This cut results in a promising enhancement in NCQE background rejection by an order of a few percent across the spectrum.

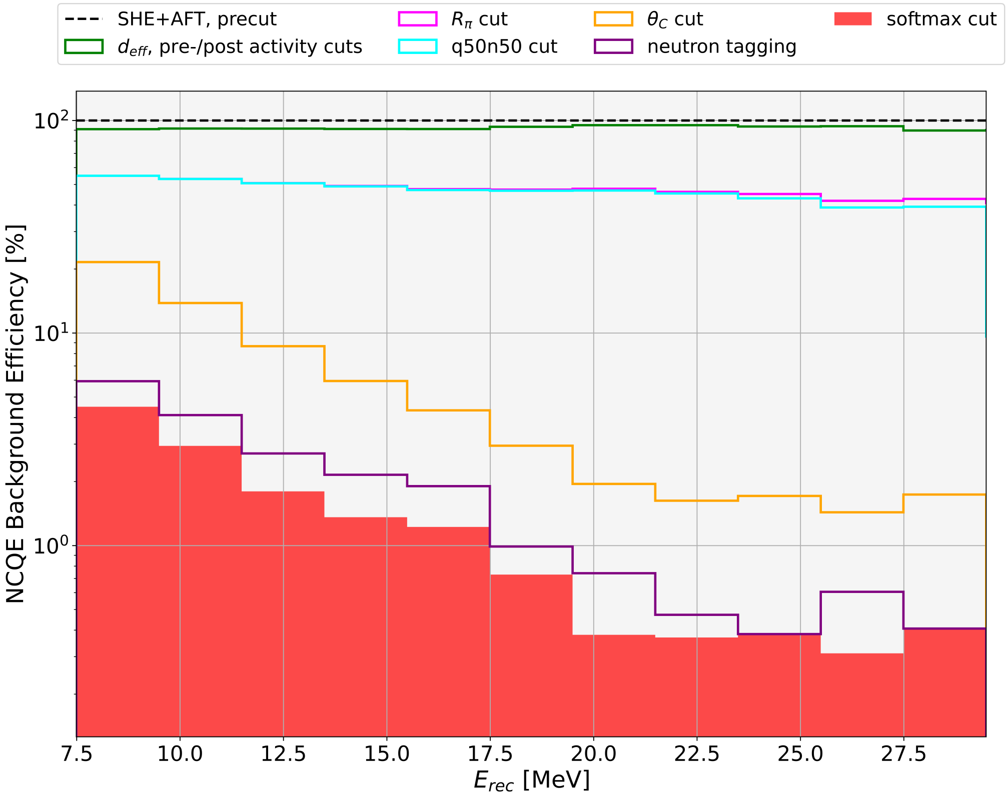

Figure 7.24: The NCQE background MC efficiencies as a function of the reconstructed kinetic energy (E_{rec}) per 2 MeV bin. The relevant atmospheric background reduction cuts are applied.

7.7.2 Signal Efficiency

Figure 7.25 presents the signal MC efficiency as a function of reconstructed energy after each cut, calculated with respect to the events passing the first reduction. Harsh spallation cuts designed to target muon spallation events dominating the background spectrum reduce the signal efficiency in the low-energy region. Above 15.49 MeV, restrictive box cuts are applied to further reduce spallation contribution, which leads to another decrease in signal efficiency at higher energies. Following the third reduction, the neutron tagging cut significantly impacts the signal efficiency by removing events lacking a tagged neutron in the final state. In addition, the softmax cut demonstrates greater impact in the lower energy region, attributed to the energy-dependent softmax spectrum and the cut criteria used in this analysis. The reduction efficiencies at each step, calculated with respect to the previous cut, are shown in Tables 7.10, 7.11 and 7.12.

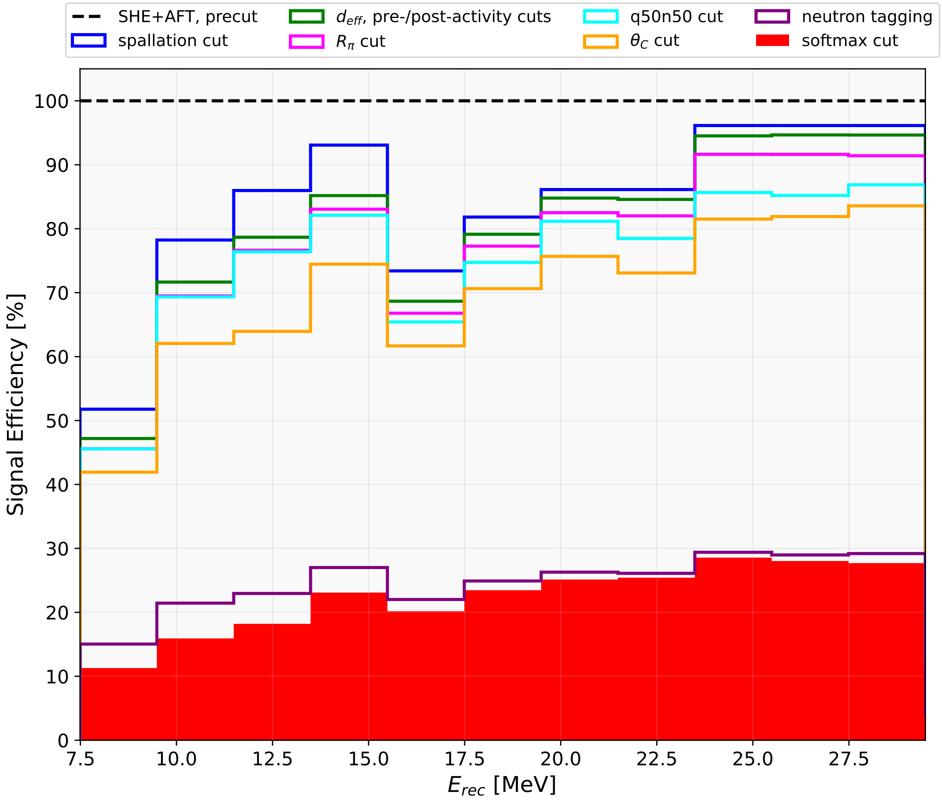

Figure 7.25: The signal MC efficiencies as a function of the reconstructed kinetic energy ($E_{\rm rec}$) per 2 MeV bin for all five reduction stages.

Energy [MeV]	**7.49 - 9.49**	**9.49 - 11.49**	**11.49 - 13.49**	**13.49 - 15.49**
Spallation cut	0.518	0.782	0.86	0.931
d_{eff} cut	0.912	0.916	0.915	0.915
$N_{\mathrm{pre}}^{\mathrm{max}}$ cut	>0.999	>0.999	>0.999	>0.999
$N_{\text{decay-e}}$ cut	>0.999	>0.999	>0.999	>0.999
$\mathcal{R}_\pi$ cut	0.966	0.97	0.974	0.975
$q50n50$ cut	1	0.998	0.997	0.989
θ_C cut	0.92	0.895	0.837	0.907
Neutron tagging	0.359	0.345	0.359	0.363
Softmax cut	0.751	0.743	0.793	0.855

Table 7.10: The signal efficiencies at each reduction stage for E_{rec} = 7.49 - 15.49 MeV.

Energy [MeV]	**15.49 - 17.49**	**17.49 - 19.49**	**19.49 - 21.49**	**21.49 - 23.49**
Spallation cut	0.734	0.818	0.861	0.861
d_{eff} cut	0.936	0.967	0.985	0.982
$N_{\mathrm{pre}}^{\mathrm{max}}$ cut	>0.999	>0.999	>0.999	>0.999
$N_{\text{decay-e}}$ cut	>0.999	>0.999	>0.999	>0.999
$\mathcal{R}_\pi$ cut	0.973	0.977	0.973	0.97
$q50n50$ cut	0.98	0.967	0.984	0.957
θ_C cut	0.943	0.945	0.932	0.931
Neutron tagging	0.357	0.353	0.347	0.357
Softmax cut	0.917	0.942	0.956	0.974

Table 7.11: The signal efficiencies at each reduction stage for E_{rec} = 15.49 – 23.49 MeV.

Energy [MeV]	**23.49 - 25.49**	**25.49 - 27.49**	**27.49 - 29.49**
Spallation cut	0.961	0.961	0.961
d_{eff} cut	0.983	0.985	0.985
$N_{\mathrm{pre}}^{\mathrm{max}}$ cut	>0.999	>0.999	>0.999
$N_{\text{decay-e}}$ cut	>0.999	>0.999	>0.999
$\mathcal{R}_\pi$ cut	0.969	0.968	0.966
$q50n50$ cut	0.935	0.93	0.95
θ_C cut	0.952	0.961	0.962
Neutron tagging	0.361	0.354	0.349
Softmax cut	0.971	0.967	0.949

Table 7.12: The signal efficiencies at each reduction stage for E_{rec} = 23.49 – 29.49 MeV.

8

Background Estimation

This chapter presents the estimation of the remaining backgrounds after event selection with their associated systematic uncertainties. The atmospheric neutrino backgrounds are estimated using a dedicated MC, as described in Chapters 4 and 5. From this point onwards, the relevant backgrounds are categorised as NCQE and non-NCQE components. Similarly, the ^{9}Li and reactor neutrino spectra are derived from IBD simulations and reweighted according to their respective fluxes. The accidental coincidence background is evaluated using data from the SK-VI period. In addition, a comparison between NCQE background spectra from this analysis and the previous study is presented to demonstrate the performance of the newly integrated energy-dependent Cherenkov angle and softmax cuts.

8.1 Atmospheric NCQE Interactions

This section outlines the estimation of the systematic uncertainties related to the NCQE-like interactions of atmospheric neutrinos.

8.1.1 Cross Section Uncertainty

Below 20 MeV, the atmospheric NCQE background dominates the spectrum in the region where the predicted DSNB flux is high. To estimate this background, the simulated spectrum of neutrino and antineutrino NCQE interactions are renormalised using the following cross section scaling factors from the T2K beam [157]:

$$f_{\nu-\mathrm{NCQE}} = 0.80 \pm 0.08(\mathrm{stat})^{+0.24}_{-0.18}$$
$$f_{\bar{\nu}-\mathrm{NCQE}} = 1.11 \pm 0.18(\mathrm{stat})^{+0.29}_{-0.22}$$

The renormalisation provides an estimate of both the NCQE and NC 2p2h interactions. The systematic uncertainty on the cross section is evaluated as the errors on the scaling factors and is set to 44% in this analysis.

8.1.2 Flux Uncertainties

The uncertainty in the atmospheric neutrino flux is determined from a study detailed in Ref. [158], which found a 15% variation in neutrino fluxes when comparing two modified interaction models. Another uncertainty arises from using T2K scaling factors $f_{\nu-\mathrm{NCQE}}$ and $f_{\bar{\nu}-\mathrm{NCQE}}$ to estimate flux and cross section uncertainties in the atmospheric neutrino flux background. To assess the impact of this, the ratios R^i_ν and $R^i_{\bar{\nu}}$ of the flux-averaged events in the T2K beam and the atmospheric neutrino fluxes for several cross section models are calculated as

$$\begin{aligned} R^i_\nu &= \frac{\int \phi^{\mathrm{T2K}}_\nu \sigma^i_{\nu-\mathrm{NCQE}}\, dE_\nu}{\int \phi^{\mathrm{ATM}}_\nu \sigma^i_{\nu-\mathrm{NCQE}}\, dE_\nu} \\ R^i_{\bar{\nu}} &= \frac{\int \phi^{\mathrm{T2K}}_{\bar{\nu}} \sigma^i_{\bar{\nu}-\mathrm{NCQE}}\, dE_{\bar{\nu}}}{\int \phi^{\mathrm{ATM}}_{\bar{\nu}} \sigma^i_{\bar{\nu}-\mathrm{NCQE}}\, dE_{\bar{\nu}}}, \end{aligned} \tag{8.1}$$

where ϕ^{T2K}_ν ($\phi^{\mathrm{T2K}}_{\bar{\nu}}$) and ϕ^{ATM}_ν ($\phi^{\mathrm{ATM}}_{\bar{\nu}}$) represent the neutrino (antineutrino) fluxes of the T2K beam and atmospheric neutrinos, respectively, and $\sigma^i_{\nu-\mathrm{NCQE}}$ ($\sigma^i_{\bar{\nu}-\mathrm{NCQE}}$) correspond to the neutrino (antineutrino) cross sections on oxygen from model i. Figure 8.1 presents the seven cross section models evaluated in this study: the function used in NEUT (see Section 4.3.1), the Spectral Function (SF) [78, 159], Relativistic Mean Field (RMF) [160–163], SuperScaling (SUSA) [164, 165], and the Relativistic Green Function (RGF) incorporating both functional forms (EDAI, Democratic) [163, 166], alongside the Relativistic Plane Wave Impulse

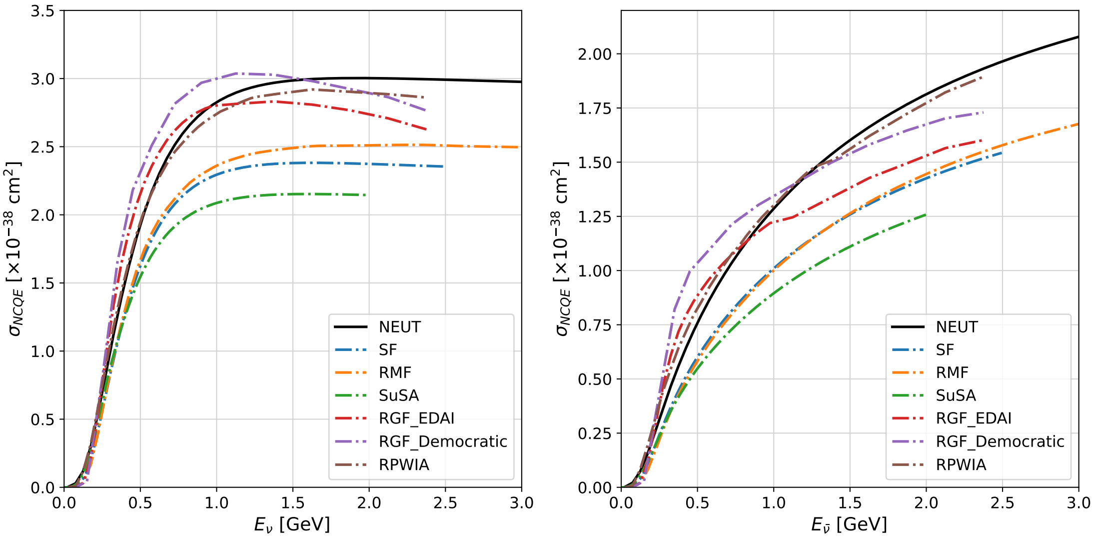

Figure 8.1: NCQE cross section for neutrino (left) and antineutrino (right) modes in the ^{16}O$(\nu, \nu' N)$ interaction as a function of neutrino energy for seven theoretical models.

Approximation (RPWIA) [163]. The maximum discrepancy between the ratios of each model is found to be 7%, which is assigned as the systematic uncertainty for this analysis.

8.1.3 Spectrum Shape Uncertainty

This section presents the evaluation of the NCQE spectrum shape systematic uncertainties in the SK-IV and SK-VI DSNB analyses. The calculation of the uncertainty was carried out by the author for the SK-IV analysis [47] and the same method was applied for the first SK-VI DSNB analysis [152]. The procedure followed for the SK-IV analysis is detailed here for demonstration, however, the final results from the SK-VI analysis are used in this work.

Systematic Uncertainty in SK-IV

The shape of the NCQE spectrum is highly dependent on the γ-ray interaction model used to simulate the primary and secondary γ-ray emissions. Recent cross section results from T2K beam measurements have highlighted a discrepancy between data and MC reconstructed Cherenkov angle θ_C distributions in the DSNB signal range $E_{\rm rec} \in [7.49, 29.49]$ MeV (refer to Figure 8.2) [157]. In the

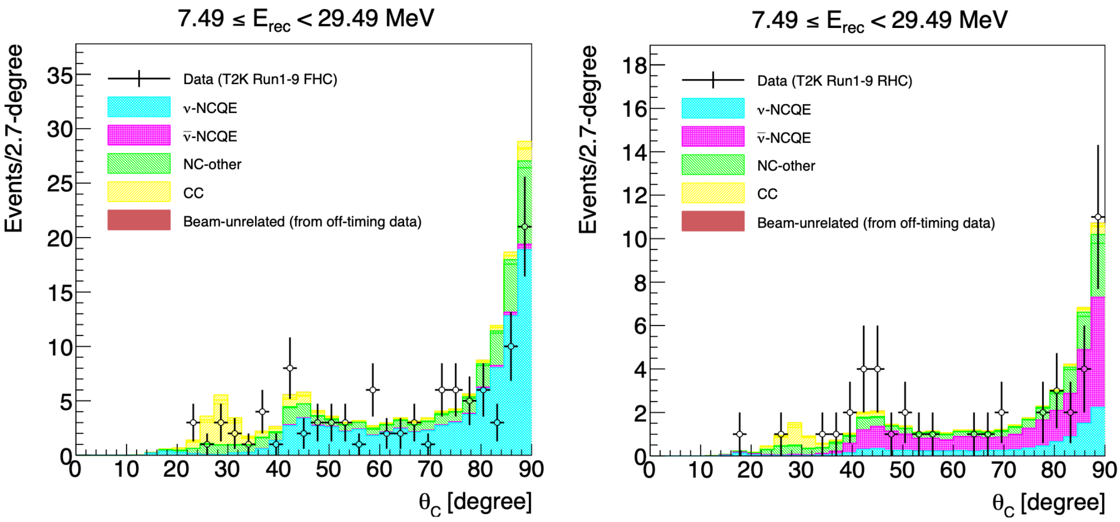

(a) **(b)**

Figure 8.2: The reconstructed Cherenkov angle θ_C distributions for $E_{\text{rec}} \in [7.49, 29.49]$ in the T2K beam flux for the FHC neutrino mode (left) and RHC antineutrino mode (right). The figures are taken from Ref. [157].

Forward Horn Current (FHC) distribution, the data exceeds MC predictions within the θ_C signal region used for the SK-IV analysis $\theta_C \in [38°, 50°]$. On the other hand, a slight excess over the data is observed in the high angle region $\theta_C \in [78°, 90°]$. Interestingly, no obvious excess is present in the Reverse Horn Current (RHC) distribution, however, this may be due to low statistics[1]. The discrepancy observed in the FHC mode is likely attributed to inaccurate modelling of secondary nucleon-nuclei interactions and their subsequent γ-ray emissions in the simulation. Therefore, accurately estimating uncertainties associated with the NCQE spectrum shape is crucial.

The systematic uncertainty cannot be estimated simply by scaling the MC prediction to data in the $\theta_C \in [78°, 90°]$ region, as the energy spectrum for multiple γ-ray emission is model-dependent. Hence, an alternative approach was developed to reproduce this effect by applying a pseudo-Gaussian distribution with an energy-dependent standard deviation $\sigma(E)$ to smear the energy spectrum. This process yields a new effective spectrum $S'(E_{\text{rec}})$ from the simulated NCQE

---

[1] FHC (RHC) refers to the configuration where the horn current is set to focus positively (negatively) charged particles for neutrino (antineutrino) production in the beam.

atmospheric spectrum $S(E_{\text{rec}})$, defined as

$$S'(E_{\text{rec}}) = \mathcal{N} \int S(E) \times \exp\left[-\frac{(E - E_{\text{rec}})^2}{2\sigma(E)^2}\right] \mathrm{d}E, \tag{8.2}$$

where $\mathcal{N}$ represents the normalisation of the pseudo-Gaussian distribution over all reconstructed energies. In both the SK-IV and SK-VI analyses, $\sigma(E_{\text{rec}})$ was set to 3 MeV, which was considered sufficient to cover the difference between the data and MC Cherenkov angle distributions shown in Figure 8.2. The systematic uncertainty is then estimated by reweighting the simulated NCQE atmospheric spectrum with the factors $\varepsilon_{\nu(\overline{\nu})}$, defined as

$$\varepsilon_{\nu(\overline{\nu})} = \frac{S'_{\nu(\overline{\nu})}(E_{\text{rec}})}{S_{\nu(\overline{\nu})}(E_{\text{rec}})}. \tag{8.3}$$

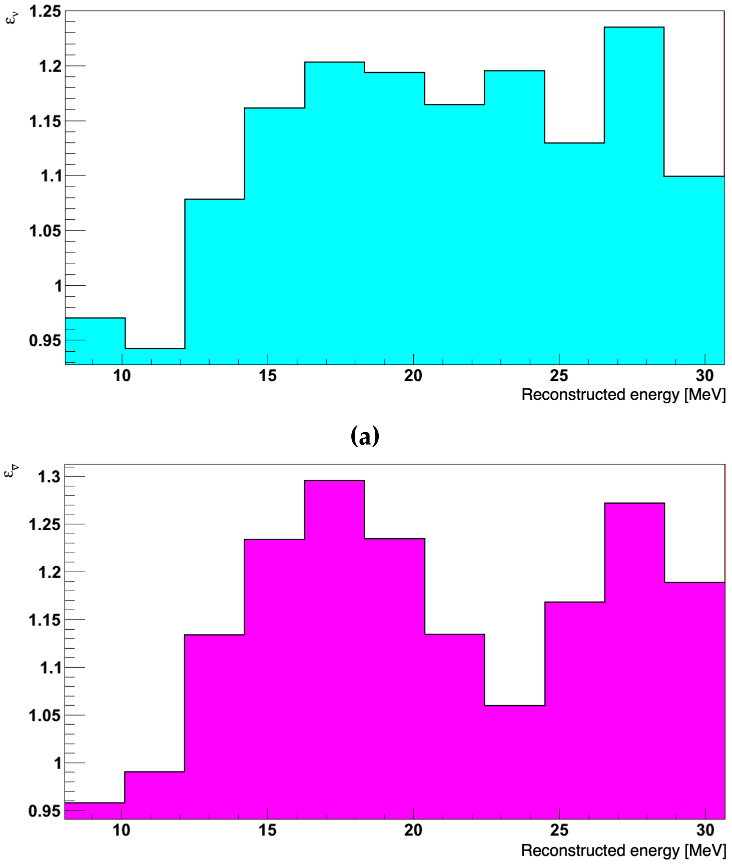

(a)

(b)

Figure 8.3: The distribution of the reweighting factors $\varepsilon_{\nu(\overline{\nu})}$ per 2 MeV bin width for the simulated NCQE neutrino spectrum (top) and antineutrino spectrum (bottom).

Figure 8.3 displays the calculated reweighting factors $\varepsilon_{\nu(\overline{\nu})}$ for each 2 MeV bin in the SK-IV analysis. These distributions exhibit larger values for higher energies as NCQE interactions in this region are more likely associated with multiple γ-rays.

The energy-dependent systematic uncertainty $\varepsilon_{\text{sys}}(E_{\text{rec}})$ is obtained by computing the relative mean difference between the reweighted and nominal NCQE neutrino and antineutrino spectra for combined ($\nu + \overline{\nu}$), after applying the third reduction,

$$\varepsilon_{\text{sys}}(E_{\text{rec}}) = \frac{S_{\nu+\overline{\nu}}(E_{\text{rec}}) - S'_{\nu+\overline{\nu}}(E_{\text{rec}})}{S_{\nu+\overline{\nu}}(E_{\text{rec}})}. \tag{8.4}$$

Figure 8.4 shows $\varepsilon_{\text{sys}}(E_{\text{rec}})$ as a function of reconstructed energy and neutron tagging scores. In the SK-IV DSNB analysis, a neutron tagging algorithm based on a Boosted Decision Tree (BDT) was utilised to identify delayed neutron captures on hydrogen (refer to Ref. [47] for further details). The systematic uncertainties are a smooth function of energy, particularly in the lower energy region. In the SK-IV analysis, the final systematic uncertainties were set to 30% – 60% for each 2 MeV bin.

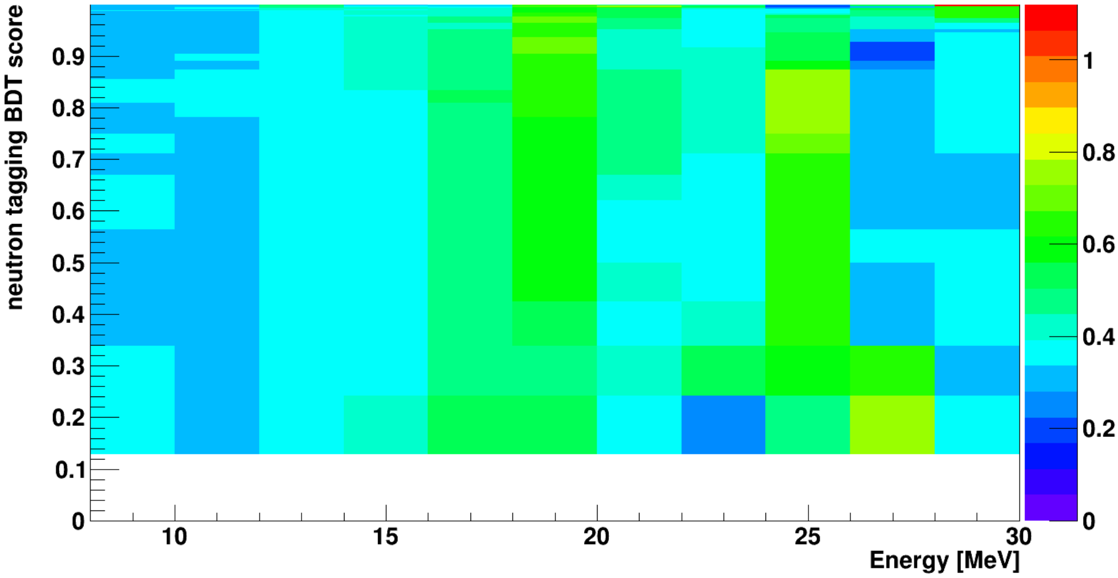

Figure 8.4: The reconstructed energy as a function of neutron tagging BDT score in the NCQE atmospheric MC in the SK-IV DSNB analysis. The colour bar of the histogram represents the NCQE spectral shape uncertainties $\varepsilon_{\text{sys}}(E_{\text{rec}})$ per 2 MeV bin width.

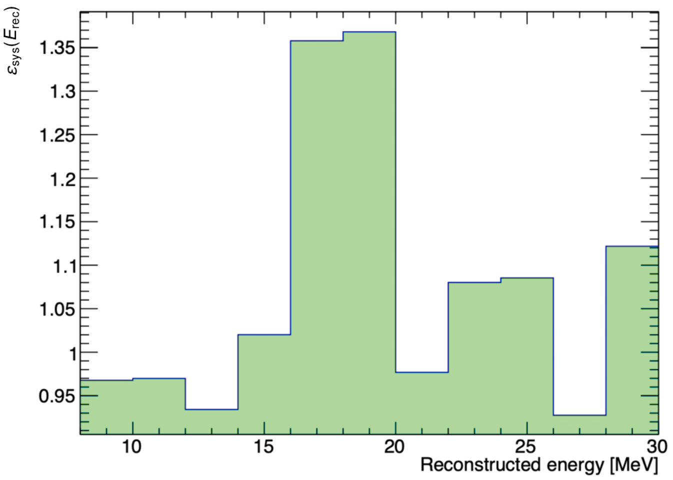

Figure 8.5: The spectrum shape uncertainty $\varepsilon_{\text{sys}}(E_{\text{rec}})$ as a function of reconstructed energy. This figure is adapted from Ref. [152].

Systematic Uncertainty in SK-VI

Figure 8.5 shows the distribution of the systematic uncertainties $\varepsilon_{\text{sys}}(E_{\text{rec}})$ as a function of reconstructed energy in the SK-VI analysis. The final systematic uncertainty was determined by selecting the largest value of $\varepsilon_{\text{sys}}(E_{\text{rec}})$, and thus set to 37%.

8.1.4 Neutron Multiplicity Uncertainty

This analysis relies on neutron tagging, which has two main sources of systematic uncertainty: the neutron tagging efficiency (see Section 7.5.3) and neutron multiplicity. The model uncertainty impacting the neutron multiplicity is estimated using measurements of CC-dominant samples from the T2K beam [167]. Figure 8.6 shows the average multiplicity of neutrons tagged as a function of the reconstructed four-momentum Q^2 for neutrino mode (FHC), and antineutrino mode (RHC). The ratio (R_{mult}) of the number of observations (N_{obs}) to the simulated predictions (N_{pred}) for each Q^2 region is defined as

$$R_{\text{mult}} = \frac{N_{\text{obs}}}{N_{\text{pred}}} = \frac{N_{\text{obs}}^{\text{FHC}} + N_{\text{obs}}^{\text{RHC}}}{N_{\text{pred}}^{\text{FHC}} + N_{\text{pred}}^{\text{RHC}}}, \tag{8.5}$$

which are summarised in Table 8.1. These values are used to renormalise the neutron multiplicity from the atmospheric neutrino MC following the procedure

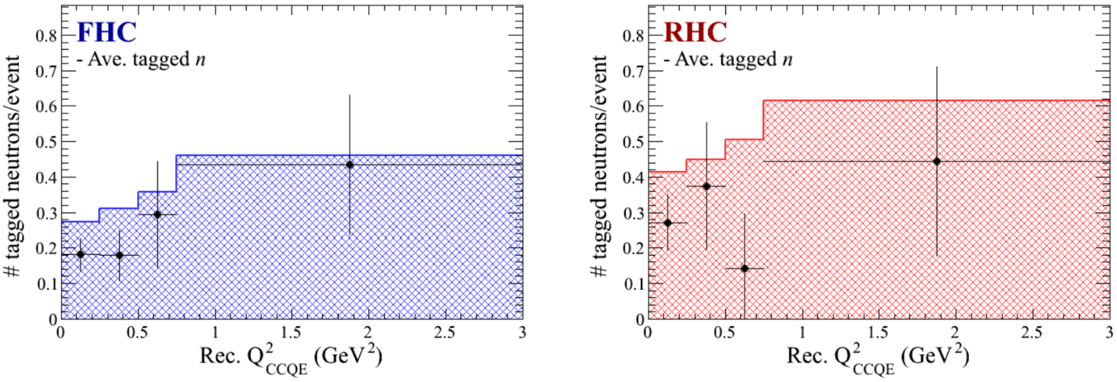

Figure 8.6: The average tagged neutron multiplicity as a function of the reconstructed Q^2 in the T2K CC-dominant dataset for FHC (left) and RHC (right). These figures are taken from Ref. [167].

$\mathbf{Q^2}$ **Range (GeV^2)**	$R_{\mathbf{mult}}$
0.00 - 0.25	0.65
0.25 - 0.50	0.72
0.50 - 0.75	0.51
0.75 - 3.00	0.82

Table 8.1: The ratio R_{mult} defined in Equation 8.5 for each Q^2 region.

outlined in Ref. [152]. The maximum variance in the bin corresponding to exactly one tagged neutron in all Q^2 regions is assigned as the systematic uncertainty. This was determined to be 30% for both neutrinos and antineutrinos in the SK-VI DSNB analysis.

8.1.5 Total Uncertainty

Table 8.2 provides a breakdown of systematic uncertainties for atmospheric NCQE interactions. Since these errors are mutually exclusive, the total systematic uncertainty is derived by summing the individual uncertainties in quadrature, resulting in a 68% uncertainty assigned in this analysis. Additional systematics associated with integrating an ML technique into the analysis, currently under development, are discussed in Section 6.6.

T2K cross section	44%
Atmospheric neutrino flux	15%
Flux difference	7%
First and third reductions	2%
Neutron tagging efficiency	9%
Neutron multiplicity	30%
Softmax reduction	10%
Spectral shape	37%
Total	68%

Table 8.2: The systematic uncertainties for the atmospheric NCQE interaction.

8.2 Atmospheric non-NCQE Interactions

Atmospheric CC and NC interactions, resulting in the production of electrons and positrons via the decay of invisible muons and pions, form a substantial background in the analysis. The systematic uncertainty associated with the spectrum shape is minimal, as it closely resembles the Michel electron spectrum derived from the stopped cosmic muon sample in SK. Therefore, the main uncertainty in non-NCQE interactions comes from the total number of predicted background events, which affects the scaling of the final distribution.

The total number of non-NCQE events is estimated by fitting the MC spectra to the data in the sideband region of $E_{\text{rec}} \in [29.49, 79.49]$ MeV before neutron tagging is applied. The minimum χ^2 from this fitting process is calculated as 0.846, which is then used to rescale the non-NCQE background [152]. The energy spectrum for both the data and MC, before and after scaling, is illustrated in Figure 8.7. The uncertainty due to statistical fluctuations associated with the number of events is found to be 17% within 1σ. The total uncertainty, considering errors from neutron tagging and neutron multiplicity, is estimated to be 36%.

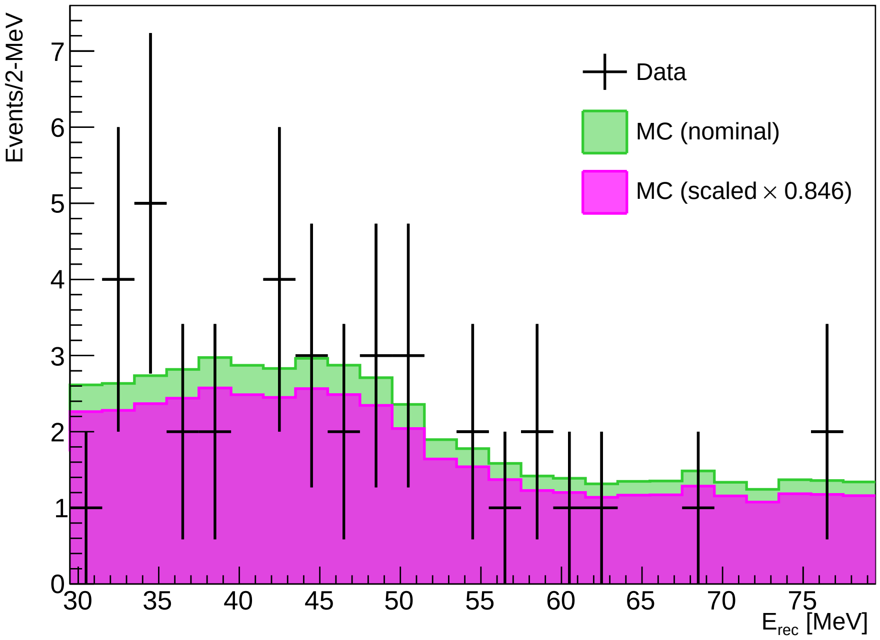

Figure 8.7: The reconstructed energy distribution in the sideband region $E_{\text{rec}} \in [29.49, 79.49]$ MeV for data (black), the nominal (green), and the scaled (magenta) atmospheric neutrino MC.

8.3 Lithium-9

The number of ^{9}Li events remaining after the event selection process ($B_{^9\text{Li}}$) is estimated as

$$B_{^9\text{Li}} = R_{^9\text{Li}} \times T_{\text{live}} \times 22.5\ \text{kton} \times \text{Br}[^9\text{Li} \to \beta^+ + n] \times f_{\text{window}} \times \varepsilon_{\text{reduc}}, \tag{8.6}$$

where $R_{^9\text{Li}}$ is the ^{9}Li production rate from spallation in SK, T_{live} is the livetime of the experimental run (552.2 days for SK-VI), $\text{Br}[^9\text{Li} \to \beta^+ + n] = 0.508$ is the branching ratio for $\beta + n$ decay, f_{window} is the fraction of the ^{9}Li decay above the DSNB search energy threshold, and $\varepsilon_{\text{reduc}}$ is the reduction efficiency.

The systematic uncertainty on the ^{9}Li spectrum due to the production rate $R_{^9\text{Li}}$ (0.86 ± 0.12 (stat.) ± 0.15 (syst.) $\text{kton}^{-1} \cdot \text{day}^{-1}$) is set to 22%, based on the previous SK analysis [168]. There are potential systematic uncertainties in the ^{9}Li efficiency due to the assumption that spallation isotopes differ only in their lifetimes. Specifically, this analysis assumes that the *dt* parameter is the only isotope-dependent spallation observable, which cannot be verified without an official SK simulation of muon spallation. Hence, a 50% systematic uncertainty is set as a conservative estimate to account for possible effects from other spallation observables. In addition, another source of uncertainty comes from the neutron tagging reduction efficiency, which accounts for $\sim$10%. The total uncertainty assigned for the $B_{^9\mathrm{Li}}$ is therefore set to be 55% by adding the relevant contributions in quadrature.

8.4 Reactor Neutrinos

The background spectrum from reactor neutrinos is estimated by reweighting the IBD signal MC, as outlined in Section 5.2.3. In this analysis, a systematic uncertainty of 100% is assigned to the reactor neutrino background, considering its contribution as an irreducible background. However, the impact of this uncertainty on the final result is minimal, given that the flux only affects the spectrum up to 10 MeV.

8.5 Accidental Coincidences

The accidental coincidence background (B_{acc}) is estimated by rescaling the number of events in data remaining after the first, spallation, and third reduction cuts ($N^{\mathrm{data}}_{\mathrm{pre\text{-}ntag}}$) by the neutron misidentification rate ($\varepsilon_{\mathrm{mis}}$), defined as,

$$B_{\mathrm{acc}} = \varepsilon_{\mathrm{mis}} \times N^{\mathrm{data}}_{\mathrm{pre\text{-}ntag}} \tag{8.7}$$

The $\varepsilon_{\mathrm{mis}}$ varies as a function of time depending on the PMT gain and dark noise. In this analysis, the systematic uncertainty is set at 5%, based on the evaluation of $\varepsilon_{\mathrm{mis}}$ in Ref. [152].

8.6 Expected Background Spectrum

The expected background spectra for the NCQE-only and all background sources are presented in this section.

8.6.1 NCQE Background Spectra

Figure 8.8 shows the expected atmospheric NCQE background spectra for the SK-VI DSNB analyses from Ref. [42], and the work presented in this thesis. The incorporation of a combined Cherenkov angle and softmax cut enhances NCQE background rejection across the spectrum. In particular, reductions of 40% and 60% are observed in the first two energy bins, respectively, demonstrating the effectiveness of integrating an ML technique into the analysis.

8.6.2 Final Background Spectra

Figure 8.9 presents the expected background spectrum after the event selection for the SK-VI livetime. The distribution is displayed in terms of 2 MeV bin widths (Figure 8.9a) and partially merged bins with widths 7.49 - 9.49 MeV, 9.49 - 11.49 MeV, 11.49 - 15.49 MeV, 15.49 - 23.49 MeV, and 23.49 - 29.49 MeV (Figure 8.9b). These specific bin widths are chosen to account for low statistics of the SK-VI period. The reactor neutrino background populates a fraction of the lowest energy bin in the spectrum. Up to 20 MeV, the background contribution is dominated by the ^{9}Li and the atmospheric NCQE spectra. The main background source in the final energy bins comes from the atmospheric non-NCQE backgrounds. The estimated background contributions with systematic errors for each merged energy bin are shown in Table 8.3.

E_{rec} **[MeV]**	**7.49 - 9.49**	**9.49 - 11.49**	**11.49 - 15.49**	**15.49 - 23.49**	**23.49 - 29.49**
non-NCQE	0.18 ± 0.07	0.13 ± 0.05	0.19 ± 0.07	0.55 ± 0.20	0.77 ± 0.28
NCQE	1.12 ± 0.00	0.48 ± 1.08	0.27 ± 0.46	0.10 ± 0.26	0.01 ± 0.09
^{9}Li	3.09 ± 1.70	1.20 ± 0.66	0.19 ± 0.10	0.00 ± 0.00	0.00 ± 0.00
Reactor	0.14 ± 0.14	0.00 ± 0.00	0.00 ± 0.00	0.00 ± 0.00	0.00 ± 0.00
Accidental	1.16 ± 0.06	0.59 ± 0.03	0.24 ± 0.01	0.00 ± 0.00	0.00 ± 0.00
Total	5.70 ± 1.80	2.40 ± 0.70	0.89 ± 0.18	0.65 ± 0.20	0.79 ± 0.28

Table 8.3: Summary of the expected background events with systematic uncertainties for this SK-VI DSNB analysis.

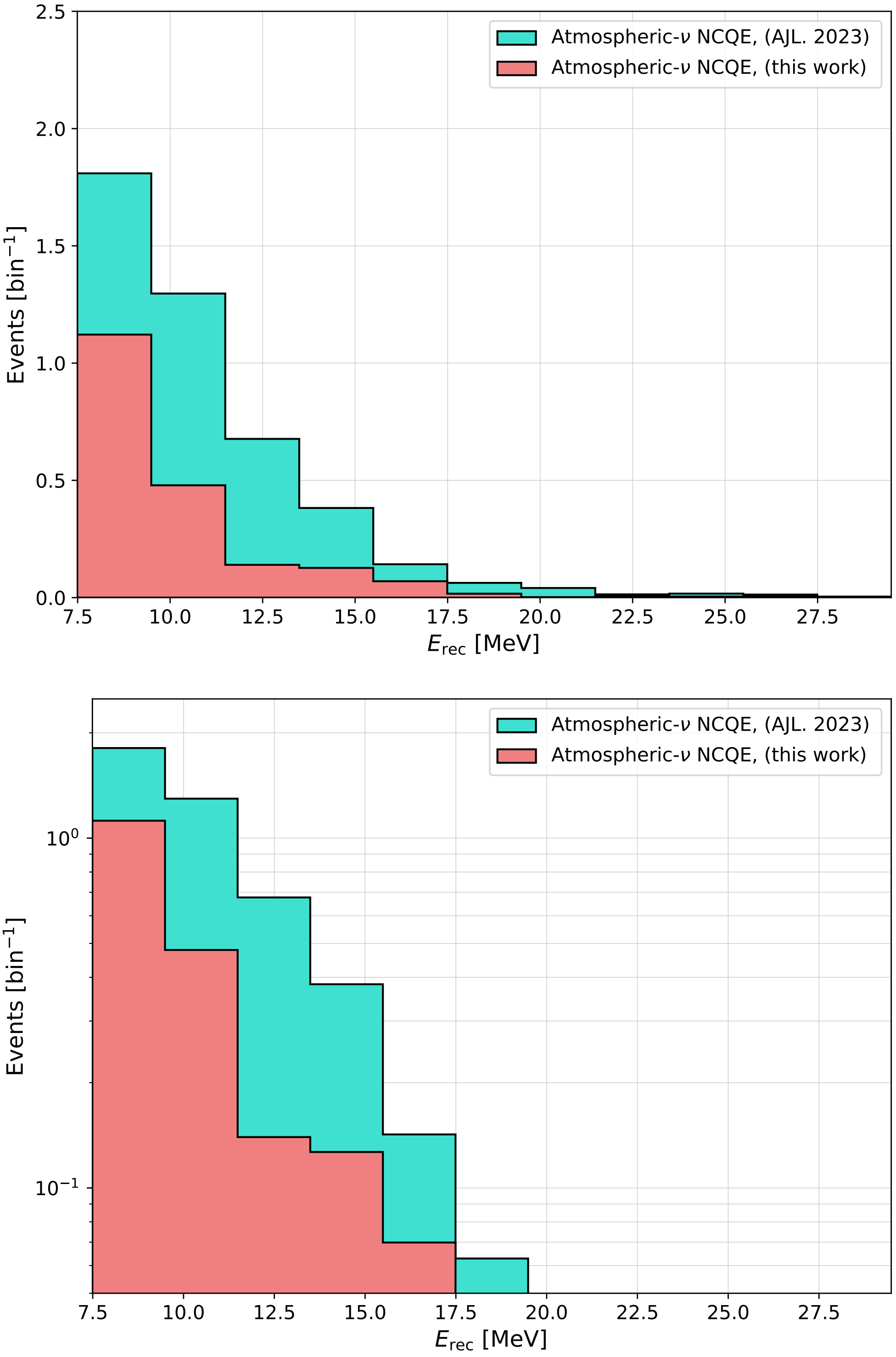

Figure 8.8: Expected NCQE background spectrum as a function of the reconstructed kinetic energy E_{rec} for the SK-VI DSNB analyses. The most recent published result from Ref. [42] (turquoise) and the result presented in this thesis (coral) are shown. The distributions are plotted in terms of a linear scale (upper) and a log scale (lower).

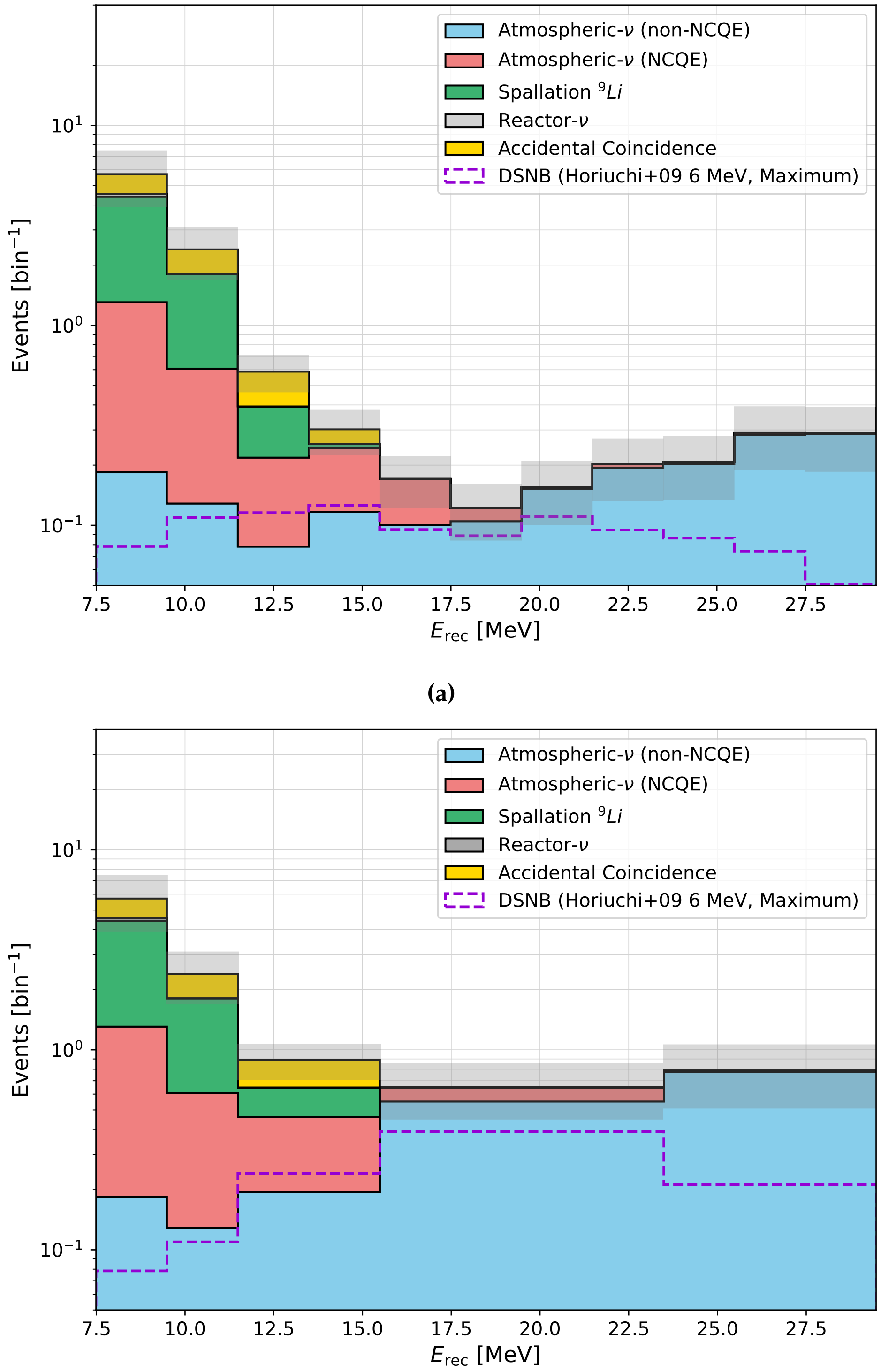

(a)

(b)

Figure 8.9: Expected background spectrum versus reconstructed kinetic energy $E_{\rm rec}$ for 2 MeV bin widths (top) and partially merged bins (bottom). Colour-filled histograms represent different background sources, with grey shaded bars indicating systematic uncertainties per energy bin. The purple dashed line shows the DSNB signal expectation from the Horiuchi+09 model [37].

9

The DSNB Analysis Results

9.1 Search Result

The event selection criteria were applied to the entire dataset from the SK-VI run period, which consisted of a total live time of 552.2 days. Table 9.1 provides a summary of the final selection following each reduction step. The final sample contains six events within the DSNB signal region. The observed spectrum and the expected background spectrum are presented in Figure 9.1.

Energy [MeV]	**7.49 - 9.49**	**9.49 - 11.49**	**11.49 - 15.49**	**15.49 - 23.49**	**23.49 - 29.49**
First reduction	204328	58993	18292	630	54
Spallation cut	13297	5773	1982	115	47
d_{eff} cut	9554	4603	1628	101	47
$N_{\mathrm{pre}}^{\mathrm{max}}$	9494	4579	1613	96	43
$N_{\mathrm{decay-e}}$	9466	4560	1593	56	14
$\mathcal{R}_\pi$	8714	4291	1541	41	8
$q50n50$ cut	8713	4288	1539	35	6
θ_C cut	5812	2927	1204	21	3
N-tagging	5	5	3	2	0
Softmax cut	1	1	3	1	0

Table 9.1: Summary of the final sample and the signal yields for each merged bin in this SK-VI DSNB analysis.

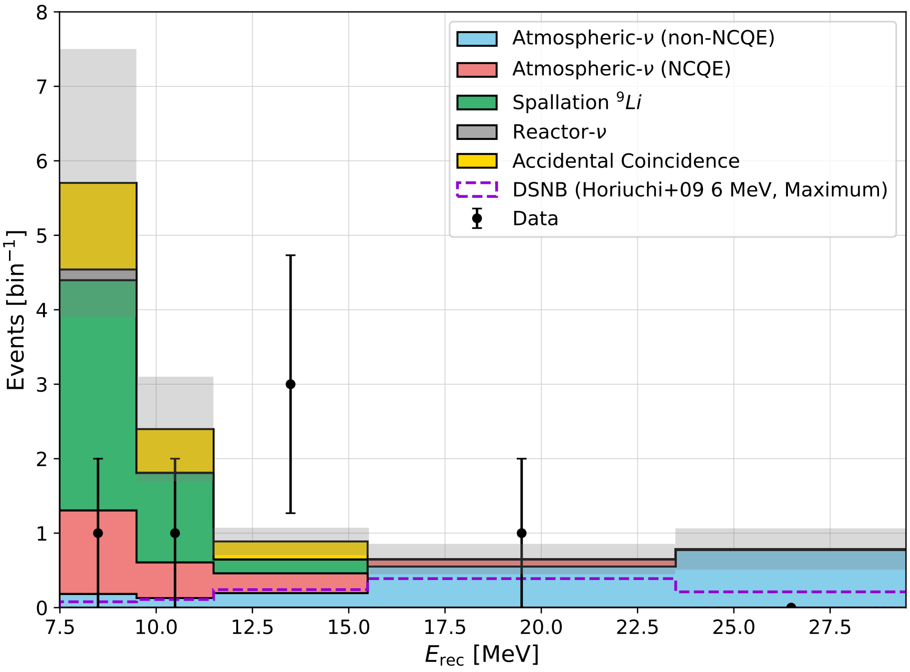

(a)

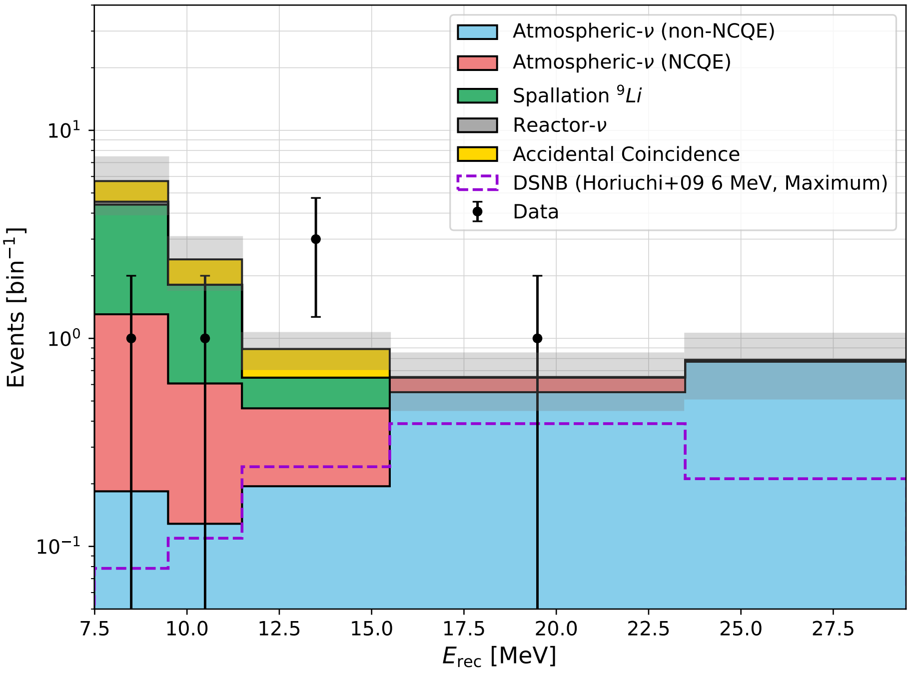

(b)

Figure 9.1: Observed (data points) and expected background spectra versus reconstructed kinetic energy E_{rec}. Colour-filled histograms represent each background, with grey-shaded boxes representing systematic uncertainties per energy bin. Statistical errors are shown as error bars on the data points. The purple dashed line represents the DSNB signal expectation from the Horiuchi+09 model [37]. Distributions are plotted on linear (top) and logarithmic (bottom) scales.

To assess the significance of the observed events (N_{obs}) compared to the expected background events (N_{exp}), a p-value is calculated for each bin. The p-value determines the probability of detecting the number of events observed given the assumption that the background estimate is correct. This is calculated for each energy bin by performing the following pseudo-experiments:

1. **Estimate the expected background**: The expected background distribution is estimated using a Gaussian, with the mean value set as the expected mean and the width set to the 1σ systematic uncertainties from each background.
2. **Generate events**: The number of events expected in each energy bin is generated using a Poisson distribution, with the above mean.
3. **Toy MC**: The previous step is repeated one million times, where each iteration of generating events is referred to as a toy MC.
4. **Count events**: For each bin, the number of toy MC runs is counted when the number of generated events exceeds the number of observed events.
5. **Calculate p-value**: The p-value is calculated as the fraction of toy MC instances where the number of generated events exceeds the observed events, divided by the total number of generated toy MC instances.

Figure 9.2 shows the p-value results from the toy MC for each energy bin. The results are summarised in Table 9.2. This concludes that no significant excess is observed in the data over the expected background distribution as the p-value exceeds 5% for all energy bins.

Energy Bin	p-value [%]
7.49 - 9.49	98.47
9.49 - 11.49	88.40
11.49 - 15.49	6.44
15.49 - 23.49	46.83
23.49 - 29.49	100
29.49 - 79.49	71.94

Table 9.2: The corresponding p-values for different energy bins.

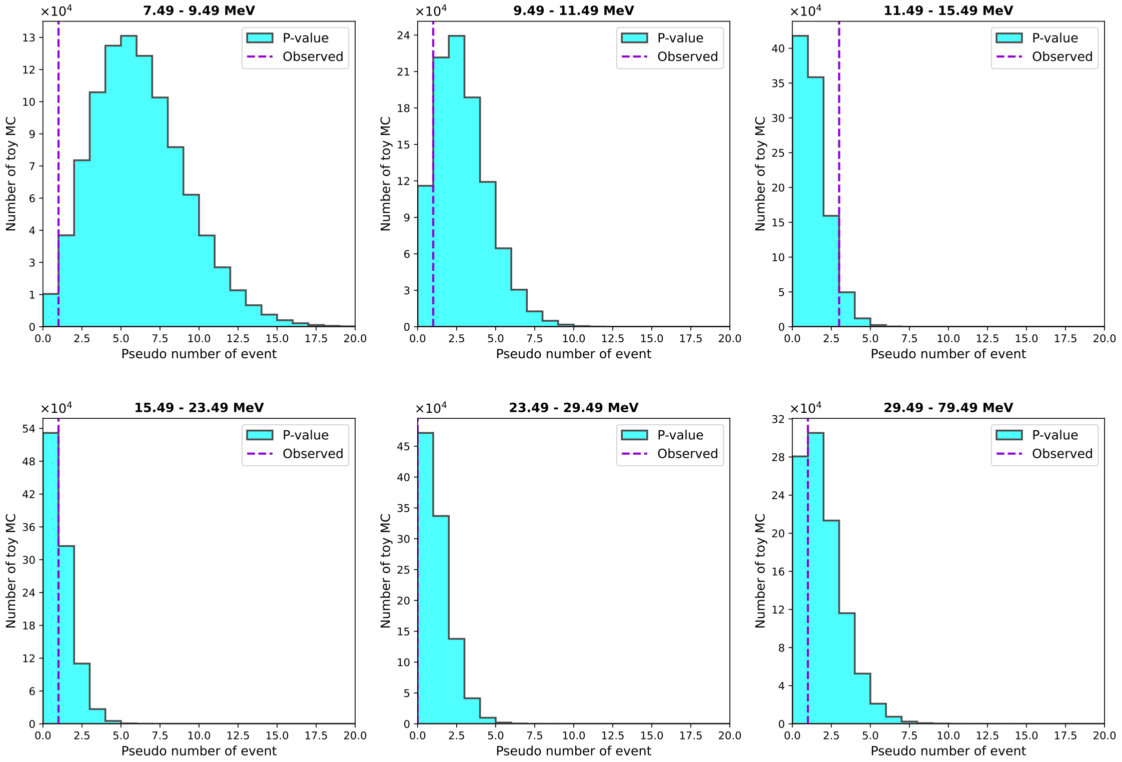

Figure 9.2: The p-value distributions across all energy bins, including data sideband regions. The purple dashed line shows the number of observed events in data for each bin.

9.2 Upper Limit Extraction

The upper limit of the $\overline{\nu}_e$ flux in excess over the background expectation at the 90% confidence level (C.L.) is calculated via the following pseudo-experiments:

1. **Observed and expected events**: The N_{obs} and N_{bkg} events are calculated for a toy dataset. Random variations of statistical errors on N_{obs} and systematic errors on N_{bkg} are taken into account by modelling them with a Gaussian distribution.

2. **Signal events**: The number of signal events in excess N_{sig} is calculated as $N_{\text{sig}} = N_{\text{obs}} - N_{\text{bkg}}$ for the toy dataset.

3. **Generate events**: The above steps are repeated for one million iterations to generate a new set of N_{obs} and N_{bkg} events using the Gaussian distribution. From this, the number of signal events for each iteration is calculated to make a distribution of N_{sig}.

4. **Upper limit**: The upper limit on the number of signal events N_{90}^{limit} is calculated by integrating the N_{sig} distribution and determining the value that contains 90% of the integrated distribution above zero. Figure 9.3 shows an example of the pseudo-experiments for the 9.49 - 11.49 MeV bin.

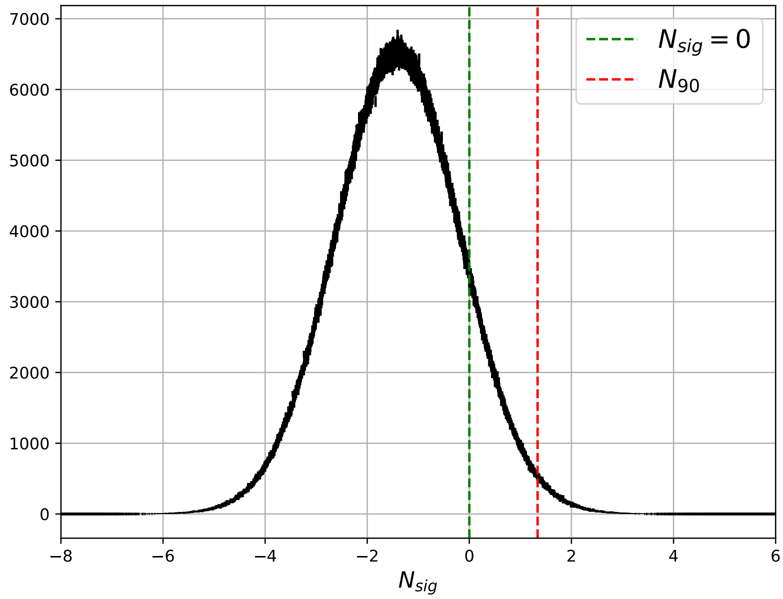

Figure 9.3: The N_{sig} distribution for the $E_{\text{rec}} \in [9.49, 11.49]$ MeV bin calculated from the pseudo-experiments. The zero line (green dashed) and the N_{90}^{limit} line (red dashed) are shown. The region between zero and N_{90}^{limit} determines the upper limit in the energy bin.

Finally, the 90% C.L. $\overline{\nu}_e$ flux upper limit (ϕ_{90}^{limit}) is calculated as

$$\phi_{90}^{\text{limit}} = \frac{N_{90}^{\text{limit}}}{\overline{\sigma}_{\text{IBD}} \cdot N_p \cdot T \cdot \varepsilon_{\text{sig}}}, \tag{9.1}$$

where $\overline{\sigma}_{\text{IBD}}$ is the IBD interaction cross-section [10^{-41} cm^2] for the average neutrino energy in the energy region, N_{p} is the number of free protons in SK, T is the SK-VI livetime [552.2 days], and ε_{sig} is the signal efficiency (see Figure 7.25). The neutrino energy is obtained as $E_\nu = E_{\text{rec}} + 1.8$ MeV for IBD interactions. The expected sensitivity (ϕ_{90}^{exp}) is determined using the same procedure, replacing N_{obs} with the number of nominal background events (see Table 8.3) in the calculation of N_{90}^{limit}.

Figure 9.4 shows the observed and expected $\overline{\nu}_e$ flux upper limits, including results from previous analyses, other experimental searches, and the theoretical flux predictions. These results are summarised in Table 9.3.

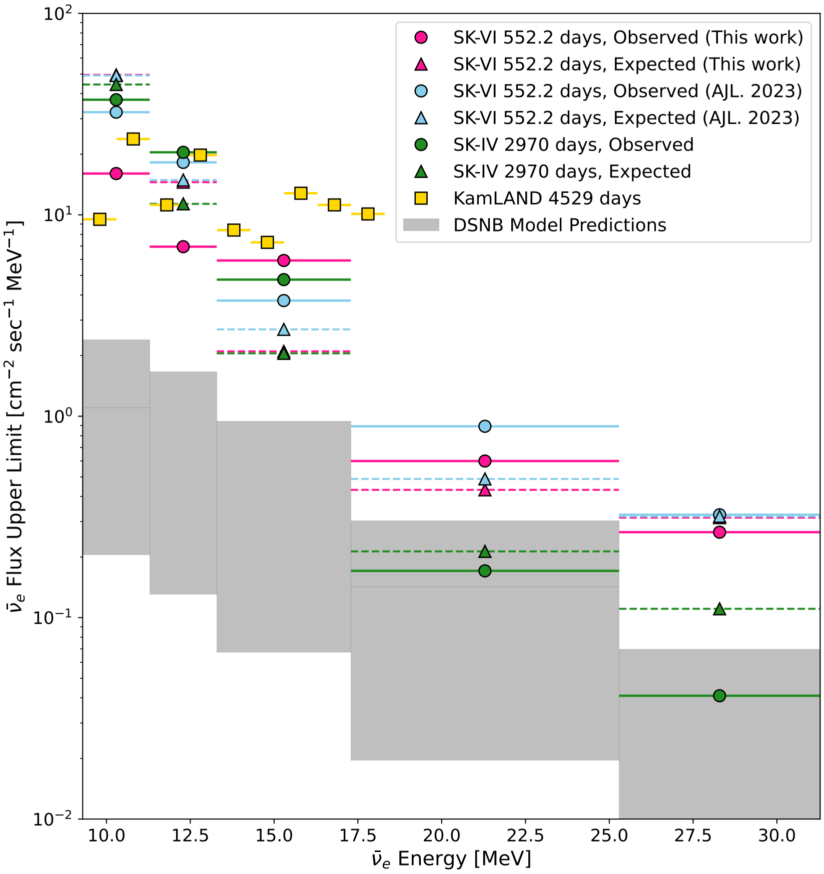

Figure 9.4: The observed and expected $\overline{\nu}_e$ flux upper limits at 90% C.L. with 552.2 days of data from the SK-VI operational period from this thesis's work (pink), the SK-VI previous result (blue) [42], the SK-IV previous result [47], and the KamLAND result [46]. The grey-shaded region shows the range for modern theoretical DSNB flux predictions [29, 30, 33–36, 38–41, 169, 170].

E_ν [MeV]	9.29 – 11.29	11.29 – 13.29	13.29 – 17.29	17.29 – 25.29	25.29 – 31.29
Live time T	552.2 days				
Protons N_p	1.5×10^{33} protons				
N_{90}^limit	1.59	1.34	4.46	1.90	1.29
N_{90}^exp	4.915	2.795	1.579	1.369	1.527
ϕ_{90}^limit	16.03	6.95	5.93	0.60	0.27
ϕ_{90}^exp	49.53	14.53	2.10	0.43	0.31

Table 9.3: Summary of the observed and expected $\overline{\nu}_e$ flux upper limits at 90% C.L. for this SK-VI DSNB analysis.

9.3 Discussion

The results demonstrate a promising reduction in the overall NCQE background spectrum with the initial implementation of the ML cut. In Figure 9.4, improvements in the last three bins of the expected upper limits are evident compared to the previous SK-VI analysis. However, further optimisation is necessary, particularly as the GAPNet model exhibits lower effectiveness in discriminating NCQE background from the signal in the 8 - 12 MeV region. Additionally, a comprehensive treatment of CNN-related systematic uncertainties is required to fully assess the impact of model dependence in the training procedure. Nevertheless, the software tools developed in this thesis will facilitate ongoing refinement of this technique for future SK DSNB analyses.

New traditional reconstruction cuts are currently under development in a separate SK-VI DSNB analysis, which has also shown promising results. Therefore, combining both of these efforts may be interesting to further target the background. The next phase of the SK experiment is currently underway, featuring additional Gd loaded into the detector to achieve a 75% neutron capture fraction on Gd. Work is ongoing to enhance the neutron tagging algorithm, address NCQE systematic uncertainties, and develop muon spallation simulations to improve the analysis.

Part II

Design Optimisation and Precision Measurements of Photosensors for the Hyper-Kamiokande Outer Detector

10

The Hyper-Kamiokande Experiment

Hyper-Kamiokande (HK) will be the next-generation water Cherenkov experiment that will leverage the high-intensity neutrino beam from J-PARC to host a vastly diverse physics program. Physics targets include constraining neutrino oscillation parameters to unprecedented precision, probing the mass-ordering, and measuring CP-violating phases in the leptonic sector [171].

This chapter provides a brief overview of the key components of the detector design relevant to this thesis. Following this, the results of the photosensor optimisation study, developed by the author, are presented.

10.1 Detector Design

HK foresees the construction of an ultra-pure water tank, 71 m in height and 68 m in diameter, with a 188 kton fiducial mass to provide an effective volume 8.4 times larger than the SK detector [172]. The detector will be deployed at the Tochibora site in Japan with a rock overburden of 650 m. Figure 10.1 shows a schematic diagram of the detector setup. The PMT support structure will optically separate the tank into regions containing the inner detector (ID) and the outer detector (OD) similar to the well-established design of SK. The ID will contain an inward-facing array of 20,000 box-and-line 20-inch PMTs that deliver competitive

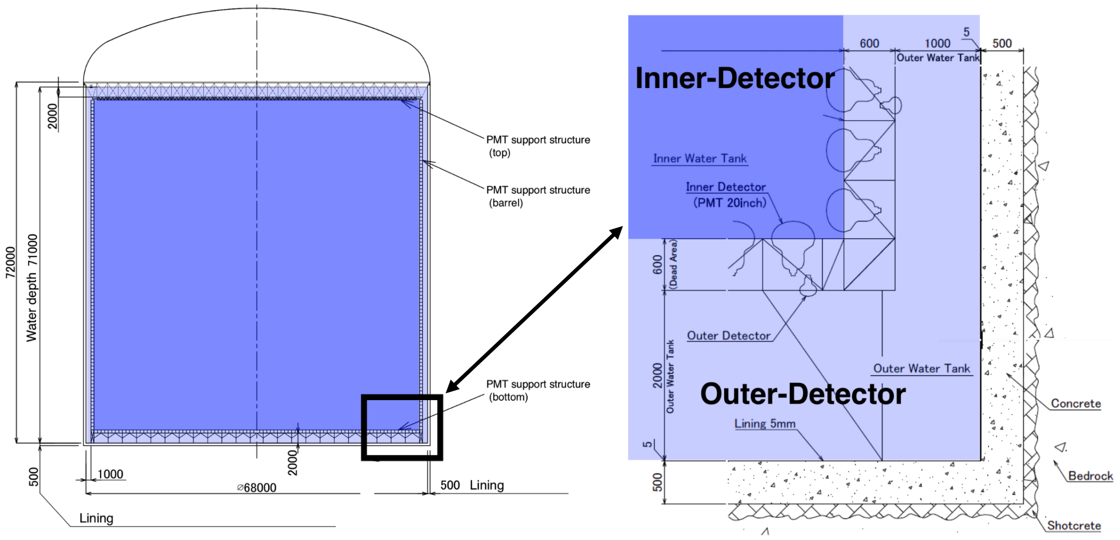

Figure 10.1: Schematic diagram of the Hyper-Kamiokande experiment. This figure is adapted from Ref. [175].

timing and charge resolution whilst doubling the photon-detection efficiency of SK PMTs [173]. In addition, ∼1000 multi-PMTs each housing nineteen 3-inch PMTs will be instrumented in the ID for improved segmentation [174].

10.2 The Outer Detector

This section covers the full design, photosensor unit specifications, and performance requirements of the OD.

10.2.1 Design

The HK-OD is the cylindrical water volume that will surround the ID and PMT support structure. The barrel and endcaps will have a 1 m and 2 m water thickness, respectively, as illustrated in Figures 10.1 and 10.2. These regions will be instrumented with up to 10,000 photosensor units, each consisting of a 3-inch (8 cm) PMT coupled to a wavelength-shifting (WLS) plate. The design optimisation has been further investigated in this thesis's work (see Section 10.3).

PMT testing of Hamamatsu and NNVT models is currently underway to select the best unit with a minimum gain of 3×10^6 at operating voltages ranging from 900 - 1500 V [176]. Additional performance requirements include maintaining a

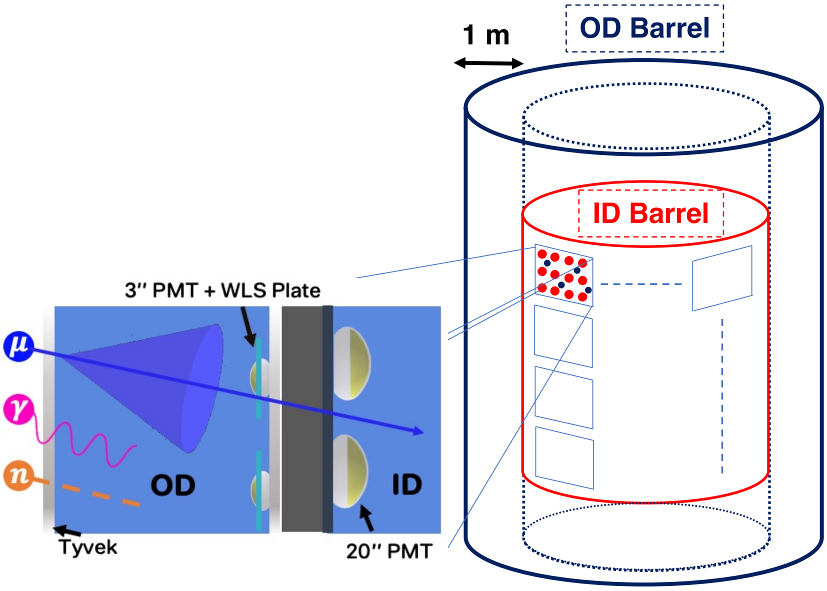

Figure 10.2: Schematic diagram of the Hyper-Kamiokande design structure. The inner (red) and outer (blue) detector regions are shown as well as a segment of the PMT support structure.

dark rate below 1 kHz above a threshold of 0.25 p.e. at an operating temperature of 20°C. Electronics and cabling modules will provide HV power to the PMTs and readout signals. The electronics design will incorporate a combination of dedicated ID and hybrid ID+OD integrated vessels to optimise PMT readout and reduce infrastructure costs. In the OD, PMT arrangement with interleaving will be utilised to minimise cable lengths and mitigate the impact of dead channels in the event of an electronics module failure. The specific design will be adjusted according to the final number of photosensor units.

The inner and outer surfaces of the OD volume will be covered with highly reflective 1082D multi-layered Tyvek material[1]. Tyvek is advantageous for maximising light collection in the OD due to its excellent diffuse reflectivity properties. Recent measurements have demonstrated that 1082D multi-layered Tyvek can provide up to ∼90% reflectivity between 350 - 700 nm [177]. The non-uniformity of the internal detector structure, which includes cables, water pipes, and PMT supporting struts, is expected to result in a slightly lower overall reflectivity to between 70 - 80% [178].

---

[1] Tyvek is made from high-density polyethylene fibres, trademarked by DuPont.

10.2.2 Photosensor Unit

The photosensor unit consists of a 3-inch hemispherical PMT coupled to a 30 × 30 × 0.6 cm WLS plate [179], as depicted in Figure 10.3. Simulations performed in the Water Cherenkov Simulator (WCSim) demonstrated that increasing the plate size beyond 30 cm did not result in a significant gain in efficiency [179]. The selection of a 0.6 cm plate thickness was determined through a series of LED measurements and simulations that evaluated the light yield of plates with varying thicknesses. These studies highlighted that shadowing effects become more pronounced with increasing plate thickness [179]. In this work, precision measurements of WLS plates have been carried out to optimise the final selection of the WLS plastic (refer to Chapters 11 and 12).

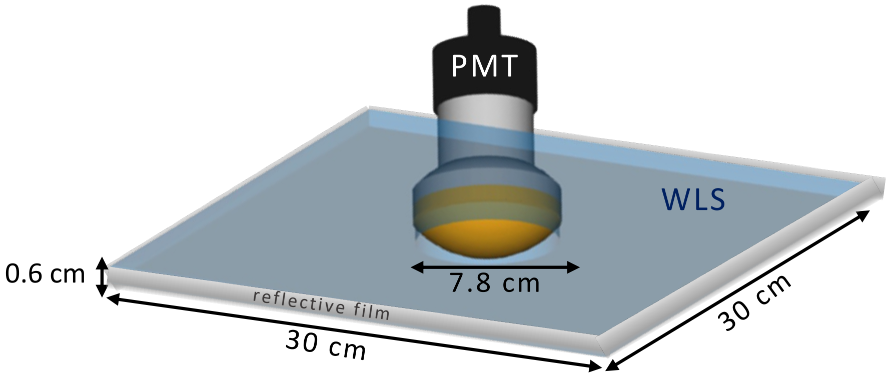

Figure 10.3: Schematic diagram of the HK-OD photosensor unit.

The PMT is positioned in the centre of the WLS plate through a cylindrical hole. This simple hole design was shown to increase the light collection by ∼20% compared to other geometrical configurations [180]. The sides of the WLS plate are covered in 3M DF2000MA polymeric film to maximise internal reflections at the plate edges. This reflector demonstrated a twofold increase in the light yield relative to Tyvek-based edge reflectors and approximately a 50% enhancement compared to a Mylar reflector [180].

The PMT and WLS plate is secured in an injection-moulded mounting structure, as shown in Figure 10.4. This assembly holds both photosensor components together as a single unit, which is then attached to the PMT support structure in

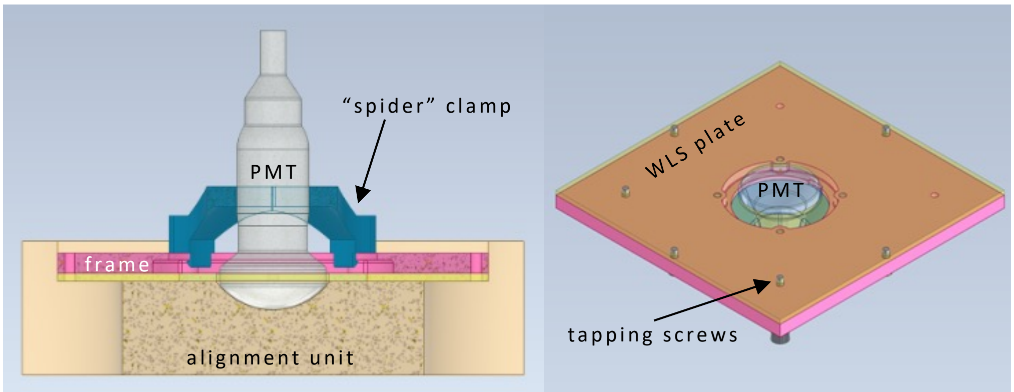

Figure 10.4: Computer Automated Design (CAD) diagram of the mounting structure viewed from above (left) and below (right). This figure is taken from Ref. [176].

the detector. The adjustable "spider" clamp and the surrounding frame ensure that the PMT's photocathode is mounted at the correct height relative to the WLS plate. Plastic tapping screws are incorporated into the design to fasten the WLS plate to the frame. A sheet of multi-layered Tyvek will be mounted behind the plate to prevent photons from passing through to the PMT support structure. The final design of the unit is currently under final optimisation, installation, and implosion tests.

10.2.3 Performance Requirements

This section summarises the key performance requirements and target backgrounds for the HK-OD:

- **Cosmic muon flux**: The cosmic ray muon flux at the HK site is expected to reach $\sim$45 Hz, equivalent to approximately four million muons per day [181]. This surpasses the muon flux observed by the SK detector by about 20 times, mainly due to the larger effective volume and shallower depth of the HK detector. Therefore, the HK-OD must achieve a high target veto efficiency of 99.99% to outperform the SK-OD. This level of efficiency will ensure that the detector misses fewer than one in a million muons per day.
- **Spallation backgrounds**: Muon spallation events dominate the background spectrum observed in low-energy analyses (see Chapter 5). In SK, dedicated

spallation cuts are implemented to identify single and multiple spallation events, which involves removing events occurring within 4 m of a muon track (see Section 7.3). To replicate this in HK, efficient muon tagging and precise determination of muon track parameters, such as entry and exit positions using OD information, will be crucial.

- **Event classification**: The OD should be robust in detecting both incoming and outgoing muons, which is necessary for categorising high-energy events in atmospheric neutrino analyses. Specifically, events are classified as Fully Contained (FC), Partially Contained (PC), or Upward-Going muons (UPMU), which are further divided into stopping and through-going muon samples. Achieving accurate energy and vertex reconstruction for these events will depend on OD triggers and the associated hit distribution.
- **Shielding**: The OD is also intended to serve as a passive shield against low-energy backgrounds, such as γ-rays or neutrons originating from natural rock radioactivity and external muon interactions.

10.3 Photosensor Configuration Optimisation

The design of the PMT arrangement has been investigated to determine whether fewer than 10,000 photosensors can maintain an effective veto capability. The photosensor layout will be selected from discrete options outlined in Table 10.1, which are determined by the PMT support and cabling designs. The final configuration must satisfy all OD performance requirements and maintain a high veto efficiency, taking into consideration the 1% predicted light loss per year from PMT failures and degradation of the Tyvek reflectivity [182]. This results in a potential loss of up to 20% in photocoverage over the projected minimum lifetime of the HK detector, which has been factored into each design option [171].

Region	**PMT Arrangement**		
	Low	**Medium**	**High**
Top endcap (edge)	200	300	400
Top endcap	750 (1/9)	1500 (2/9)	~~2250 (3/9)~~
Barrel (upper half)	1700 (1/8)	2250 (1/6)	3350 (1/4)
Barrel (lower half)	1700 (1/8)	2250 (1/6)	3350 (1/4)
Bottom endcap	750 (1/9)	1500 (2/9)	~~2250 (3/9)~~
Total	**5100**	**7800**	~~**11500**~~

Table 10.1: PMT instrumentation for each detector region, specified in terms of number of photosensors and cabling arrangement. Configurations that have been previously ruled out are shown as red deleted elements.

10.3.1 Masking PMT Channels

A data-driven optimisation study based on masking SK-OD channels has been performed to extrapolate an equivalent photocathode coverage in the HK-OD. The performance of the masked SK-OD is then evaluated in terms of the muon background remaining in the atmospheric neutrino sample after the standard event selection process. The derived scaling factor is used to evaluate the relative muon background contamination in the HK-OD for three distinct PMT arrangements. Finally, the optimal PMT arrangement based on the available options in Table 10.1 is determined.

This analysis utilises a full 24-hour trigger level data sample from SK-IV, containing mostly downward-going cosmic muons, low-energy radioactivity from radon, and atmospheric neutrinos [183]. The OD hits are masked at different levels of photocathode coverage using raw PMT cable information. Two masking methods are employed: uniform single and uniform clustered masking. This procedure aims to evaluate whether topological differences between the detector configurations affect the background rate differently for the same level of photocathode coverage. This is important to consider as the failure of an electronics module would lead to the loss of multiple clustered PMTs.

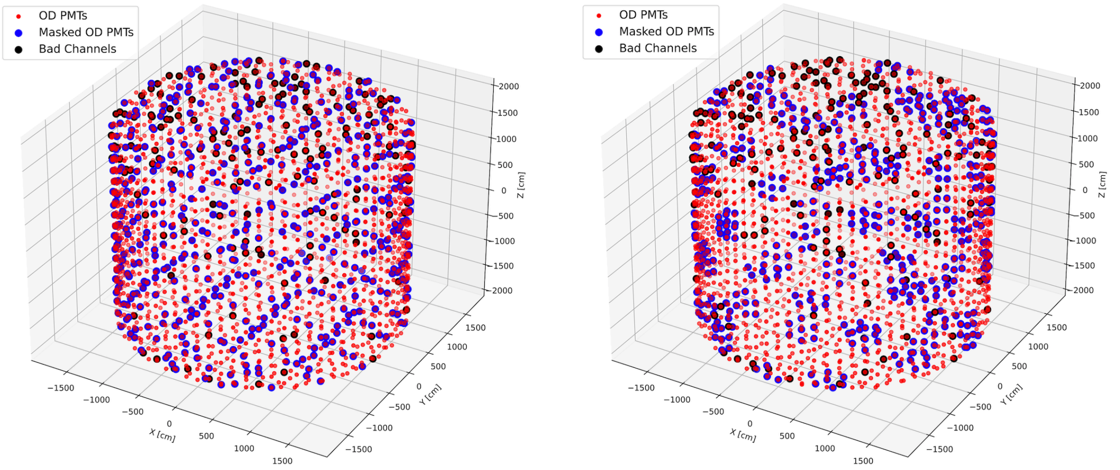

(a) **(b)**

Figure 10.5: 3D PMT maps of the OD with 25% masking for uniform single (left) and uniform clustered masking (right), which corresponds to 0.66% photocathode coverage in the SK-OD (including bad channels).

For uniform clustering, an algorithm has been developed by the author to aggregate all nearest neighbours to a selected cable, considering the detector's geometry. This process involves calculating the Euclidean distance (D) between the chosen PMT (X_0, Y_0, Z_0) and all other PMTs (X_i, Y_i, Z_i) in 3-dimensional space:

$$D = \sqrt{(X_i - X_0)^2 + (Y_i - Y_0)^2 + (Z_i - Z_0)^2}. \tag{10.1}$$

In the SK-OD, photosensors are evenly distributed with approximately 2 m separation along the same axis [48]. Therefore, adjacent PMTs within D < ∼2 m are selected for each cluster. This typically results in clusters comprising up to seven PMTs on average. The masked PMT cable list for both uniform single and clustered masking is combined with the list of 215 bad channels from this run period to generate the masked detector configuration. Figure 10.5 illustrates the masked PMT arrangement for a 25% reduction in photocathode coverage for both masking techniques.

10.3.2 PMT Hit Distributions

Events from each masking configuration are processed through the standard FC reduction used in the atmospheric neutrino analysis [183]. The initial step

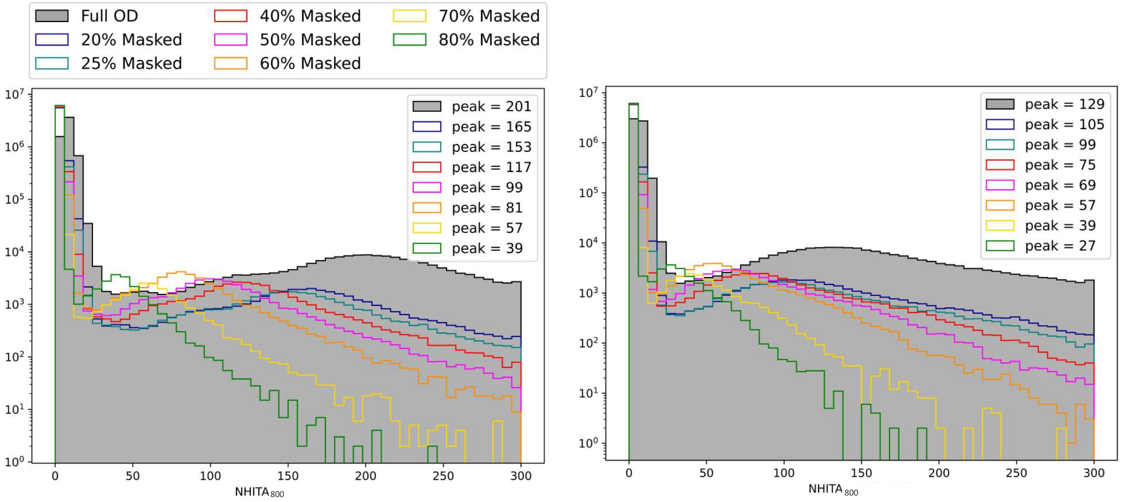

(a) All **(b)** Barrel

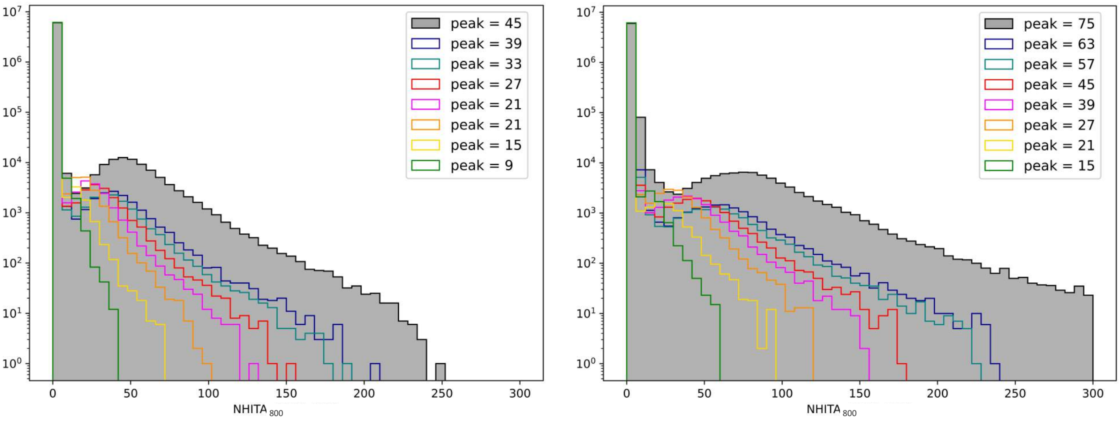

(c) Top endcap **(d)** Bottom endcap

Figure 10.6: SK-OD hit distributions within an 800 ns window around the trigger time (NHITA$_{800}$), with varying levels of uniform single masking applied, separated by detector regions.

(FC1) filters out most of the high-energy backgrounds from cosmic ray muons by applying stringent cut criteria on the charge and hit deposition in both the ID and OD. Specifically, events with more than 55 OD hits within 800 ns around the trigger time (NHITA$_{800}$) are rejected.

Figure 10.6a shows the NHITA$_{800}$ distributions for full coverage and all uniform single masking configurations across the entire detector. The full SK-OD exhibits a distinctive three-peak structure, corresponding to stopping muons, top-to-bottom, and top-to-barrel through-going muons, occurring at approximately 50, 100, and 200 hits, respectively. These features diminish when more than 25%

masking is applied, which causes the main peak to shift towards lower OD hits for decreasing photocoverage. The dominant peak in every distribution corresponds to mostly dark noise hits and low-energy γ-rays from the surrounding rock. However, Figure 10.6b shows that this peak is broader in the barrel due to corner-clipper muons that produce minor OD depositions in the top-to-barrel and bottom-to-barrel regions (see Section 7.3.2). Reconstruction becomes more challenging in these edge cases, especially if one of the OD depositions is not fully resolved due to reduced photocathode coverage.

Figure 10.6c and Figure 10.6d demonstrate that asymmetrical PMT arrangements in the top and bottom endcaps result in different hit distributions. Although muon backgrounds are predominately downward-going, the 84 bad OD channels and support structure instrumented in the top-endcap reduce the light collection. This discrepancy is further suspected to arise from the difference in water levels between the top and bottom endcaps [48]. The corresponding distributions for the uniform clustered masking scenarios showed similar behaviour for all detector regions.

10.3.3 Scaling Factor

An equivalence between the SK-OD and the HK-OD is established based on the OD hit distributions rather than photocathode coverage, as this method automatically incorporates all aspects of the detector geometry, WLS plates and Tyvek reflectivity. The HK-OD hit distribution for four PMT configurations, obtained from a full WCSim simulation with 10^5 through-going cosmic muons [182], is directly compared against the masked SK-OD distributions. All scenarios are simulated with 80% Tyvek reflectivity to reproduce the expected performance for the assumed detector condition after 20 years of operation. Instead of comparing the means, a comparison is made between the relative peak heights, as it is less sensitive to outliers and excludes muons that will be rejected by the cuts.

Table 10.2 provides a summary of the extrapolated SK-HK scaling for each detector region. This allows for the optimisation of PMT arrangement in the

	OD PMTs (WCSim)	HK-OD Peak	SK-OD Peak		SK-OD Masking	
			Singles	Clusters	Singles	Clusters
All	3.2k	80	81	69-93	60%	$\sim$ 56%
	5.0k	135	117-153	135	$\sim$ 33%	36%
	7.2k	185	165-201	189	$\sim$ 10%	7%
	10.0k	245	-	-	>full OD	>full OD
Barrel	2.2k	30	27	45	80%	$<$ 58%
	3.2k	55	57	57	60%	54%
	4.9k	80	75	81	40%	36%
	6.8k	115	105-129	111	$\sim$ 10%	13%
Top	500	30	27-33	33	$\sim$ 33%	35%
	900	55	45	45	full OD	full OD
	1.15k	77	-	-	>full OD	>full OD
	1.60k	100	-	-	>full OD	>full OD

Table 10.2: Summary of SK-HK scaling extrapolated for each detector region using peak heights obtained from WCSim simulation with aged-detector conditions (80% Tyvek reflectivity) and SK-OD hit distributions for both uniform single and uniform clustered masking configurations.

barrel and endcaps, separately. The scaling procedure indicates that a HK-OD instrumented with 7,200 PMTs is approximately equivalent to the full SK-OD. In addition, this approach correlates 700 PMTs in HK-OD to the full SK-OD top-endcap. However, this is likely underestimated as no top structure is simulated in WCSim, which has been demonstrated to reduce light collection by up to 40% in separate studies [182]. Therefore, the PMT arrangement in the top endcap should include additional photosensors as a contingency for shadowing caused by the infrastructure.

It is important to note that, in WCSim, the PMT arrangement is uniform across the detector and not interleaved according to the cabling design in Table 10.1. This, coupled with the potentially exaggerated quantum efficiency (QE) factor implemented in WCSim, may lead to an overestimation of the simulated hit collection [182]. Therefore, the extrapolated scaling only provides an estimate of the relative performance of the actual PMT configurations proposed for the HK-OD.

Figure 10.7 displays two-dimensional OD hit distributions with the FC1 cut

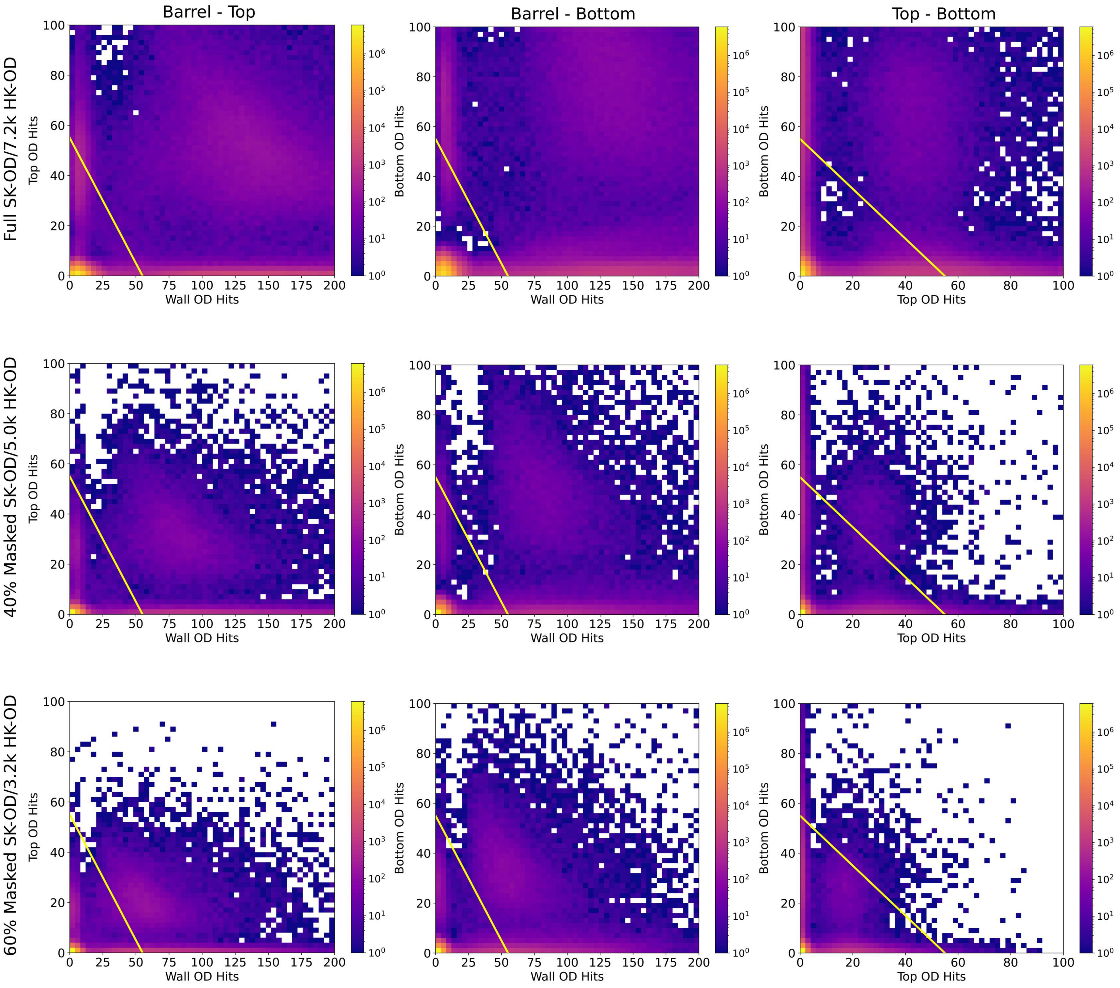

Figure 10.7: 2D SK-OD hit distributions comparing deposition across two detector regions with the FC1 cut threshold ($\mathrm{NHITA}_{800} < 55$) shown (yellow line). Columns: hits in barrel-to-top endcap (left), barrel-to-bottom endcap (centre), and top-to-bottom endcaps (right). Rows: different levels of uniform singles masking corresponding to PMT configurations in the HK-OD MC: full SK-OD/7.2k HK-OD (top), 40% masked SK-OD/5.0k HK-OD (centre), and 60% masked SK-OD/3.2k HK-OD (bottom).

applied to demonstrate the effect of masking on each region. As the photocoverage decreases, events that were previously rejected by the NHITA_{800} selection threshold tend to migrate towards the cut region, particularly for muons in the top endcap. This effect is expected to be more pronounced in the HK-OD, where hits from through-going muons are more likely to be confined to the top endcap due to the size of the detector. In addition, reducing photocoverage in the bottom endcap leads to the misclassification of through-going muons as stopping muons as the exit point of the muon cannot be fully resolved. This analysis does not take the UPMU sample[2] into consideration as there are only 1.45 ± 0.03 events per day in the SK-IV atmospheric data sample [177]. Therefore, the effect on the bottom region may be more significant when considering its impact on the UPMU sample.

10.3.4 Residual Muon Background

The number of events remaining after the FC reduction in both the uniform single and clustered masking configurations is used to assess the level of muon background contamination in the final sample. The photocathode coverage ratio (R) in the SK-OD is calculated as

$$R = \frac{(N_{\text{all}} - N_{\text{masked}} - N_{\text{bad}})A_{\text{PMT}}}{A_{\text{SK-OD(inner)}}}, \tag{10.2}$$

where N_{all}, N_{masked}, and N_{bad} represent the number of PMTs for the full detector, masked detector, and bad channels, respectively. A_{PMT} and $A_{\text{SK-OD(inner)}}$ denote the surface area of the PMT and the inner wall of the OD, respectively.

Figure 10.8 shows the fractional increase in events surviving the FC selection criteria as a function of R with the equivalent HK-OD photocoverage. Initially, there is a gradual rise in the event count as R decreases. However, once R reaches 0.65%, the increase becomes exponential, indicating significant muon background contamination within the selection. This threshold effect is also evident in the uniform clustered masking scenario, with only a marginally higher impact for the same coverage. Both masking configurations suggest that the HK-OD will accumulate excessive background contamination with fewer than 5,000 PMTs. Considering the expected light loss from ageing, a minimum of 6,000 PMTs should be installed at the start of HK-OD operations.

---

[2] The UPMU sample relies on projecting the reconstructed track back into the bottom OD endcap.

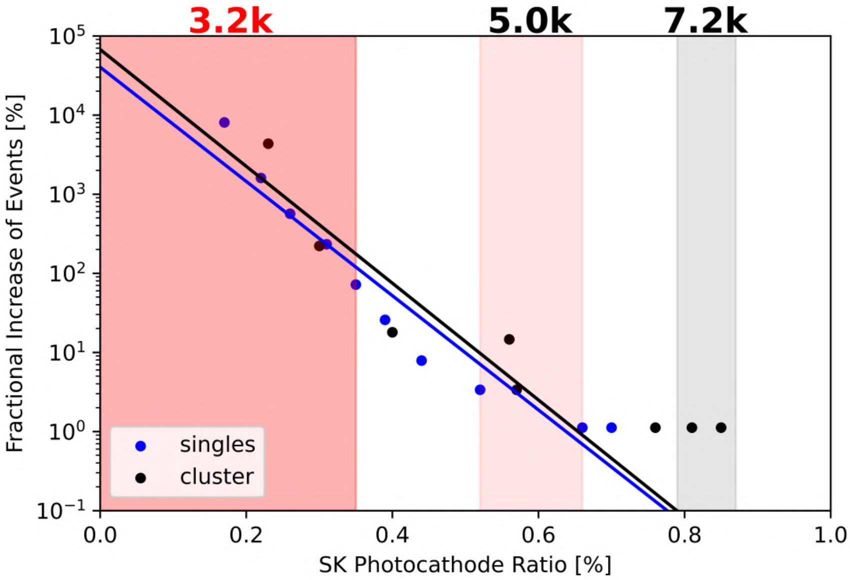

Figure 10.8: Fractional increase of events surviving the FC reduction as a function of varying levels of photocathode coverage ratio in the SK-OD for uniform singles (blue) and uniform clustered (black) PMT masking applied. The HK-OD equivalence is shown by the shaded regions: 7,200 PMTs (grey), 5,000 PMTs (light red), and 3,200 PMTs (red).

10.3.5 Final Background Samples

The events passing the FC reduction are reconstructed using the conventional neutrino fitter APFit [99]. Figure 10.9 presents the distribution of several reconstructed variables for masking configurations that correlate to HK-OD PMT arrangements. The reconstructed $\cos(\theta)$ distribution, in Figure 10.9a, shows that reducing the photocathode coverage allows for more high-energy downward-going cosmic muons to leak into the final sample. These events are mostly localised near the detector walls, particularly in the top and barrel regions (see Figures 10.9b and 10.9c). This increased activity in the barrel is more concerning for the HK-OD since the volume thickness proposed is half that of the SK-OD.

Figure 10.9d shows the *nhitac* distribution, which represents the number of PMT hits in the highest OD charge cluster calculated during the second FC reduction step. In the atmospheric analysis, FC events are distinguished from PC events by applying the cut *nhitac* < 16 [184]. However, achieving clear separation between FC and PC events at this cut threshold becomes challenging when significant PMT masking is applied.

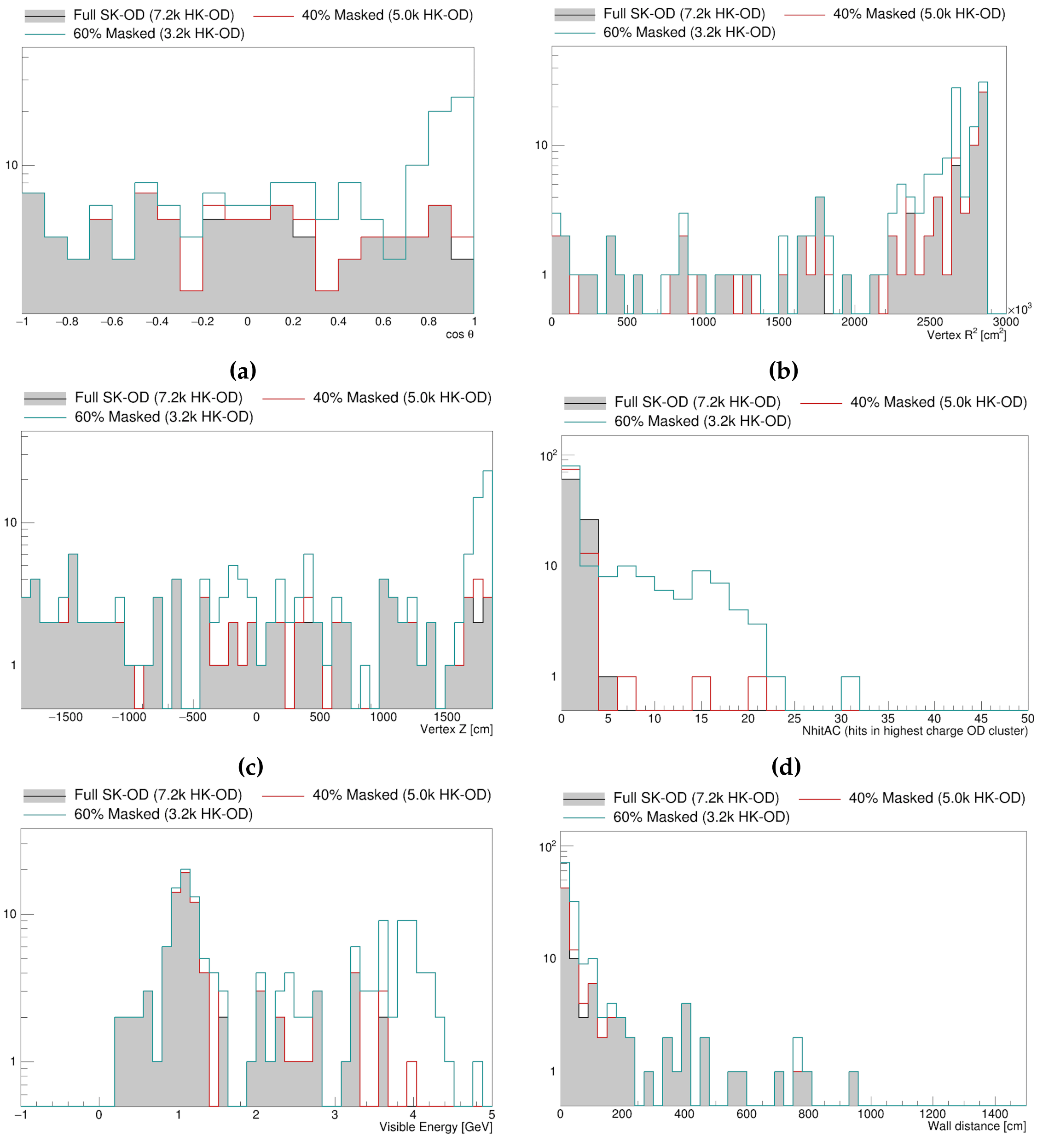

(a) **(b)** **(c)** **(d)** **(e)** **(f)**

Figure 10.9: Distributions of APFit reconstruction variables after applying the FC reduction for the full SK-OD/7.2k HK-OD (grey), 40% masked SK-OD/5.0k HK-OD (red) and 60% masked SK-OD/3.2k HK-OD (turquoise) PMT configurations.

In the full analysis, additional cuts on the reconstructed energy and distance from the wall are implemented to further reduce background contamination in the final sample. Figure 10.9f shows that a single muon is reconstructed at 800 cm, which will pass the FV cut (see Section 7.2.3). Therefore, this background event is classified as an atmospheric neutrino. Given that SK typically detects around 10 atmospheric neutrinos per day, these muons can significantly impact the analysis [177]. This effect will be more pronounced in HK due to higher event statistics, potentially affecting the ability to achieve 99.99% target veto efficiency. Although background rejection can be improved by constraining the FV this is an undesirable approach that limits the statistics capability and physics reach of HK.

10.3.6 Design Guideline

Based on these findings, considering the expected degradation over 20 years and accounting for uncertainties in the SK-HK scaling, the recommended PMT arrangements for the HK-OD are as follows:

- **Top endcap**: 1,500 PMTs (2/9 cable arrangement) with an additional 400 PMTs at the edge.
- **Barrel**: Opt for either 4,500 PMTs (1/6 cable arrangement) or 5,000 PMTs (3/16 cable arrangement), which can be supported by a combination of electronics modules.
- **Bottom endcap**: 750 or 1,500 PMTs (1/9 or 2/9 cable arrangement), provided that an asymmetrical detector configuration in the endcaps is capable of rejecting muon backgrounds.

This work recommends instrumenting at least 7,200 PMTs in the OD to meet target performance requirements, a design configuration that was accepted by the HK collaboration. However, since 2022, ongoing optimisation studies have focused on further reducing the photosensor coverage due to budget constraints. These studies explore whether an optimised FC reduction can compensate for an even sparser PMT arrangement (see Ref. [185] for further details).

11

Optical Measurements of WLS Plastics

11.1 Wavelength-Shifting Concept

Wavelength-shifting (WLS) plastics are doped with organic fluorescent compounds, known as fluors, to facilitate the absorption and re-emission of UV light [186]. This process, referred to as *active* absorption, is initiated through the absorption of incident photons, exciting fluor molecules to higher energy states. Subsequent rapid non-radiative de-excitation transitions ultimately lead to the emission of less-energetic photons consistent with the Stokes shift principle [187]. Re-emitted photons have longer wavelengths (λ) and minimal overlap with the absorption spectrum. Figure 11.1a shows a schematic diagram of Stokes shift with an ideal peak separation between the two spectra.

A critical aspect influencing the performance of WLS plastics is the fluor composition. Primary fluors, dissolved at high concentrations of 1% or more by weight, are effective for the initial absorption and re-emission. A large Stokes shift is preferred to mitigate the negative effect of *self-absorption*, where emitted photons are re-absorbed by nearby fluors [188]. The addition of secondary fluors can recover self-absorption loses by absorbing and re-emitting photons released by the primary fluor at the desired wavelength. Therefore, using multiple fluors with different absorption and emission characteristics helps distribute absorbed

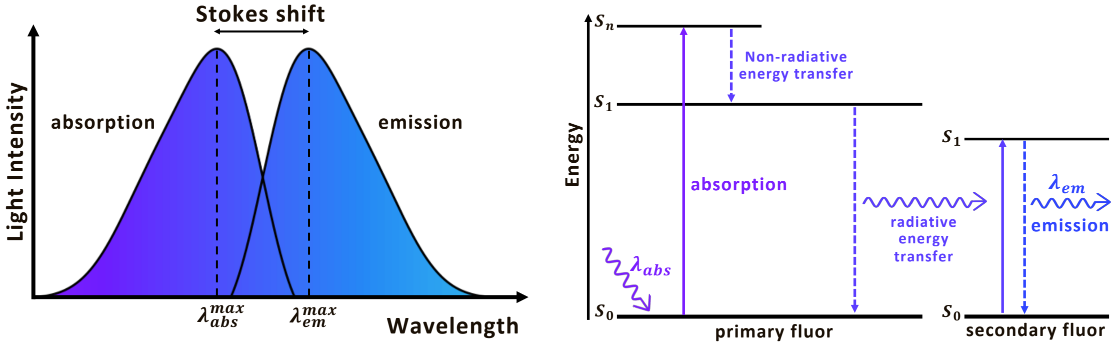

(a) Illustration of the Stokes shift principle.

(b) Active absorption with two fluors.

Figure 11.1: Schematic diagrams of the WLS concept.

energy across a broader range of wavelengths, improving the efficiency of WLS materials. Figure 11.1b illustrates this effect in a schematic energy-level diagram.

WLS light is re-emitted isotropically and captured within the plate via Total Internal Reflection (TIR). This phenomenon involves the complete reflection of incident light at the interface between two media with refractive indices of n_1 and n_2, respectively. The smallest angle of incidence at which TIR occurs is defined as the *critical angle* (θ_{crit}) and is determined by Snell's Law [189],

$$\theta_{\text{crit}} = \sin^{-1}\left(\frac{n_2}{n_1}\right) . \tag{11.1}$$

According to this relation, TIR is observed only when light propagates from a medium with a higher refractive index to a medium with a lower refractive index ($n_1 > n_2$).

WLS plastics are typically made via bulk free-radical polymerisation, often using an acrylic base. These materials are selected for their high refractive indices, homogeneity and optical clarity, facilitating the efficient transmission of wavelength-shifted photons throughout the plate. However, polymer bases also feature an intrinsic light-absorbing property attributed to UV stabilisers added during polymerisation. These additives, formulated to absorb and dissipate UV light's energy, serve as a *passive* component within the overall absorption spectrum. The interplay of active and passive absorption components guides the selection criteria for optimising the WLS plastic for the HK-OD.

11.2 Performance Requirements

The WLS plate design for the HK-OD must meet specific performance requirements to enhance the detection of Cherenkov radiation. Key criteria guiding the design include:

- **Active fluor:** Select an active fluor with robust absorption between 300 - 400 nm to wavelength-shift the UV component of Cherenkov light. Since the spectrum falls as $1/\lambda^2$ (see Equation 3.2), peaking in the UV, an effective fluor can enhance detection to a broader range of photon energies. Re-emission should be maximal in the visible blue to align with the spectral sensitivity of the PMT, shown in Figure 11.2. Commercially available fluors for this purpose include 2,5-Diphenyloxazole (PPO), 1,4-Bis(5-phenyl-2-oxazolyl)benzene (POPOP), and 1,4-Bis(2-methylstyryl)benzene (BisMSB). These fluors are known to possess high quantum yields[1] of at least 0.93 [190] [191]. In addition, a short active absorbance decay time of a few nanoseconds is required, as a longer re-emission time can introduce uncertainties in the detector trigger timing.
- **Polymer base:** The polymer base should exhibit UV stability, bulk material uniformity and optical transparency in the re-emission region. The selection of an intermediate refractive index between the surrounding medium ($n_{\text{water}} = 1.33$) and the PMT glass ($n_{\text{glass}} = 1.6$), is crucial to facilitate TIR and ensure the transmission of WLS photons to the PMT. Commonly used polymer bases such as polystyrene (PS), polyvinyltoluene (PVT), or polymethyl methacrylate (PMMA) are well-suited to meet these criteria.
- **Low intrinsic scintillation:** Certain fluor compositions are prone to generating intrinsic scintillation light when exposed to ionising radiation. This contributes to the background noise of the photosensor and thus reduces the signal-to-noise ratio of the system. Studies conducted outside the scope of this thesis demonstrated that double-fluor WLS plates, incorporating

---

[1] The ratio of the number of emitted photons to the number of absorbed photons.

the PPO compound, exhibit twice as high dark rates as single-fluor plates. Therefore, the selection of the WLS plate must balance increased light yield with potential challenges posed by scintillation light and dark rates.

- **Ageing and handling:** WLS plastics undergo degradation over time, resulting in a reduction in light yield. Factors such as exposure to solvents, water absorption, high temperatures, mechanical stress, irradiation, or rough handling can accelerate this ageing process. The surface is susceptible to *crazing*; the development of microcracks that suppress WLS plastic's ability to transmit light through TIR. PS-based plastic scintillators doped with POPOP used in the T2K detectors showed a $0.9 - 2.2\%$ reduction of the light signal per year operating in air at room temperature [192]. Considering this, the HK-OD photosensor is designed to assume a 20% loss of light yield after 20 years of operation as an upper estimate.
- **Scale and cost:** Develop a scalable manufacturing process that meets the HK-OD size requirements while aligning with overall production budget constraints. This includes machining holes, surface polishing, assembly and mounting of the photosensor.

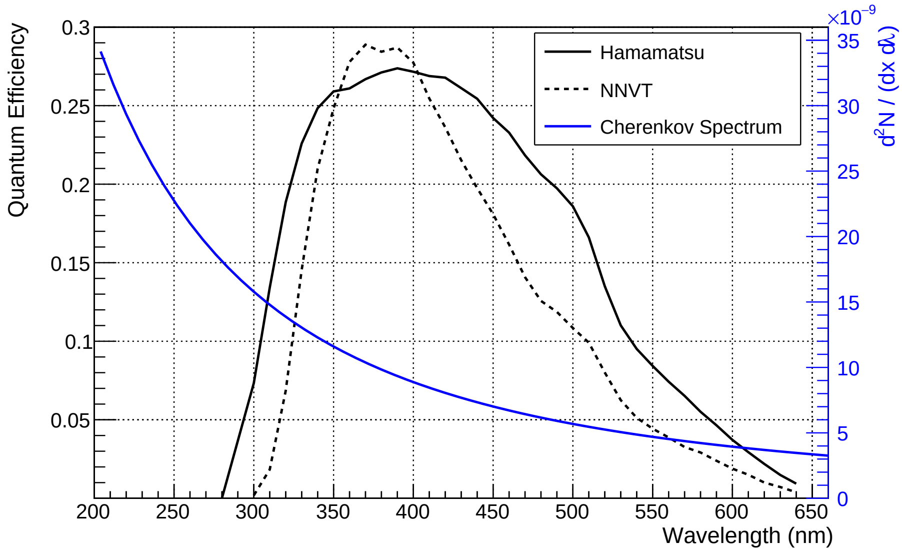

Figure 11.2: PMT QE for the Hamamatsu and NNVT candidate PMTs overlaid with the Cherenkov spectrum as a function of wavelength.

11.3 Candidate WLS Samples

In the initial phase of this thesis's investigations, four major suppliers were under consideration for the provision of WLS plates: Eljen, Kuraray, V.A. Kargin Polymer Research Institute in Russia, and LabLogic UK. Table 11.1 summarises these suppliers and the comprehensive tests performed as part of this thesis's work. Optimal selection of WLS plastic requires precision in-air optical and water-based (BabyK) measurements of all candidate samples over the relevant portion of the UV-VISIBLE spectrum.

Supplier	**Base**	**Name**	**Dimension [cm]**	**Optical**	**BabyK**
Kuraray	PMMA	UVOK-WLS	$25 \times 25 \times 0.5$	✓	-
		UVOK-WLSA	$25 \times 25 \times 0.5$	✓	-
		UVOK-WLSB	$25 \times 25 \times 0.5$	✓	-
		B2-1	$39 \times 18 \times 1.3$	✓	✓
		B2-2	$30 \times 30 \times 1.3$	-	✓
		B2-3	$30 \times 30 \times 0.6$	-	✓
Eljen	PVT	EJ286-1	$25 \times 25 \times 0.6$	✓	✓
		EJ286-2	$30 \times 30 \times 0.7$	-	✓
		EJ292 (*)	$20 \times 10 \times 5.0$	✓	-
V.A. Kargin Polymer Research Institute	PMMA	POPOP200	$39 \times 18 \times 0.95$	✓	✓
		BisMSB50	$39 \times 39 \times 0.95$	✓	✓
		MSB350-PPO3000	$27 \times 26 \times 0.5$	✓	-
		POPOP50-PPO3000-1	$27 \times 26 \times 0.5$	✓	-
		POPOP50-PPO3000-2	$30 \times 30 \times 0.6$	-	✓
LabLogic	PS	2020	20 x 20 x 0.5	✓	-
		2022	20 x 20 x 0.5	✓	-

Table 11.1: Candidate WLS samples dimensions and measurements carried out, where BabyK refers to the water-based measurements discussed in Chapter 12. The Eljen EJ292 is not a candidate WLS plate for the HK-OD, and is only used for measurements discussed in Section 11.7.1.

11.4 UV-VISIBLE Spectrophotometry

UV-VISIBLE spectrophotometry is used in this work to quantify the optical properties of WLS plastics in air. Since commercially sourced WLS samples use various fluors with different chemical compositions and concentrations, measuring the relative absorbance spectra (A) is crucial for evaluating their performance [177]. This technique involves comparing the intensity (I) of laser

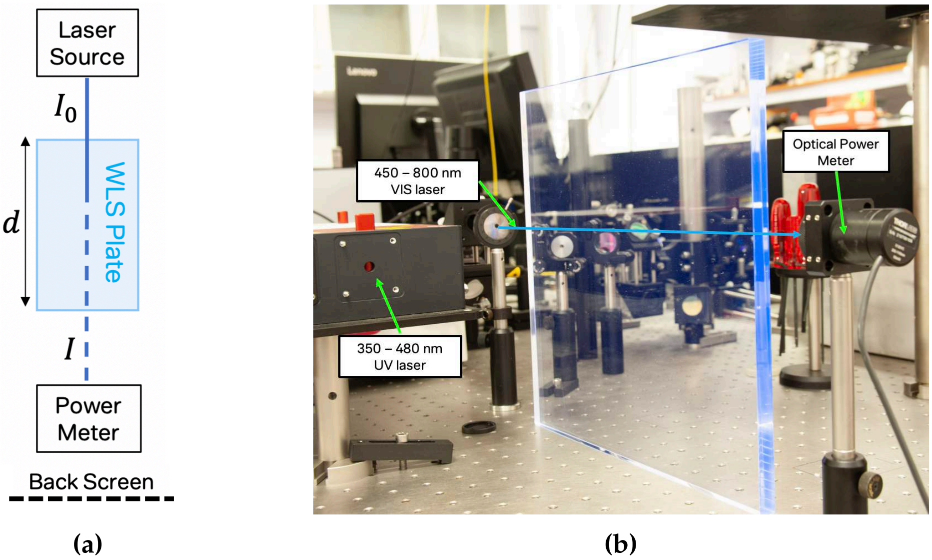

Figure 11.3: Optical measurement setup: Left: Schematic diagram of the experimental setup. Right: Photograph showing the experimental setup with a Kuraray B2 WLS sample.

light transmitted (T) through a sample with respect to the incident intensity (I_0), as shown in the schematic diagram in Figure 11.3a.

$$T = \frac{I}{I_0} \qquad\qquad A = -ln(T) \tag{11.2}$$

Reflection at normal incidence accounts for approximately 3 - 5% light loss at the air-plate boundary [186]. The light reflected from the WLS-air boundary is measured across the full UV-VISIBLE spectrum and subtracted from the measurements of the light transmitted. The transmittance and the length of the sample (d) is used to calculate the attenuation length ($\mu_{\text{eff}}(\lambda)$),

$$\mu_{\text{eff}}(\lambda) = -\frac{d}{ln(T(\lambda))}. \tag{11.3}$$

The reduction in the intensity of transmitted light observed due to the combined action of absorption and reflection is described by the Beer-Lambert Law, where Equation 11.4 shows the probability of absorption [193],

$$P(\lambda) = e^{-\frac{d}{\mu_{\text{eff}}(\lambda)}}. \tag{11.4}$$

All quantities are effective since the relation between absorbance and pathlength is only strictly valid for a homogeneous medium with no re-emission of light.

Accurate absorbance measurements require long optical pathlengths, particularly at large wavelengths where the attenuation of light is minimal. Although spectrophotometers are standard laboratory tools for such measurements, most models only accommodate samples up to 1 cm in length. Since fluctuations in the transmitted signal from detector noise are automatically attributed to absorbance, measurements are subject to greater uncertainty when d is small. In addition, apertures instrumented at the detector opening typically restrict the photosensitive area to 1 mm, which can artificially amplify transmission loss if the beam diverges in the sample. Thus, a specialised setup capable of measuring optical properties over long pathlengths is used for this study.

11.5 Experimental Setup

A SuperK Extreme supercontinuum laser is used in this experimental setup to measure absorbance and attenuation length. Two filters are utilised, enabling the generation of a single-line laser with tunable coverage between 350 - 800 nm. WLS plates are orientated such that the beam propagates through the longest optical pathlength possible, as depicted in Figure 11.3b. A calibrated silicon photodiode, with a 9.5 mm diameter aperture connected to a Thorlabs PM400 power metre, is carefully aligned at the exit point of the sample. Absolute power measurements are made in 2 nm and 5 nm increments for the UV and VISIBLE laser filters, respectively, for all WLS plates. In Figure 11.4, the spectral distribution of the average power intensity of the UV and VISIBLE lasers is shown.

11.6 Mie Scattering

Visual inspection of light projected onto a back screen highlights the prominent artefact of Mie scattering in these WLS plastics. Impurities, polymer molecule clusters and undissolved fluors create small local non-uniformities in density which become centres for deflecting light and produce characteristic interference fringes [194]. The scattering occurs predominately in the forward direction

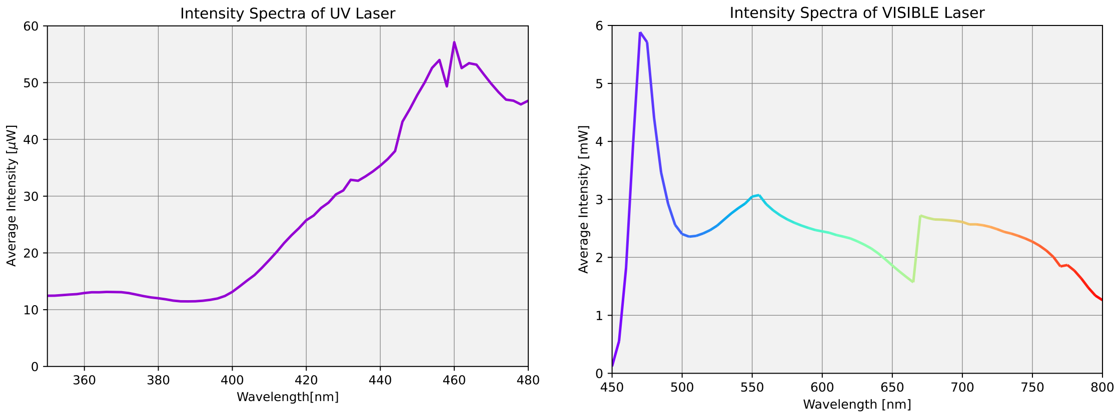

(a) **(b)**

Figure 11.4: Power intensity spectra for the UV (left) and VISIBLE (right) SuperK continuum lasers that cover a combined range of 350 - 800 nm.

from microstructures with dimensions comparable to the wavelength of light, as illustrated in Figure 11.5. Upward and downward scatters are absorbed due to the orientation of the plates such that a pattern elongated in the horizontal remains. As the incident wavelength increases, the Mie effect becomes less pronounced [195].

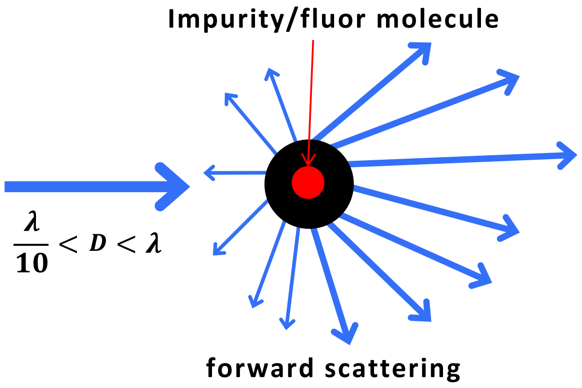

Figure 11.5: Schematic diagram of the Mie scattering effect, where D denotes the particle diameter.

Photographs of light scattering in the experimental setup observed in the LabLogic 2020 WLS sample are shown in Figure 11.6a. Surface inclusions from the fabrication process of injection moulding further amplify the effect to the point where the beam completely diffuses into the plastic. This effect is apparent in the side view photograph of the same sample shown in Figure 11.6b. Since scattering

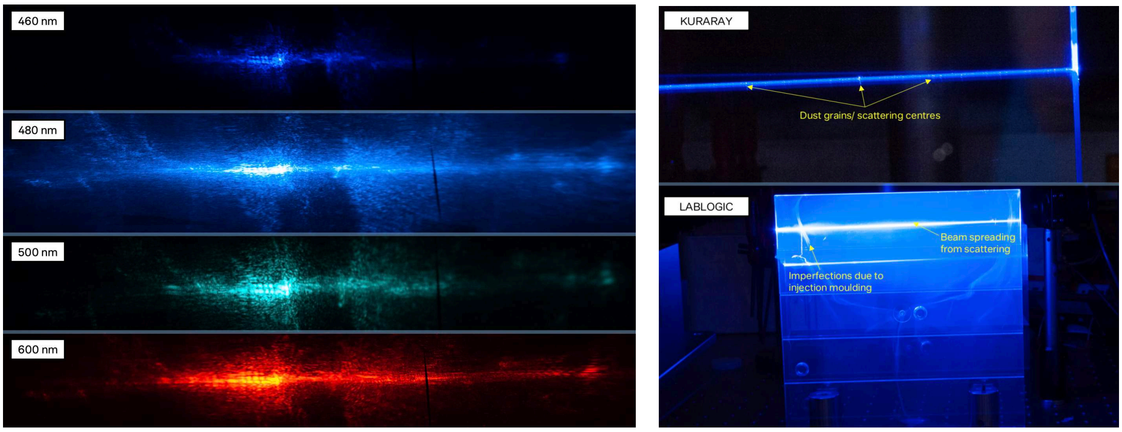

(a) Mie scattering projections from LabLogic 2020. **(b)** Mie scattering in WLS samples.

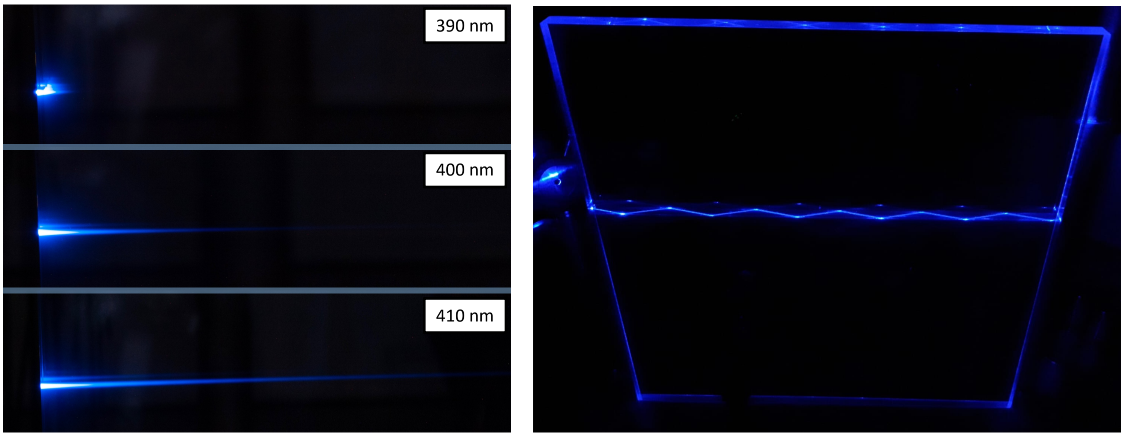

(c) Light attenuation in Kuraray B2. **(d)** Multiple reflections in Kuraray B2.

Figure 11.6: Photographs of WLS samples in the UV-VISIBLE spectrophotometry setup.

is automatically integrated into the observed transmission loss it is extremely difficult to distinguish intrinsic light absorption from scattering, therefore only the net effect can be measured.

In the context of the HK-OD photosensor, Mie scattering can cause photons to scatter anisotropically, impacting the collection efficiency of Cherenkov light. The scattered light may not contribute to the desired Cherenkov signal, resulting in reduced overall light collection efficiency. Current simulations of the HK-OD do not account for Mie scattering and therefore do not fully capture the complexities introduced by its effect. This underscores the importance of conducting both optical and water-based measurements of WLS plastics.

11.7 Absorbance and Attenuation Length

Figure 11.7a shows the measured absorbance and attenuation length spectra for all candidate WLS plates in the near-UV region. Note that measurements with maximal absorbance (A $\sim$ 1) are subject to large uncertainty due to the lack of precision in measuring low light intensities. Small deviations in the transmittance typically fluctuate the measured absorbance due to the logarithmic relationship described in Equation 11.3. However, using a highly sensitive power sensor with 1 nW resolution facilitates precision measurements even at low transmittance, such that performance in the UV region is well-defined for all samples.

Both single and double-fluor variants of the V.A. Kargin samples demonstrate high absorptivity with less than 10% light transmission below 400 nm. This prominent absorption arises from the combination of active and passive absorption. In contrast, the Kuraray B2 and Eljen EJ286, exhibit a comparatively lower net absorbance between 0.5 - 0.8. This reduction in absorbance can be attributed to a combination of either a lower concentration of the active fluor, less passive absorption in the plastic base and less scattering of light. Therefore, some UV light can transmit through without being absorbed, contributing to the observed decrease in overall absorbance.

Above 400 nm, a noticeable shift occurs in the optical behaviour of the majority of WLS samples. As active absorption of the fluor diminishes, there is a distinct and steep decline in the absorption curve. Specifically, Eljen EJ286, Kuraray B2, UVOK-WLS2 and POPOP50-PPO3000 samples show a well-defined transition to optical clarity. Given that re-emission peaks at approximately 420 nm, this indicates that their fluors exhibit a large Stokes shift. However, UVOK-WLS2A and UVOK-WLS2B deviate from this behaviour, displaying a gradual decline from 370 nm into the visible region. This characteristic makes them unsuitable for meeting the requirements of the HK-OD photosensor such that these plates are excluded from further consideration.

Absorption observed in the re-emission region is primarily attributed to Mie scattering and passive absorption in the polymer base. Figure 11.7b shows that Mie scattering dominates both LabLogic spectra well into the visible region such that the plastic appears to be virtually opaque to wavelength-shifted light. This measurement justifies excluding all LabLogic samples as candidate WLS plates for the OD photosensor.

In contrast, the Kuraray B2 plate has twice the attenuation length of all other samples at 420 nm, which firmly establishes its suitability as a WLS candidate. Figure 11.6c visually illustrates the observed attenuation length and optical clarity in the wavelength region between active absorption and re-emission.

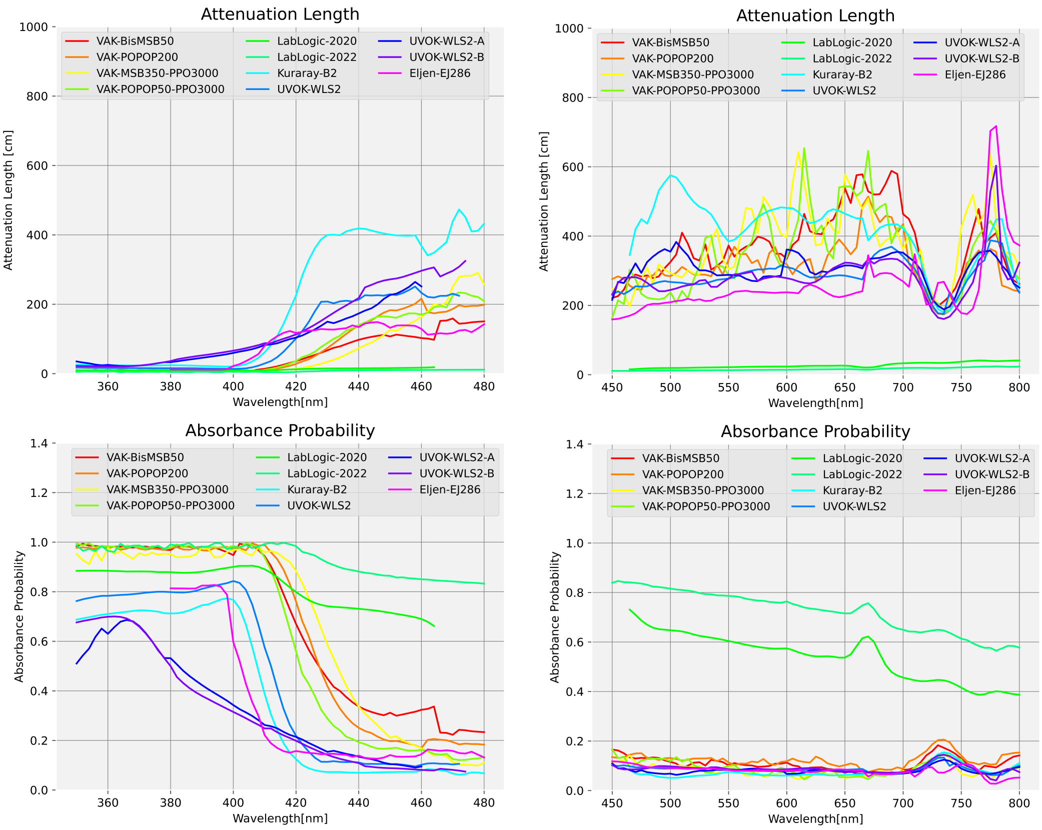

(a) UV-VISIBLE spectrum.

(b) VISIBLE spectrum.

Figure 11.7: Attenuation length (top) and absorbance probability (bottom) spectra for measured WLS samples.

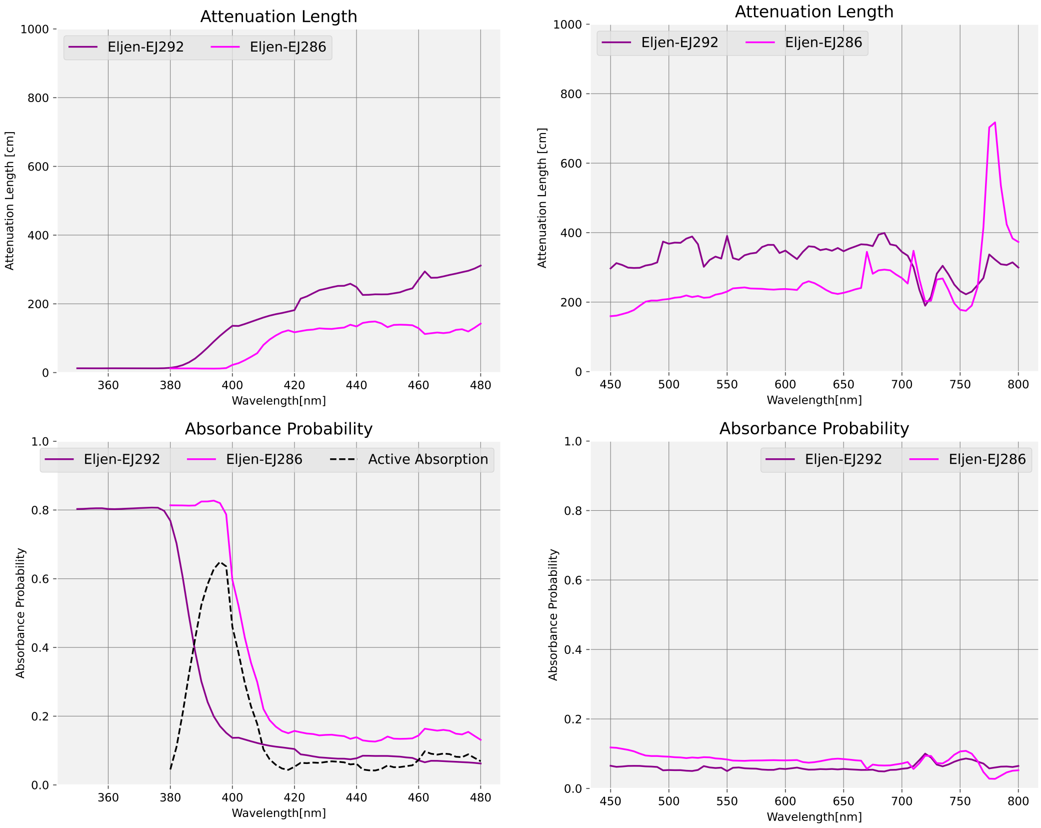

(a) UV-VISIBLE spectrum.

(b) VISIBLE spectrum.

Figure 11.8: Attenuation length (top), absorbance probability (bottom) spectra with active absorption superimposed for the Eljen EJ292 base PVT and EJ286 WLS samples.

11.7.1 Active and Passive Absorption

Optical measurements were performed on an undoped PVT sample to directly extract the active absorption spectra of the Eljen EJ286 fluor. The EJ292 sample analysed in this study serves as the polymer base used across several of Eljen's standard WLS and scintillating plastics. Although PVT plastic has an intrinsic weak scintillating property with an emission maximum near 320 nm, as indicated in Eljen's provided specification, it contains no UV-absorbing WLS fluors. Therefore, this plastic is used as a non-scintillating reference for the Eljen EJ286 candidate WLS sample.

Figure 11.8 shows the measured absorbance and attenuation length spectra for both Eljen samples. Subtracting the spectra highlights the active absorption component, peaking at 400 nm and falling sharply at 420nm. The enhancement of the net absorption observed in the EJ286 WLS sample between 380 - 400 nm is directly attributed to the active fluor. This suggests an effective separation between the active absorption and re-emission spectra. Passive absorption dominates below 380 nm and above 420 nm where the active component has minimal influence.

11.7.2 Multiple Reflections

Light lost at each TIR point can impact the detected light yield. To investigate this effect, absorbance measurements were carried out on the Kuraray B2 plate, varying its orientation to increase the number of TIRs. Figure 11.6d illustrates the experimental setup for inducing 10 TIRs, and Figure 11.9 presents the measured absorbance for multiple reflections within the WLS plate. The absorbance spectra are consistent between all measurements demonstrating that minimal light loss occurred in each setup. It is crucial to note that these measurements were conducted in air. According to Equation 11.1, the θ_{crit} for a WLS plastic PMMA plate with a n_{PMMA} of 1.49 in air is 42.31° such that light emitted within ±47.69° of the horizontal can be captured by TIR. However, in water, this reduces to ±26.80°, potentially enhancing light loss. Despite this effect, the highly reflective Tyvek covering the HK-OD region will allow for the recovery of light leaking out of the plate at reflection boundaries or via Mie scattering.

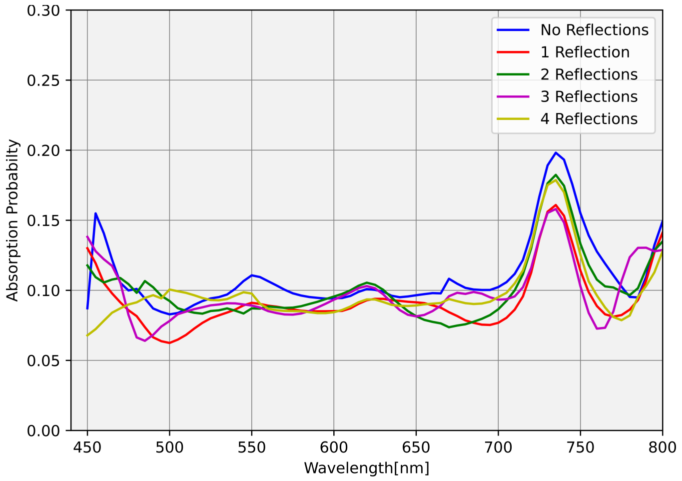

Figure 11.9: Absorption in the VISIBLE region for multiple TIRs in the Kuraray B2 plate.

12

The BabyK WLS Plate Test Facility

The BabyK WLS plate test facility is designed to evaluate candidate WLS plates in response to cosmic muons in ultra-pure water. This chapter details the complete R&D process, covering hardware design, electronics, materials testing, software, detector assembly, and calibration. The setup delivers the first comprehensive measurements of the relative light yield of WLS plates in experimental conditions similar to the HK-OD. A detailed investigation is carried out to analyse key performance metrics and to determine the optimal WLS plate. Final comparisons are made between Eljen, Kuraray and V.A. Kargin Polymer Research Institute manufactured samples to guide the final selection of the WLS plate in the HK-OD.

12.1 Photosensor Unit Design

The photosensor unit contains a 3-inch Hamamatsu R6091 flat-faced PMT, securely housed within a 3D-printed acrylonitrile butadiene styrene (ABS) holder. This PMT has a spectral response between 300 - 650 nm, with a peak quantum efficiency of 25% at 390 nm, and operates at a gain of 5×10^6 via a 12-stage linear-focused dynode chain [196]. A Hamamatsu E5859-03 positive polarity base connects the PMT readout to external electronic equipment. Four custom 3D-printed ABS brackets, featuring adjustable clamps, work to stabilise the

WLS plate beneath the PMT and provide flush surface contact between the photosensor components through press-fitting. A thin layer of Saint Gobain BC-630 optical-grade silicone grease is applied between the PMT-WLS plate interface to eliminate the water gap, improving photon transmission into the PMT. Stainless-steel threaded inserts, rods, nuts, bolts and washers are used to assemble all WLS bracket components to ensure structural integrity. The finalised design is illustrated in the Computer Automated Design (CAD) diagram in Figure 12.1.

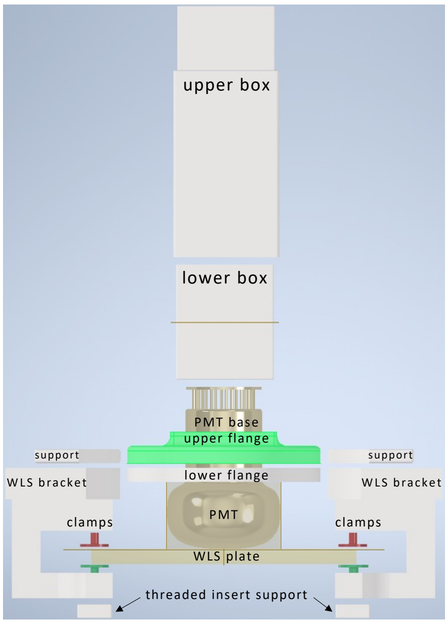

Figure 12.1: CAD diagram of the 3D-printed WLS brackets and PMT holder components.

The decision to opt for a flat-faced PMT, as opposed to the hemispherical geometry used for the HK-OD, offers distinct advantages. In the hemispherical photosensor unit, variations of the PMT's bulb diameter, contour, surface finishes and the machined hole in the WLS plate may introduce inconsistencies in the press-fit quality. This can result in fewer photons detected and therefore impact the reproducibility of light yield measurements. In contrast, the BabyK photosensor design has the benefit of ensuring uniform optical coupling between the PMT and WLS plate for all samples.

12.2 Tank Specifications

The experimental setup consists of a cylindrical lacquer-lined steel tank, measuring 58.4 × 87.6 cm, filled with ∼200 L of de-ionised (DI) water held at room temperature. A layer of DOWSIL 881 glass silicone sealant is applied to exposed points, unvarnished tank edges, and welded joints to counteract rusting. Once cured, a clear polypropylene (PP) drum liner is inserted into the inner volume for further protection. Reflectivity measurements of the tank and PP liner are conducted using a Lambda 1050 UV-VISIBLE spectrophotometer with an integrating sphere. The results presented in Figure 12.2 indicate that the combined tank and PP liner unit exhibit low reflectivity in the UV spectrum, reaching a peak of 40% at 300 nm, and stronger reflectivity in the visible spectrum, exceeding 85% above 450 nm. This discrepancy introduces a bias in the Cherenkov spectrum observed by the photosensor unit, favouring visible light, which the WLS plate is less efficient at collecting.

The photosensor unit and WLS brackets are mounted to the upper lid of the tank, facing downwards such that the photosensitive area is fully submerged in the water. The drum lid is securely fastened with a latch ring, and black electrical tape covers the exposed parts of the PMT holder and WLS brackets to prevent photon contamination from the surroundings. A schematic diagram and photographs of the complete setup are presented in Figures 12.3 and 12.4, respectively.

12.3 Materials Testing

Before installation into the BabyK tank, soak tests were performed on various materials to assess their performance in DI water at room temperature. Since purified water can be highly corrosive, the material selection was based on the proven compatibility observed during these tests.

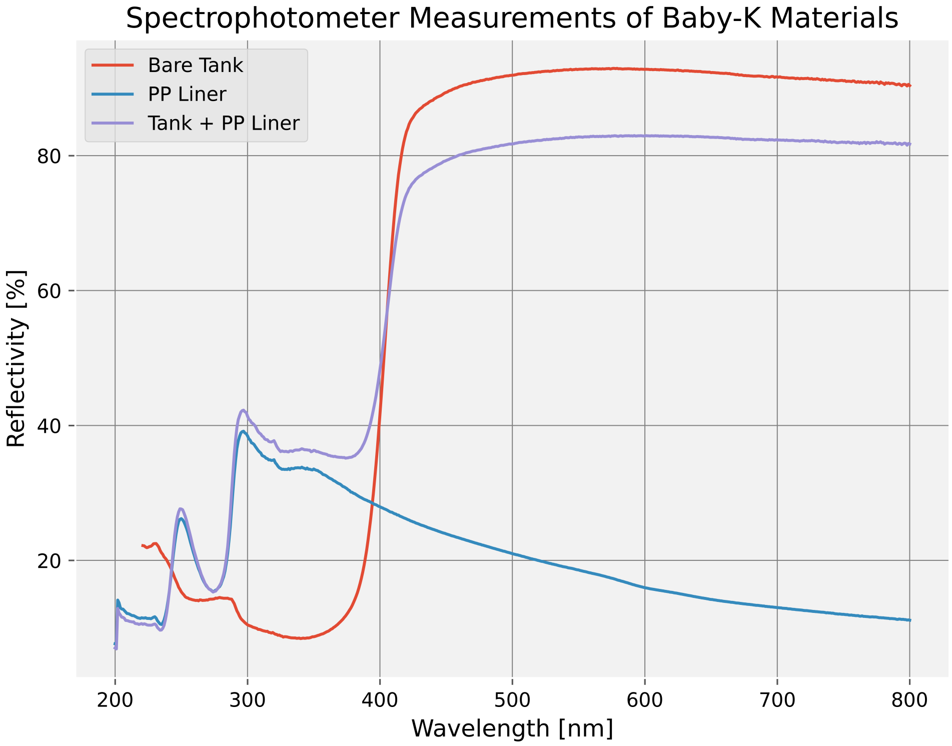

Figure 12.2: Absorbance spectra of the lacquer-lined side of the bare tank (red), PP drum liner (blue), and combined (purple).

The materials tested included A2 (304, 18/8), A4 (316, 18/10)[1] and unidentified grades of stainless steel fixtures (with some parts deliberately subjected to scratches and cuts), Teflon fixtures and tape, heat shrink material, ABS for the WLS brackets, a tank piece partially coated in DOWSIL 881 glass silicone sealant, and a cutout of the PP drum liner. The selection process relied on visual inspection after a two-week testing period. All unidentified stainless steel components and A4 grade washers showed significant degradation whereas A2 grade components remained unaffected. The glass silicone sealant effectively prevented rusting on the exposed tank edge, confirming its suitability for the experimental setup. Photographs of the soak test and A2 grade fixtures selected are shown in Figure 12.5. All assembly and photosensor components were routinely cleaned with 70% concentration isopropyl alcohol (IPA) solution during open-tank work and prior to each WLS plate measurement to mitigate material and water degradation.

---

[1] 18/8 and 18/10 refers to the percentage of chromium and nickel used in the stainless steel.

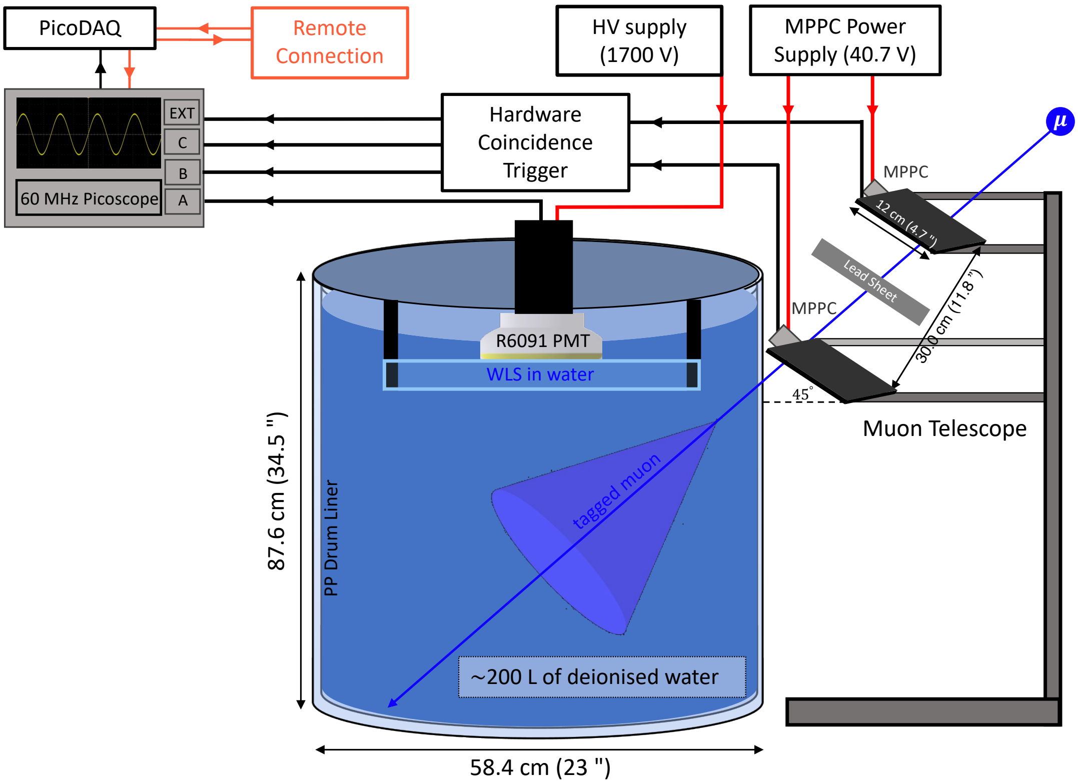

Figure 12.3: Schematic diagram of the BabyK WLS plate test facility with the cosmic muon telescope, hardware trigger system and DAQ pipeline labelled. An example of a tagged cosmic muon triggering the scintillator paddles and emitting Cherenkov radiation in the tank is shown for reference.

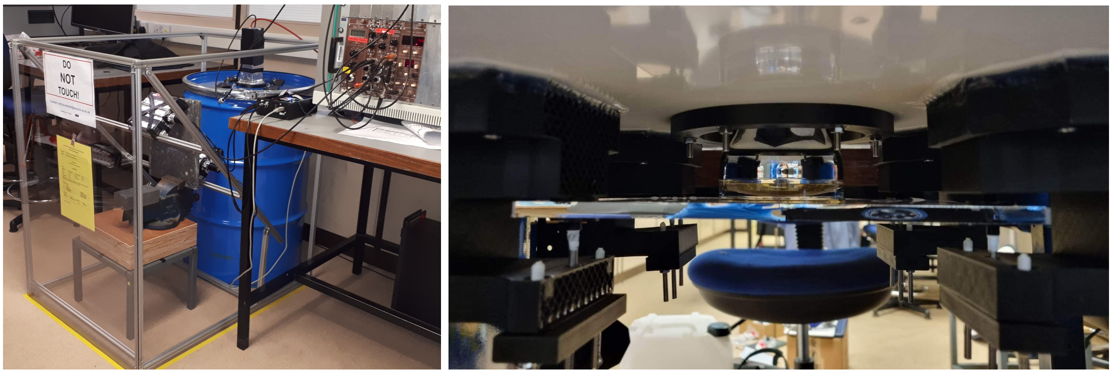

(a) The full setup.

(b) The photosensor unit.

Figure 12.4: Photographs of the BabyK WLS plate test facility.

Figure 12.5: Photographs of the soak testing procedure. Left: stainless steel, tank and drum liner materials are immersed in DI water, held within separate jars at room temperature. Right: A2 grade steel components are shown upon completion of the testing process.

12.4 Cosmic Muon Telescope

A purpose-built cosmic muon telescope was constructed to trigger the cosmic muon flux in BabyK. The setup consists of two 12 × 12 cm PVT-based scintillators optically coupled to Hamamatsu S14160-6050HS 6 × 6 mm Multi-Pixel Photon Counters (MPPCs). Plastic scintillators are chosen due to their high sensitivity to relativistic cosmic muons, which behave as Minimum Ionising Particles (MIPs), depositing approximately 2 MeV/cm in 1 g/cm^3 material [197]. The MPPCs provide a 50% photon detection efficiency at the peak wavelength $\lambda = 450$ nm up to 25° C [198]. Prior to assembly, each MPPC is surface-mounted onto support boards and carefully enclosed within a Thorlabs lens tube and adjustable cage unit. The photosensor components are clamped together, with optical grease applied at the interface, to form a paddle coincidence detector. The combined unit is covered in aluminium foil and subsequently wrapped in black electrical tape to maximise internal reflections and enable permanent light sealing. Figure 12.6 shows the materials and assembly of the paddles.

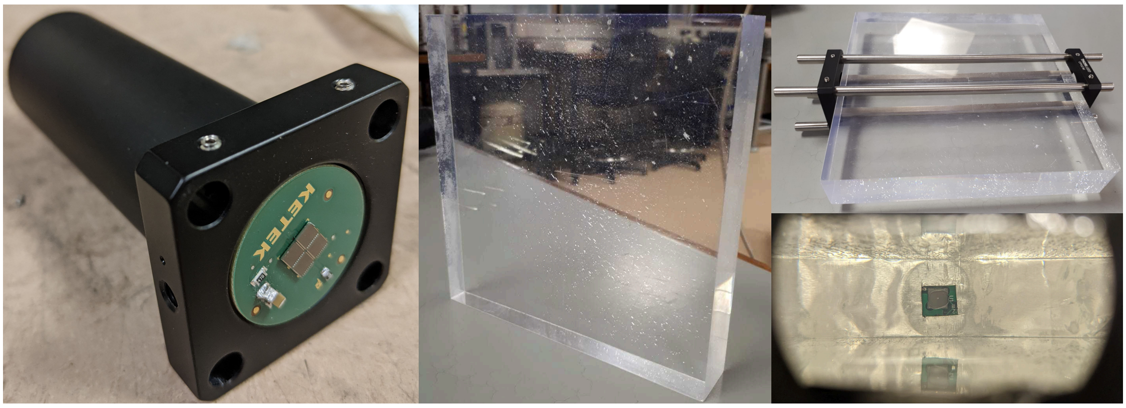

Figure 12.6: Photographs of the MPPC mounted onto the PCB board, held in the optical tube (left), the PVT scintillator (centre), the frame (upper right) and an inside view of the MPPC optically coupled to the scintillator (lower right).

12.4.1 Multi-Pixel Photon Counter

MPPCs are functionally equivalent to Silicon Photomultipliers (SiPMs). They comprise a matrix of silicon single-photon avalanche photodiodes (APDs), connected in series, and operate in Geiger mode when biased above their *breakdown* voltage (V_{BR}) [199]. The gain is determined by the applied *overvoltage* (ΔV): the difference between the operational voltage V_{bias} and the V_{BR}.

$$\Delta V = V_{\mathrm{bias}} - V_{\mathrm{BR}} \tag{12.1}$$

Figure 12.7 shows the basic circuit diagram of the MPPC. Photons striking the MPPC initiate an avalanche of electron-hole pairs within the APDs, generating a measurable electrical signal. In Geiger mode, a substantial electric field is established within the APD that discharges upon detecting individual photons. A quenching resistor is connected in series with the APD to stop continued avalanche multiplication and facilitate detection of the next photons [200]. The output current flows through the resistor and produces a pulse waveform with a sharp rise time.

Maintaining a stable temperature is crucial for single-photon detection since the MPPC's breakdown voltage is linearly dependent on its operating temperature. Dark noise pulses, caused by thermally generated avalanche pairs, are highly temperature-dependent and can be mistaken for real signals. Lowering

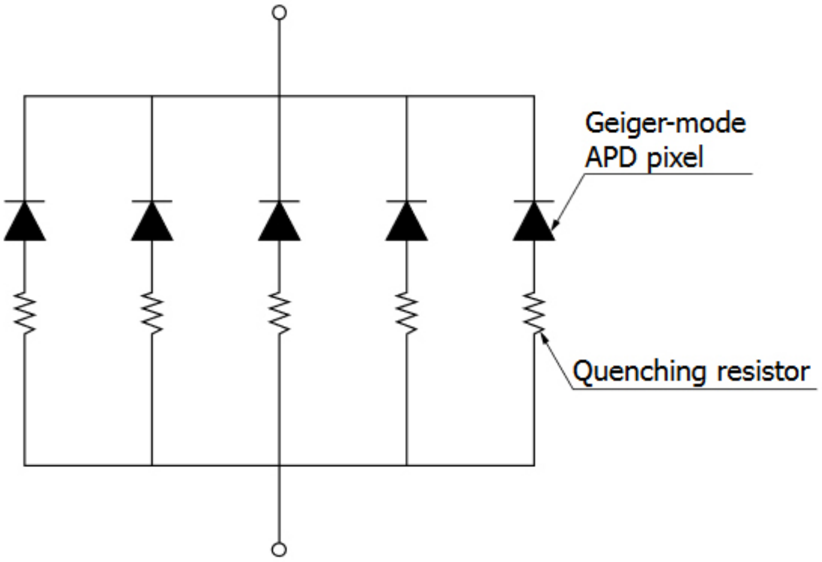

Figure 12.7: The basic circuit diagram for a Hamamatsu MPPC. This figure is taken from Ref. [201].

the temperature or the input V_{bias} effectively reduces the dark noise contribution. Therefore, in this setup, the MPPCs deliberately operate at the minimum allowable V_{bias} of 40.7 V ($V_{\mathrm{BR}} + 2.7$ V).

12.4.2 Mechanical Support Structure

The scintillator paddles are mounted onto a $2{\times}1{\times}1$ m support structure, constructed from aluminium RS PRO struts and reinforced with a sheet of Plexiglas. The CAD assembly design, depicted in Figure 12.8, includes an adjustable frame that secures the paddles in parallel, separated by 30 cm. Pivot joints, shown in Figure 12.4a, connect the adjustable frame to the main structure to position the muon telescope at a 45° angle. This constrains the solid angle coverage to only accept incident muons following a direct trajectory into the side of the tank. In this configuration, the photosensor unit only detects Cherenkov radiation, rather than scintillation light produced by muons passing through the back of the WLS plate. The solid angle subtended by the detector assembly is approximated to be 0.55 sr, using the method outlined in Appendix B.1.

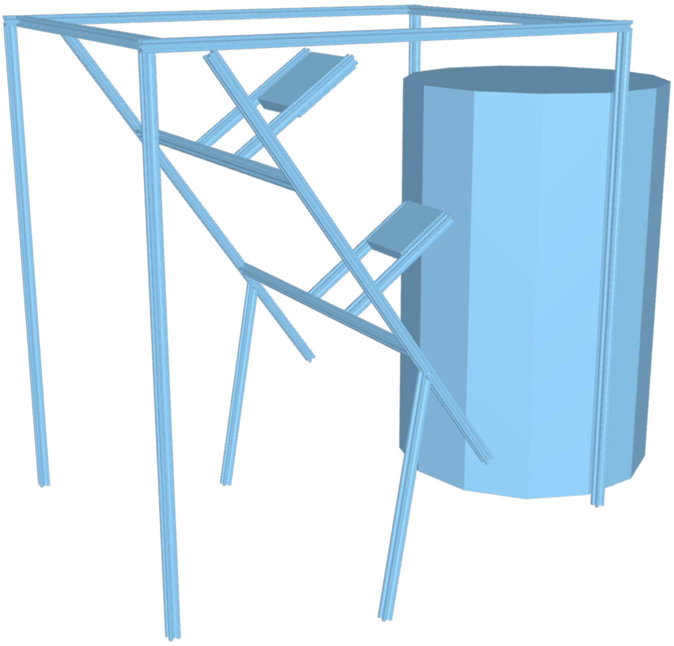

Figure 12.8: CAD diagram of the support structure for the cosmic muon telescope, created in Autodesk Inventor 2020.

12.4.3 Electronics

Custom-built front-end electronics have been developed by technicians to supply each MPPC with precisely 40.7 V. The system consists of four Printed Circuit Boards (PCBs) housed within an enclosed electronics box, as shown in Figure 12.9. The power supply functions with a standard 5 V USB input, featuring a USB Type B socket for connection to the USB input circuit board. A Double Pole Double Throw (DPDT) switch controls the connection of USB data lines (D+ D-) to an ESP32 microcontroller, located on a separate board. When switched towards the terminal blocks, the data lines enable either programming or communication with the ESP32 microcontroller; otherwise, they are disconnected. The board is also equipped with a linear regulator, the output of which is directed to the ESP32 microcontroller to supply the device with 3.3 V. To ensure stability, the USB power is filtered by three capacitors (100 nC, 10 μC, 22 μC) and a resistor that safely discharges the capacitors during power-off. In addition, a fuse is incorporated into the board design to limit the current supplied to devices powered by this board.

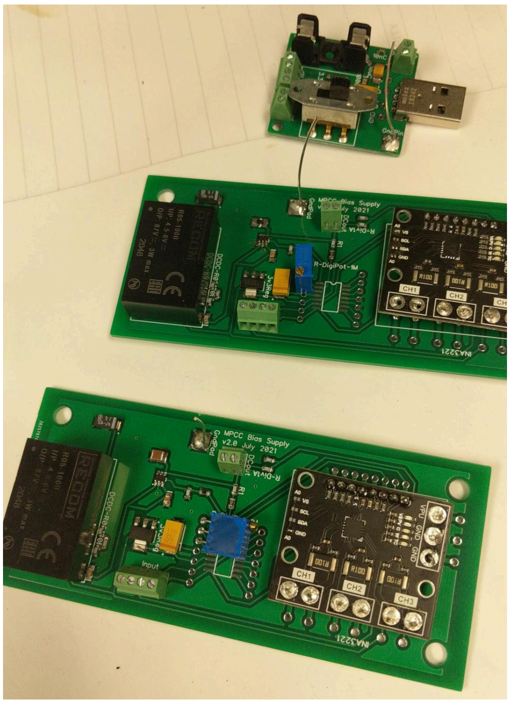

Figure 12.9: Photograph of the custom-built MPPC power supply and USB input boards (the ESP32 microcontroller board is not shown here).

Two identical MPPC power supply boards, designed to step up and continuously monitor the voltage, are directly connected to the 5V power line from the USB input board. The circuit diagram, shown in Figure 12.10, contains a Recom R05-100B DC-DC converter with specific resistors R-Adj, R-Adj2 and R-Ref set to 300 Ω, 4.7 kΩ and 5.1 kΩ, respectively to convert the voltage to 46 V. The output is connected to a variable linear voltage regulator (DCReg), enabling precise voltage adjustment via a 20-turn 1 MΩ potentiometer (R4). The potentiometer is in series with three resistors R1, R2 and R3 (470 kΩ, 760 kΩ, 1 MΩ) to set the total resistance required to achieve the desired voltage of 40.7 V. This replaced a digital Inter-Integrated Circuit (I2C) 1 MΩ potentiometer previously used, which experienced operational issues during the design phase. Several smoothing capacitors are integrated around the input and outputs to the DC-DC converter and DCReg to regulate voltage drops.

An INA3221 triple-channel current and voltage sensor module continuously monitor the power line and the output voltage from the DCReg. A 3.3 V linear voltage regulator (3×3Reg) is used to step down the 5 V input voltage to power

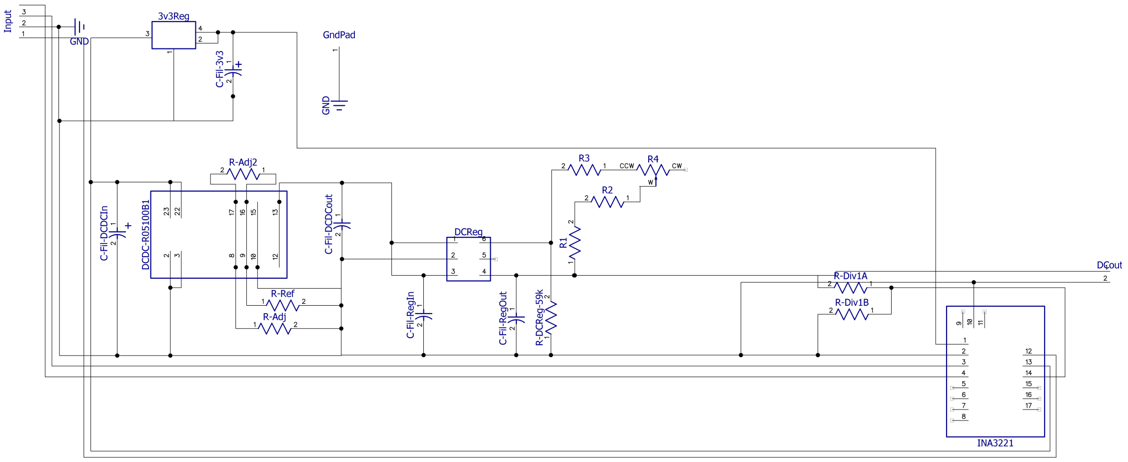

Figure 12.10: Circuit diagram of the MPPC power supply board.

the INA3221. The voltage from the DCReg is directed through a potential divider, formed by a 62 kΩ (R-DIV1A) and a 56 kΩ resistor (R-DIV1B), to halve the voltage delivered to the INA3221. This adjustment is necessary as the INA3221 has a maximum readable voltage of 26 V. The voltage readout is connected to the ESP32 microcontroller board via I2C data lines.

The microcontroller board includes a set of Dual In-Line (DIP) switches for efficient power control, including one for regulating the 3.3 V power to an LED screen. The embedded software on the device, programmed to account for the voltage division, interprets data from the INA3221 sensor modules to print the real-time voltage onto the LED screen. Circuit diagrams of the USB input and microcontroller boards are shown in Appendix B.2.

12.4.4 Coincidence Trigger

The hardware trigger system uses the raw MPPC signals from each scintillator paddle to generate an external coincidence trigger for the DAQ system. A schematic overview of the Nuclear Instrumentation Modules (NIM) electronics chain, detector components and DAQ readout is shown in Figure 12.11. Signal processing of each channel, including shaping, amplification (AMP) and pulse discrimination, is carried out by two ORTEC 590A units. To ensure weaker signals meet the required detection threshold, the amplification gain is set to the highest level. In the same unit, the Timing Single Channel Analyser (TSCA) component performs pulse discrimination and produces an output logic pulse when the signal's peak amplitude falls within a pulse-height window [202]. The level discriminator is defined by two preset threshold levels: an Upper-Level Discriminator (ULD) and a Lower-Level Discriminator (LLD), each calibrated to exclude noise and low-energy backgrounds from environmental radioactivity. The TSCA output typically occurs within 500 ns after the peak of the AMP output. Previously, an ORTEC 416A gate and delay generator unit was utilised after the AMP+TSCA unit to enable precise timing alignment between the two logic pulses. This step became unnecessary, once equal-length cables were introduced, and the unit was subsequently removed.

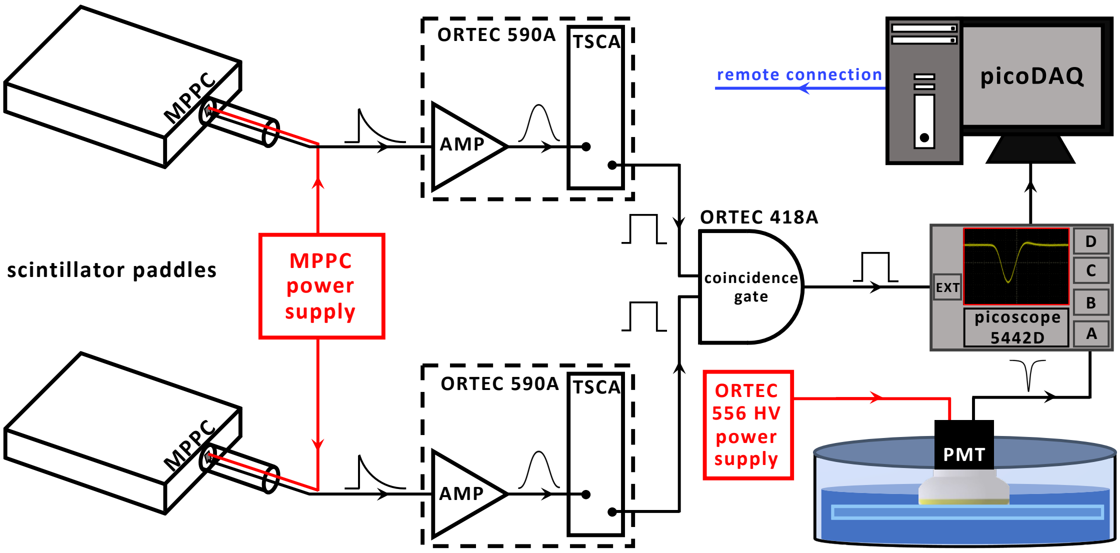

Figure 12.11: Schematic diagram of the hardware trigger system and the DAQ chain.

The ORTEC 418A universal coincidence module functions as an AND gate for the two logic inputs, with a 1 μs resolving time window per input channel. This window is selected to accommodate propagation delays in pulses from each MPPC. Once coincidence requirements are met, a single output logic pulse is produced and directed to the external trigger input of the DAQ system.

12.5 Data Acquisition

To digitise the PMT signals, the setup utilises a PicoScope 5442D 4-channel oscilloscope with an analogue bandwidth of 60 MHz, triggered through the external input. Although the oscilloscope supports multi-channel recording, this feature compromises the timing resolution. To overcome this, the hardware trigger system, described in Section 12.4.3, was created to enable exclusive recording and digitisation of the PMT channel at its maximum resolution.

A custom-built software package, called picoDAQ, was developed by the author using PicoSDK Python libraries to facilitate fast readout and remote control of the oscilloscope over Ethernet. The software interfaces directly with the digitiser, capturing event-by-event information and transmitting it to a data storage server in HDF5 file format. Full waveform traces, sampled every 2 ns for a duration of 4 μs, are captured for all light yield measurements. The oscilloscope offers a flexible resolution set to a 12-bit Analogue-to-Digital Converter (ADC) that provides a 488 μV vertical resolution for a 2 V dynamic range. Data is acquired continuously during a five-day run period for each light yield measurement. Figure 12.12 displays waveform traces in the PicoScope6 Graphical User Interface (GUI) for a typical triggered cosmic muon event.

12.6 Calibration

This section provides a detailed overview of the end-to-end calibration procedures implemented for the BabyK setup. Calibration is essential for ensuring the accuracy and reliability of experimental measurements and the characterisation of WLS samples. The following studies cover several critical aspects, including input HV tuning, gain stability monitoring, calibration of discriminator thresholds for the hardware trigger system, and water quality checks.

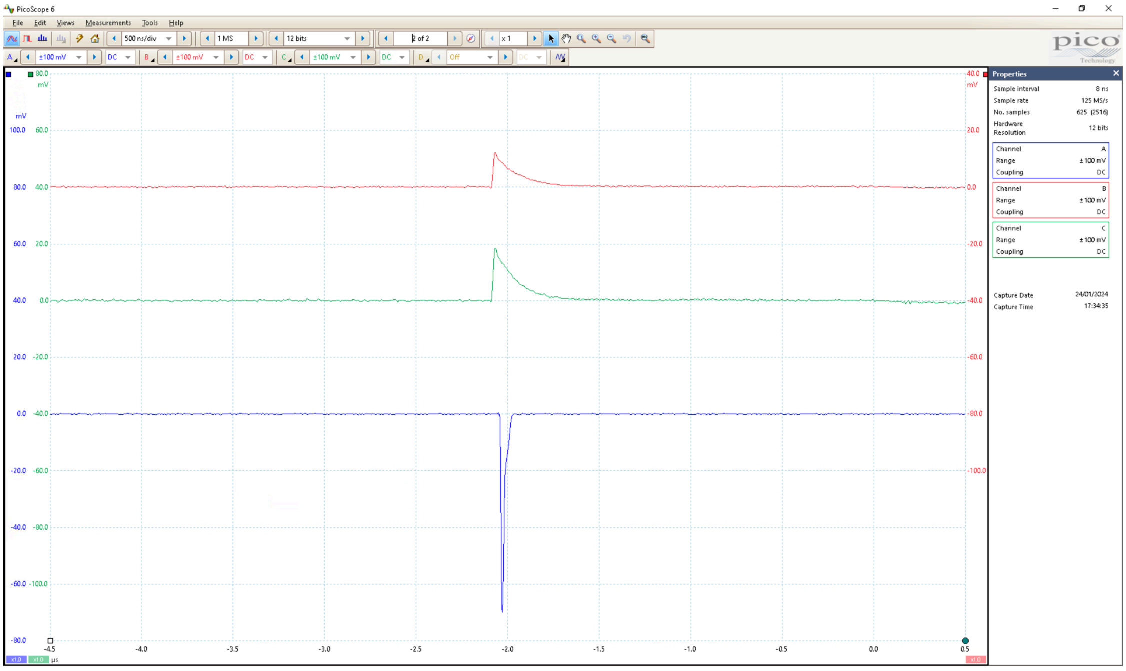

Properties

Sample interval 8 ns
Sample rate 125 MS/s
No. samples 625 (2516)
Hardware Resolution 12 bits

Channel A
Range ±100 mV
Coupling DC

Channel B
Range ±100 mV
Coupling DC

Channel C
Range ±100 mV
Coupling DC

Capture Date 24/01/2024
Capture Time 17:34:35

Figure 12.12: Screenshot of the PicoScope6 GUI for the PicoScope 5442D oscilloscope. The raw output from the MPPCs (red and green) and the PMT (blue) is shown for a triggered cosmic muon event.

12.6.1 High-Voltage Tuning

The calibration of the input HV for the Hamamatsu R6091 PMT is required to ensure optimal PMT operation at a nominal gain of 5×10^6. The procedure involves analysing the Single Photon Electron (SPE) spectrum from dark pulses produced at three distinct input high-voltages: 1500 V, 1600 V and 1700 V. These events originate from thermal electron emissions from the photocathode in complete darkness, generating a signal with an amplitude at the SPE level [203].

The picoDAQ software is configured to trigger a million PMT dark pulses at a threshold of -1 mV, storing a 1 μs window around each pulse. Waveforms with amplitudes exceeding the dynamic range of the oscilloscope were removed, which accounted for 0.001% of the total dataset. A DC offset correction is applied to each waveform by subtracting the mean amplitude displacement from the baseline, calculated over the first 400 ns of the waveform, from every data point. The total charge deposited (Q) is obtained by integrating waveforms in a fixed time window of [-17, 43] ns around the peak height. The averaged SPE waveform

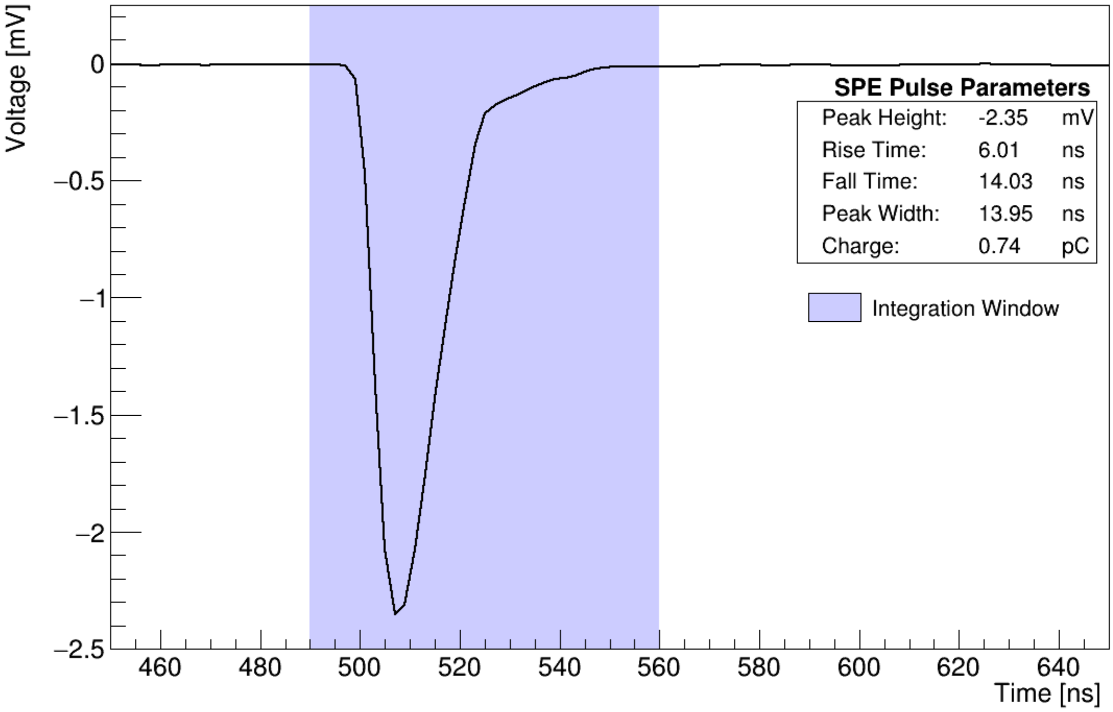

Figure 12.13: The average SPE waveform for the PMT at a gain of 5×10^6, with the pulse integration window highlighted.

is shown in Figure 12.13. The rise time corresponds to the time required for the pulse to increase from 10% to 90% of the peak amplitude and vice versa for the fall time.

Figure 12.14 shows the SPE charge distribution corresponding to the chosen input HV of 1700 V. The charge response shows two distinct features: the electronics noise peak and the SPE peak, both of which can be parameterised with separate Gaussian fits. A detailed description of the gain calculation and the extraction of SPE fit parameters follows:

- **Electronic Noise FWHM:** The electronics noise peak, often referred to as the pedestal, is the prominent narrow peak centred at 0 pC. These events are produced from the inherent electronic noise of the whole system. The Full Width Half Maximum (FWHM) of this peak is obtained from a Gaussian fit that uses bins equivalent to half the peak height on both sides of the peak.

- **Charge Peak:** The SPE distribution includes all instances of dark pulses produced by the PMT. Another Gaussian fit is applied that covers a range from 1/3 to 3/2 of the maximum peak height. The mean is taken as the SPE charge peak (Q_{SPE}) and the standard deviation (σ_{SPE}) is used to calculate the charge FWHM ($2\sqrt{2ln(2)}\sigma_{\text{SPE}}$).

- **Peak-to-Valley (P-V) Ratio:** This is obtained by comparing the amplitude of the SPE peak to the point where the pedestal distribution is exponentially falling as the valley. The valley minimum is extracted from a quadratic fit between the pedestal and the SPE charge peak. The P-V ratio is typically used as a figure of merit of PMT performance. A higher P-V ratio indicates better signal clarity, such that the PMT can effectively discriminate SPE signals from electronic noise.
- **Gain:** This is calculated as $g = Q_{\text{SPE}}/e$, where e is the elementary charge (1.6×10^{-19} pC).
- **High Charge Tail:** This ratio quantifies the number of events above $3\sigma_{\text{SPE}}$ relative to events above the electronic noise FWHM. It defines the extent of multi-PE contamination in the SPE peak, which is indistinguishable from the SPE peak for this particular PMT.

The results of the measurements of the SPE charge distribution fits at each input HV for the PMT are shown in Table 12.1. The statistical uncertainties on all SPE parameters extracted are at or below the 1% level. The PMT exhibits the best charge response and a gain of 5.29×10^6 at 1700 V, which is then chosen as the operating HV for all further measurements.

HV [V]	Charge Peak [pC]	Charge FWHM [pC]	P-V	Gain [10^6]
1500	0.34	0.19 ±0.01	2.31 ±0.02	2.11 ± 0.02
1600	0.50	0.51 ±0.01	2.26 ±0.02	3.11 ± 0.02
1700	0.74	0.81 ±0.03	2.64 ±0.03	5.29 ± 0.05

Table 12.1: The SPE peak parameters extracted from Gaussian fits to the charge distribution for varying input high-voltages.

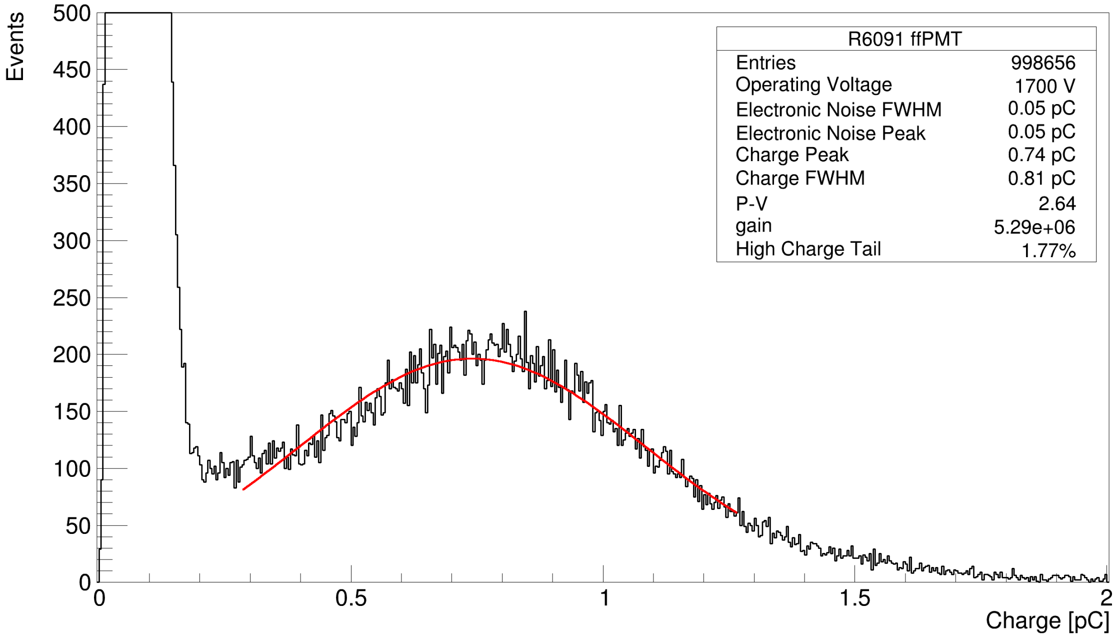

Figure 12.14: The charge distribution for the Hamamatsu R6091 PMT operating at 1700 V. The Gaussian fit to the SPE peak (red curve) and the extracted fit parameters are shown.

12.6.2 Gain Stability

The gain stability is continuously monitored to ensure consistent PMT performance throughout all experimental measurements. Gain fluctuations mainly arise from variations in temperature, operating voltage, and incident light exposure [204]. Figure 12.15 shows the gain evolution over the full data-taking period, with the main run periods highlighted. All measurements were taken following system-wide shutdowns, after performing open tank work necessary for the installation of the next WLS plate and prior to each light yield data run. The PMT gain exhibited relatively stable behaviour, with fluctuations remaining within $\sim$5% of the nominal gain. These differences are likely attributed to HV instabilities in the ORTEC 556 HV power supply, which was found to drift by up to 10% during operation. Minor HV adjustments were made to fine-tune the gain following prolonged periods of detector dead time. A systematic uncertainty due to gain instabilities is accounted for in all light yield measurements.

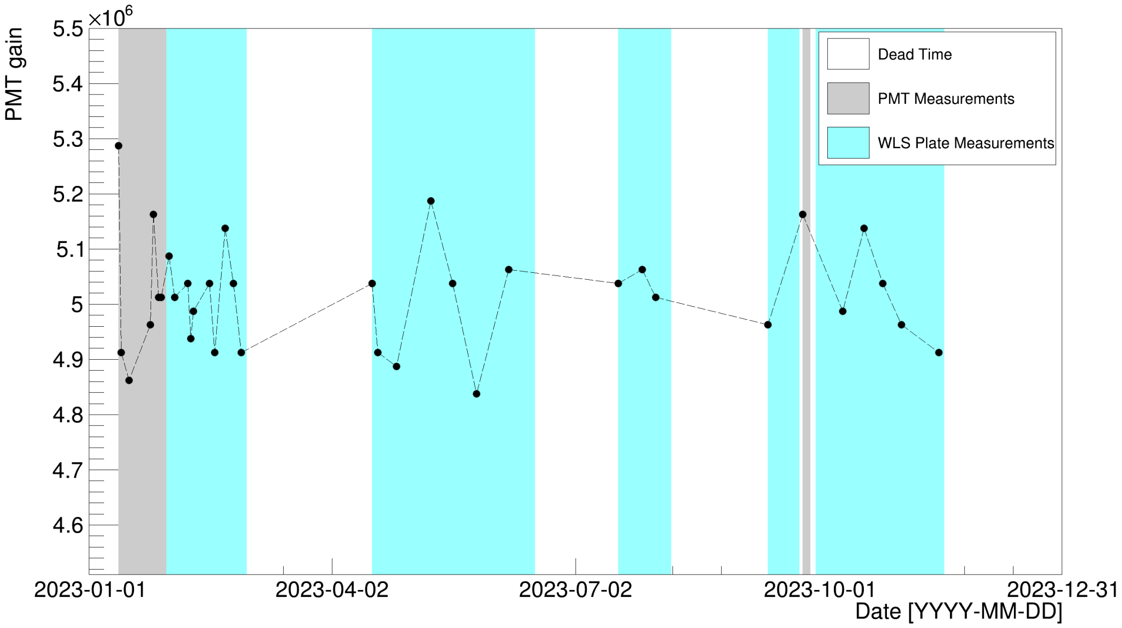

Figure 12.15: Time evolution of the PMT gain over the full run period for BabyK. Data-taking periods with a WLS plate sample (blue), bare PMT (grey) and dead time (white) are highlighted.

12.6.3 Coincidence Trigger Threshold

Calibration of the discriminator thresholds in the ORTEC 590A amplifier and TSCA units is required to maximise the trigger efficiency for cosmic muons. At low thresholds, the signal is dominated by electronic noise, MPPC dark pulses, and environmental γ-ray activity. Incident γ-rays between 10 keV - 10 MeV predominately undergo Compton scattering in plastic scintillators, transferring a fraction of their energy to produce an energetic recoil electron [106]. This interaction produces a pulse at low resolution and triggers a coincidence if the scattered γ-ray is detected in both scintillators.

Individual discriminator thresholds are defined for each detector to reduce the γ-ray and noise contribution to the signal. Coincidence events were recorded by adjusting the LLD between 10 - 80 mV, in 10 mV intervals. For each threshold measurement, picoDAQ either captures 10,000 events or records for two hours from both MPPC channels. In the offline analysis, triggered waveforms are integrated within a 500 ns time slice centred around the peak height.

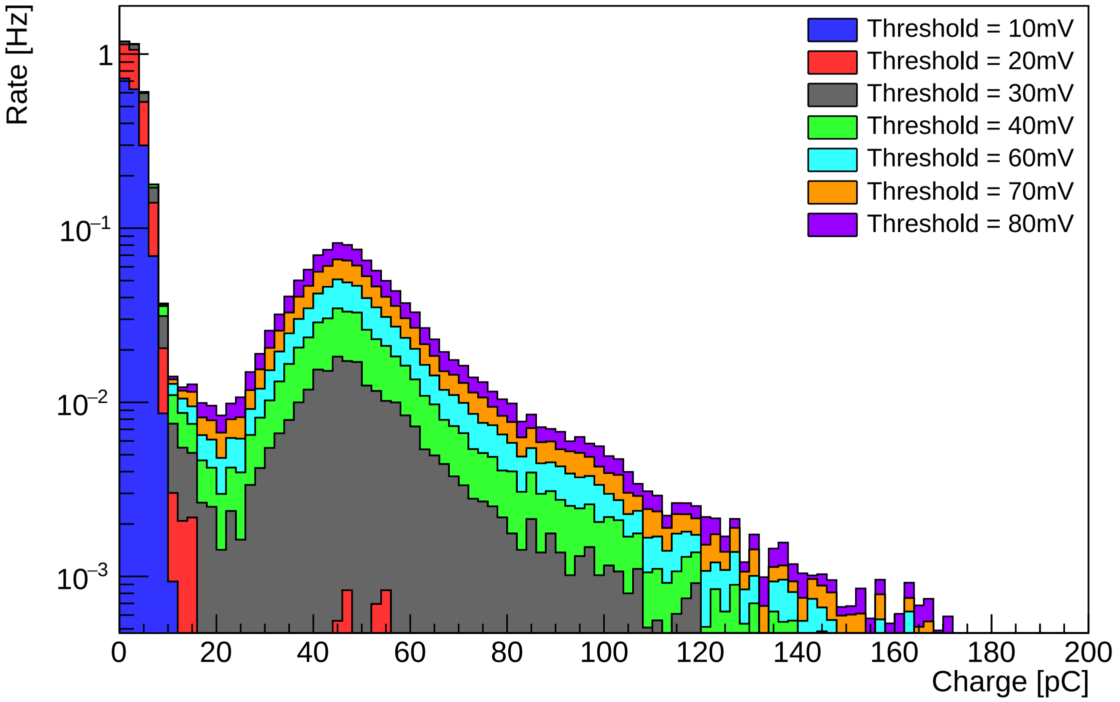

Figure 12.16: Charge distribution from a single plastic scintillator paddle for varying discriminator thresholds, between 10 - 80 mV.

The resulting spectrum for a single detector is shown in Figure 12.16[2]. The distribution consists of three main contributions: an initial peak dominated by MPPC dark noise and low-energy γ-rays, a peak centred at 50 pC mostly containing cosmic muons, and a subtle feature overlapping at 80 pC attributed to high-energy γ events. Setting a 40 mV threshold for both detectors effectively eliminates over 95% of the background peak while minimising the loss of muon signals. To remove the residual high-energy γ-ray induced-coincidences, a 30 $\times$ 30 $\times$ 1 cm lead sheet is placed between the plastic scintillators (see Figure12.4a). In this configuration, the muon event rate observed in BabyK is 0.2 Hz.

12.6.4 Water Transparency

Water quality and its stability are critical for the long-term operation of BabyK. Impurities such as bacteria, dust, and ions can affect the attenuation of Cherenkov light and thus compromise the detector's performance over time [48]. Since a

---

[2] The data run for the discriminator threshold at 50 mV has been omitted due to corruption of data files.

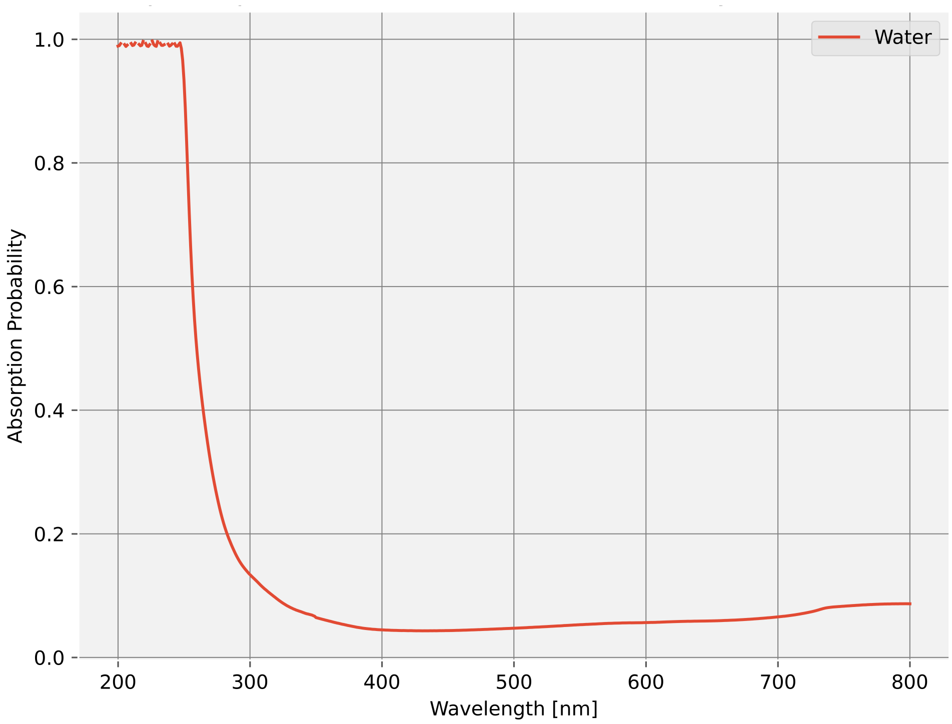

Figure 12.17: Absorbance spectrum of DI water obtained from the BabyK setup before data collection.

water purification and recirculation system is not integrated into the setup, the absorbance spectra were monitored at the start and end of the experiment's lifetime. The spectrum in Figure 12.17, taken prior to detector operation, shows significant absorption and scattering below 250 nm, transitioning sharply to near-optical transparency beyond 300 nm. The measurement recorded at the conclusion of the data-taking period, not shown, exhibited negligible variation, remaining consistent within approximately 2%. Therefore, minimal degradation in water quality is assumed over the experiment's operation.

12.7 Analysis

In the BabyK setup, an entirely data-driven approach is implemented to thoroughly characterise the performance of WLS plates in terms of two key performance metrics: the absolute and relative light yields. The following section provides a detailed description of the measurement and analysis procedure used to produce the final results.

12.7.1 Measurement Procedure

A series of light collection measurements are made in three detector configurations. An initial measurement of the bare PMT is performed to establish its baseline light yield (bare PMT). Subsequent data runs are carried out with the PMT-WLS plate photosensor unit (WLS) in place, following the installation procedure outlined in Section 12.1. In the third configuration, 3M DF2000MA polymeric film (WLS+tape) is adhered to the outer edges of the WLS plate to maximise light trapping via TIR. The tape is applied, without altering the photosensor assembly, to ensure consistent optical contact at the PMT-WLS plate interface. This cycle of WLS plate measurements is repeated for each sample listed in Table 11.1.

12.7.2 Relative Light Yield

The absolute light yield (LY), defined as the average number of p.e. produced by PMT signals, is essential for characterising the performance of each WLS plate. To extract the LY, offline signal processing techniques, illustrated in Figure 12.18, are applied directly to digitised PMT waveforms acquired from picoDAQ. This involves several steps:

- **Baseline correction**: Adjusting the baseline to account for any initial offset in the signal.
- **ADC saturation check**: Ensuring the ADC has not saturated, which would distort the measurement.
- **Noise event elimination**: Removing residual noise events using a dedicated peak-finding algorithm.

The peak-finding algorithm identifies and selects distinct peaks that fall below a -7 mV threshold within 200 ns of the trigger time. To quantify the total charge deposited, each waveform is integrated within a $[-50, 100]$ ns time window around the peak. This integrated charge is then normalised to the single photoelectron charge (Q_{SPE}), resulting in a distribution of detected photoelectrons. Finally, the absolute LY is determined by extracting the mean value from this distribution.

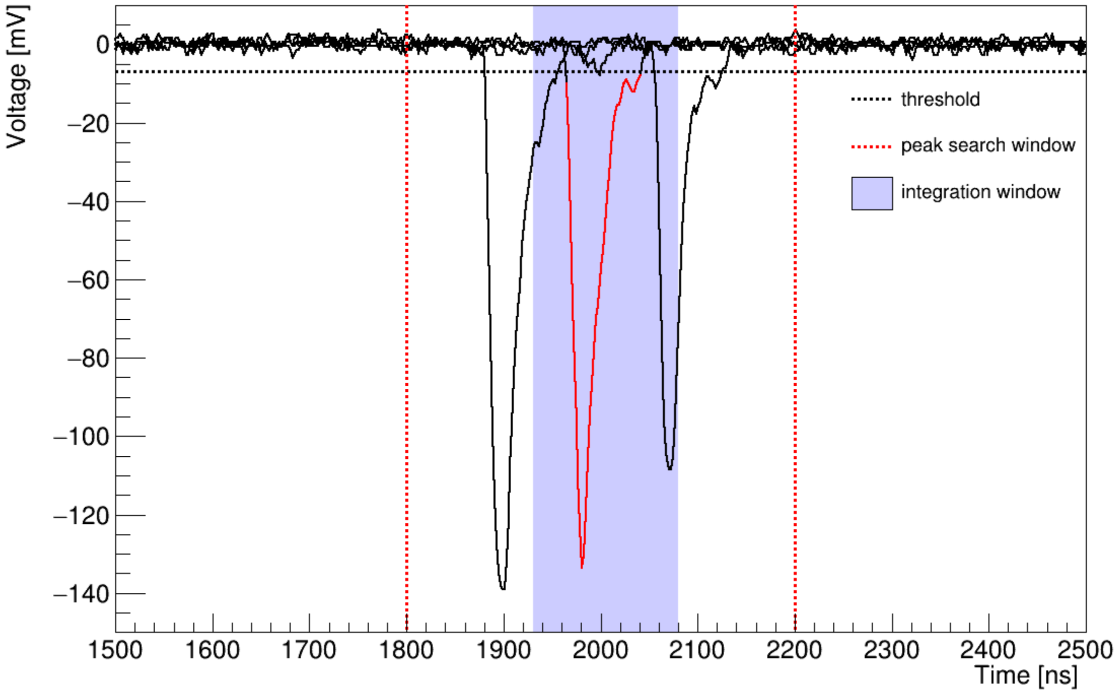

Figure 12.18: Digitised PMT waveforms showcasing the criteria for the peak-finder algorithm. The peak search window (red dashed), minimum threshold (black dashed) and integration window (purple) around a selected waveform are drawn.

Estimating the light collection enhancement of the WLS plate with respect to the bare PMT is challenging due to the geometric configuration of the BabyK photosensor unit. The bare PMT exclusively detects photons directly incident on the photocathode, while the WLS plate, covering the entire photocathode surface, introduces a shadowing effect. This results in a fraction of the direct light being obscured due to passive absorption and Mie scattering, which influences the measured LY. Therefore, performance evaluation is carried out by comparing the entire PMT+WLS plate unit across different samples.

A direct comparison of the light yields requires a detailed simulation to scale between the various plate geometries. Although initial studies were performed to reproduce the complete BabyK setup in a GEANT4-based MC framework, the simulation could not fully replicate the intricacies of the Mie effect observed in the in-air optical WLS plate measurements (refer to Chapter 11). These studies are now only used to evaluate the geometric effects of the WLS plates (see Appendix B.3).

Therefore, for the final comparison study, the relative light yield (RLY) compared to a reference WLS plate (ref) is used, calculated as

$$\mathrm{RLY} = \frac{\mathrm{LY}_{\mathrm{WLS}}}{\mathrm{LY}_{\mathrm{ref}}}. \tag{12.2}$$

By leveraging the availability of a large Kuraray B2 WLS plate, several smaller samples were prepared to serve as suitable reference standards. A similar figure of merit is calculated to determine the relative tape enhancement (RTE),

$$\mathrm{RTE} = \frac{\mathrm{LY}_{\mathrm{WLS(+tape)}}}{\mathrm{LY}_{\mathrm{ref(+tape)}}}. \tag{12.3}$$

12.7.3 Systematic Uncertainties

The systematic uncertainty on the measured LY is estimated by considering all potential detector and measurement effects. The primary source of uncertainty arises from the reproducibility of the optical coupling between the PMT and WLS plate. This is due to challenges associated with ensuring precise control over the uniformity of optical grease, maintaining consistent press-fit quality, and achieving accurate WLS plate positioning during assembly. To quantify this effect, a comparative analysis is performed by measuring the light yields of a single Kuraray B2-3 WLS plate twice within the experimental setup. The process involves dismounting the plate, cleaning the photosensor components, reapplying optical grease, and remounting the assembly in between measurements. The observed variance in the measured light yields is 4.5%, which is used as the overall systematic uncertainty for this analysis. Although fluctuations in PMT gain and water quality also influence the measured LY, the reproducibility study already incorporates these effects as the measurements were taken several months apart. To obtain the total error on each LY measurement, the systematic and statistical uncertainties are summed in quadrature. Thus, the error on the RLY and RTE performance metrics are calculated as

$$\sigma_{\mathrm{RLY(RTE)}} = \sqrt{\left(\frac{\sigma_{\mathrm{LY}_{\mathrm{WLS(+tape)}}}}{\mathrm{LY}_{\mathrm{WLS(+tape)}}}\right)^2 + \left(\frac{\sigma_{\mathrm{LY}_{\mathrm{ref(+tape)}}}}{\mathrm{LY}_{\mathrm{ref(+tape)}}}\right)^2}. \tag{12.4}$$

12.8 Results

This section presents a thorough investigation into the key factors influencing the performance of WLS plates. The analysis covers the impact of variations in plate dimensions, plastic bases, fluor compositions, and reflective tape on both light collection enhancement and timing. Following this, a direct comparative study of the three main WLS plate manufacturers, Eljen, Kuraray, and V.A. Kargin Polymer Research Institute are carried out. This analysis, being the first of its kind, provides valuable insights to guide the final selection of the WLS plate in the HK-OD.

12.8.1 Varying Plate Geometry

This study explores the variation in absolute LY across different geometric configurations of the Kuraray B2 WLS plate. Figure 12.19 shows the photoelectron distributions for the bare PMT, rectangular (B2-1), and square (B2-2) WLS plates, both with and without reflective tape.

The rectangular plate exhibits a 41% lower absolute LY than the square plate, primarily due to an asymmetry in the light collection efficiency between the two sides. Photons emitted within the longer sides experience more attenuation as they traverse extended distances to reach the PMT, which increases light loss through self-absorption and Mie scattering. These effects are less severe on the narrower sides of the plate, allowing for a greater detection efficiency in this region. In contrast, the radial symmetry of the square shape enables a more uniform light collection around the PMT, resulting in a higher LY. Simulations of both WLS plate geometries in a hemispherical photosensor configuration, separate from this thesis, support these findings [177]. The enhancement with reflective tape is slightly more pronounced for the rectangular plate (23%) compared to the square plate (12%). This can also be attributed to geometry-related factors, as the tape maximises light transmission more efficiently in the narrower edges of the rectangular plate than around the square plate edges.

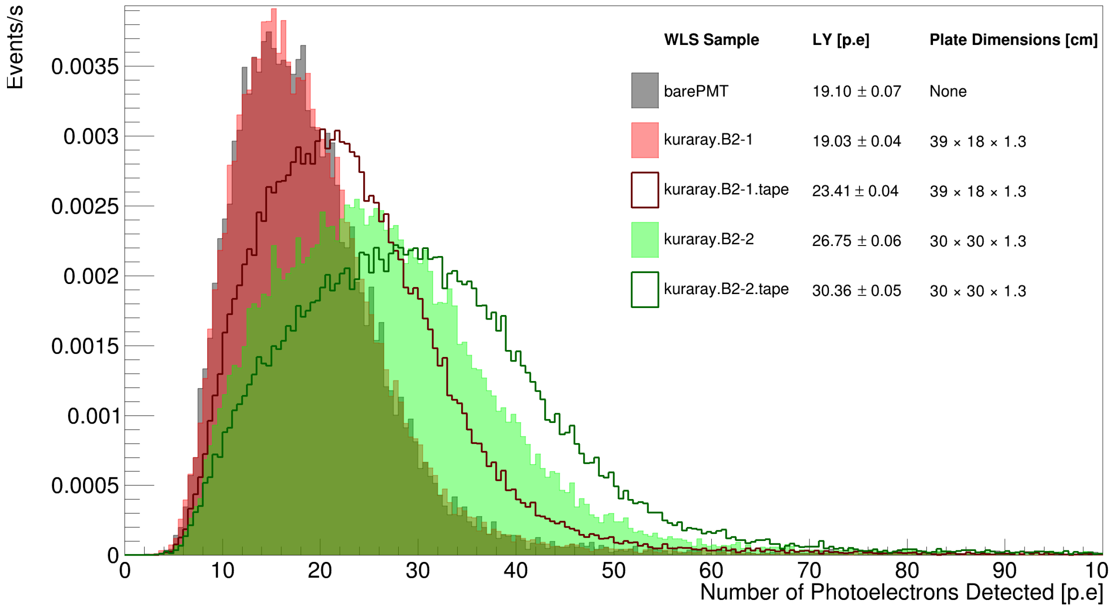

Figure 12.19: Distributions of the number detected p.e. for the bare PMT (grey), Kuraray B2-1 (red), and Kuraray B2-2 (green) WLS plates, with and without reflective tape. The LY, with its statistical error, and plate dimensions are shown for each measurement.

However, the overall increase for both configurations with reflective tape is moderate in comparison to recent experimental findings from a prototype HK-OD photosensor at the Institute for Nuclear Research (INR). Their study demonstrated a two-fold improvement in the light collection efficiency using the same reflective tape [179]. These results are not consistent as each photosensor geometry is better suited for detecting photons trapped by TIR along different propagation paths, as shown in Figure 12.20.

The hemispherical photosensor unit has greater acceptance to the horizontally going component of the isotropically re-emitted photons as the PMT interfaces with the inner edge of the WLS plate. The reflective tape further amplifies light collection by increasing reflections in this direction. In contrast, the flat-faced PMT in the BabyK photosensor unit is more likely to detect photons that reflect from the upper and lower surfaces of the WLS plate, rather than at the edges. Although the BabyK photosensor geometry does not fully reproduce the enhancement that will be observed for the HK-OD photosensor unit, all LY measurements reaffirm the effectiveness of the reflective tape.

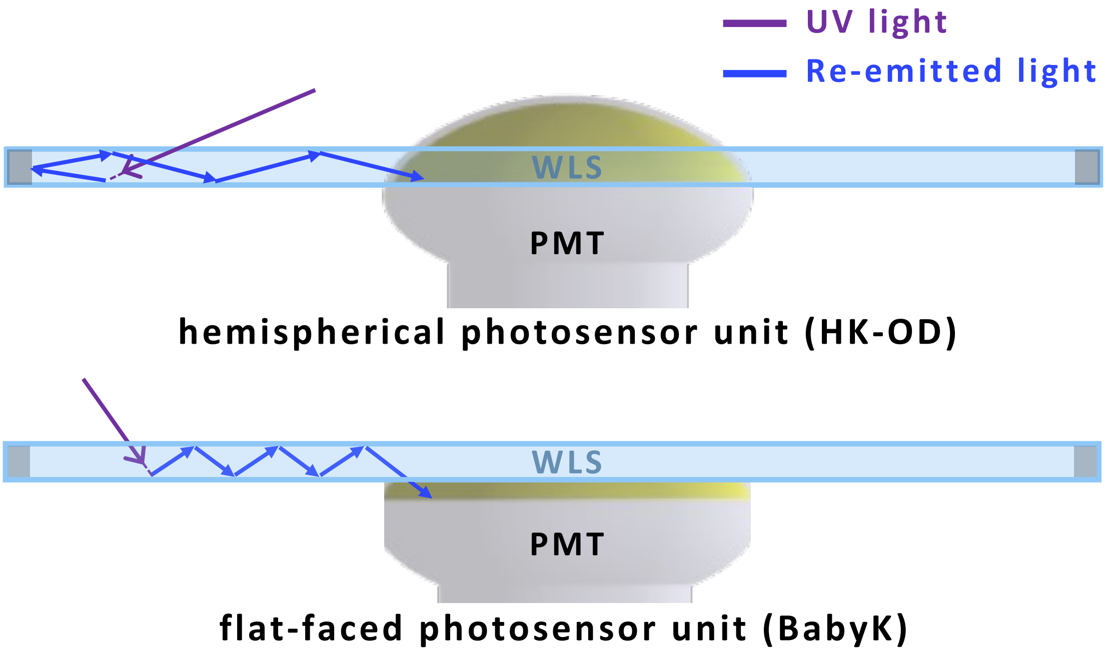

Figure 12.20: Schematic diagrams of two photosensor units with hemispherical (upper) and flat-faced (lower) geometries. UV light (purple) incident on the photosensor unit is absorbed, re-emitted in the visible spectrum (blue) and undergoes TIR within the plate before detection at the PMT.

The comparison of the absolute LY between the two Kuraray B2 WLS plates with varying thicknesses is presented in Figure 12.21. The distributions show no significant enhancement in LY for approximately doubling the plate thickness. This is expected, as the active absorption length of the fluor is constrained to a few millimetres (see Chapter 11). The only advantage a thicker plate provides is that the photon undergoes fewer TIRs before detection, minimising light loss associated with multiple reflections. Increasing the plate thickness further will eventually elevate losses due to shadowing effects and attenuation. These findings experimentally verify that the square shape and thickness chosen for the HK-OD photosensor are correctly optimised.

12.8.2 Impact on Timing

The time distribution of average waveforms, presented in Figure 12.22, illustrates the influence of the WLS plate and reflective tape on timing resolution. The ±10 ns offset observed between measurements is caused by minor variations

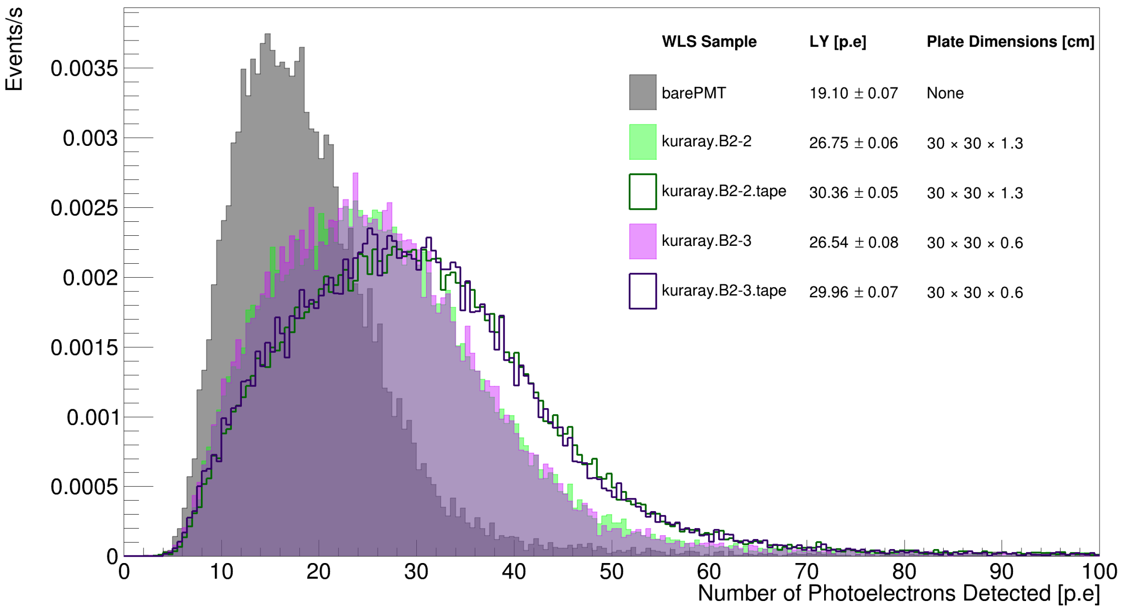

Figure 12.21: Distributions of the number detected p.e. for the bare PMT (grey), Kuraray B2-2 (green), and Kuraray B2-3 (magenta) WLS plates, with and without reflective tape. The LY, with its statistical error, and plate dimensions are shown for each measurement.

in the alignment of the muon telescope between runs. Across different plate geometries, an increase in pulse amplitude is observed with minimal effect on time spread. Given the fluor's short decay time constant $\mathcal{O}(2\text{ ns})$, the primary factor influencing the time spread is the occurrence of multiple reflections of re-emitted photons. Although the reflective tape enhances photon detection at larger radial distances, as demonstrated in BabyK simulations (see Appendix B.3), the majority of detected photons remain concentrated near the PMT. The effect of the reflective tape on timing may be more pronounced for the hemispherical photosensor geometry, particularly with the addition of reflective Tyvek on the back side. In summary, these results indicate that the timing is not significantly affected by the incorporation of a WLS plate and reflective tape for the BabyK photosensor unit.

12.8.3 PMMA versus PVT

To evaluate the performance of PMMA (Kuraray and V.A. Kargin) and PVT-based (Eljen) WLS plates, it is crucial to understand their material properties.

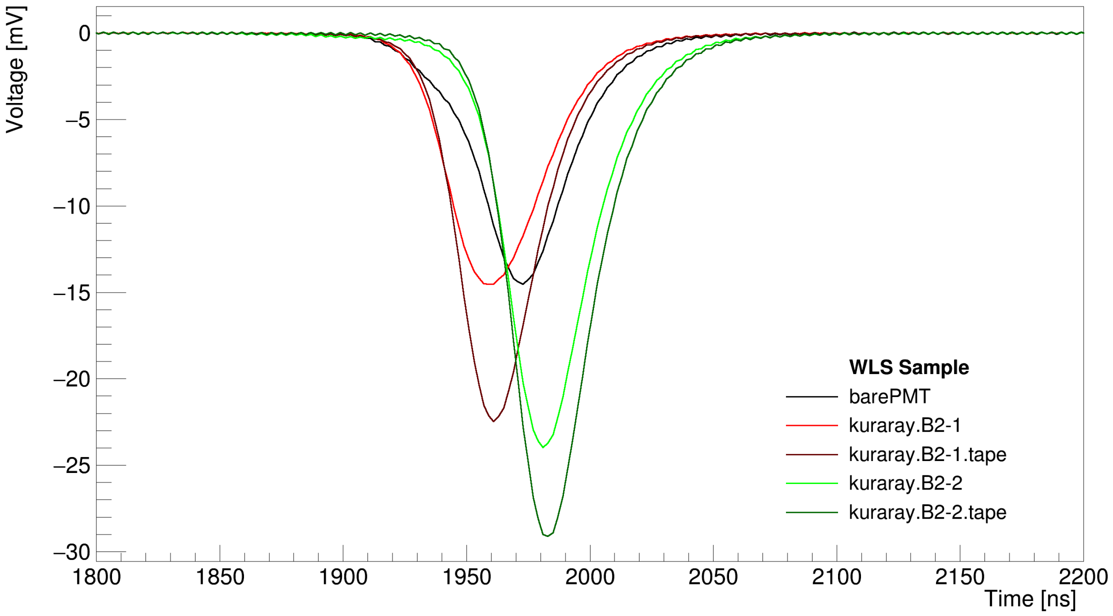

Figure 12.22: The average waveform for the bare PMT (black), Kuraray B2-1 (red) and Kuraray B2-2 (green) WLS plates, with and without reflective tape.

Specifically, the refractive index of the WLS plastic determines the reflectance and critical angle at optical boundaries, which directly influences the LY. For these studies, the PMMA and PVT plastics under evaluation in BabyK have refractive indices of $n_{\text{PMMA}} = 1.49$ and $n_{\text{PVT}} = 1.58$. The capture efficiency of the WLS plate is determined by,

$$\epsilon_{\text{TIR}} = \cos(\theta_{\text{crit}}) = \sqrt{1 - \left(\frac{n_2}{n_1}\right)^2} \tag{12.5}$$

where n_1 and n_2 are the refractive indices of the base plastic and the surrounding medium, respectively [205, 206]. The full derivation considers the solid angle subtended over an area ($\theta \in [0, \theta_c]$, $\phi \in [0, 2\pi]$) and substitutes Equation 11.1 into θ_{crit}. Equation 12.5 is only applicable when light is incident on an optical boundary with $n_1 > n_2$. For a WLS plate-water interface, $\epsilon_{\text{TIR}} = 0.45$ for PMMA and $\epsilon_{\text{TIR}} = 0.54$ for PVT. While the PVT plate is more effective at retaining light via TIR in the plate, this characteristic also results in a greater amount of light loss at the photosensor coupling interface.

In the BabyK photosensor unit, optical-grade silicone grease, with a refractive index of $n_{\text{grease}} = 1.465$, is applied between the PMT-WLS plate interface to

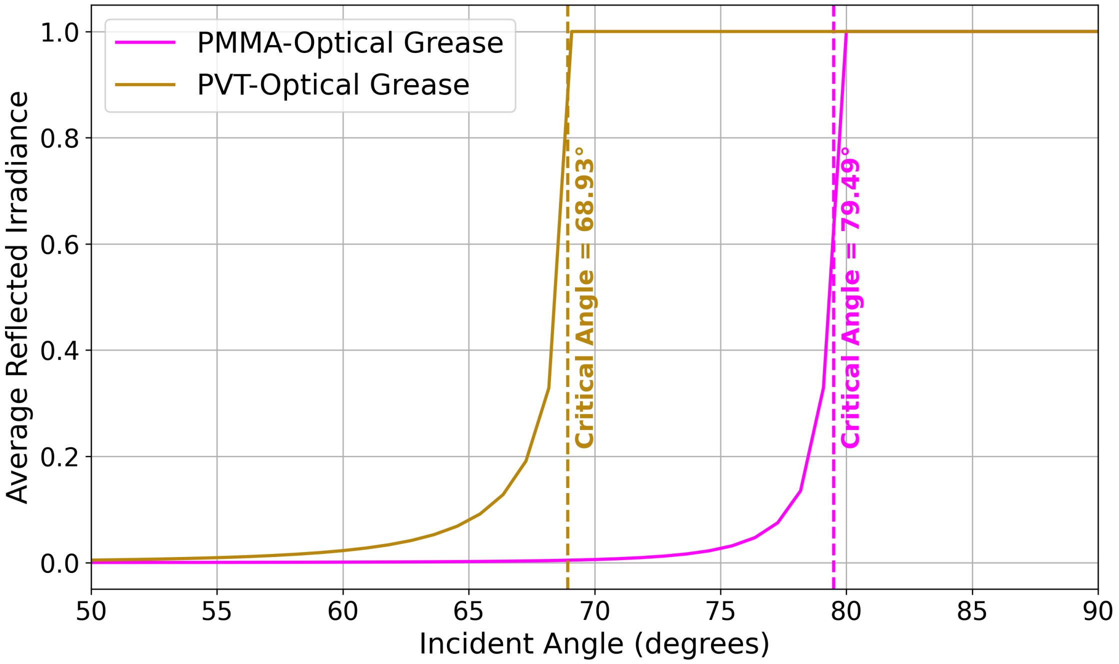

Figure 12.23: The effective reflection coefficients at the PMMA-grease and PVT-grease optical boundaries, with the critical angle labelled.

maximise transmission. Reflections at the WLS plate-grease boundary will still occur depending on the extent of the refractive index mismatch. Figure 12.23 shows the effective reflection coefficients (R_{eff}) for the PVT-grease and PMMA-grease interfaces, calculated using the Fresnel equations (see Appendix B.4) [207].

The general trend follows a gradual increase in the R_{eff} at small angles, with a sharp rise occurring at θ_{crit}, beyond which the distribution plateaus at a theoretical maximum for TIR. Due to the smaller θ_{crit} for the PVT-grease interface, light has a higher probability of experiencing TIR compared to the PMMA-grease interface, resulting in less efficient transmission to the PMT. At normal incidence, the reflectivity is 0.14% (PVT-grease) and 7.16×10^{-3}% (PMMA-grease). Simultaneously, reflections will influence the degree of shadowing at the WLS plate-water interface, with values of 0.74% for PVT and 0.32% for PMMA. Considering these effects, the measured light yield for the PVT plate might be lower than its actual value due to the photosensor geometry and materials used in the BabyK setup.

12.8.4 Performance Comparison of Single Fluor Plates

A comparison of the measured LY between the Kuraray B2-1 plate and two V.A. Kargin WLS plates, doped with separate concentrations of POPOP200 and BisMSB50 fluors, is presented in Figure 12.24. The performance across the WLS plate samples without reflective tape is consistent, with fluctuations within ∼5%. Despite this apparent uniformity, subtle variations in the behaviour of the fluors and the PMMA bases contribute to the observed results.

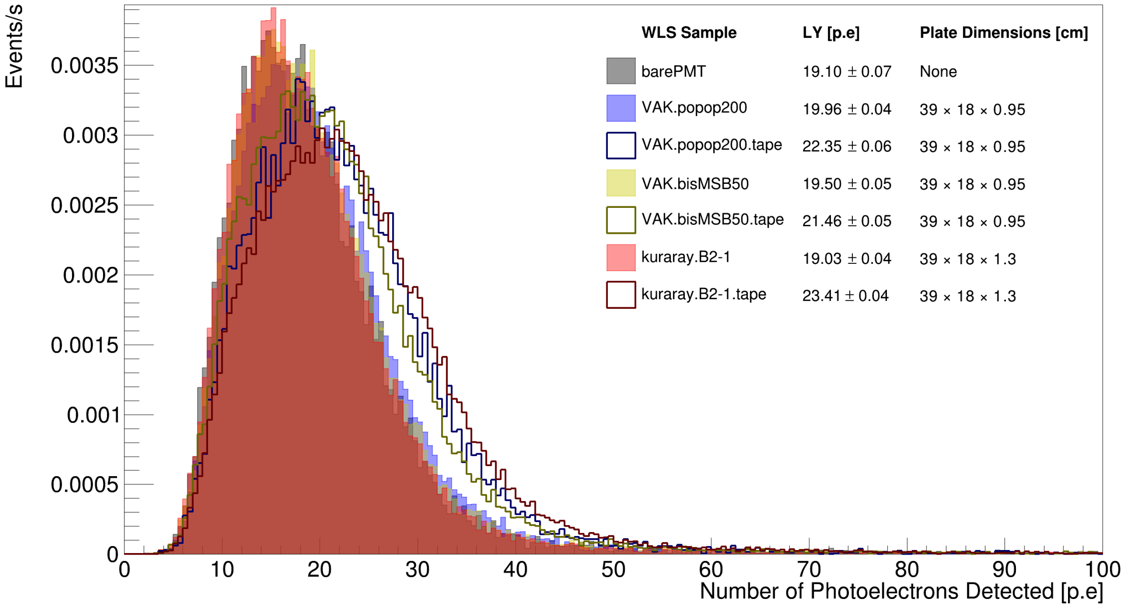

Figure 12.24: Distributions of the number detected p.e. for the bare PMT (grey), V.A. Kargin POPOP200 (blue), BisMSB50 (yellow), and Kuraray B2-1 (red) WLS plates, with and without reflective tape. The LY, with its statistical error, and plate dimensions are shown for each measurement.

The POPOP200 and BisMSB50 WLS plates demonstrated the highest absorption across the entire UV-VISIBLE range in the in-air optical measurements (see Figure 11.7). The additional augmentation in the spectrum is likely attributed to self-absorption and Mie scattering effects. This is evident in the BabyK results, as no substantial increase in the LY is observed for the POPOP200 and BisMSB50 WLS plates compared to the Kuraray B2-1 sample. There is a noticeable upturn in the light collection efficiency for the Kuarary B2-1 WLS plate, with the addition of the reflective tape. The measured LY for the Kuraray B2-1 surpasses both single fluor samples by approximately 5 - 10% in this configuration. The Kuraray B2-1 plate experiences fewer losses due to its superior optical transparency to re-emitted light, mitigating the impact on the overall LY.

During the timeframe of this thesis, V.A. Kargin developed and produced a new batch of WLS samples with double-fluor concentrations. These samples replace the single fluor plates to serve as one of the flagship candidates for the HK-OD photosensor unit. For completeness, the RLY and RTE for the single fluor plates are shown in Table 12.2.

WLS Sample	**LY [p.e]**	**TE [p.e]**	**RLY**	**RTE**
VAK-POPOP200	19.96 ± 0.90	22.35 ± 1.00	1.05 ± 0.06	0.95 ± 0.06
VAK-BisMSB50	19.50 ± 0.88	21.46 ± 0.97	1.02 ± 0.06	0.92 ± 0.06
Kuraray B2-1	19.03 ± 0.87	23.41 ± 1.05	1.00	1.00

Table 12.2: Summary of the performance metrics of the V.A. Kargin POPOP200, BisMSB50 and the Kuraray B2-2 WLS plates. The Kuraray B2-1 is used as the reference for the calculations of the RLY and RTE.

12.8.5 Performance Comparison of OD Candidates

A quantitative comparison of the Eljen EJ286, Kuraray B2 and VAK-POPOP50-PPO3000 WLS plates, with near identical dimensions, is presented in Figure 12.25. The absolute and relative LY results, with statistical and systematic uncertainties, are shown in Table 12.3.

The experimental results show optimal performance for all three WLS plates in the BabyK setup. While the Kuraray B2 WLS plate, with and without reflective tape, shows a slight edge, the enhancement is not statistically significant above measurement uncertainties. Considering financial aspects, the Eljen EJ286 WLS plate is several times more expensive per unit, yet, provides no substantial performance advantage to justify the increase in expenditure. Therefore, the preferred choices for the HK-OD are the V.A. Kargin POPOP50-PPO3000 and the Kuraray B2 WLS plates, both of which offer cost-effectiveness and demonstrated functionality.

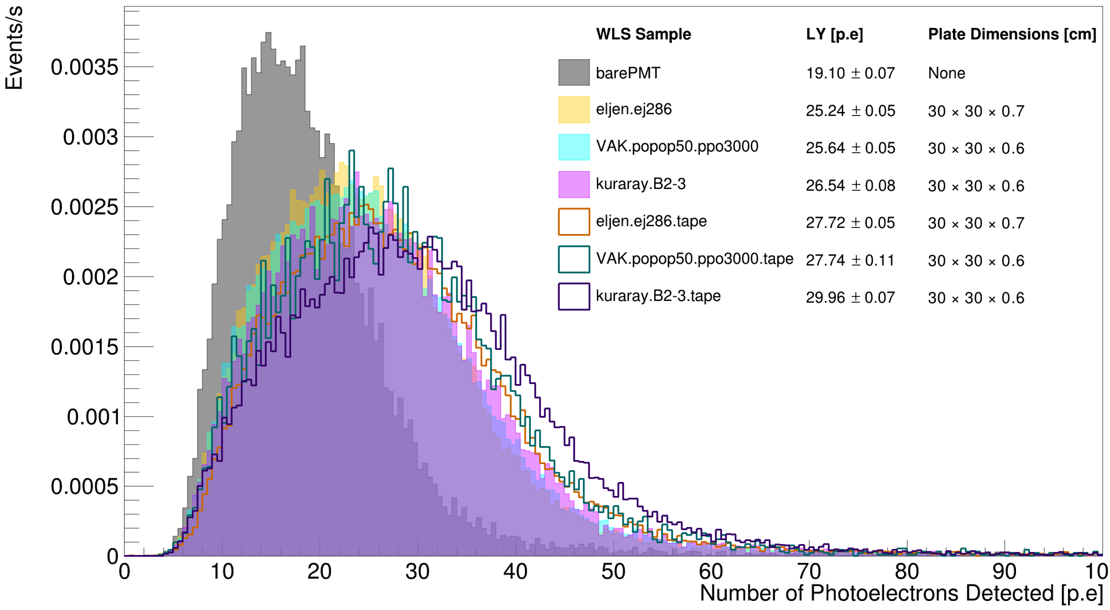

Figure 12.25: Distributions of the number detected p.e. for the bare PMT (grey), Eljen EJ286 (yellow), VAK-POPOP50-PPO3000 (cyan), and Kuraray B2 (magenta) WLS plates, with and without reflective tape. The LY, with its statistical error, and plate dimensions are shown for each measurement.

WLS Sample	LY [p.e]	TE [p.e]	RLY	RTE
VAK-POPOP50-PPO3000-2	25.64 ± 1.15	27.74 ± 1.25	0.97 ± 0.06	0.93 ± 0.06
Eljen EJ286-2	25.24 ± 1.14	27.72 ± 1.25	0.95 ± 0.06	0.93 ± 0.06
Kuraray B2-3	26.54 ± 1.19	29.96 ± 1.35	1.00	1.00

Table 12.3: Summary of the performance metrics of the V.A. Kargin POPOP50-PPO3000-2, Eljen EJ286-2, and the Kuraray B2-3 WLS plates. The Kuraray B2-3 is used as the reference for the calculations of the RLY and RTE.

12.9 Next Steps

A second iteration of the detector setup, called InfantK, is currently under construction at INR. InfantK will be dedicated to comparing the performance of the V.A. Kargin POPOP50-PPO3000 and Kuraray B2 WLS plates using the HK-OD photosensor geometry as a continuation of the work completed in this thesis. The detector setup includes the Hamamatsu R14734 3-inch hemispherical PMT and double-layered Tyvek to more closely match the conditions of the HK-OD. This next phase of experimentation is expected to conclusively determine the optimal WLS plate for the HK-OD.

Part III

Summary

13

Conclusions and Outlook

This thesis covers two main topics. First, a search for the DSNB using 552.2 days of live data from the SK-VI phase has been carried out. A novel ML technique, called the Gamma And Positron CNN model (GAPNet), was developed and integrated into the analysis to enhance the rejection of the atmospheric NCQE background. This involved training a ResNet18 CNN architecture to discriminate between e^+/γ signals from IBD and NCQE MC events based on the spatial and temporal distribution of raw PMT hit information. The output classification score of the GAPNet model, representing the "IBD-likeness" of an event, was introduced into the analysis as a new positron observable, called softmax.

The classification capability of the GAPNet model was evaluated using an independent MC test set and calibration data acquired from SK-VI LINAC runs. These studies revealed that the model exhibits strong performance above 12 MeV but demonstrates an inherent energy-dependence effect. Therefore, a new set of energy-dependent softmax cuts was introduced as a supplementary reduction technique, alongside the traditional Cherenkov angle cut. These cuts, along with other positron observables, were optimised in the SPLASH framework, which the author extended to incorporate new tools for ML-based analysis into the traditional SK analysis pipeline. The softmax cut resulted in a reduction of the NCQE background spectrum by 40% - 60%, depending on the energy bins, compared to the previous SK-VI DSNB analysis.

The full analysis procedure and reduction criteria were applied to the SK-VI SHE+AFT triggered dataset. The final sample consisted of six events in the 8 - 30 MeV energy search window. Since the p-value test confirmed that no significant excess over the background was observed, a 90% C.L. upper limit on the $\overline{\nu}_e$ was set. The observed and expected upper limits of DSNB flux are 0.27 – 16.03 and 0.31 – 49.53 $\mathrm{cm}^{-2}\mathrm{s}^{-1}\mathrm{MeV}^{-1}$ across the energy bins, respectively. This result demonstrated improved expected upper limits in three energy bins compared to the previous SK-VI DSNB analysis, which is due to the new softmax cut. However, further treatment of the ML-related systematic uncertainties is required to fully quantify this result, as well as an *interpretability* analysis of the model training and performance. Nevertheless, the methods presented in this thesis are applicable to future DSNB searches in the SK detector and may aid in potential discoveries.

The second part of this thesis focused on optimising the design and performing precision measurements of photosensor components for the HK-OD. A data-driven study was conducted to determine the optimal number of photosensors needed for the HK-OD while maintaining its veto capability. This involved masking SK-OD channels from a one-day dataset from the SK-IV atmospheric sample and comparing the OD hit distributions to HK simulations. This allowed for the extrapolation of a photocathode coverage scaling between the two detector configurations. From this analysis, it was determined that a HK-OD containing 7,200 photosensors is approximately equivalent to the full SK-OD. Based on the findings of this analysis, a design guideline proposing reducing the instrumentation from 10,000 to 7,200 OD photosensors in the HK-OD was put forward and accepted by the HK collaboration. However, recent budget constraints have necessitated further re-evaluation of this design, which is currently ongoing.

Furthermore, optical in-air and water-based measurements of WLS plates were conducted in two custom-built setups, developed by the author, to optimise the selection of WLS plates for the HK-OD. Both studies evaluated eleven candidate samples from Eljen, Kuraray, V.A. Kargin Polymer Research Institute in Russia, and LabLogic UK manufacturers. In the first setup, UV-VISIBLE spectrophotometry using a powerful laser was carried out to measure the absorption and attenuation length of the samples in the air. These measurements demonstrated a previously unknown artefact of Mie scattering present in all candidate WLS samples. In the second setup, known as the BabyK WLS plate test facility, the performance of the WLS plates was evaluated in response to cosmic muons in ultra-pure water. The full R&D process of the detector construction was presented in detail. The final results indicate that the preferred choices for the HK-OD are the V.A. Kargin POPOP50-PPO3000 or the Kuraray B2 WLS plates. Therefore, the research in this thesis has significantly influenced the design of the HK-OD.

Appendices

A
Positron Selection Criteria

This appendix documents the cut optimisation procedure and provides supplementary figures of positron observables used as part of the third reduction in Section 7.4.

A.1 Cut Optimisation

The cut optimisation procedure for prompt positron selection variables is based on comparing the IBD MC with the atmospheric neutrino MC. Since the effectiveness of the cuts is not strongly influenced by the choice of the DSNB model, this analysis only considers the Horiuchi+09 model [37]. In SPLASH, the cut criteria for the Cherenkov angle, charge over hit and softmax cuts are determined by maximising the following figure of merit (FOM):

$$\mathrm{FOM} = \frac{\mathrm{S}}{\sqrt{\mathrm{S}+\mathrm{B}}},$$

which represents the statistical significance of the signal (S) in presence of a background (B). For energy-dependent cuts, the optimisation is carried out per 2 MeV bin.

A.2 Effective Wall Distance

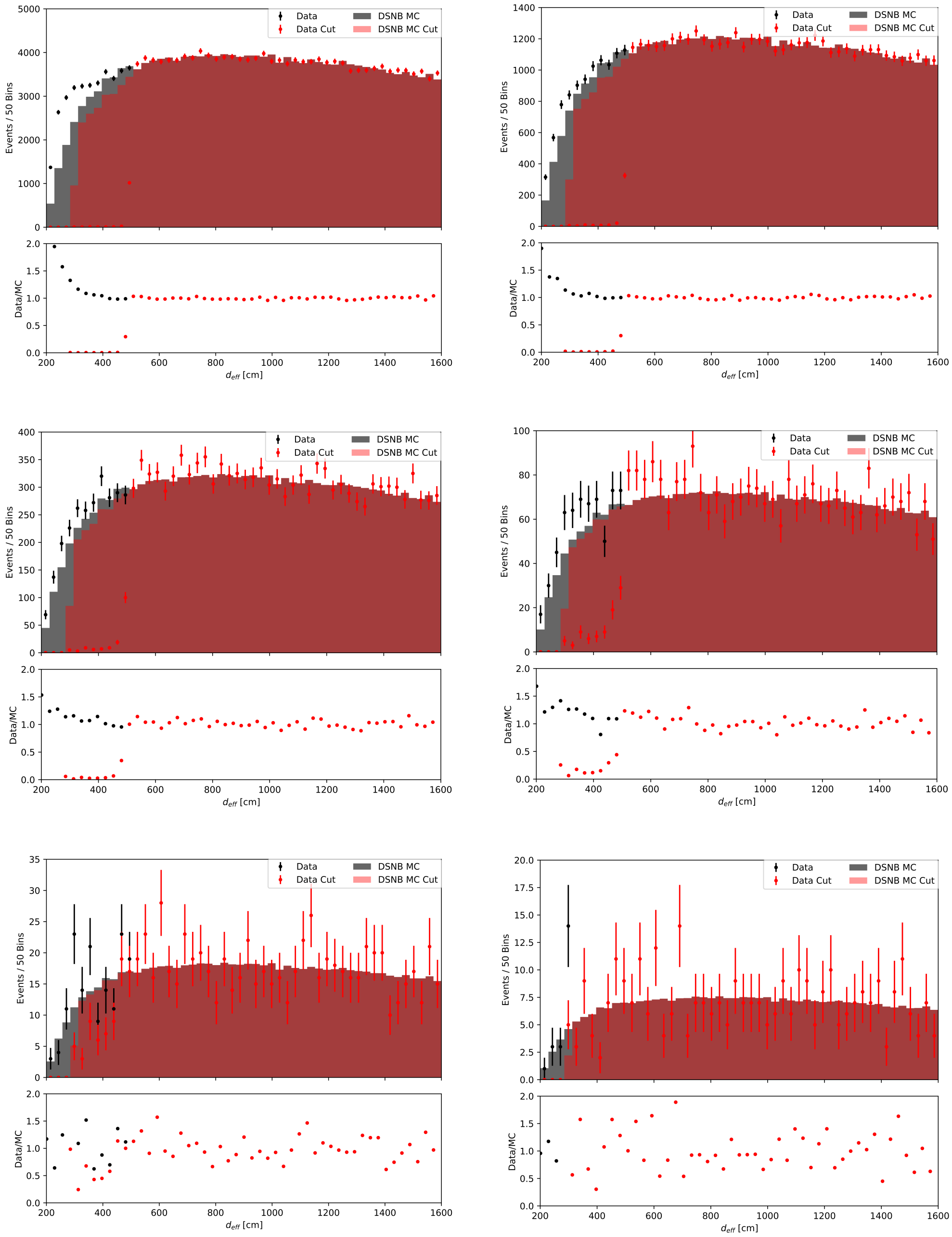

Figure A.1: The d_{eff} distributions for data (points) and DSNB MC (histogram), with the Horiuchi+09 DSNB model assumed, before (black, grey) and after (red) the cut is applied. Each figure shows a different energy region: E > 8 MeV (top left), E > 10 MeV (top right), E > 12 MeV (centre left), E > 14 MeV (centre right), E > 16 MeV (lower left) and E > 20 MeV (lower right). The data/MC ratio is shown in the lower panel of each figure.

A.3 LINAC Calibration of Positron Observables

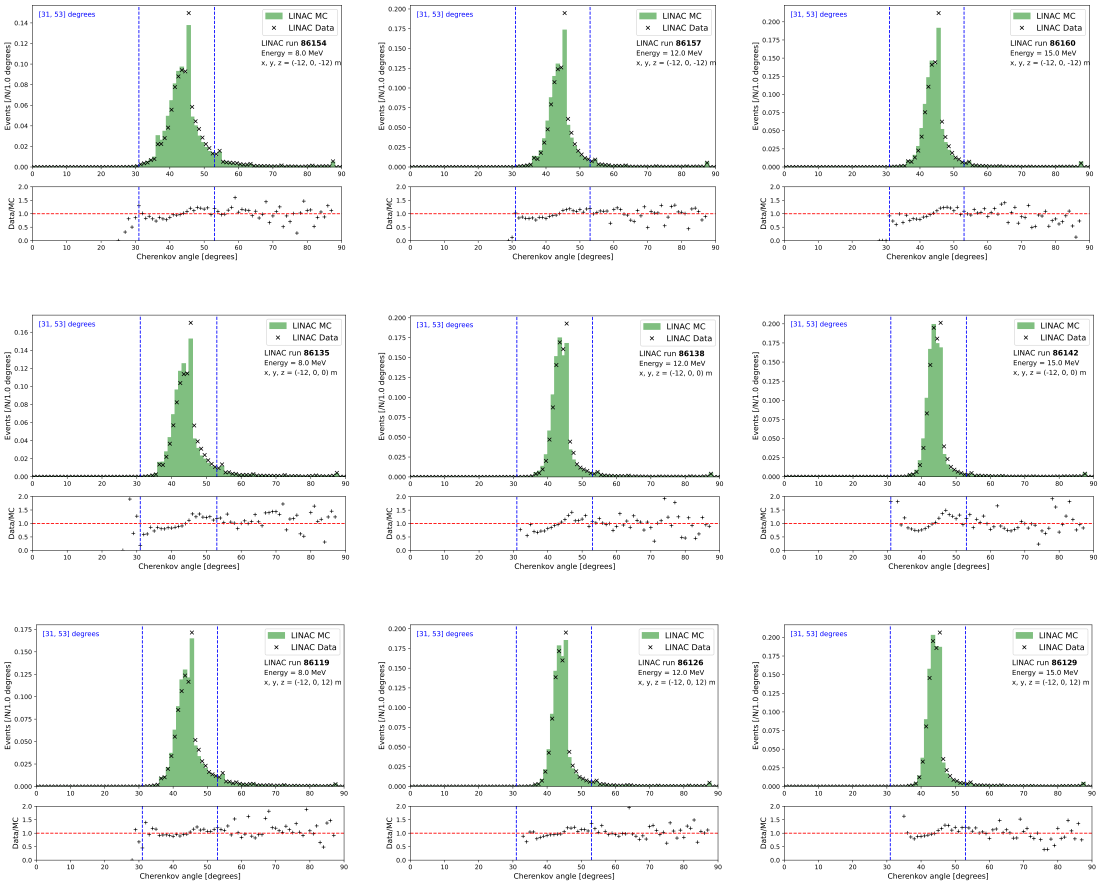

Figure A.2: Distribution of the Cherenkov angle θ_C in the LINAC MC (green) and data (black points) calibration samples. The cut window $\theta_C \in [31°, 53°]$ is displayed as two vertical blue lines. The data/MC ratio is shown in the below panel of each figure. The LINAC energy is E = 8 MeV (left), E = 12 MeV (centre), and E = 15 MeV (right). The LINAC positions shown are z = 12 m (top), z = 0 m (centre), and z = 12 m (bottom).

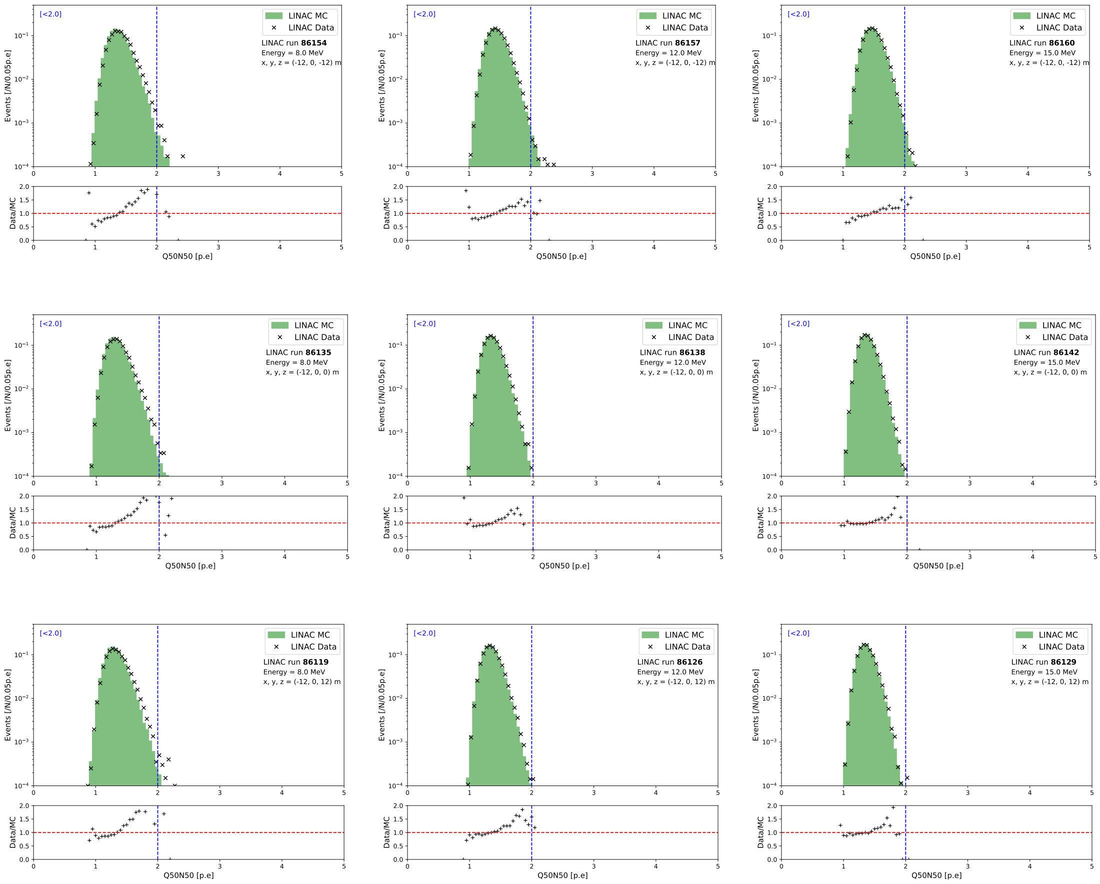

Figure A.3: Distribution of the *q50n50* in LINAC MC (green) and data (black points) calibration samples with $E = 12$ MeV. The vertical blue line represents the *q50n50* < 2 cut. The data/MC ratio is shown in the below panel of each figure. The LINAC energy is E = 8 MeV (left), E = 12 MeV (centre), and E = 15 MeV (right). The LINAC positions shown are z = 12 m (top), z = 0 m (centre), and z = 12 m (bottom).

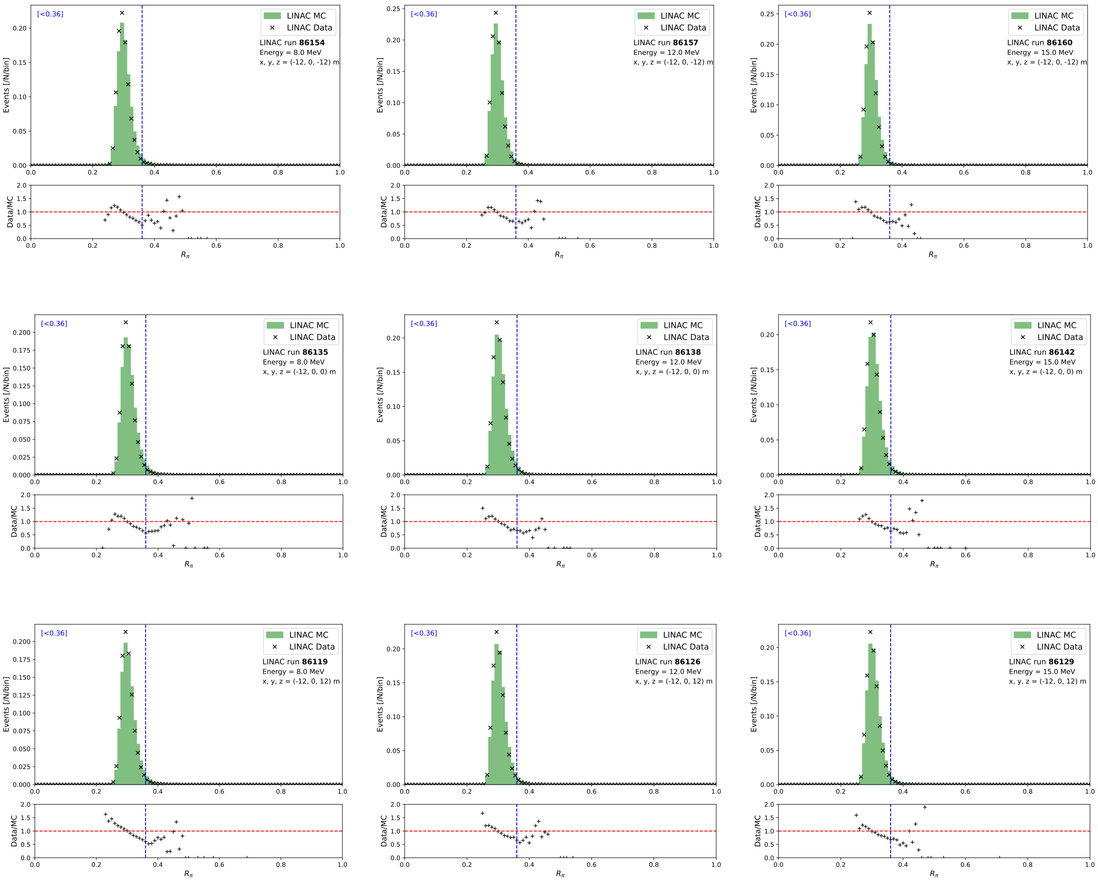

Figure A.4: Distribution of the R_π in the LINAC MC (green) and data (black points) calibration samples. The cut $R_\pi < 0.36$ is displayed as a vertical blue line. The data/MC ratio is shown in the below panel. The LINAC energy is E = 8 MeV (left), E = 12 MeV (centre), and E = 15 MeV (right). The LINAC positions shown are z = 12 m (top), z = 0 m (centre), and z = 12 m (bottom).

B

BabyK Supplementary Materials

This appendix documents supplementary information for the BabyK setup in Chapter 12. It includes a derivation of the solid angle formula used for the muon telescope, supplementary circuit diagrams of the electronics board, simulations of the BabyK setup and a theoretical overview of the Fresnel equations.

B.1 Solid Angle Calculation

The geometric configuration of the plastic scintillator paddles is illustrated in Figure B.1. The solid angle acceptance (Ω) for incident muons to trigger coincident detection in both scintillators is determined by considering a projected area (A_P) as seen from an arbitrary point (P). The differential of the projected area (dA_P) is calculated as

$$dA_\mathrm{P} = dA \cdot \cos(\theta) = dA \cdot \frac{z}{R}, \tag{B.1}$$

where θ is the angle between the detector surface and the line of sight to point P, z is the perpendicular distance halfway between the detectors, dA is the differential area in the x-y plane and R is the distance of the line projected from dA to point P. The differential solid angle ($d\Omega$) is then determined from the following relation

$$d\Omega = \frac{dA_\mathrm{P}}{R^2} = \frac{z dA}{R^3} = \frac{z dx dy}{(x^2 + y^2 + z^2)^{\frac{3}{2}}}. \tag{B.2}$$

If we consider point P as the fixed midway between the two detectors then the expression in Equation B.2 can be integrated as

$$\Omega = 4z \int_0^{\frac{L}{2}} \int_0^{\frac{W}{2}} \frac{1}{(x^2+y^2+z^2)^{\frac{3}{2}}}\, dx\, dy, \tag{B.3}$$

to give

$$\Omega = 4\tan^{-1}\left(\frac{WL}{2H\sqrt{\left(\frac{W}{2}\right)^2 + \left(\frac{L}{2}\right)^2 + \left(\frac{H}{2}\right)^2}} \right), \tag{B.4}$$

where the paddle width (W) and length (L) as well as separation height (H) are substituted into the expression [208].

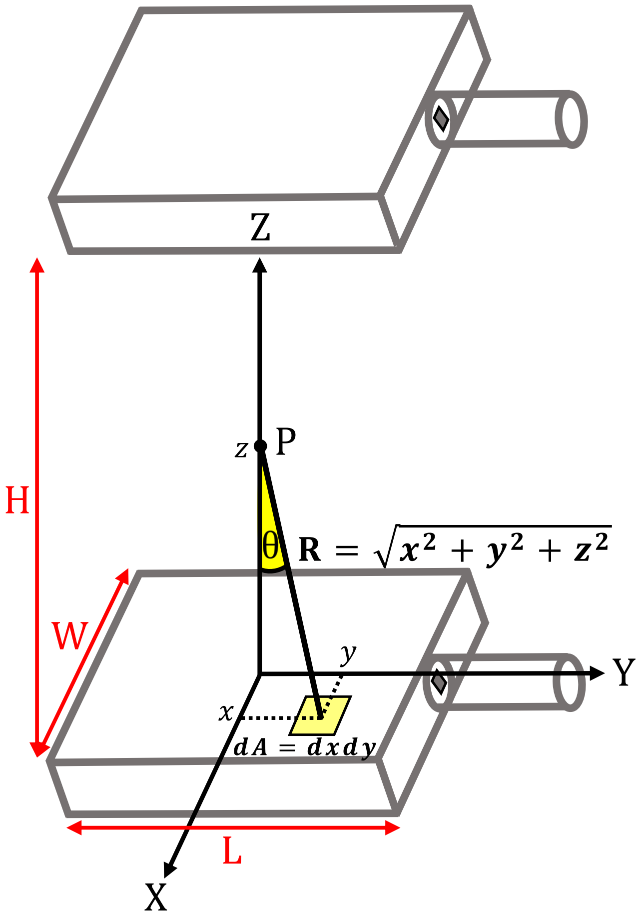

Figure B.1: Schematic diagram of the solid angle subtended by a 2D plane between two plastic scintillator paddles.

B.2 Electronics Boards

The schematic circuit diagrams for the USB input and ESP32 microcontroller boards are shown in Figure B.2 and Figure B.3, respectively.

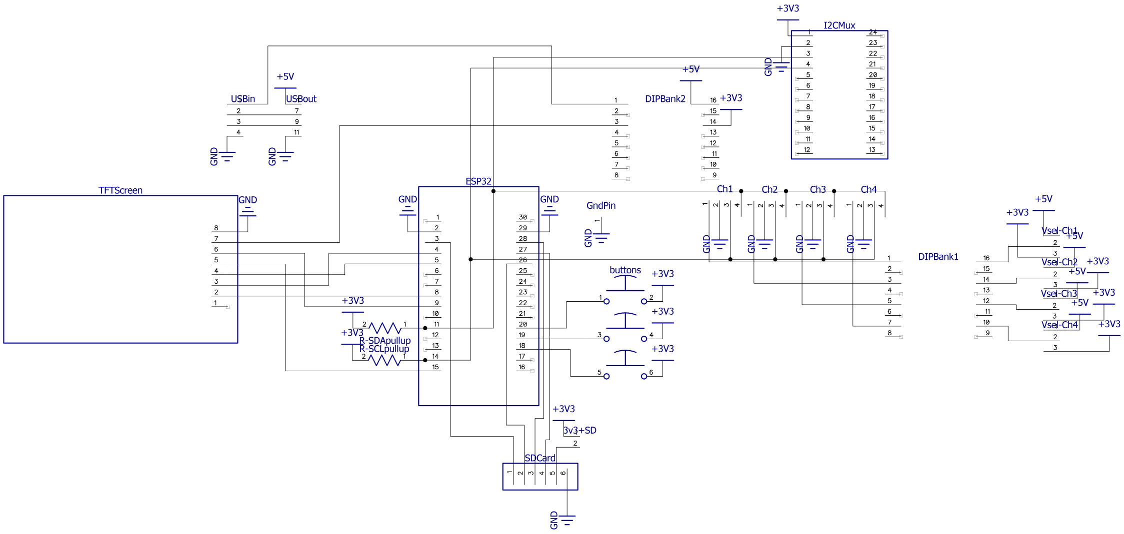

Figure B.2: Circuit diagram of the ESP32 microcontroller board with an LED screen.

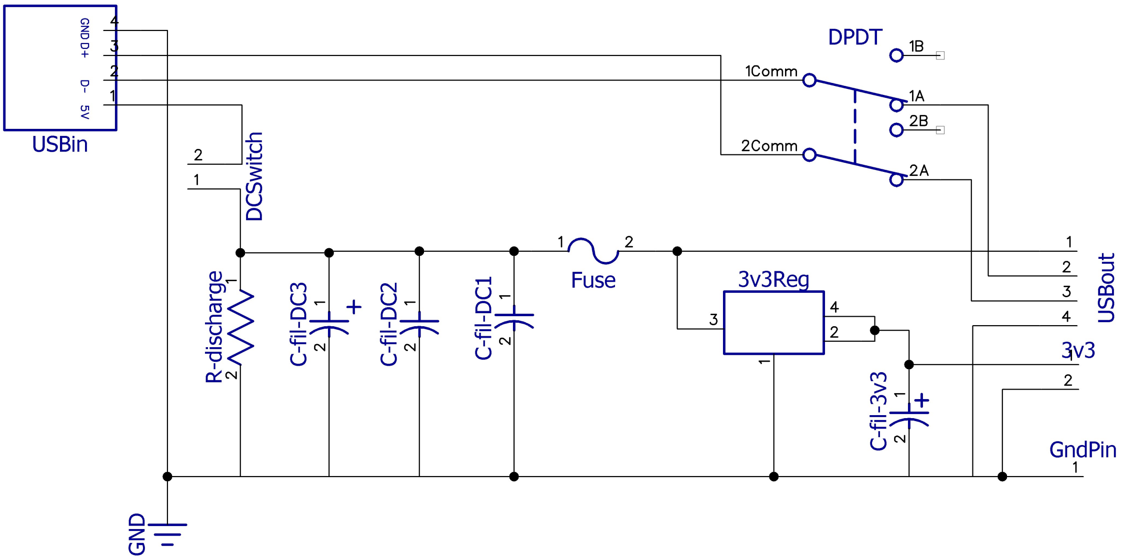

Figure B.3: Circuit diagram of the USB input board.

B.3 Simulations of the BabyK Photosensor

The photosensor geometry has been studied in a GEANT4 simulation of the BabyK tank setup [209]. The implemented structure consists of a 57.2 × 85.1 cm cylindrical volume of ultra-pure water, with an outer shell opaque to light and a photosensor unit. Water optical properties are obtained from SKDetSim, which includes the refraction and absorption spectrum between 300 - 700 nm [56]. The 3-inch hemispherical and flat-faced PMT is modelled using the quantum efficiency from the HZC XP72B2F PMT's spectra[1]. Optical parameters of the WLS plate and reflective tape are tuned using experimental measurements of a Kuraray B2 WLS plate [177]. One million optical photons are simulated homogeneously across a square plane directly below the WLS plate, with an energy between 3.34 – 3.36 eV to emulate Cherenkov light production from muons.

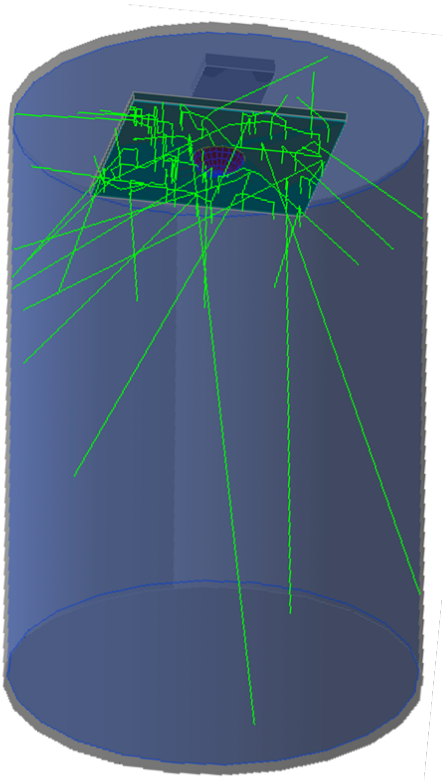

Figure B.4: Visualisation of the BabyK tank with the hemispherical PMT-WLS plate photosensor geometry simulated in GEANT4. Optical photons (green) are incident on the WLS plate.

---

[1] HZC Photonics has ceased manufacturing since 2020.

Figure B.5 shows the emission points of detected photons across the X-Y plane for each photosensor configuration. The highest concentration of detected photons originates directly below the PMT, with the efficiency dropping for increasing radial distance from the centre. The addition of 95% specular reflective tape to the outer edges improves the statistical response of the photosensor. On average, the flat-faced photosensor unit has a lower collection efficiency due to shadowing effects.

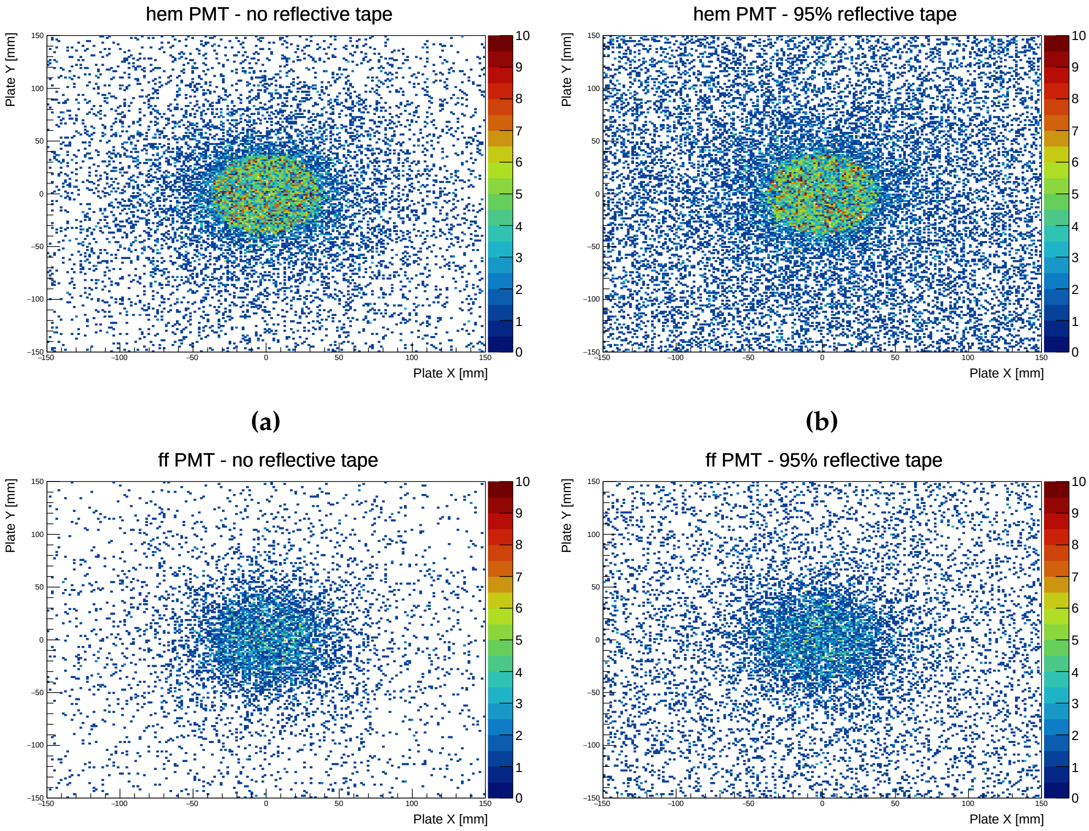

(a) (b)

(c) (d)

Figure B.5: The emission points of detected photons across the X-Y plane of a hemispherical and flat-faced photosensor geometry using the Kuraray B2 WLS plate with and without reflective tape, titled accordingly.

B.4 Fresnel Equations

The proportion of light reflected at an interface between two media is determined using the Fresnel equations, which are polarisation dependent [207]. For photons propagating across an optical boundary with refractive indices of n_1 and n_2, the reflection coefficients are

$$R_s = \left| \frac{n_1 \cos(\theta_1) - n_2 \cos(\theta_2)}{n_1 \cos(\theta_1) + n_2 \cos(\theta_2)} \right|^2, \tag{B.5}$$

$$R_p = \left| \frac{n_1 \cos(\theta_2) - n_2 \cos(\theta_1)}{n_1 \cos(\theta_2) + n_2 \cos(\theta_1)} \right|^2, \tag{B.6}$$

where R_s is for the s-polarisation (parallel), R_p is for the p-polarisation (perpendicular) and θ_1 and θ_2 are the propagation angles with respect to the normal of the surface plane. For unpolarised light, the effective reflection coefficient is calculated by taking the average

$$R_{\text{eff}} = \frac{1}{2}(R_s + R_p). \tag{B.7}$$

At normal incidence ($\theta_1 = \theta_2 = 0$), it is not required to distinguish between parallel and perpendicular polarisations. Thus, the reflection coefficient simplifies to

$$R = \left| \frac{n_1 - n_2}{n_1 + n_2} \right|^2. \tag{B.8}$$

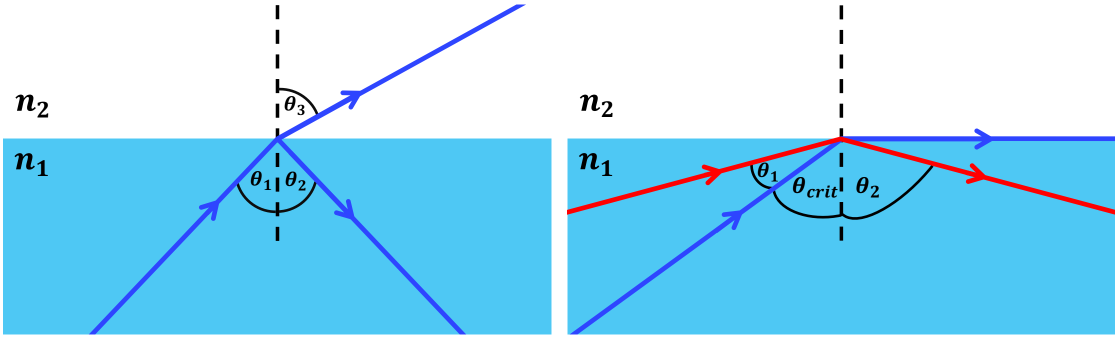

(a) Light incident with angle θ_1, which is partially reflected by θ_2 and transmitted by θ_3.

(b) Light undergoing TIR with incident angle $\theta_1 > \theta_{\text{crit}}$.

Figure B.6: Reflection and transmission of light at an optical boundary where $n_1 > n_2$.

References

[1] Karolina Rozwadowska, Francesco Vissani, and Enrico Cappellaro. “On the rate of core collapse supernovae in the milky way”. In: *New Astron.* 83 (2021), p. 101498. arXiv: `2009.03438 [astro-ph.HE]`.

[2] Wolfgang Pauli. “Über den Zusammenhang des Abschlusses der Elektronengruppen im Atom mit der Komplexstruktur der Spektren”. In: *Zeitschrift für Physik* 31.1 (1925), pp. 765–783.

[3] B. Pontecorvo. “Inverse Beta Processes and Nonconservation of Lepton Charge”. In: *Sov. Phys. JETP* 26 (1962), p. 984.

[4] Z. Maki, M. Nakagawa, and S. Sakata. “Remarks on the unified model of elementary particles”. In: *Prog. Theor. Phys.* 28 (1962), p. 870.

[5] Yasuo Takeuchi. “Recent results and future prospects of Super-Kamiokande”. In: *Nuclear Instruments and Methods in Physics Research Section A: Accelerators, Spectrometers, Detectors and Associated Equipment* 952 (2020). 10th International Workshop on Ring Imaging Cherenkov Detectors (RICH 2018), p. 161634. URL: `https://www.sciencedirect.com/science/article/pii/S0168900218317200`.

[6] B. Aharmim et al. “Combined analysis of all three phases of solar neutrino data from the Sudbury Neutrino Observatory”. In: *Physical Review C* 88 (Aug. 2013).

[7] A. Gando et al. “Reactor on-off antineutrino measurement with KamLAND”. In: *Physical Review D* 88 (Aug. 2013), p. 033001.

[8] D. Adey et al. “Measurement of the electron antineutrino oscillation with 1958 days of operation at daya bay”. In: *Physical Review Letters* 121 (2018), p. 241805.

[9] The T2K Collaboration. “Constraint on the matter–antimatter symmetry-violating phase in neutrino oscillations”. In: *Nature* 580 (2020), pp. 339–344.

[10] W. Baade and F. Zwicky. “Cosmic rays from super-novae”. In: *Proceedings of the National Academy of Sciences* 20 (1934), pp. 259–263.

[11] W. Baade and F. Zwicky. “Remarks on super-novae and cosmic rays”. In: *Physical Review* 46 (1934), pp. 76–77.

[12] Hans-Thomas Janka. “Neutrino-Driven Explosions”. In: *Handbook of Supernovae*. Springer International Publishing, 2017, 1095–1150.

[13] F. Hoyle and William A. Fowler. “Nucleosynthesis in Supernovae.” In: *apj* 132 (Nov. 1960), p. 565.

[14] E. Margaret Burbidge et al. “Synthesis of the Elements in Stars”. In: *Rev. Mod. Phys.* 29 (4 Oct. 1957), pp. 547–650.

[15] Stirling A. Colgate and Richard H. White. “The Hydrodynamic Behavior of Supernovae Explosions”. In: *apj* 143 (Mar. 1966), p. 626.

[16] J. R. Wilson. “Supernovae and post-collapse behavior”. In: *Numerical Astrophysics*. Ed. by J. M. Centrella, J. M. Leblanc, and R. L. Bowers. Boston: Jones and Bartlett Publishers, 1985, pp. 422–434.

[17] Rudolph Minkowski. “Spectra of Supernovae”. In: *Publications of the Astronomical Society of the Pacific* 53.314 (1941), p. 224.

[18] Yosuke Ashida. “Measurement of Neutrino and Antineutrino Neutral-Current Quasielastic-like Interactions and Applications to Supernova Relic Neutrino Searches”. PhD thesis. Kyoto U., 2020.

[19] K. Nomoto. “Evolution of 8-10 solar mass stars toward electron capture supernovae. I - Formation of electron-degenerate O + NE + MG cores.” In: *apj* 277 (Feb. 1984), pp. 791–805.

[20] Thierry Foglizzo. “Explosion Physics of Core-Collapse Supernovae”. In: *Handbook of Supernovae*. Ed. by Anas Alsabti and Paul Murdin. Cham: Springer, 2016.

[21] Stuart L. Shapiro and Saul A. Teukolsky. *Black Holes, White Dwarfs, and Neutron Stars: The Physics of Compact Objects*. Wiley, July 1983.

[22] Sean M. Couch. “The mechanism(s) of core-collapse supernovae”. In: *Philosophical Transactions of the Royal Society A* 375 (2017), p. 20160271.

[23] T. Totani et al. “Future detection of supernova neutrino burst and explosion mechanism”. In: *Astrophys. J.* 496 (1998), pp. 216–225. arXiv: `astro-ph/9710203`.

[24] Marc Herant et al. “Inside the Supernova: A Powerful Convective Engine”. In: *apj* 435 (Nov. 1994), p. 339. arXiv: `astro-ph/9404024 [astro-ph]`.

[25] John M. Blondin, Anthony Mezzacappa, and Christine DeMarino. “Stability of Standing Accretion Shocks, with an Eye toward Core-Collapse Supernovae”. In: *apj* 584.2 (Feb. 2003), pp. 971–980. arXiv: `astro-ph/0210634 [astro-ph]`.

[26] J. R. Wilson, G. J. Mathews, and H. E. Dalhed. “On Rapidly Rotating Magnetic Core-Collapse Supernovae”. In: *The Astrophysical Journal* 628.1 (July 2005), p. 335.

[27] Ken’ichiro Nakazato et al. “Supernova neutrino light curves and spectra for various progenitor stars: from core collapse to proto-neutron star cooling”. In: *The Astrophysical Journal Supplement Series* 205.1 (Feb. 2013), p. 2.

[28] John F. Beacom. “The Diffuse Supernova Neutrino Background”. In: *Annual Review of Nuclear and Particle Science* 60.1 (2010), pp. 439–462.

[29] Ken’ichiro Nakazato and et al. “Spectrum of the supernova relic neutrino background and metallicity evolution of galaxies”. In: *The Astrophysical Journal* 804.1 (June 2015), p. 75.

[30] Shunsaku Horiuchi and et al. “Diffuse supernova neutrino background from extensive core-collapse simulations of 8–100 M progenitors”. In: *Monthly Notices of the Royal Astronomical Society* 475.1 (Dec. 2017), pp. 1363–1374.

[31] Steven Weinberg. *Cosmology*. 1st. Oxford University Press, 2008.

[32] S. P. Mikheyev and A. Y. Smirnov. “Resonance amplification of oscillations in matter and solar-neutrino spectroscopy”. In: *Nuclear Physics B* 276.1 (1986), pp. 1–12.

[33] S. Galais and et al. “Shock waves in supernovae: New implications on the diffuse supernova neutrino background”. In: *Physical Review D* 81 (Mar. 2010), p. 053002.

[34] Zahra Tabrizi and Shunsaku Horiuchi. “Flavor triangle of the diffuse supernova neutrino background”. In: *Journal of Cosmology and Astroparticle Physics* 2021.05 (June 2021), p. 011.

[35] Daniel Kresse, Thomas Ertl, and Hans-Thomas Janka. “Stellar collapse diversity and the diffuse supernova neutrino background”. In: *The Astrophysical Journal* 909.2 (Mar. 2021), p. 169.

[36] Manoj Kaplinghat, Gary Steigman, and Terry P Walker. “Supernova relic neutrino background”. In: *Physical Review D* 62 (July 2000), p. 043001.

[37] Shunsaku Horiuchi, John F. Beacom, and Eli Dwek. “The Diffuse Supernova Neutrino Background is detectable in Super-Kamiokande”. In: *Phys. Rev. D* 79 (2009), p. 083013. arXiv: `0812.3157 [astro-ph]`.

[38] Shin’ichiro Ando, Katsuhiko Sato, and Tomonori Totani. “Detectability of the supernova relic neutrinos and neutrino oscillation”. In: *Astroparticle Physics* 18.4 (2003), pp. 307–318.

[39] Cecilia Lunardini. “Diffuse neutrino flux from failed supernovae”. In: *Physical Review Letters* 102 (June 2009), p. 231101.

[40] Robert A Malaney. “Evolution of the cosmic gas and the relic supernova neutrino background”. In: *Astroparticle Physics* 7.1 (1997), pp. 125–136.

[41] D. H. Hartmann and S. E. Woosley. “The cosmic supernova neutrino background”. In: *Astroparticle Physics* 7.1 (1997), pp. 137–146.

[42] M. Harada et al. “Search for Astrophysical Electron Antineutrinos in Super-Kamiokande with 0.01% Gadolinium-loaded Water”. In: *Astrophys. J. Lett.* 951.2 (2023), p. L27. arXiv: `2305.05135 [astro-ph.HE]`.

[43] M. Malek et al. “Search for Supernova Relic Neutrinos at Super-Kamiokande”. In: *Phys. Rev. Lett.* 90 (6 Feb. 2003), p. 061101.

[44] K. Bays et al. “Supernova relic neutrino search at super-Kamiokande”. In: *Phys. Rev. D* 85 (5 Mar. 2012), p. 052007. URL: `https://link.aps.org/doi/10.1103/PhysRevD.85.052007`.

[45] H. Zhang et al. “Supernova Relic Neutrino search with neutron tagging at Super-Kamiokande-IV”. In: *Astroparticle Physics* 60 (2015), pp. 41–46. URL: `https://www.sciencedirect.com/science/article/pii/S0927650514000681`.

[46] S. Abe et al. “Limits on Astrophysical Antineutrinos with the KamLAND Experiment”. In: *The Astrophysical Journal* 925.1 (Jan. 2022), p. 14. URL: `https://dx.doi.org/10.3847/1538-4357/ac32c1`.

[47] K. Abe et al. “Diffuse supernova neutrino background search at Super-Kamiokande”. In: *Phys. Rev. D* 104.12 (2021), p. 122002. arXiv: `2109.11174 [astro-ph.HE]`.

[48] “The Super-Kamiokande detector, K. Abe et al”. In: *Nuclear Instruments and Methods in Physics Research Section A: Accelerators, Spectrometers, Detectors and Associated Equipment* 501.2 (2003), pp. 418–462.

[49] Ilya M. Frank and Igor Y. Tamm. “Coherent Visible Radiation of Fast Electrons Passing Through Matter”. In: *Comptes Rendus de l’Académie des Sciences de l’URSS* 14 (1937), pp. 109–114.

[50] Alberto Giampaolo. “À la recherche du fond diffus de neutrinos de supernovas avec Super-Kamiokande : dernières analyses et perspectives pour l’ère du Gdlatest searches and prospects for the Gd era”. Theses. Institut Polytechnique de Paris, Jan. 2023.

[51] H. Kume et al. “20 inch diameter photomultiplier”. In: *Nuclear Instruments and Methods in Physics Research* 205.3 (1983), pp. 443–449. URL: `https://www.sciencedirect.com/science/article/pii/0167508783900078`.

[52] R. Becker-Szendy et al. “IMB-3: a large water Cherenkov detector for nucleon decay and neutrino interactions”. In: *Nuclear Instruments and Methods in Physics Research Section A: Accelerators, Spectrometers, Detectors and Associated Equipment* 324.1 (1993), pp. 363–382. URL: `https://www.sciencedirect.com/science/article/pii/016890029390998W`.

[53] Y. Nakano et al. “Measurement of the radon concentration in purified water in the Super-Kamiokande IV detector”. In: *Nuclear Instruments and Methods in Physics Research Section A: Accelerators, Spectrometers, Detectors and Associated Equipment* 977 (2020), p. 164297.

[54] K. Abe aet al. “First gadolinium loading to Super-Kamiokande”. In: *Nuclear Instruments and Methods in Physics Research Section A: Accelerators, Spectrometers, Detectors and Associated Equipment* 1027 (2022), p. 166248. URL: `https://doi.org/10.1016%2Fj.nima.2021.166248`.

[55] H. Nishino et al. “High-speed charge-to-time converter ASIC for the Super-Kamiokande detector”. In: *Nuclear Instruments and Methods in Physics Research Section A: Accelerators, Spectrometers, Detectors and Associated Equipment* 610.3 (Nov. 2009), 710–717. URL: `http://dx.doi.org/10.1016/j.nima.2009.09.026`.

[56] K. Abe et al. “Calibration of the Super-Kamiokande detector”. In: *Nuclear Instruments and Methods in Physics Research Section A: Accelerators, Spectrometers, Detectors and Associated Equipment* 737 (2014), pp. 253–272. URL: `https://www.sciencedirect.com/science/article/pii/S016890021301646X`.

[57] K.A. Olive and et al. (Particle Data Group). “Review of Particle Physics”. In: *Chin. Phys. C* 38.9 (2014), p. 090001. URL: `http://pdg.lbl.gov`.

[58] T. K. Gaisser and M. Honda. “Flux of atmospheric neutrinos”. In: *Ann. Rev. Nucl. Part. Sci.* 52 (2002), pp. 153–199. arXiv: `hep-ph/0203272 [hep-ph]`.

[59] M. Honda et al. “Improvement of low energy atmospheric neutrino flux calculation using the JAM nuclear interaction model”. In: *Phys. Rev. D* 83 (12 June 2011), p. 123001. URL: `https://link.aps.org/doi/10.1103/PhysRevD.83.123001`.

[60] J. Alcaraz et al. “Helium in near Earth orbit”. In: *Physics Letters B* 494.3 (2000), pp. 193–202. URL: `https://www.sciencedirect.com/science/article/pii/S037026930001193X`.

[61] S. Haino et al. "Measurements of primary and atmospheric cosmic-ray spectra with the BESS-TeV spectrometer". In: *Physics Letters B* 594.1 (2004), pp. 35–46. URL: `https://www.sciencedirect.com/science/article/pii/S0370269304007567`.

[62] T. Gaisser et al. "Primary spectrum to 1 TeV and beyond". In: *Proceedings of the 27th International Cosmic Ray Conference*. Aug. 2001, p. 1643.

[63] Morihiro Honda et al. "A New calculation of the atmospheric neutrino flux in a 3-dimensional scheme". In: *Phys. Rev. D* 70 (2004), p. 043008. arXiv: `astro-ph/0404457`.

[64] Robert C. Reedy. "Meteorites, Cosmic Ray Record". In: *Encyclopedia of Physical Science and Technology (Third Edition)*. Ed. by Robert A. Meyers. Third Edition. New York: Academic Press, 2003. Chap. A Nature of Cosmic Rays, pp. 575–601. URL: `https://www.sciencedirect.com/science/article/pii/B012227410500435X`.

[65] Thomas Wester. *Discerning the neutrino mass ordering using atmospheric neutrinos in Super-Kamiokande I-V*. 2023. URL: `https://open.bu.edu/handle/2144/46427`.

[66] E. Thebault et al. "International Geomagnetic Reference Field: The 12th Generation". In: *Earth, Planets and Space* 67 (2015), pp. 1–19.

[67] NOAA, U. and Force, U. A. *US Standard Atmosphere, 1976*. Tech. rep. NOAA-S/T. National Oceanic and Atmospheric Administration (NOAA), 1976.

[68] Stefan Roesler, Ralph Engel, and Johannes Ranft. "The Monte Carlo event generator DPMJET-III". In: *International Conference on Advanced Monte Carlo for Radiation Physics, Particle Transport Simulation and Applications (MC 2000)*. Dec. 2000, pp. 1033–1038. arXiv: `hep-ph/0012252`.

[69] A. Capella et al. "Dual parton model". In: *Physics Reports* 236.4 (1994), pp. 225–329. URL: `https://www.sciencedirect.com/science/article/pii/0370157394900647`.

[70] Koji Niita et al. "PHITS—a particle and heavy ion transport code system". In: *Radiation Measurements* 41.9 (2006). Space Radiation Transport, Shielding, and Risk Assessment Models, pp. 1080–1090. URL: `https://www.sciencedirect.com/science/article/pii/S1350448706001351`.

[71] K. Abe et al. "Atmospheric neutrino oscillation analysis with external constraints in Super-Kamiokande I-IV". In: *Phys. Rev. D* 97 (7 Apr. 2018), p. 072001. URL: `https://link.aps.org/doi/10.1103/PhysRevD.97.072001`.

[72] Yoshinari Hayato. "A neutrino interaction simulation program library NEUT". In: *Acta Phys. Polon. B* 40 (2009). Ed. by Arthur Ankowski and Jan Sobczyk, pp. 2477–2489.

[73] G L Fogli et al. "Probing supernova shock waves and neutrino flavour transitions in next-generation water Cherenkov detectors". In: *Journal of Cosmology and Astroparticle Physics* 2005.04 (Apr. 2005), p. 002.

[74] C.H. Llewellyn Smith. "Neutrino reactions at accelerator energies". In: *Physics Reports* 3.5 (1972), pp. 261–379. URL: `https://www.sciencedirect.com/science/article/pii/0370157372900105`.

[75] R.A. Smith and E.J. Moniz. "Neutrino reactions on nuclear targets". In: *Nuclear Physics B* 43 (1972), pp. 605–622. URL: `https://www.sciencedirect.com/science/article/pii/0550321372900405`.

[76] Yusuke Koshio. "Observation of Atmospheric Neutrinos". In: *Universe* 6.6 (2020). URL: `https://www.mdpi.com/2218-1997/6/6/80`.

[77] Artur M. Ankowski et al. "Analysis of γ-ray production in neutral-current neutrino-oxygen interactions at energies above 200 MeV". In: *Phys. Rev. Lett.* 108 (2012), p. 052505. arXiv: `1110.0679 [nucl-th]`.

[78] Omar Benhar et al. "Electron- and neutrino-nucleus scattering in the impulse approximation regime". In: *Phys. Rev. D* 72 (5 Sept. 2005), p. 053005. URL: `https://link.aps.org/doi/10.1103/PhysRevD.72.053005`.

[79] R. Bradford et al. "A New Parameterization of the Nucleon Elastic Form Factors". In: *Nuclear Physics B - Proceedings Supplements* 159 (2006). Proceedings of the 4th International Workshop on Neutrino-Nucleus Interactions in the Few-GeV Region, pp. 127–132. URL: `https://www.sciencedirect.com/science/article/pii/S0920563206005184`.

[80] S. Sakai et al. "Measurement of the neutrino-oxygen neutral-current quasielastic cross section using atmospheric neutrinos in the SK-Gd experiment". In: *Phys. Rev. D* 109.1 (2024), p. L011101. arXiv: `2311.03842 [hep-ex]`.

[81] L. Wan et al. "Measurement of the neutrino-oxygen neutral-current quasielastic cross section using atmospheric neutrinos at Super-Kamiokande". In: *Phys. Rev. D* 99.3 (2019), p. 032005. arXiv: `1901.05281 [hep-ex]`.

[82] K. Kobayashi et al. "De-excitation gamma-rays from the s-hole state in N-15 associated with proton decay in O-16". In: (Apr. 2006). arXiv: `nucl-ex/0604006`.

[83] A. A. Aguilar-Arevalo et al. "First measurement of the muon neutrino charged current quasielastic double differential cross section". In: *Phys. Rev. D* 81 (9 June 2010), p. 092005. URL: `https://link.aps.org/doi/10.1103/PhysRevD.81.092005`.

[84] J. Nieves, I. Ruiz Simo, and M. J. Vicente Vacas. "Inclusive charged-current neutrino-nucleus reactions". In: *Phys. Rev. C* 83 (4 Apr. 2011), p. 045501. URL: `https://link.aps.org/doi/10.1103/PhysRevC.83.045501`.

[85] Dieter Rein and Lalit M Sehgal. "Neutrino-excitation of baryon resonances and single pion production". In: *Annals of Physics* 133.1 (1981), pp. 79–153. URL: `https://www.sciencedirect.com/science/article/pii/0003491681902426`.

[86] Ch. Berger and L. M. Sehgal. "Partially conserved axial vector current and coherent pion production by low energy neutrinos". In: *Phys. Rev. D* 79 (5 Mar. 2009), p. 053003. URL: `https://link.aps.org/doi/10.1103/PhysRevD.79.053003`.

[87] Torbjorn Sjostrand. "Pythia 5.7 and Jetset 7.4 Physics and Manual". In: (1995). CERN-TH/7112/93, CERN-TH/7112/93 (revised).

[88] M. Glück, E. Reya, and A. Vogt. "Dynamical Parton Distributions of the Proton and Small-x Physics". In: *Z. Phys. C - Particles and Fields* 67 (1995), pp. 433–447.

[89] A. Bodek and U. K. Yang. “Modeling neutrino and electron scattering cross-sections in the few GeV region with effective LO PDFs”. In: *AIP Conf. Proc.* 670.1 (2003). Ed. by U. Cotti, M. Mondragon, and G. Tavares-Velasco, pp. 110–117. arXiv: `hep-ex/0301036`.

[90] Alessandro Strumia and Francesco Vissani. “Precise quasielastic neutrino/nucleon cross-section”. In: *Phys. Lett. B* 564 (2003), pp. 42–54. arXiv: `astro-ph/0302055`.

[91] *SNOwGLoBES*. `http://webhome.phy.duke.edu/~schol/snowglobes/`. Last checked: 2019-11-18.

[92] Fumi Nakanishi et al. *Supernova burst and Diffuse Supernova Neutrino Background simulator for Water Cherenkov Detectors*. 2024. arXiv: `2402.00283 [astro-ph.IM]`.

[93] J. Allison et al. “Recent developments in Geant4”. In: *Nuclear Instruments and Methods in Physics Research Section A: Accelerators, Spectrometers, Detectors and Associated Equipment* 835 (2016), pp. 186–225. URL: `https://www.sciencedirect.com/science/article/pii/S0168900216306957`.

[94] Tomoyuki Tanaka et al. “Gamma-ray spectra from thermal neutron capture on gadolinium-155 and natural gadolinium”. In: *Progress of Theoretical and Experimental Physics* 2020.4 (Apr. 2020), p. 043D02. URL: `https://doi.org/10.1093/ptep/ptaa015`.

[95] Masayuki Nakahata et al. “Atmospheric Neutrino Background and Pion Nuclear Effect for KAMIOKA Nucleon Decay Experiment”. In: *Journal of the Physical Society of Japan* 55.11 (1986), pp. 3786–3805. URL: `https://doi.org/10.1143/JPSJ.55.3786`.

[96] A. S. Carroll et al. “Pion-nucleus total cross sections in the (3,3) resonance region”. In: *Phys. Rev. C* 14 (2 Aug. 1976), pp. 635–638. URL: `https://link.aps.org/doi/10.1103/PhysRevC.14.635`.

[97] E Bracci et al. *Compilation of cross-sections*. Updated version of CERN-HERA 70-04 and 70-06. Geneva: CERN, 1972. URL: `https://cds.cern.ch/record/111777`.

[98] M. Smy. “Low Energy Event Reconstruction and Selection in Super-Kamiokande-III”. In: *30th International Cosmic Ray Conference*. Vol. 5. July 2007, pp. 1279–1282.

[99] M. Shiozawa. “Reconstruction algorithms in the Super-Kamiokande large water Cherenkov detector”. In: *Nuclear Instruments and Methods in Physics Research Section A: Accelerators, Spectrometers, Detectors and Associated Equipment* 433.1 (1999), pp. 240–246. URL: `https://www.sciencedirect.com/science/article/pii/S0168900299003599`.

[100] Shantanu Desai. “High energy neutrino astrophysics with Super-Kamiokande”. PhD thesis. Boston U., 2004.

[101] Zoa Conner. “A Study of solar neutrinos using the Super-Kamiokande Detector”. PhD thesis. Maryland U., 1997.

[102] K. Abe et al. “Solar neutrino measurements using the full data period of Super-Kamiokande-IV”. In: (Dec. 2023). arXiv: `2312.12907 [hep-ex]`.

[103] Y. Koshio. “Data analysis for solar neutrinos observed by water Cherenkov detectors”. In: *Eur. Phys. J. A* 52 (2016), p. 84.

[104] J. Hosaka et al. "Solar neutrino measurements in Super-Kamiokande-I". In: *Phys. Rev. D* 73 (11 June 2006), p. 112001. URL: `https://link.aps.org/doi/10.1103/PhysRevD.73.112001`.

[105] J. Dumazert et al. "Gadolinium for neutron detection in current nuclear instrumentation research: A review". In: *Nuclear Instruments and Methods in Physics Research Section A: Accelerators, Spectrometers, Detectors and Associated Equipment* 882 (2018), pp. 53–68. URL: `https://www.sciencedirect.com/science/article/pii/S0168900217312421`.

[106] Glenn F. Knoll. *Radiation Detection and Measurement, 3rd ed.* 3rd edition. New York: John Wiley and Sons, 2000.

[107] "Measurement of atmospheric neutrino oscillation parameters by Super-Kamiokande I". In: *Phys. Rev. D* 71 (11 2005), p. 112005. URL: `https://link.aps.org/doi/10.1103/PhysRevD.71.112005`.

[108] K. Abe et al. "Measurement of the neutrino-oxygen neutral-current interaction cross section by observing nuclear deexcitation γ rays". In: *Phys. Rev. D* 90.7 (2014), p. 072012. arXiv: `1403.3140 [hep-ex]`.

[109] Cristiano Galbiati and John F. Beacom. "Measuring the cosmic ray muon-induced fast neutron spectrum by (n, p) isotope production reactions in underground detectors". In: *Phys. Rev. C* 72 (2 Aug. 2005), p. 025807. URL: `https://link.aps.org/doi/10.1103/PhysRevC.72.025807`.

[110] J. Hosaka et al. "Solar neutrino measurements in Super-Kamiokande-I". In: *Phys. Rev. D* 73 (11 June 2006), p. 112001. URL: `https://link.aps.org/doi/10.1103/PhysRevD.73.112001`.

[111] Shirley Weishi Li and John F. Beacom. "First calculation of cosmic-ray muon spallation backgrounds for MeV astrophysical neutrino signals in Super-Kamiokande". In: *Phys. Rev. C* 89 (2014), p. 045801. arXiv: `1402.4687 [hep-ph]`.

[112] Shirley Weishi Li and John F. Beacom. "Spallation backgrounds in Super-Kamiokande are made in muon-induced showers". In: *Phys. Rev. D* 91 (10 June 2015), p. 105005. URL: `https://link.aps.org/doi/10.1103/PhysRevD.91.105005`.

[113] Shirley Weishi Li and John F. Beacom. "Tagging spallation backgrounds with showers in water Cherenkov detectors". In: *Phys. Rev. D* 92 (10 Nov. 2015), p. 105033. URL: `https://link.aps.org/doi/10.1103/PhysRevD.92.105033`.

[114] G. Battistoni and et al. "The FLUKA code: description and benchmarking". In: *AIP Conference Proceedings*. Vol. 896. 1. Mar. 2007, pp. 31–49.

[115] T. Mueller. "The Double Chooz Experiment: Simulation of Reactor Antineutrino Spectra". TH. France: FRCEA, Sept. 2010.

[116] André de Gouvêa and Ivan Martinez-Soler. "Reactor Antineutrino Oscillations at Super-Kamiokande". In: *Phys. Lett. B* 809 (2020), p. 135751. arXiv: `2006.01155 [hep-ph]`.

[117] P. Vogel, L. Wen, and C. Zhang. "Neutrino oscillation studies with reactors". In: *Nature Communications* 6 (2015), p. 6935.

[118] Shota Izumiyama. “Measurement of electron antineutrino flux in Super-Kamiokande with gadolinium-loaded water”. PhD thesis. Tokyo Institute of Technology, 2024.

[119] Alexander Goldsack. “Reactor Neutrinos in a Gadolinium-Loaded Super-Kamiokande”. PhD thesis. University of Oxford, Oxford U., 2022.

[120] Marica Baldoncini et al. “Reference worldwide model for antineutrinos from reactors”. In: *Phys. Rev. D* 91.6 (2015), p. 065002. arXiv: `1411.6475 [physics.ins-det]`.

[121] S.J. Brice. *The Results of a Neural Network Statistical Event Class Analysis*. Technical Report SNO-STR-96-001. Oxford University, Jan. 1996.

[122] A. Aurisano et al. “A Convolutional Neural Network Neutrino Event Classifier”. In: *JINST* 11.09 (2016), P09001. arXiv: `1604.01444 [hep-ex]`.

[123] R. Acciarri et al. “Convolutional Neural Networks Applied to Neutrino Events in a Liquid Argon Time Projection Chamber”. In: *JINST* 12.03 (2017), P03011. arXiv: `1611.05531 [physics.ins-det]`.

[124] The Water Cherenkov Machine Learning (WatChMaL) group. URL: `https://www.watchmal.org`.

[125] Blair Jamieson et al. “Using machine learning to improve neutron identification in water Cherenkov detectors”. In: *Frontiers in big Data* 5 (2022), p. 978857.

[126] Nick Prouse. “Advances in simulation and reconstruction for Hyper-Kamiokande”. In: *PoS* 390 (2021), p. 919.

[127] D. Maksimović, M. Nieslony, and M. Wurm. “CNNs for enhanced background discrimination in DSNB searches in large-scale water-Gd detectors”. In: *Journal of Cosmology and Astroparticle Physics* 2021.11 (Nov. 2021), p. 051. URL: `http://dx.doi.org/10.1088/1475-7516/2021/11/051`.

[128] Christopher M. Bishop. *Pattern Recognition and Machine Learning (Information Science and Statistics)*. Berlin, Heidelberg: Springer-Verlag, 2006.

[129] Simon Haykin. *Neural Networks: A Comprehensive Foundation*. 2nd. USA: Prentice Hall PTR, 1998.

[130] F. Rosenblatt. *The Perceptron, a Perceiving and Recognizing Automaton Project Para*. Report: Cornell Aeronautical Laboratory. Cornell Aeronautical Laboratory, 1957. URL: `https://books.google.co.uk/books?id=P_XGPgAACAAJ`.

[131] Sepp Hochreiter. “The Vanishing Gradient Problem During Learning Recurrent Neural Nets and Problem Solutions”. In: *International Journal of Uncertainty, Fuzziness and Knowledge-Based Systems* 06.02 (1998), pp. 107–116. URL: `https://doi.org/10.1142/S0218488598000094`.

[132] Kunihiko Fukushima. “Visual Feature Extraction by a Multilayered Network of Analog Threshold Elements”. In: *IEEE Transactions on Systems Science and Cybernetics* 5.4 (1969), pp. 322–333.

[133] Vinod Nair and Geoffrey E. Hinton. “Rectified linear units improve restricted boltzmann machines”. In: *Proceedings of the 27th International Conference on International Conference on Machine Learning*. ICML’10. Omnipress, 2010, 807–814.

[134] P.Y. Simard, D. Steinkraus, and J.C. Platt. "Best practices for convolutional neural networks applied to visual document analysis". In: *Seventh International Conference on Document Analysis and Recognition, 2003. Proceedings.* 2003, pp. 958–963.

[135] Sebastian Ruder. "An overview of gradient descent optimization algorithms". In: *arXiv preprint arXiv:1609.04747* (2016).

[136] David E. Rumelhart, Geoffrey E. Hinton, and Ronald J. Williams. "Learning representations by back-propagating errors". In: *Nature* 323.6088 (1986), pp. 533–536.

[137] Léon Bottou, Frank E. Curtis, and Jorge Nocedal. *Optimization Methods for Large-Scale Machine Learning*. 2018. arXiv: `1606.04838 [stat.ML]`. URL: `https://arxiv.org/abs/1606.04838`.

[138] Xue Ying. "An Overview of Overfitting and its Solutions". In: *Journal of Physics: Conference Series* 1168.2 (Feb. 2019), p. 022022. URL: `https://dx.doi.org/10.1088/1742-6596/1168/2/022022`.

[139] Ian Goodfellow, Yoshua Bengio, and Aaron Courville. *Deep Learning*. `http://www.deeplearningbook.org`. MIT Press, 2016.

[140] Yann LeCun et al. "Backpropagation Applied to Handwritten Zip Code Recognition". In: *Neural Computation* 1.4 (1989), pp. 541–551.

[141] Chris and Hugh Bishop. *Deep Learning Foundations and Concepts*. 1st ed. Springer, 2023. URL: `https://link.springer.com`.

[142] Charu C. Aggarwal. *Neural Networks and Deep Learning: A Textbook*. Springer, 2021.

[143] MathWorks. *Introduction to Deep Learning: What Are Convolutional Neural Networks?* `https://uk.mathworks.com/videos/introduction-to-deep-learning-what-are-convolutional-neural-networks--1489512765771.html`.

[144] J. Pivarski et al. *uproot: ROOT I/O in pure Python and NumPy*. `https://github.com/scikit-hep/uproot`. 2023.

[145] Wes McKinney et al. *pandas: Powerful data analysis tools for Python*. `https://github.com/pandas-dev/pandas`. 2023.

[146] Kaiming He et al. "Deep Residual Learning for Image Recognition". In: *Proceedings of the IEEE Conference on Computer Vision and Pattern Recognition (CVPR)*. IEEE. 2016, pp. 770–778. URL: `https://arxiv.org/abs/1512.03385`.

[147] Andrew Chappell and Leigh H. Whitehead. "Application of transfer learning to neutrino interaction classification". In: *The European Physical Journal C* 82.12 (Dec. 2022). URL: `http://dx.doi.org/10.1140/epjc/s10052-022-11066-6`.

[148] Kaiming He et al. "Identity Mappings in Deep Residual Networks". In: *European Conference on Computer Vision (ECCV)*. Springer. 2016, pp. 630–645. URL: `https://arxiv.org/abs/1603.05027`.

[149] Adam Paszke et al. *PyTorch: An Imperative Style, High-Performance Deep Learning Library*. `https://pytorch.org`. 2019.

[150] Diederik P. Kingma and Jimmy Ba. "Adam: A Method for Stochastic Optimization". In: *CoRR* abs/1412.6980 (2014). URL: `https://api.semanticscholar.org/CorpusID:6628106`.

[151] Tom Fawcett. "Introduction to the ROC curve". In: *Proceedings of the 14th International Conference on Machine Learning* 1 (2006), pp. 152–167.

[152] Masayuki Harada. "Development of Neutron Tagging Algorithm and Search for Supernova Relic Neutrino in SK-Gd Experiment". PhD thesis. Okayama University, 2023.

[153] Alice Coffani. "New studies on cosmogenic induced spallation background for Supernova relic neutrino search in the Super-Kamiokande experiment". English. PhD Thesis. Institut Polytechnique de Paris, 2021. eprint: `tel-03591741`.

[154] M. Shinoki et al. "Measurement of the cosmogenic neutron yield in Super-Kamiokande with gadolinium loaded water". In: *Phys. Rev. D* 107 (9 May 2023), p. 092009. URL: `https://link.aps.org/doi/10.1103/PhysRevD.107.092009`.

[155] K. Abe et al. "Measurement of neutrino and antineutrino oscillations by the T2K experiment including a new additional sample of ν_e interactions at the far detector". In: *Phys. Rev. D* 96.9 (2017). [Erratum: Phys.Rev.D 98, 019902 (2018)], p. 092006. arXiv: `1707.01048 [hep-ex]`.

[156] Masayuki Harada. "Evaluation of neutron tagging efficiency for SK-Gd experiment". In: *Proceedings of 41st International Conference on High Energy physics — PoS(ICHEP2022)*. Vol. 414. 2022, p. 1178.

[157] K. Abe et al. "Measurement of neutrino and antineutrino neutral-current quasielasticlike interactions on oxygen by detecting nuclear deexcitation γ rays". In: *Phys. Rev. D* 100 (11 Dec. 2019), p. 112009. URL: `https://link.aps.org/doi/10.1103/PhysRevD.100.112009`.

[158] M. Honda et al. "Calculation of atmospheric neutrino flux using the interaction model calibrated with atmospheric muon data". In: *Phys. Rev. D* 75 (4 Feb. 2007), p. 043006. URL: `https://link.aps.org/doi/10.1103/PhysRevD.75.043006`.

[159] O. Benhar et al. "Spectral function of finite nuclei and scattering of GeV electrons". In: *Nucl. Phys. A* 579 (1994), pp. 493–517.

[160] C.J. Horowitz and Brian D. Serot. "The relativistic two-nucleon problem in nuclear matter". In: *Nuclear Physics A* 464.4 (1987), pp. 613–699. URL: `https://www.sciencedirect.com/science/article/pii/0375947487903708`.

[161] C. Maieron et al. "Nuclear model effects in charged-current neutrino-nucleus quasielastic scattering". In: *Phys. Rev. C* 68 (4 Oct. 2003), p. 048501. URL: `https://link.aps.org/doi/10.1103/PhysRevC.68.048501`.

[162] J. A. Caballero et al. "Superscaling in Charged Current Neutrino Quasielastic Scattering in the Relativistic Impulse Approximation". In: *Phys. Rev. Lett.* 95 (25 Dec. 2005), p. 252502. URL: `https://link.aps.org/doi/10.1103/PhysRevLett.95.252502`.

[163] R. González-Jiménez et al. “Relativistic description of final-state interactions in neutral-current neutrino and antineutrino cross sections”. In: *Phys. Rev. C* 88 (2 Aug. 2013), p. 025502. URL: `https://link.aps.org/doi/10.1103/PhysRevC.88.025502`.

[164] J. E. Amaro et al. “Using electron scattering superscaling to predict charge-changing neutrino cross sections in nuclei”. In: *Phys. Rev. C* 71 (1 Jan. 2005), p. 015501. URL: `https://link.aps.org/doi/10.1103/PhysRevC.71.015501`.

[165] J. E. Amaro et al. “Superscaling and neutral current quasielastic neutrino-nucleus scattering”. In: *Phys. Rev. C* 73 (3 Mar. 2006), p. 035503. URL: `https://link.aps.org/doi/10.1103/PhysRevC.73.035503`.

[166] Andrea Meucci and Carlotta Giusti. “Final-state interaction effects in neutral-current neutrino and antineutrino cross sections at MiniBooNE kinematics”. In: *Phys. Rev. D* 89.5 (2014), p. 057302. arXiv: `1401.3650 [nucl-th]`.

[167] Ryosuke Akutsu. “A Study of Neutrons Associated with Neutrino and Antineutrino Interactions on the Water Target at the T2K Far Detector”. PhD thesis. Tokyo U., 2019.

[168] Y. Zhang et al. “First measurement of radioactive isotope production through cosmic-ray muon spallation in Super-Kamiokande IV”. In: *Phys. Rev. D* 93.1 (2016), p. 012004. arXiv: `1509.08168 [hep-ex]`.

[169] Shunsaku Horiuchi and et al. “Impact of binary interactions on the diffuse supernova neutrino background”. In: *Physical Review D* 103 (Feb. 2021), p. 043003.

[170] N. Ekanger and et al. “Impact of late-time neutrino emission on the diffuse supernova neutrino background”. In: *Physical Review D* 106 (Aug. 2022), p. 043026.

[171] Francesca Di Lodovico and. “The Hyper-Kamiokande Experiment”. In: *Journal of Physics: Conference Series* 888 (2017), p. 012020. URL: `https://doi.org/10.1088/1742-6596/888/1/012020`.

[172] Hyper-Kamiokande Proto-Collaboration and : *Hyper-Kamiokande Design Report*. 2018. URL: `https://arxiv.org/abs/1805.04163`.

[173] Yoshitaka Itow. “Construction status and prospects of the Hyper-Kamiokande project”. In: *PoS* ICRC2021 (2021), p. 1192.

[174] J.R. Wilson. “The Hyper-Kamiokande Experiment”. In: *Journal of Physics: Conference Series* 2156.1 (2021), p. 012153. URL: `https://doi.org/10.1088/1742-6596/2156/1/012153`.

[175] Kamioka Observatory, Institute for Cosmic Ray Research, University of Tokyo. *Hyper-Kamiokande Detector*. `https://www-sk.icrr.u-tokyo.ac.jp/en/hk/about/detector/`.

[176] Hyper-Kamiokande Collaboration. *OD Design Summary Report*. Technical Report Version 4. HK Technical Note 0055, 2 October 2023.

[177] Mahdi Taani. “Non-Standard Neutrino Interaction Analysis with Atmospheric Neutrino Data in Super-Kamiokande I-IV and the Design of the Hyper-Kamiokande Outer Detector”. Edinburgh Archive. PhD thesis. Nagoya University/The University of Edinburgh, Edinburgh U., 2020.

[178] Alex Goldsack for the OD Working Group (FD3). *Hyper-Kamiokande Tyvek Tech Note*. Tech. rep. King's College London, April 2023.

[179] Hyper-Kamiokande Collaboration. *OD WLS Plate Report*. Technical Report Version 1. HK Technical Note 0057, 6 October 2023.

[180] Y. Kudenko et al. "Development and tests of WLS plates for Outer Detector of Hyper-Kamiokande". In: *Nuclear Instruments and Methods in Physics Research Section A: Accelerators, Spectrometers, Detectors and Associated Equipment* 1045 (2023), p. 167543.

[181] J.R. Wilson and the Hyper-Kamiokande Collaboration. "The Hyper-Kamiokande Experiment". In: *Journal of Physics: Conference Series* 2156.1 (Dec. 2021), p. 012153. URL: `https://dx.doi.org/10.1088/1742-6596/2156/1/012153`.

[182] F. Di Lodovico et al. *Outer Detector Technical Report*. Technical Report Version 5.0. HK OD group, 28 March 2022.

[183] M Jiang et al. "Atmospheric neutrino oscillation analysis with improved event reconstruction in Super-Kamiokande IV". In: *Progress of Theoretical and Experimental Physics* 2019.5 (May 2019). URL: `http://dx.doi.org/10.1093/ptep/ptz015`.

[184] Lee Ka Pik. "Study of the neutrino mass hierarchy with the atmospheric neutrino data observed in Super-Kamiokande". PhD thesis. Tokyo U., 2012.

[185] F. Di Lodovico et al. *OD Strategy Task Force Report (ODSTF)*. Version 2 2 October 2023. Hyper-Kamiokande Collaboration.

[186] P. Soler and Z. H. Wang. "Optical properties of wavelength shifting panels". In: *Nucl. Instrum. Meth. A* 324 (1993), pp. 482–490.

[187] G. G. Stokes. "On the Change of Refrangibility of Light". In: *Philosophical Transactions of the Royal Society of London* 142 (1852), pp. 463–562. URL: `http://www.jstor.org/stable/108550` (visited on 01/02/2024).

[188] J.R. Albani. "Chapter 2 - Fluorescence: Principles and Observables". In: *Structure and Dynamics of Macromolecules: Absorption and Fluorescence Studies*. Ed. by J.R. Albani. Amsterdam: Elsevier Science, 2004, pp. 55–98. URL: `https://www.sciencedirect.com/science/article/pii/B9780444514493500022`.

[189] F Bryant. "Snell's Law of Refraction". In: *Physics Bulletin* 9.12 (Dec. 1958), p. 317. URL: `https://dx.doi.org/10.1088/0031-9112/9/12/004`.

[190] Xue-Feng Ding et al. "Measurement of the fluorescence quantum yield of bis-MSB". In: *Chin. Phys. C* 39.12 (2015), p. 126001. arXiv: `1506.00240 [physics.ins-det]`.

[191] L. S. B. "Handbook of fluorescence spectra of aromatic molecules . Isadore B. Berlman, Academic Press, New York and London, 2nd. edition, 1971, pp. xiv + 473, price £8.85". In: *Journal of Molecular Structure* 13.1 (July 1972), pp. 140–140.

[192] Katsushige Abe et al. "Scintillator ageing of the T2K near detectors from 2010 to 2021". In: *Journal of Instrumentation* 17 (Oct. 2022), P10028.

[193] Thomas G. Mayerhöfer, Susanne Pahlow, and Jürgen Popp. "The Bouguer-Beer-Lambert Law: Shining Light on the Obscure". In: *ChemPhysChem* 21.18 (2020), pp. 2029–2046.

[194] Christian-Alexander Bunge, Roman Kruglov, and Hans Poisel. "Rayleigh and Mie Scattering in Polymer Optical Fibers". In: *Lightwave Technol.* 24.8 (Aug. 2006).

[195] A. L. Fymat and K. D. Mease. "Mie forward scattering: improved semiempirical approximation with application to particle size distribution inversion". In: *Appl. Opt.* 20.2 (Jan. 1981), pp. 194–198.

[196] Hamamatsu Photonics K.K. *R6091 Series Photomultiplier Tube Data Sheet*. 2016.

[197] Donald E. Groom, Nikolai V. Mokhov, and Sergei I. Striganov. "Muon stopping power and range tables 10 MeV–100 TeV". In: *Atomic Data and Nuclear Data Tables* 78.2 (2001), pp. 183–356. URL: `https://www.sciencedirect.com/science/article/pii/S0092640X01908617`.

[198] Hamamatsu Photonics K.K. *Hamamatsu S14160-6050HS Multi-Pixel Photon Counter*. 2020.

[199] Nicoleta Dinu. "8 - Silicon photomultipliers (SiPM)". In: *Photodetectors*. Ed. by Bahram Nabet. Woodhead Publishing, 2016, pp. 255–294. URL: `https://www.sciencedirect.com/science/article/pii/B9781782424451000087`.

[200] Valeri Saveliev. "Silicon Photomultiplier - New Era of Photon Detection". In: *Advances in Optical and Photonic Devices*. Ed. by Ki Young Kim. Rijeka: IntechOpen, 2010. Chap. 14. URL: `https://doi.org/10.5772/7150`.

[201] Hamamatsu Photonics K.K. *Multi-Pixel Photon Counter (MPPC) - KAPD-9008E*. 2024. URL: `https://www.hamamatsu.com/content/dam/hamamatsu-photonics/sites/documents/99_SALES_LIBRARY/ssd/mppc_kapd9008e.pdf`.

[202] James Kelly Milam. "Single-Channel Analyzers". In: *Instrumentation in Applied Nuclear Chemistry*. Ed. by Jan Krugers. Boston, MA: Springer US, 1973, pp. 245–261. URL: `https://doi.org/10.1007/978-1-4684-1953-5_8`.

[203] Sergey V. Polyakov. "Chapter 3 - Photomultiplier Tubes". In: *Single-Photon Generation and Detection*. Ed. by Alan Migdall et al. Vol. 45. Experimental Methods in the Physical Sciences. Academic Press, 2013, pp. 69–82. URL: `https://www.sciencedirect.com/science/article/pii/B9780123876959000032`.

[204] Hamamatsu Photonics K.K. *Photomultiplier Tubes: Basics and Application*. 3rd. 2007.

[205] William Johnston. "Design, simulation, and prototyping of wavelength-shifting plate light collector for a large water Cherenkov detector". In: (Jan. 2014), p. 42.

[206] Dustin Hebecker. "Development of a single photon detector using wavelength-shifting and light-guiding technology". PhD thesis. Humboldt-Universität zu Berlin, Mathematisch-Naturwissenschaftliche Fakultät, 2021, pp. 36,37.

[207] J. Peatross and M. Ware. *Physics of Light and Optics*. 2015 edition. Available at optics.byu.edu. 2015, pp. 73–86.

[208] R.E. Pevey. *Lesson 2: Directions and Solid Angles*. NE 406 Radiation Protection and Shielding. `http://web.utk.edu/~rpevey/NE406/lesson2.htm`. 1998.

[209] S. Agostinelli et al. "Geant4—a simulation toolkit". In: *Nuclear Instruments and Methods in Physics Research Section A: Accelerators, Spectrometers, Detectors and Associated Equipment* 506.3 (2003), pp. 250–303.